Spectroscopy, Fabrication, and Electronic Characterization of Molecular Electronic Devices

DISSERTATION

Presented in Partial Fulfillment of the Requirements for the Degree Doctor of Philosophy in the Graduate School of The Ohio State University

By

Andrew Paul Bonifas

Graduate Program in Materials Science and Engineering

The Ohio State University

2011

Dissertation Committee:

Prof. Gerald S. Frankel, Advisor

Prof. Richard L. McCreery, Advisor

Prof. Roberto Myers

Prof. Nitin P. Padture

Abstract

Molecular electronics is the study of charge transport through single molecules or molecular ensembles. Molecular electronic junctions consist of single molecules or an ensemble of molecules positioned between two conducing contacts. To fabricate and measure the electronic properties of molecular junctions, several techniques have been employed such as scanning tunneling microscopy, conducting probe atomic force microscopy, and vapor deposition of top contacts. Charge transport observed through molecular junctions has been shown to exhibit technologically important phenomena such as rectification, conductance switching, and orbital gating. The primary focus of the field of molecular electronics is to understand the effect of molecular properties, such as structure and molecular orbitals, on charge transport mechanisms through molecular junctions. In this dissertation, the various techniques to fabricate and characterize molecular junctions are discussed, along with an introduction to charge transport mechanisms expected to control transport through molecular junctions.

More specifically, this dissertation is primary focused on the fabrication and characterization of molecular junctions fabricated through the formation of an electronic contact on a molecular layer through physical vapor deposition. A common problem

with this technique is structural damage to the molecular layer or metal penetration through the molecular layer during the contact formation. To overcome these limitations, a novel fabrication technique was developed and employed to fabricate reproducible molecular junctions through a physical vapor deposition technique without molecular damage or metal penetration. Termed surface diffusion mediated deposition (SDMD), the technique remotely deposits a metallic contact adjacent to and about 10 – 100 nm away from the molecular layer. Surface diffusion causes the metallic contact to migrate towards and onto the molecular layer to form an electronic contact. With SDMD, single molecule and many-molecule junctions are fabricated and electronically characterized.

To probe electronic states and molecular structure in molecule/oxide junctions, an in-situ optical absorbance spectroscopy technique was developed and employed to monitor bias induced molecular redox events in solid-state molecular junctions. Correlation of the observed spectral changes with molecular redox events allows characterization of the electronic properties of molecules which are critical in understanding charge transport through molecules. In a related application, the developed in-situ optical absorbance spectroscopy technique was used to probe doping events in polypyrrole/oxide junctions. Doping reactions in polypyrrole are shown to strongly depend on the surrounding environment. For application to both molecular and conjugated polymer junctions, in-situ absorbance spectroscopy is shown to be a useful analytical tool to determine charge transport mechanisms.

Finally, a thermal oxidation technique is introduced to increase the resolution of nanoimprint lithography to fabricate nanogap electrodes for molecular junctions. The

advantage of this technique is the ability to use a simple, fast, and reliable oxidation process to increase the resolution of standard nanofabrication techniques.

Dedication

This dissertation is dedicated to my family.

Acknowledgments

First, I would like to thank my research advisor, Prof. Richard McCreery. Through his constant support of my research, both academically and financially, he provided me with a stimulating research environment which was critical to my research success. He was always available to answer my questions and shared his personal views on science, society, and how the two interacted. His has provided significant influence on my graduate research and my future career, and for that I will be forever grateful. In addition, I would like to thank my academic advisor Prof. Gerald Frankel for his constant support and allowing me to remotely perform my research.

Second, I would like to thank my colleagues and group members at The Ohio State University and The National Institute for Nanotechnology for all their contributions throughout my graduate studies. I am grateful to Dr. Kenneth Harris, Dr. Haijun Yan, Dr. Jing Wu, and Dr. Adam Bergren for engaging in scientific discussions regarding my graduate research and research within the general realm of science. I also would like to thank the research and academic staff at The Ohio State University, National Institute for Nanotechnology, and the University of Alberta. Especially I would like to thank Daniel Saloman and Peng Li for their help with SEM and TEM, Scott Munroe for help with

microfabriation processes, Dr. Gino Dilabio for help with theoretical calculations, and Judy Brown and Mark Cooper for always making sure that my research appointment and graduation requirements were correct.

Third, I would like to thank the members of my dissertation committee, Prof. Roberto Myers and Prof. Nitin Padture for their time and effort in writing this dissertation. Their individual contributions to this dissertation are highly appreciated and I am grateful for their expertise.

Finally, and most importantly, I would like to thank my family and friends that have supported me throughout my academic pursuits. Without their dedication and unwavering encouragement I would not have obtained all my successes in my life. To Teresa, Paul, Joyce, Dale, Michele, Alan, Jean, Kevin, Tracy, Michael, Sam, Zack, Payton, Mason, Katie, Megan, Olivia, Morgan, Dylan, Eric, my two loving grandmothers, and all my cousins: Thank you.

Vita

June 17, 1982 ..... Born in Lima, Ohio

June, 2001 ..... High School Diploma

Kalida High School, Kalida OH

June, 2002 – Sept., 2002 ..... Co-op, Research and Development

Elmer's Products, Columbus OH

April, 2004 – Sept., 2004 ..... Co-op, Research and Spaceport

Kennedy Space Center, FL

Dec., 2006 ..... B.S. (Materials Science & Engineering)

The Ohio State University, Columbus OH

June, 2008 ..... M.S. (Materials Science & Engineering)

The Ohio State University, Columbus OH

Publications

1. Bonifas, A. P., Calle, L. M., Hintze, P. E. "Partial vacuum-gasketed electrochemical cell." *NASA Tech Briefs.* ***25****, 2006.*
2. Yoon, W., Bonifas, A. B., McCreery, R. L., & P. R. Berger. P. R. "Resonant tunneling and room temperature negative differential resistance in TiO_2/MEH-PPV junctions for quantum functional circuits." *Frontiers in Optics,* OSA Technical Digest (CD) (2006).
3. Bonifas, A. P. & McCreery, R. L. "In-situ optical absorbance spectroscopy of molecular layers in carbon based molecular electronic devices." *Chem. Mater.* **20**, 3849-3856 (2008).
4. Bonifas, A. P. & McCreery, R. L. "Soft Au, Pt and Cu contacts for molecular junctions through surface-diffusion-mediated deposition." *Nature Nanotechnol.* **5**, 612-617 (2010).
5. Ru, J., Szeto, B., Bonifas. A. P., McCreery, R. L., "Microfabrication and integration of diazonium-based aromatic molecular junctions." *ACS Appl. Mater. Interfaces*, **2,** 3693-3701 (2010).

Fields of Study

Major Field: Materials Science and Engineering

Table of Contents

List of Tables

List of Figures

CHAPTER 1

INTRODUCTION

The use of molecules as electronic components was conceptually introduced in a 1974 paper by Aviram and Ratner entitled "Molecular Rectifiers", where the paper presented a theoretical model involving a single molecule with a preferential conduction direction constituting single molecule rectification[1]. Over the past 37 years, charge transport through molecular based devices have been reported to exhibit technologically important phenomena such as conductance switching, rectification, negative differential resistance, and charge storage[2-7]. The proposed benefits of employing molecules as electronic components is commonly identified as inherent size reduction, novel device functionality, and reduction in fabrication cost[8]. The inherent molecular length scale, on the order of nanometers, is attractive as devices in electronic circuits are continually developed with smaller feature sizes. Molecular orbitals have been shown to strongly affect molecular conduction, and orbital gating is expected to allow new electronic functionalities. Finally, molecular electronics are expected to be compatible with

massively parallel device fabrication through self assembly techniques, which is envisioned to lead to less expensive device processing. Although significant experimental obstacles exist, the overall pursuit of understanding charge transport mechanisms through molecules has scientific merit and potential technological benefits.

This dissertation is composed of eight chapters including this introduction chapter and one appendix. It should be noted that a significant portion of this dissertation has been published or is under consideration in a peer reviewed journal. Previously published material has been identified at the beginning of each chapter. This dissertation provides additional experimental details, experimental results, and discussions allowing a more complete understanding of the major scientific findings.

Chapter 2 is a comprehensive literature review on the field of molecular electronics, which discusses common experimental approaches, charge transport mechanisms, and experimental successes and difficulties. Although theoretical studies have provided significant advancements to the field, Chapter 2 primarily focuses on the experimental studies of molecular electronics. This chapter concludes with a section discussing unresolved issues in the field of molecular electronics.

Chapter 3 discusses an experimental paradigm to fabricate molecular junctions through direct evaporation of top metallic contacts onto covalently attached molecular layers. The molecular layers are electrochemically attached to an amorphous, mostly sp^2 hybridized, carbon electrode resulting in robustly attached molecular layers. After direct metal evaporation, Raman spectroscopy is used to characterize potential molecular damage during metal evaporation. By introducing an experimentally simple approach of

varying the deposition angle, key insights into the difficulties to fabricate molecular junctions through metal evaporation techniques are identified.

Chapter 4, building upon the results in Chapter 3, discusses a novel method to fabricate molecular junctions where a metallic contact is formed on a molecular layer through a technique termed surface diffusion mediated deposition (SDMD). The physics behind the technique and the advantages and disadvantages of the SDMD technique are discussed. With the SDMD technique, molecular junctions consisting of single/several molecules or many molecules ($> 10^2$) are fabricated without molecular damage or metal penetration allowing fundamental questions about charge transport through single-molecule and many-molecule junctions to be addressed.

Chapter 5 discusses the use of in-situ optical absorbance spectroscopy as a method to monitor bias induced absorbance changes in molecular layers "buried" in solid-state molecular junctions. Observed bias induced absorbance changes are correlated to molecular redox events within the molecular layer. To the knowledge of the author, this is the first successful demonstration of employing absorbance spectroscopy to monitor redox events in 2-5 nm thick molecular layers incorporated into solid-state molecular junctions.

Chapter 6 builds upon the development of the in-situ optical absorbance spectroscopy technique in Chapter 5 to monitor bias induced redox events in the conjugated polymer polypyrrole. Potential redox events in polypyrrole layers are complex because its structural backbone is suitable for both electronic doping and proton (acid/base) exchange. With in-situ absorbance spectroscopy, bias induced redox events

within polypyrrole/oxide junctions are characterized allowing insight into observed electronic properties such as resistance switching.

Chapter 7 shows an approach to fabricate electrodes with nano-scaled separation for application to molecular electronics and nanoimprint lithography (NIL). Through a simple thermal oxidation technique of initially patterned Si substrates, the resolution of both nano-scaled electrode fabrication and NIL pattern transfer can be increased. The greatest advantage of this approach is that the resolution of standard fabrication techniques can be increased with a simple and reliable post-process thermal oxidation.

Chapter 8 identifies and discusses the major scientific findings of the dissertation as an entire body of work. The chapter concludes with a brief perspective of the relevance of this dissertation to the field of molecular electronics and the general field of electronics.

REFERENCES

1. Aviram, A.; Ratner, M. A., Molecular rectifiers. *Chem. Phys. Lett.* **1974,** 29, (2), 277-283.

2. Adams, D. M.; Brus, L.; Chidsey, C. E. D.; Creager, S.; Creutz, C.; Kagan, C. R.; Kamat, P. V.; Lieberman, M.; Lindsay, S.; Marcus, R. A.; Metzger, R. M.; Michel-Beyerle, M. E.; Miller, J. R.; Newton, M. D.; Rolison, D. R.; Sankey, O.; Schanze, K. S.; Yardley, J.; Zhu, X. Y., Charge transfer on the nanoscale: current status. *J. Phys. Chem. B* **2003,** 107, (28), 6668-6697.

3. Akkerman, H. B.; de Boer, B., Electrical conduction through single molecules and self-assembled monolayers. *J.Phys. Conden. Mat.* **2008,** 20, (1), 20.

4. James, D. K.; Tour, J. M., Electrical measurements in molecular electronics. *Chem. Mater.* **2004,** 16, (23), 4423-4435.

5. McCreery, R. L., Molecular electronic junctions. *Chem. Mater.* **2004,** 16, (23), 4477-4496.

6. McCreery, R. L., Advanced carbon electrode materials for molecular electrochemistry. *Chem. Rev.* **2008,** 108, (7), 2646-2687.

7. Mirkin, C. A.; Ratner, M. A., Molecular Electronics. *Ann. Rev. Phys. Chem.* **1992,** 43, 719-754.

8. McCreery, R. L.; Bergren, A. J., Progress with molecular electronic junctions: meeting experimental challenges in ddesign and fabrication. *Adv. Mater.* **2009,** 21, (43), 4303-4322.

CHAPTER 2

LITERATURE REVIEW

2.1 INTRODUCTION

2.1.1 Overview of Molecular Electronics

Since the first published work on molecular rectifiers in 1974, the idea of using molecules in electronic circuits has evolved into the modern field of molecular electronics[1]. As the fundamental limits of semiconductor based devices are currently being reached, molecular based devices have been proposed as a possible next generation of electronics. The three fundamental reasons that have propelled molecular electronics to the scientific forefront are the ability to scale on the molecular size regime, advancements in logic and memory applications, and economical device fabrication. Molecular based devices have been reported to exhibit electronically important characteristics such as rectification[2, 3], conductance switching[4, 5], negative differential resistance[6, 7], bistability[8, 9], and orbital gating[10-12]. A key issue that has limited the field is the lack of an universal approach to electronically address both single molecule and many-molecule junctions. As will be discussed in this chapter, electronically addressing a single molecule or molecular layer has been achieved through various experimental platforms. In addition to the molecular identity, the measured molecular conductance strongly depends on the entire molecular system, which includes intermolecular interactions, interfacial chemistry, and contact geometry. Since individual experimental platforms impose different conditions on the molecular system, comparison between platforms for the same molecule has been experientially challenging, and has attributed to the difficulties within the field. Also, reproducibility within a single paradigm is far from been considered acceptable compared to the current semiconductor standard as reported

molecular conductance values measured with the same platform have been reported to differ by several orders of magnitude. Although the field of molecular electronics faces many scientific challenges, the potential for improving on the capability of semiconductor physics provides a solid scientific reason to continue pursuing molecular based electronics.

2.1.2 Geometry of Molecular Junctions

Molecular junctions, consisting of a single molecule or many molecules, can be separated into three distinct regions: electronic contacts, constituent molecules, and the interfaces between the molecules and contacts. Commonly overlooked, the reported electronic characteristics of a molecular junction are a function of all of the above regions and the system as a whole should be considered when comparing reported properties of molecular devices.

2.1.2.1 Contacts (Electrodes)

In a two terminal device, the electronic contacts can be viewed as electron reservoirs that attempt to redistribute their electrons with the attached molecules to lower the free energy of the system; provided sufficient electronic coupling between the molecules and contacts. Since the density of states near the Fermi energy of the contacts are orders of magnitude higher than the molecular density of states, molecular energy levels of an attached molecular layer are expected to be strongly influenced by the contacts. Contacts employed for molecular junctions usually consist of noble metals where their geometry, surface morphology, and surface chemistry are critical to the interaction with the attached molecules. The benefits of noble metals as electronic

contacts are high electronic conductivity and stability against oxidation. Alternatively, using carbon based contacts is attractive due to the ability to form strong C-C bonds between the molecules and contact. Several potential carbon based molecular contacts include graphene, carbon nanotubes, graphite, and glassy carbon. The fabrication paradigm through which molecular contacts are formed has been shown to significantly affect the observed molecular conductance. For all reported molecular junction types, the fabrication paradigm should be considered as important as the identity of the molecular constituents. In general, molecular junction fabrication paradigms can be separated in two approaches. The first approach is to form two contacts with a molecular-scaled gap and then attach a single molecule or a molecular layer. The attached molecule or molecular layer bridges the two contacts to form the molecular junction. Although this approach appears straightforward, fabrication of reproducible, molecular-scaled spaced contacts is difficult to experimentally achieve. The other approach is to first form a molecular layer on a "bottom" contact and then form the second contact on top of the molecular layer. In contrast to the previous approach, the molecular-scaled gap between the contacts is defined by the presence of the molecular layer requiring less complicated fabrication techniques. The difficulties of this approach have severely limited its overall success. Fabrication of the second contact on the molecular layer can cause structural damage to the molecular layer and create molecular contacts at non-equilibrium conditions. Furthermore, the second contact can penetrate through the molecular layer leading to electronic properties non-characteristic of molecular charge transport. For

both types of approaches, numerous experimental platforms have been designed where each platform have specific advantages and disadvantages.

2.1.2.2 Molecules/Molecular Layer

The second region of a molecular junction is the molecular layer, which can contain a wide range of molecules such as aliphatic molecules, aromatic molecules, and organometallic complexes. The goal of molecular electronics is to design molecular junctions that have electronic characteristics dependent on the molecular properties of the constituent molecules. Ideally, the electronic characteristics depend on the unique quantized nature of the molecular orbitals. The bonding nature along the molecular backbone strongly influences the molecular energy levels, which directly affect molecular conductance. In general, an aromatic molecule is expected to have higher conductivity compared to an aliphatic molecule as molecular energy levels of aromatic molecules are typically closer to the Fermi energy of commonly used contacts (~5 eV). Although aliphatic molecules have been reported to have lower conductivity, they are commonly used as the standard system to calibrate results between research groups, various experimental platforms, and experimental and theoretical results. There are several reasons why aliphatic systems constitute a wise choice for calibration: electronic interaction between an aliphatic molecule and a contact is expected to be minimal (discussed below) since the molecular energy levels are a few eV away from the Fermi energy of the contacts, widely available methods exist to fabricate self-assembled molecular layers, and relatively simple analysis of the measured molecular conductance. In contrast, aromatic molecules are viewed as the most promising class of molecules for

potential electronic and optical applications because their molecular energy levels are near the Fermi energy of the contacts. Aromatic molecular systems also have the potential for intermolecular interactions within a molecular layer which could result in additional electronic properties suitable for technological applications. Organometallic complexes, such as metal centered porphyrins, are attractive since they can undergo multiple redox events suitable for charge storage applications (e.g. memory). In general, each class of molecules is envisioned to have potential technological applications but harnessing their potentials has been difficult to achieve experimentally.

2.1.2.3 Molecule/Contact Interface

The third component of a molecular junction is the interface between the molecules and the contact, a critical component that is commonly overlooked. The chemistry at the molecule/contact interface is dictated by both the terminal groups of the molecule and the electronic properties of the contact. Depending on the attachment paradigm, the interfacial chemistry can range from strong covalent bonding to weak Van der Waals bonding. The bonding nature within the interface can strongly affect molecular conductivity. A common approached used to model charge transport through molecular junctions is the Landauer formalism:

$$g = \frac{2e^2}{h}\sum_i \left(T_{mol}^i T_1^i T_2^i\right) \qquad \text{Eq. 2.1}$$

where g is the conductance, ($2e^2/h$) is the quantum of conductance for ballistic charge transfer, T^i_{mol} is the transmission matrix through the molecule, T_1^i and T_2^i are the transmission matrices for the first and second interfaces, respectively[13]. The interface transmission matrices are influenced by the interfacial bonding and give the probability of interfacial scattering between the contacts and molecules.

2.1.2.4 Energy Level Alignment and Broadening

To understand charge transport through molecular junctions, determining alignment of the molecular energy levels with the Fermi energy of the contact is critical. In the Landauer formalism, this energy alignment determines the interfacial transmission matrices, where a small offset between energy levels alignment results in a high transmission probability. For the electronic contacts, the energy level of primary interest is the Fermi energy (commonly near -5 eV relative to vacuum). For molecules, the molecular energy level of primary interest depends on the charge carrier: hole transport occurs through the highest occupied molecular orbital (HOMO) and electron transport occurs through the lowest unoccupied molecular orbital (LUMO). Electronic interaction and charge transfer at the contact/molecule interface causes electronic redistribution and molecular reorganization to occur until the Fermi energy of the contact lies within the HOMO-LUMO gap of the molecules. The Fermi energy of the contact can reside anywhere within the HOMO-LUMO gap and is not necessarily positioned half way between the HOMO and LUMO because of the limited density of states and high electron charging energy of a molecule. For off-resonant tunneling, the tunneling barrier is commonly estimated as the difference between the contact Fermi energy and the HOMO,

as hole tunneling is the widely accepted mechanism through most molecular systems. Understanding the dynamics of energy level alignment is an active area of interest in both experimental and theoretical research into charge transport through molecular junctions.

In addition to a shift in the molecular energy levels, electronic redistribution also causes the discrete energy level of the free molecule to become broadened. This broadening is caused by the electrons in the contact having a finite lifetime in the molecular layer and the degree of broadening is determined by the electronic coupling between the two systems. As mentioned earlier, the molecular attachment paradigm influences the electronic coupling, which strongly affects energy level alignment and molecular energy level broadening. This insight identifies an important paradox for molecular based electronics; increased electronic coupling results in higher molecular conductivity but also causes broadening of the molecular energy levels. Significant broadening can "wash out" the quantized nature of molecular energy levels.

2.1.3 Scope of Chapter

The scope of this chapter will be limited to experimental approaches to characterize the electronic properties of molecular devices. Although not discussed herein, theoretical calculations have played and will continue to play an important role in the field of molecular electronics.

2.2 CHARGE TRANSPORT MECHANISMS

In an attempt to understand charge transport through molecular systems, modeling observed molecular conductance is commonly approached through fitting semi-empirical

tunneling or charge hopping equations. Charge transfer through organic molecules (1-5 nm long) can be separated into two classifications: strongly distance-dependent tunneling and weakly distance-dependent charge transfer mechanisms[14].

2.2.1 Coherent Tunneling

In molecular electronics, typical molecular lengths cause tunneling to be the primary conduction mechanism. In simple terms, coherent tunneling can be mathematically defined by the equation:

$$J = J_o \exp(-\beta d) \qquad \text{Eq. 2.2}$$

where J is the current density, J_o is the pre-exponential term that contains the contact resistance, β is the tunneling decay constant, and d is the tunneling distance.[14, 15] β is commonly used as the standard to compare tunneling probability for various molecular types. For aliphatic molecules, β has been reported to be in the range of 0.7 – 1.0 $Å^{-1}$. For aromatic molecules, the reported β is typically in the range of 0.2 - 0.4 $Å^{-1}$, which is lower than for aliphatic molecules. A critical parameter in understanding tunneling through molecules is the time a charge carrier spends in a molecular energy level given by the Landauer-Buttiker contact time τ_{LB}:

$$\tau_{LB} \approx \frac{Nh}{E_G} \qquad \text{Eq. 2.3}$$

where N is the number of energy levels, h is Plank's constant, and E_G is the energy gap between the Fermi energy of the contact and the molecular energy level through which transport occurs[16]. For aliphatic molecules the E_G is large causing the τ_{LB} to be on the order of sub-femtoseconds; a short time relative to molecular vibrations and rotations. Two important conclusions can be drawn from considering the τ_{LB} for aliphatic systems: oxidation or reduction of the molecular systems is highly unlikely because redox activity is too slow compared to τ_{LB}, and molecular energy level broadening is minimized. In contrast, aromatic molecules have a smaller E_G resulting in a longer τ_{LB} compared to aliphatic molecules. This increase in τ_{LB} is still not high enough to allow redox activity, at least for metal-molecule-metal junctions, but can have an effect on molecular energy broadening. For tunneling through molecular systems, observed molecular conductivities are generally temperature independent to a first order approximation.

2.2.1.1 Non-Resonant Tunneling

Non-resonant coherent direct tunneling occurs when the wave functions of the two contacts overlap and become directly electronically coupled, as in the case of tunneling through a vacuum gap.[14] For this type of tunneling, observed electronic properties are dependent on the electronic energy levels of the contacts relative to the vacuum energy.

2.2.1.2 Non-Resonant Superexchange Tunneling

In non-resonant coherent superexchange tunneling, the tunneling process is facilitated by the presence of molecular orbitals and their respective energy levels.[14] Since τ_{LB} is shorter than the molecular vibrations, superexchange is commonly referred to

as a "virtual excitation" of a molecule. In terms of β, superexchange causes β to be significantly decreased compared to a vacuum gap as the molecular energy levels couple with the tunneling process. For this type of transport, the tunneling current is dependent on the molecular energy levels allowing β to be used as an indicator of the molecular influence on charge transport. It is this principle of superexchange that allows the molecular electronic characteristics to influence conductivity. In this dissertation, superexchange tunneling will be noted simply as "tunneling" because the principle of superexchange is inherently implied with tunneling through molecular layers.

To gain additional understanding behind charge transport through molecular systems, such as the effect of molecular layer thickness and energy levels, measured current-voltage (I-V) curves are commonly fitted to a tunneling model proposed by Simmons:

$$I = \frac{qnA}{4\pi^2\hbar(\Delta s)^2}\left\{\left(\bar{\phi} - \frac{qV}{2}\right)\exp\left(-\frac{2d\sqrt{2m_{eff}}}{\hbar}\sqrt{\bar{\phi} - \frac{qV}{2}}\right) - \left(\bar{\phi} + \frac{qV}{2}\right)\exp\left(-\frac{2d\sqrt{2m_{eff}}}{\hbar}\sqrt{\bar{\phi} + \frac{qV}{2}}\right)\right\} \quad \text{Eq. 2.4}$$

where n is the number of conducting molecules, A is the area per molecule, Δs is the tunneling distance, m_{eff} is the electron effective mass, $\bar{\phi}$ is the average barrier height, q is the electronic charge, ħ is the reduced Planck constant, and V is the applied voltage[17, 18]. The first important note from Eq. 2.4 is that the rest mass of an electron is replaced

with an effective mass, which accounts for electron interaction with molecular orbitals. As a simplification, a scalar value of the effective mass can be approximated as:

$$m_{eff} = \hbar^2 \cdot \left[\frac{d^2 E}{dk^2} \right]^{-1} \qquad \text{Eq. 2.5}$$

where E is the energy of the molecule energy level and k is the wave vector. The above approximation is only valid near an energy minimum where the effective mass is equal in all directions[19]. The fitted tunneling barrier in Eq. 2.4 is an average barrier height, where the barrier height is fitted as the offset between the Fermi energy of the contact and the molecular energy level through which tunneling occurs.

In contrast to the full barrier height, which is the offset between the Fermi energy of the contact and the HOMO, the average barrier height fitted in Eq. 2.4 takes into account the notion that the barrier height is not constant along the entire length of the molecule. In addition, the formation of an image charge on the contacts during an applied voltage causes significant changes to both the tunneling barrier and tunneling distance. Taking into consideration image charge effects, the full shape of the barrier height is given by:

$$\bar{\phi} = \phi_o - qV\left(\frac{s_2 - s_1}{2d} \right) - \left[1.15\lambda \frac{d}{s_2 - s_1} \right] \times \ln\left[\frac{s_2 (d - s_1)}{s_1 (d - s_2)} \right] \qquad \text{Eq. 2.6}$$

where ϕ_o is the full barrier height, d is the molecular length, and s_i is distance from the respective i^{th} contact to the intercept of the molecular energy level and the contact's Fermi energy. λ is defined as:

$$\lambda = \frac{q^2 \ln(2)}{8\pi\varepsilon_o \varepsilon d} \qquad \text{Eq. 2.7}$$

where ε_o is the permittivity of free space and ε is the relative dielectric constant of the molecular layer[20]. Incorporation of the image charge results in a lower average barrier height compared to the full energy offset and the actual tunneling distance is less than the molecular length. The primary motive to fit observed I-V curves to Eq. 2.4, with or without incorporation of an image charge, is to allow quantitative comparisons over a wide range of molecular systems.

2.2.1.3 Resonant Tunneling

Resonant tunneling occurs when the Fermi energy of a contact is within k_BT of a molecular energy level[14]. Unlike superexchange, resonant tunneling is weakly length dependent and scales linearly with the transmission matrix[21]. Resonant tunneling is a highly attractive transport mechanism because it allows enhanced conductivity within a small energy range (several k_BT), potentially leading to negative differential resistance. It should be noted that strong electronic coupling between the contacts and molecules can prohibit the observance of resonant tunneling[16, 21]. If the electronic coupling is strong,

broadening leads to the loss of discrete energy levels minimizing the effect of resonant transport.

2.2.2 Incoherent Tunneling

Incoherent tunneling occurs when a scattering event alters the phase of the electron during tunneling. The scattering event is caused when the charge carrier is temporary localized on a molecular or interfacial energy state[22,23,24]. Coherency in charge transport is especially important for the field of spintronics, as the fundamental information is stored as the quantum spin state of an electron.

2.2.3 Thermally Activated "Hopping" Transport

Thermally activated "hopping" transport occurs when the work function of the contact is within k_BT of a molecular energy level allowing facile charge injection.[15] Unlike resonant tunneling, τ_{LB} is sufficient to allow redox events to occur within the transport layer. "Hopping" can be viewed as discrete charge carrier exchange between a neutral and charged molecule[15]. Charge transport occurs through thermally accessible molecular energy states by "hopping" along the molecular system. "Hopping" transport is temperature dependent and the charge transport rate constant (k_{ET}) follows Arrhenius behavior:

$$k_{ET} = k_{ET}^{o} \exp\left(\frac{-E_a}{k_B T}\right) \qquad \text{Eq. 2.8}$$

where E_a is the activation energy, k_B is the Boltzmann constant, and T is the temperature. Besides being thermally activated, "hopping" transport is weakly dependent on distance ($\sim d^{-1}$) and incoherent.[15] In general, the Marcus formalism is employed instead of Landauer because Marcus theory takes into consideration nuclear motion associated with the "hopping" mechanism[25]. Hopping can be an attractive mechanism for memory applications where modulation of the concentration of charge carriers can change the conductivity by many orders of magnitude allowing a memory state to be read as simple resistance[26, 27].

2.3 MOLECULAR ATTACHMENT PARADIGMS

The interface between the contacts and molecules plays a significant role in determining charge transport. In some cases where a charge injection barrier forms within the contacts, the electronic properties are completely governed by the contact/molecular interface. The molecular attachment paradigm not only determines the stability and potential applications of a molecular system but also strongly affects the electrical coupling at the contact/molecule interface. Comparison of commonly employed molecular attachment paradigms shows their differences and allows the identification of each paradigm's advantages and disadvantages.

2.3.1 Langmuir-Blodgett Paradigm

The Langmuir-Blodgett (LB) paradigm creates a highly ordered molecular film by orienting amphiphilic molecules at a water/air interface[28, 29]. After the molecules orient at the water/air interface, the molecules are carefully transferred to a metallic or oxide

substrate as shown in Figure 2.1. An advantage of this paradigm is the weak bonding at the water/molecule interface, which allows the molecules to orient into a 2-D crystalline lattice[30, 31]. Through both experimental results and theoretical calculations, the 2-D lattice is well known for molecular systems under many environmental conditions. The LB paradigm is experimentally straightforward and can be used to create large area devices several cm^2 in area. The major disadvantage is that bonding at the molecule/contact interface is a weak electrostatic bond, usually only several $kcal \cdot mol^{-1}$, which is unstable to thermal fluctuations or applied mechanical loads[15, 32]. For practical applications, the LB paradigm lacks the stability required to achieve consistent results and should be avoided as a molecular attachment paradigm.

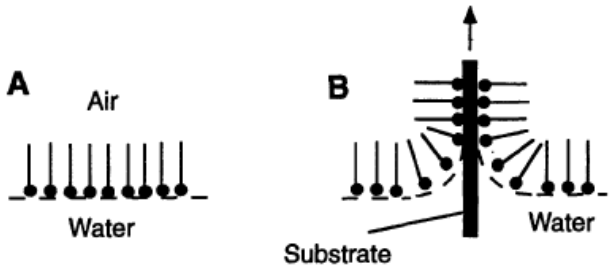

Figure 2.1: Schematic of the LB technique: **a,** monolayer forms at water/air interface. **b,** monolayer is transferred by passing the substrate through the interface[30].

2.3.2 Self-Assembly Paradigms

Currently the most popular molecular attachment paradigm is the self-assembly of thiols on metallic surfaces, commonly Au (111)[33-35]. Extensively studied by Whitesides et al., solutions of alkanethiols spontaneously attach and self-order on an Au surface to form a chemisorbed Au-S bond, as shown in Figure 2.2[36]. Although chemisorbed, the 40 $kcal \cdot mol^{-1}$ reversible bonds allows the molecules to order into a closed-packed 2-D lattice

by lateral diffusion as well as repeated desorption and adsorption[15, 36]. Similar to the LB paradigm, the fabrication process is straightforward and large area devices can be fabricated. With the use of alkanedithiols, a molecule can spontaneously bridge a molecular-sized gap or attach to an Au probe to create single molecule devices[37]. Although the Au-S is a chemisorbed bond, the constant desorption and adsorption process even at room temperature leads to a constantly changing interface. This fluctuation in the bonding geometry can lead to molecular damage during fabrication and uncertainly during electronic measurements. Although this paradigm has a role in future experiments, such as single molecule measurements, the field of molecular electronics is realizing the limitations of this technique and is moving to paradigms that involve stronger bonding characteristics.

Another self-assembly paradigm commonly employed is the attachment of organosilanes on Si and SiO_2 surfaces. Organosilanes, SiR_nX_{4-n}, spontaneously react with hydrogen terminated Si or the hydroxyl groups on SiO_2 to create siloxane (Si-O-Si) bonds, as shown in Figure 2[38, 39]. In contrast to Au-S self-assembly, strong covalent bonding at the interface prohibits reorganization of the molecules after attachment leading to only short range order. The major disadvantages of this paradigm are that dense ordered films are difficult to achieve, the aggressive nature of the attachment can lead to multilayered films, and the bonding characteristics are still debatable[40].

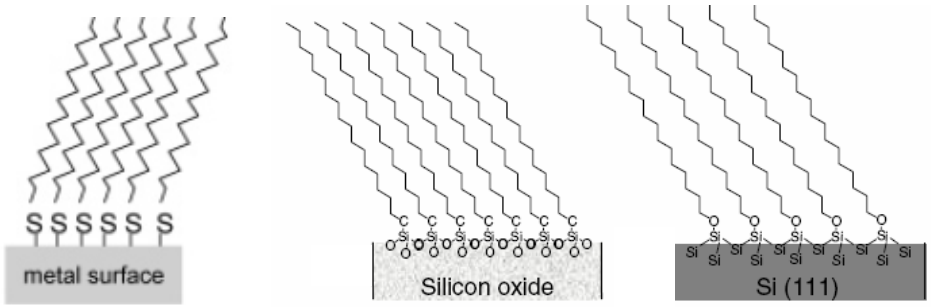

Figure 2.2: Schematic of two paradigms for self-assembled monolayers[15, 39].

2.3.3 Irreversible Attachment Paradigms

The irreversible molecular attachment paradigm involves surface electrochemistry to covalently attach molecules to a conductive substrate. One such paradigm is the free radical attachment during the electrochemical reduction of a diazonium molecule, as shown in Figure 2.3[41, 42]. The advantage of this paradigm is that the aggressive free radical reaction creates a dense molecular layer that is covalently bonded to the surface. If a carbon contact is used, the molecular attachment is through a C-C bond which has a high bond strength of 80 kcal/mol[15]. The major disadvantages of this technique are that the molecular layer is disordered, aggressive free radical chemistry leads to molecular multilayers, and diazonium chemistry limits the molecules to aromatic systems[43]. A similar paradigm employs the electrochemical oxidation of a primary amine to create a covalently attached molecular layer where the thickness of the layer is controlled by the oxidation potential[44, 45]. The oxidation of primary amines provides a complementary paradigm to diazonium chemistry.

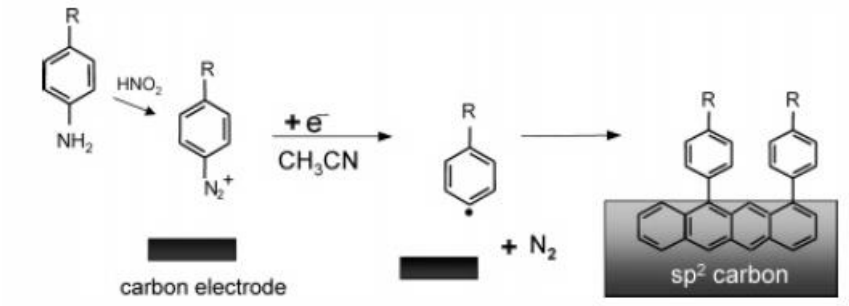

Figure 2.3: Molecular attachment through the electrochemical reduction of a diazonium molecule on a carbon surface[15].

2.3.4 Emerging Paradigms

Emerging paradigms are focused on creating covalently attached, well ordered molecular monolayers, therefore combining the advantages of the above paradigms. One such paradigm uses diazonium chemistry to create free radicals on a hydrogen terminated Si surface, allowing a free molecule in a surrounding solution or gas to covalently attach to the surface[40, 46]. Another emerging paradigm termed "click chemistry" allows attachment of complex molecules such as DNA, porphyrins, and rotaxanes, which are difficult to attach with self-assembly or electrochemical paradigms[47, 48]. For "click chemistry", alkyne-terminated molecules are covalently attached to a surface bonded triazole molecule through a Cu(I) catalyzed cycloaddition reaction, as shown in Figure 2.4. Overall, the trend within molecular electronics is to develop molecular attachment paradigms that can produce stable and well-ordered molecular layers; however, the advantages of self assembly paradigms are fundamental to single and many molecules experiments.

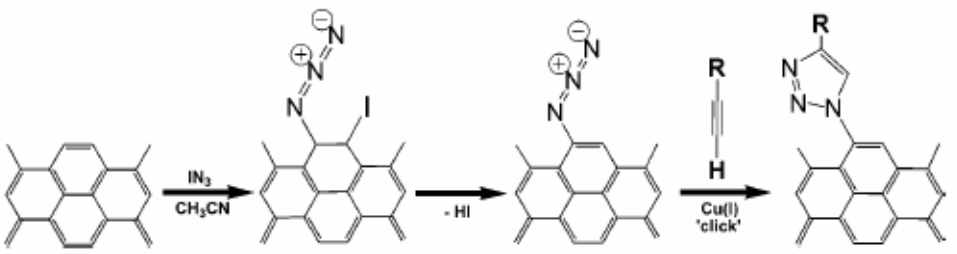

Figure 2.4: Molecular attachment through "click chemistry" where surface bonded azides react with solution alkynes to create the molecular layer[47].

2.4 EXPERIMENTAL PLATFORMS

2.4.1 Single/Several Molecules

2.4.1.1 Scanning Tunneling Microscopy

Scanning tunneling microscopy (STM) is a high resolution surface imaging technique that has been shown to be especially useful in the electronic characterization of single molecules and molecular layers[49-51]. In STM, a nearly atomically sharp conducting probe is scanned over a molecular layer allowing molecular morphology (constant current mode) and molecular conductivity (constant height mode) to be measured. To measure conductivity, the tunneling current passes through the molecular layer. A schematic representing the geometry of a STM measurement is shown in Figure 2.5.

Since STM has lateral resolution down to the molecular scale, it can be used to electronically address a single molecule of interest and monitor its conductance characteristics. In 1998, Weiss et al. focused on the stochastic changes in the conductance of phenylene ethynylene oligomers[52, 53]. By measuring the molecular height and conductance with STM, a high conductivity state was determined to occur when the oligomer undergoes a conformational change leading to a decrease of 3 Å in height. The

conformational change requires that actively changing oligomers reside at defects in the molecular layer. The attempt to manually switch the conductance state by the application of a high applied voltage was shown to be ineffective. A possible explanation of the change in conductance is conformational twisting caused by the motion of the molecular dipole in an applied electric field, which has been theoretically confirmed[53].

Figure 2.6 shows an STM measured differential conductance curve for a dithiol self-assembled molecular monolayer reported by Tian et al.[51]. The molecular junction is made by first forming a self-assembled monolayer of α, α′-xylyl dithiol molecules on an Au surface. The Au STM tip is brought into close contact with the molecule, resulting in a weak bond that does not break the S-H . The measured molecular conductance shown in Figure 2.6 is nearly symmetric between ± 3V and the exponential increase in conductance is the result of off-resonant tunneling through the molecules. For negative applied voltages greater than -3 V, the change in the differential conductance becomes negative which is indicative of resonant tunneling. The lack of a negative differential conductance region for the positive applied voltages suggests asymmetry in the molecular system although the molecule is symmetric. The asymmetry was explained by considering the difference in the bonding chemistry at both interfaces: the bottom contact is a chemisorbed Au-S bond and the top STM contact consists of a weakly coupled physisorbed Au-SH bond. As shown here, the observed electronic characteristics of a molecule depends strongly on the bonding and coupling at the molecule/contact interface. Although these results show the signature of resonant tunneling through a molecular

energy level about 1.5 eV away from the Fermi energy of the contact, subsequent papers on this molecular system were not forthcoming.

Although STM measurements have proven suitable to probe charge transport through molecules, using STM to probe molecular conductivity has several disadvantages. Although STM results are presented as the conductance of a single molecule, intermolecular effects with the neighboring molecules are commonly ignored[49]. Uncertainty about the bonding characteristics of the molecules with the STM tip has proven to be a difficult experimental obstacle to overcome. Although the STM has adequate height resolution, understanding the interfacial bonding at the tip is difficult, since it could be a vacuum gap, physisorption, or chemisorption[54]. An additional issue is that the stability of the molecular contacts during electronic measurements is questionable since previous STM analysis has shown that molecules can remain mobile on the surface even at 4K[55]. Finally, the STM platform lacks the ability to be fabricated in a massively parallel process, thus confining this approach solely to basic research.

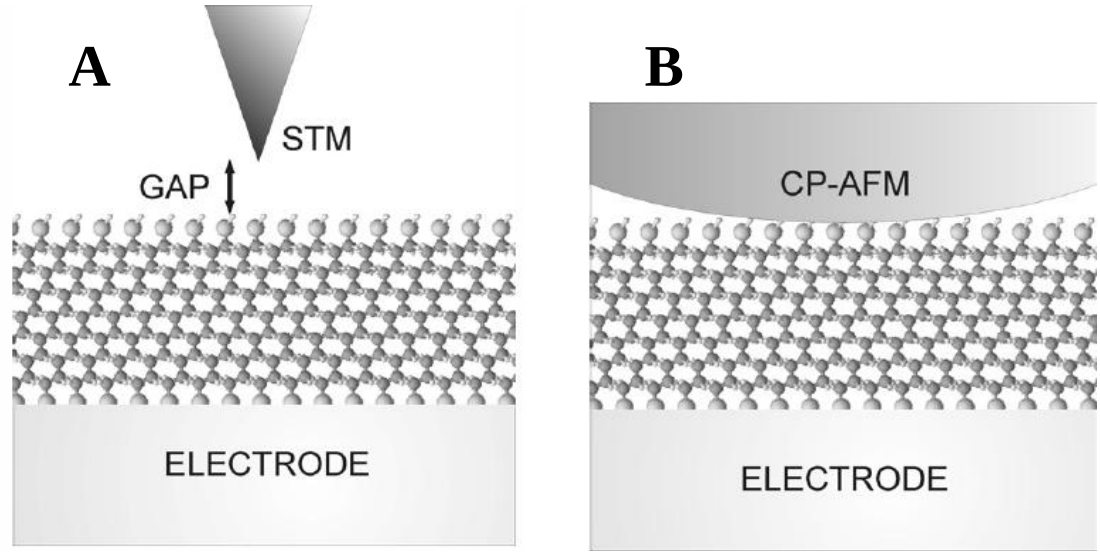

Figure 2.5: Schematic representing the geometry of **a,** STM measurement and **b,** CP-AFM measurement[13].

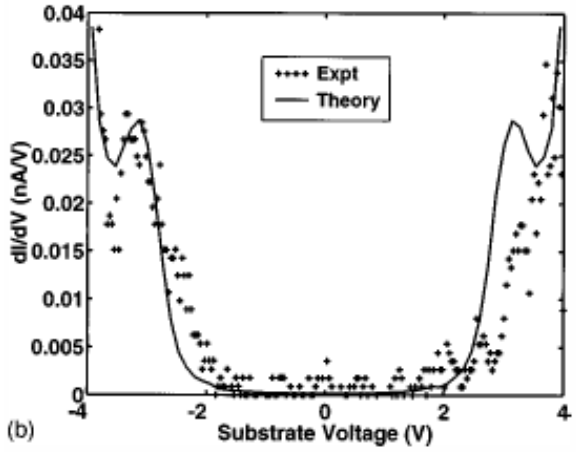

Figure 2.6: Experimental and theoretical conductance-voltage characteristics for a xylyl dithiol self-assembled molecule measured with STM[51].

2.4.1.2 Conducting Probe Atomic Force Microscopy

Conducting probe atomic force microscopy (CP-AFM) is a common technique employed to directly probe charge transport through a single molecule or several

molecules in parallel[17, 54, 56-58]. For CP-AFM, a traditional AFM probe is coated with a metallic layer and scanned over the molecular monolayer while a bias is applied between the probe and the substrate. Similar to STM, the junction substrate must consist of a conducting material and the current is measured as a function of applied bias, lateral position, and applied contact force. The major advantages of CP-AFM are that the technique is experimentally straightforward and the probe is in direct contact with the terminal group of the molecules during the conductance measurement. The major disadvantage of CP-AFM is the size of a metallic coated AFM probe (~10 nm) is much larger than an STM probe, thus decreasing lateral resolution, as shown in Figure 2.5.

Numerous studies have been performed using CP-AFM to directly measure the conductivity of molecules in both LB and SAM monolayers[13, 54]. In studies that focused on alkanedithiols, the measured electronic characteristics are consistent with non-resonant coherent tunneling. Although tunneling is the generally accepted mechanism, the value of β varies between experimental reports. Reported β in alkanedithiols is between 0.70 and 1.1 $Å^{-1}$. This large range in β is significant because the observed current is exponentially dependent on β[13, 54]. To explain these large differences, several possible reasons have been proposed, such as differences in the tunneling distance based on molecular tilt angles, probe contamination, unknown contact configurations, and differences in the probe force[13, 57].

An alternative approach is to disperse nanoparticles of a well defined shape and size on top of the molecular layer to create "nanojunctions"[57, 59, 60]. CP-AFM is then used to contact the nanoparticles and thus measure the conductance of these

"nanojunctions". Figure 2.7 shows histograms of measured conductivities of decanedithiol and dodecandithiol molecules using this technique. Analysis has shown that the measured conductivities are an integral multiple of the fundamental conductance of a single molecule. Although this technique was shown to improve the reproducibility of the measurements, the measured conductance was lower than STM results. It was shown that if the Au particles were less than 2 nm, charging of the nanoparticles could lead to columbic blockage. When the nanoparticles were larger than 5 nm, the measured conductance was similar to STM results. Although not addressed, Smith et al. have shown that nanoparticles selectively sit on defect sites, suggesting the measured conductivity is influenced by defect sites in the molecular layer[61]. The nanoparticles also introduce an additional interface, which complicates analysis of the measurements. Charging of the nanoparticles, contact resistance between the nanoparticles and probe, and molecular strain caused by the nanoparticles should all be considered.

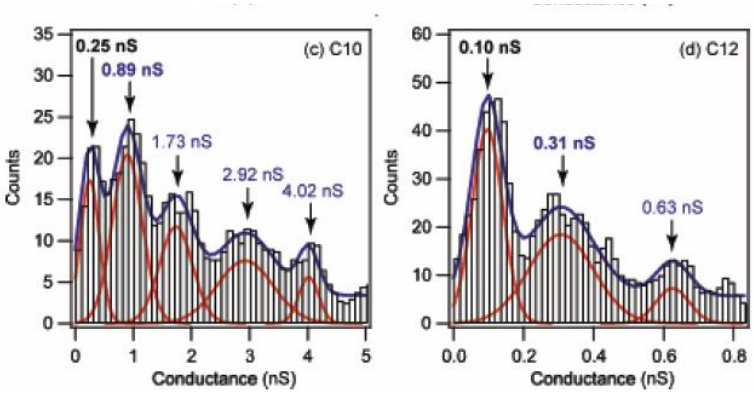

Figure 2.7: Conductance histograms of decanedithiol and dodecanedithiol bonded to Au nanoparticles measured with CP-AFM[57].

Although CP-AFM has numerous experimental advantages, this method has several key disadvantages. Since the probe comes in direct contact with the addressed molecules, the molecules are measured in a "compressed fashion", which affects their measured conductivities. The choice of the terminal group and the probe's metallic coating causes significant changes in the measured conductance[15]. For example, if the molecule is terminated with a thiol group the Au coated probe can attach to the molecular layer, thereby increasing conductivity. The large diameter of the AFM tip compared to the diameter of a molecule results in junctions containing several to hundreds of molecules, which results in uncertainty in the number of contacted molecules.

2.4.1.3 Break Junctions

In the break junction approach, molecular conductance is measured by suspending molecules across a controlled "break" in a metallic wire. This technique allows for the formation of molecular sized gaps in the 0.5-2 nm range, a range that is difficult to achieve with lithography techniques. Break junctions are usually formed by two methods: hard contact and mechanically controlled. The hard contact method brings an Au STM tip in hard contact with an Au substrate. As the STM tip is slowly raised, an Au filament forms and subsequently "breaks", creating an atomically sharp break that can be temporary bridged by surrounding molecules[37, 62, 63]. By continually repeating this process in solution or on a molecular monolayer, the conductivity of the molecules can be measured. Figure 2.8 shows results of the hard contact approach to measure the conductance of 4, 4' bipyridine[63].

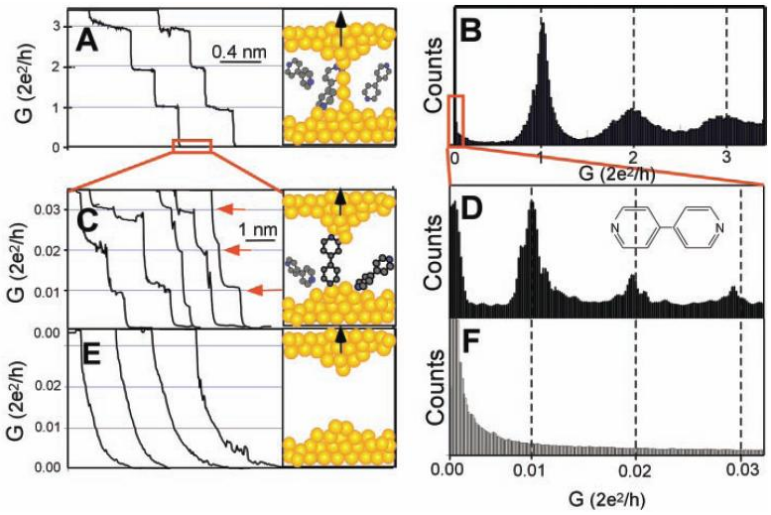

Figure 2.8: a, c, e, Measured conductance as the STM tip was raised from the Au surface. **b, d, f,** Histograms of 1000 measurements of the observed conductivity[63].

As shown in Figures 2.8a and 2.8b, the observed decrease in conductivity occurs in quantum conductance (G_o) steps, which is consistent with previous investigations of metal point contacts. Further analysis in the low conductivity region of Figure 2.8b shows the presence of integral multiples of sub-quantum conductance. These results show that a 4, 4' bipyridine molecule has a conductance of 0.01 G_o and the observed quanta correspond to multiple molecules bridging the gap. Figures 8E and 8F show that the observed conductance measurements only occur when molecules are present. In this experiment, β of alkanedithiols was determined to be 0.8 $Å^{-1}$, which is consistent with previous STM measurements. Although similar, the major difference between this technique and STM or CP-AFM is that the molecules are measured in a state of tension. The broadening of the conductance peaks in the histograms was identified as broadening caused by molecular vibrations, temporal changes in the bonding leading to various bonding geometries, and measurement error within the instrument.

Mechanically controllable break junctions (MCBJ) are formed by placing a lithographically defined Au wire in tension with a piezoelectric controlled 3-point bending apparatus. The gap formed during the break is monitored by measuring the tunneling current, allowing the gap size to be controlled to the sub-nanometer range[64, 65]. Introduction of a solution containing the molecule of interest allows the molecules to be captured across the gap and the molecular conductance to be measured. As reported by Tsutsui et al, the conductivity of benzenedithiol was strongly dependent on the Au-S bonding configurations[66]. This result illustrates that molecular conductance strongly depends on the bonding configurations and not just the constituent molecules.

2.4.1.4 Electromigration Nanogap Junctions

Electromigration gaps are fabricated by passing a current through a thin, lithography defined Au wire on an insulator surface such as SiO_2[11, 67-69]. Formation of the Au wire usually involves electron beam lithography (EBL) to define two overlapping Au wires, where the Au wires are tapered towards the intersection point of the lines to ensure that the highest resistance point occurs at the intersection. Commonly, the width of the Au wire is between 10 – 40 nm, with a deposition thickness of 8-30 nm. Under the application of a controlled bias along the Au wire, the passing current causes Au electromigration to occur resulting in the formation of a gap. By carefully controlling the applied voltage while simultaneously monitoring the tunneling current across the forming nanogap, the length of the nanogap can be highly controlled. The electromigration process has been shown to fabricate highly controllable nanogaps between 1-5 nm under ambient conditions. The formation of molecular junctions across the electromigration

gaps is completed by introducing a solution containing dithiol molecules, which form chemisorbed contacts with both sides of the nanogap. The length of the nanogap and the bridging molecules are required to have similar lengths. Formation of molecular junctions with this technique has been shown by several research groups[67-69].

One key advantage of this technique is that it allows the incorporation of a third electrode as a gate electrode similar to traditional field effect transistors. As mentioned earlier, fabrication of the overlapping Au layers usually occurs on a SiO_2 surface. By growing a thin SiO_2 (50 – 300 nm) layer on a Si wafer prior to fabrication of the Au wires, the underlying Si can be used in back-gate geometry. Recently, Lee et al. have shown the ability to modulate the molecular conductance through both alkanedithiol and benzenedithiol molecules through the use of the back-gate geometry[11]. To further prove that the observed conductance is through the attached molecules, they employed inelastic tunneling spectroscopy (IETS) to show that the charge transport was coupled to specific molecular vibrational states. These results demonstrate the ability to modulate molecular conductance through the application of an electric field perpendicular to the molecular conductance path. This result demonstrates a significant step towards using molecules in traditional FET configurations.

Although experimentally straightforward, forming nano-scaled gaps through electromigration of Au has experimental limitations. Primarily, nano-scaled gaps fabricated through electromigration commonly exhibit irregular gap shapes with length variations along the gap. The edge roughness of the irregular contacts can lead to an inhomogeneous electric field across the bridging molecules. Recently, theoretical

calculation of the electromigration process has provided a better physical insight into the process, allowing the technique to achieve better reproducibility and control[70]. A critical unknown parameter with this technique is the number of incorporated molecules bridging the gap, which can vary from a single to hundreds of molecules. In addition, the molecular attachment paradigm is limited to self-assembly capable molecules. Overall, electromigration formed molecular junctions provide a critical platform to measure molecular conductance.

2.4.2 Many-Molecule Junctions

2.4.2.1 Mercury Drop

A simple way to form a molecular junction is to place a drop of mercury (Hg) onto the surface of a molecular monolayer where the Hg drop becomes the top contact. A slightly more complicated version of the Hg drop platform is the formation of molecular monolayers on two drops of Hg followed by bringing the Hg drops together to form a molecular junction, as shown in Figure 2.9[13]. Measured β of alkanedithiols self-assembled on Au contacts were determined to be 0.7 – 1.0 $Å^{-1}$.[47] The major advantage of this technique is that the experimental setup is straightforward compared to complex methods such as STM and CP-AFM. Since the surface tension associated with an Hg drop is high, the Hg drop does not penetrate into the molecular layer. To estimate the number of contacted molecules in the molecular junction, an optical microscope is used to measure the contact area of the Hg drop. A commonly overlooked problem with this method is the potential for the formation of Hg oxide on the surface of the Hg drop before contact occurs with the molecular layer. If surface oxidation occurs on the Hg

drop, the electronic properties of the Hg and the interfacial bonding can be significantly affected. In addition, applied voltages across the junction can form mobile Hg^{+} ions which can penetrate into the molecular layer. Also, it has been shown that the contact geometry of a Hg droplet changes with applied potential, leading to changes in contact area during an experiment[71]. A more recent adaptation of the Hg drop experiments is to replace Hg with a GaIn eutectic, which is a liquid at room temperature. Advantages and disadvantages of GaIn contacts are similar to Hg drop contacts[72, 73].

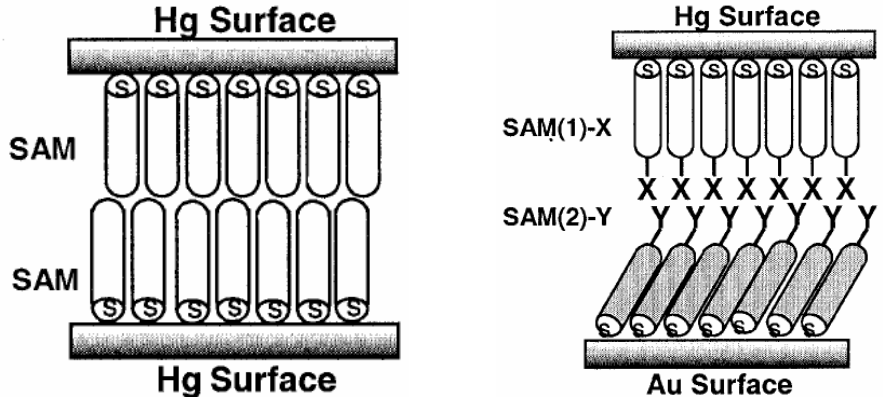

Figure 2.9: Schematic of two Hg drop conductance measurements on self-assembled monolayers[74].

2.4.2.2 Direct Metal Evaporation

Another method to fabricate many-molecule devices is by direct metal deposition of Au, Pt, or Ti on top of a molecular layer with thermal or electron beam evaporation[75, 76]. The are several advantages of this platform: straightforward fabrication of molecular junctions, the platform is compatible with standard microfabrication processing, and the work function of the top contact can be easily altered by depositing various metallic

contacts. The experimental problem with this technique is the tendency of the evaporated metal to penetrate or damage the molecular layer, leading to the formation of metallic filaments. For LB and self-assembled molecular layers, direct metal evaporation has been shown to cause severe damage to the molecular layer leading to electronic shorts, especially for Ti deposition[39, 77-79]. These results show that a stable molecular attachment paradigm is desired when performing direct metal evaporation on a molecular layer. A recent statistical analysis report by Kim et al. showed that Au evaporation on self-assembled alkanedithiols resulted in 98.8% electronic shorts out of 13,440 devices[80]. This analysis exemplifies the experimental limitations of self-assembly techniques when used together with standard microfabrication techniques. One approach that has been successful in fabricating molecular junctions through direct evaporation is the use of Cu as the top contact on irreversibly bonded molecular monolayers. Although not fully understood, Cu does not penetrate the molecular layer because of its low surface energy compared to Au and potential bonding between the Cu atoms and the molecular layer.

2.4.2.3 Indirect Metal Evaporation

This technique uses an indirect deposition method to reduce the kinetic energy of the incident metal atoms. For indirect deposition, Ar gas is back-filled into the evaporation chamber and the molecular layer is positioned to only permit Au atoms that have collided with an Ar atom to be deposited on the molecular surface[80-82]. According to Szablewski et Al., Au evaporation on cryogenically cooled LB monolayers eliminated damage to the molecular layer, as indicated by infrared spectroscopy[81]. This result shows that controlling the kinetic energy of the deposition vapor and controlling the temperature

of the substrate Au evaporation on LB monolayers can be achieved without creating molecular damage. One major problem with this approach, although not addressed by Szablewski et al, is the possibility of H_2O deposition on the LB layer when the substrate is cryogenically cooled. The presence of H_2O can lead to the formation of metal hydroxides at the interface and uncertainty in the interfacial chemistry[83].

2.4.2.4 Nanopores

The premise of the nanopore technique is that, by decreasing the junction area the probability for electronically shorted devices should decrease. Nanopore devices are fabricated by etching a pore though a SiO_2 or Si_3N_4 insulating layer on a Si wafer using electron beam lithography to define the pore size (~30-60 nm). After the formation of the nanopore, a self-assembled molecular layer is formed in the pore and metal is evaporated on top of the molecular layer, as shown in Figure 2.10. Several reports have shown that this technique can significantly improve the device yield; although the results seem strongly dependent on the molecule and substrate type[84-88]. This result provides evidence that "electronic shorts" are commonly caused by metal penetration at defect sites in the molecular layer. The major problem with this technique is that it does not address the fundamental reasons why damage to molecular layer occurs during the metal evaporation process.

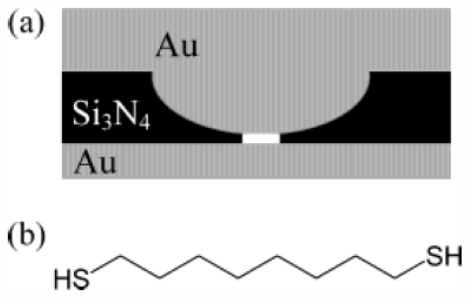

Figure 2.10: a, Schematic of a nanopore device where the Si_3N_4 is an insulating layer between the Au contacts. **b,** Chemical structure of octanedithiol[88].

2.4.2.5 Transfer Top Contact

As previously mentioned, formation of a top contact on a molecular layer commonly results in damage to the molecular layer or metal penetration through the molecular layer resulting in electronic behavior not characteristic of the molecular layer. One way to circumnavigate this problem is to form the top metallic contact on a sacrificial substrate and then transfer the contact onto of the molecular layer. With this method, the incident kinetic energy and heat of condensation during deposition are dissipated off the molecular layer. This energy is commonly assumed to be the cause of damage to the molecular layer during direct deposition. After the contact is formed with conventional deposition techniques, the contact is removed from the sacrificial substrate and placed onto the molecular layer. The key to the technique is developing a method to successfully transfer the formed contact form the sacrificial substrate on to the molecular layer.

Nanotransfer printing in one method to transfer a formed contact onto a molecular layer, as initially demonstrated by Hsu and further refined by Rogers[89, 90]. First, an elastomeric stamp was fabricated from poly(dimethylsiloxane) (PDMS) with designed

relief features. After coating the stamp with a layer of Au, the stamp is brought into contact with a thiol terminated molecular layer. Since surface bonding at the molecule/Au interface is higher compared to the bonding at the PDMD/Au interface, the Au layer remains on the molecular layer when the stamp is retracted. The major limitation of this technique is that the terminal group on the molecular layer must form a stronger bond with the Au layer than at the PDMD/Au interface. In addition, the applied force between the stamp and the molecular layer needs to be carefully controlled to eliminate damage to the molecular layer during transfer.

Another approach to transfer the contact onto the molecular layer is the polymer-assisted lift-off (PALO) technique[91, 92]. Similar to the nanotransfer technique, Au contacts are patterned onto a sacrificial mica substrate. The contacts are detached from the substrate by placing the substrate into a water bath at an angle, where the weak surface interaction between the Au and the mica allows the Au contacts to float onto the surface of the water. A molecular layer attached to the bottom contact is placed into the water bath and carefully removed in a manner where the Au contact floats onto the molecular layer. After the substrate is removed from the water with the Au contact positioned on the molecular layer, the junction is heated to remove residual water. In contrast to nanotransfer, this method does not contact the molecular layer with a stamp and the interaction at the contact /molecule interface can be relatively weak. The major disadvantage of this technique is that Au contact can buckle during the dying process resulting in an unknown contact area. Overall, both transfer techniques result in large

area molecular junctions without observable damage to the molecular layer or metal penetration into the molecular layer.

2.4.2.6 Conducting Polymer Top Contact

A growing trend to fabricate many-molecule junctions is to use a conducting polymer as the top contact. After a molecular layer is attached to the bottom contact, a conducting polymer is spin coated over the molecules and then a metallic layer is evaporated on top of the conducting polymer[75, 83]. The benefit of this technique is that the conducting polymer acts as a barrier to minimize both the formation of filaments and damage to the molecular layer. Akkerman et. al. has shown that spin coating the conducting polymer PEDOT:PSS over the molecular layer before metal deposition leads to reproducible results with a high yield (>95%)[75, 93, 94]. As shown in Figure 2.11, the measured current density exponentially increases as the alkanedithiol chain decreases suggesting that the conduction mechanism is tunneling. According to Akkerman et. al., conductivity was temperature independent for the temperature range of 199-293 K, which provides additional evidence of tunneling through the molecules.[75] Although this technique successfully prevents metal penetration into the molecular layer and damage to the molecular layer through the use of a sacrificial conducting film, several disadvantages of this technique are evident. First, controlling the conductivity in the PEDOT:PSS layer is difficult from sample to sample. The conductivity of the PEDOT:PSS layer is crucial because the layer is in series with the molecular layer. Second, the interface between the molecular layer and an amorphous conducting polymer is difficult to characterize, especially for further fitting or theoretical modeling. For the aqueous suspended

PEDOT:PSS layer to wet the hydrophobic aliphatic molecular layer, an organic surfactant (Zonyl FSO-100, Dupont) was used. The effect of the surfactant, which resides at the molecule/contact interface, on the observed molecular conductance is unknown and leads to uncertainty in the results.

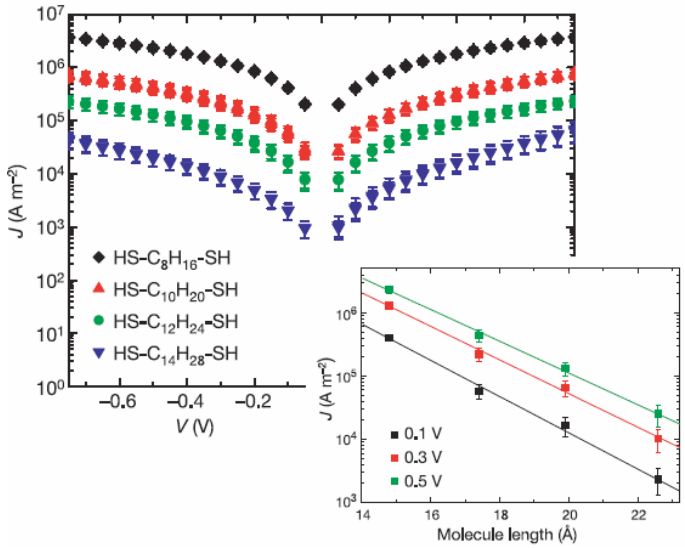

Figure 2.11: Current density versus applied voltage for alkanedithiols with PEDOT:PSS as the top electronic contact[75].

2.5 UNRESOLVED ISSUES

Although the field of molecular electronics has seen significant advancements since its conception, many experimental obstacles are currently limiting its progression into a commercial reality. Currently, the major issue within this field is the ability to create stable devices while maintaining the ability to control energy level alignment within an active device. Although strong electronic coupling between the molecules and contacts facilitate facile electron transport, energy level broadening can remove the

molecular identity of a molecular electronic device. New molecular attachment approaches are needed to form stable molecular junctions while maintaining the ability to control and modulate the alignment between the energy levels of the contacts and molecular orbitals.

Single/several molecule experimental platforms have provided significant insight into charge transport mechanisms through molecules. Although these techniques have the resolution required to probe single molecules, uncertainties in the molecular contact confirmation causes the reported β values to have a large range. Without controlling the contact geometry, designing a molecular device based on these measured properties has proven elusive. For single/several molecule platforms, the contacts are commonly formed at non-equilibrium conditions, which can result in a wide range of contact geometries and a wide range of measured molecular conductances. Although single molecule experiments have provided invaluable insight into molecular conduction, scaling of these platforms is unrealistic for future commercial applications with billions of devices are fabricated in parallel.

For fabrication methods which are compatible with standard micro-fabrication processing, designing experiments which exhibit technologically important phenomena has proven difficult. Direct metal deposition has been shown to cause damage to the molecular layer or metal penetration into the molecular layer causing electronic shorts. By employing cold evaporation techniques, the probability for molecular layer damage and filament formation has been shown to be decreased. Unfortunately the slow deposition times and cryogenic cooling can cause reactions at the molecular interface

leading to undesired interfacial contamination. Although the nanopore platform was shown to decrease the probability of fabricating electronically shorted molecular junctions, it does not address the problems associated with metal penetration during direct evaporation. The recent trend is to use a spin coated conducting polymer layer as the top molecular contact, where molecular junctions have been successfully fabricated without molecular damage or metal penetration. The limitation of this technique is the unknown properties of the interface between the conducting polymer and molecular layer.

2.6 REFERENCES

1. Aviram, A.; Ratner, M. A., Molecular Rectifiers *Chem. Phys. Lett.* **1974,** 29, (2), 277-283.

2. Martin, A. S.; Sambles, J. R.; Ashwell, G. J., Molecular Rectifier. *Phys. Rev. Lett.* **1993,** 70, (2), 218-221.

3. Chabinyc, M. L.; Holmlin, R. E.; Haag, R.; Chen, X. X.; Ismagilov, R. F.; Rampi, M. A.; Whitesides, G. M., Molecular electronics with a metal-insulator-metal junction based on self-assembled monolayers. *ACS Sym. Ser.* **2003,** 844, 16-35.

4. Chen, J.; Wang, W.; Klemic, J.; Reed, M. A.; Axelrod, B. W.; Kaschak, D. M.; Rawlett, A. M.; Price, D. W.; Dirk, S. M.; Tour, J. M.; Grubisha, D. S.; Bennett, D. W., Molecular wires, switches, and memories. In *Molecular Electronics Ii*, New York Acad Sciences: New York, 2002; Vol. 960, pp 69-99.

5. Blum, A. S.; Kushmerick, J. G.; Long, D. P.; Patterson, C. H.; Yang, J. C.; Henderson, J. C.; Yao, Y. X.; Tour, J. M.; Shashidhar, R.; Ratna, B. R., Molecularly inherent voltage-controlled conductance switching. *Nat. Mater.* **2005,** 4, (2), 167-172.

6. Chen, F.; He, J.; Nuckolls, C.; Roberts, T.; Klare, J. E.; Lindsay, S., A molecular switch based on potential-induced changes of oxidation state. *Nano Let.* **2005,** 5, (3), 503-506.

7. Kiehl, R. A.; Le, J. D.; Candra, P.; Hoye, R. C.; Hoye, T. R., Charge storage model for hysteretic negative-differential resistance in metal-molecule-metal junctions. *Appl. Phys. Lett.* **2006,** 88, (17).

8. Lortscher, E.; Ciszek, J. W.; Tour, J.; Riel, H., Reversible and controllable switching of a single-molecule junction. *Small* **2006,** 2, (8-9), 973-977.

9. Jang, S. S.; Jang, Y. H.; Kim, Y. H.; Goddard, W. A.; Flood, A. H.; Laursen, B. W.; Tseng, H. R.; Stoddart, J. F.; Jeppesen, J. O.; Choi, J. W.; Steuerman, D. W.; DeIonno, E.; Heath, J. R., Structures and properties of self-assembled monolayers of bistable [2]rotaxanes on Au(111) surfaces from molecular dynamics simulations validated with experiment. *J. Am. Chem. Soc.* **2005,** 127, (5), 1563-1575.

10. Piva, P. G.; DiLabio, G. A.; Pitters, J. L.; Zikovsky, J.; Rezeq, M.; Dogel, S.; Hofer, W. A.; Wolkow, R. A., Field regulation of single-molecule conductivity by a charged surface atom. *Nature* **2005,** 435, (7042), 658-661.

11. Song, H.; Kim, Y.; Jang, Y. H.; Jeong, H.; Reed, M. A.; Lee, T., Observation of molecular orbital gating. *Nature* **2009,** 462, (7276), 1039-1043.

12. Osorio, E. A.; O'Neill, K.; Wegewijs, M.; Stuhr-Hansen, N.; Paaske, J.; Bjornholm, T.; van der Zant, H. S. J., Electronic excitations of a single molecule contacted in a three-terminal configuration. *Nano Lett.* **2007,** 7, (11), 3336-3342.

13. Akkerman, H. B.; de Boer, B., Electrical conduction through single molecules and self-assembled monolayers. *J. Phys. Condens. Matter.* **2008,** 20, (1), 013001-013001.

14. Weiss, E. A.; Kriebel, J. K.; Rampi, M. A.; Whitesides, G. M., The study of charge transport through organic thin films: mechanism, tools and applications. *Phil. Trans. Math. Phys. Eng. Sci.* **2007,** 365, (1855), 1509-1537.

15. McCreery, R. L., Molecular electronic junctions. *Chem. Mater* **2004,** 16, (23), 4477-4496.

16. Datta, S., *Quantum transport atom to transistor*. Cambridge University Press: Cambridge, UK, 2005.

17. Engelkes, V. B.; Beebe, J. M.; Frisbie, C. D., Length-dependent transport in molecular junctions based on SAMs of alkanethiols and alkanedithiols: effect of metal work function and applied bias on tunneling efficiency and contact resistance. *J. Am. Chem. Soc.* **2004,** 126, (43), 14287-14296.

18. Bergren, A. J.; McCreery, R. L.; Stoyanov, S. R.; Gusarov, S.; Kovalenko, A., Electronic characteristics and charge transport mechanisms for large area aromatic molecular junctions. *J. Phys. Chem. C* 114, (37), 15806-15815.

19. Harrison, W. A., *Electronic Structure and the Properties of Solids: The Physics of the Chemical Bond*. Dover: 1989.

20. Bergren, A. J.; McCreery, R. L.; Stoyanov, S. R.; Gusarov, S.; Kovalenko, A., Electronic characteristics and charge transport mechanisms for large area aromatic molecular junctions. *J. Phys. Chem. C* **2009,** 114, (37), 15806-15815.

21. Galperin, M.; Ratner, M. A.; Nitzan, A., Molecular transport junctions: vibrational effects. *J. Phys. Condens. Matter* **2007,** 19, (10), 103201 (81pp).

22. Flood, A. H.; Wong, E. W.; Stoddart, J. F., Models of charge transport and transfer in molecular switch tunnel junctions of bistable catenanes and rotaxanes. *Chem. Phys.* **2006,** 324, (1), 280-290.

23. Buttiker, M., Coherent and sequential tunneling in series barriers. *IBM J. Res. Develop.* **1988,** 132, (1), 63-75.

24. Zhang, H. Y.; Li, X. Q.; Han, P.; Yu, X. Y.; Yan, Y. J., A partially incoherent rate theory of long-range charge transfer in deoxyribose nucleic acid. *J. Chem. Phys.* **2002,** 117, (9), 4578-4584.

25. Nitzan, A.; Jortner, J.; Wilkie, J.; Burin, A. L.; Ratner, M. A., Tunneling time for electron transfer reactions. *J. Phys. Chem. B* **2000,** 104, (24), 5661-5665.

26. Barman, S.; Deng, F. J.; McCreery, R. L., Conducting polymer memory devices based on dynamic doping. *J. Am. Chem. Soc.* **2008,** 130, (33), 11073-11081.

27. Lee, D.; Swager, T. M., Toward isolated molecular wires: A pH-responsive canopied polypyrrole. *Chem. Mater.* **2005,** 17, (18), 4622-4629.

28. Collier, C. P.; Wong, E. W.; Belohradsky, M.; Raymo, F. M.; Stoddart, J. F.; Kuekes, P. J.; Williams, R. S.; Heath, J. R., Electronically configurable molecular-based logic gates. *Science* **1999,** 285, (5426), 391-394.

29. Metzger, R. M.; Baldwin, J. W.; Shumate, W. J.; Peterson, I. R.; Mani, P.; Mankey, G. J.; Morris, T.; Szulczewski, G.; Bosi, S.; Prato, M.; Comito, A.; Rubin, Y., Electrical rectification in a Langmuir-Blodgett monolayer of dimethyanilinoazafullerene sandwiched between gold electrodes. *J. Phys. Chem. B* **2003,** 107, (4), 1021-1027.

30. Zasadzinski, J. A.; Viswanathan, R.; Madsen, L.; Garnaes, J.; Schwartz, D. K., Langmuir-Blodgett films. *Science* **1994,** 263, (5154), 1726-1733.

31. Peterson, I. R., Langmuir-blodgett films. *J. Phys. D-Appl. Phys.* **1990,** 23, (4), 379-395.

32. Kraack, H.; Ocko, B. M.; Perhan, P. S.; Sloutskin, E.; Deutsch, M., Structure of a Langmuir Film on a Liquid Metal. *Science* **2002,** 298, 1404-1407.

33. Porter, M. D.; Bright, T. B.; Allara, D. L.; Chidsey, C. E. D., Spontaneously organized molecular assemblies. 4 Structural characterization of normal-alkyl thiol monolayers on gold by optical ellipsometry, infrared-spectroscopy, and electrochemistry. *J. Am. Chem. Soc.* **1987,** 109, (12), 3559-3568.

34. Xue, Y.; Datta, S.; Hong, S.; Reifenberger, R.; Henderson, J. I.; Kubiak, C. P., Negative differential resistance in the scanning-tunneling spectroscopy of organic molecules. *Phys. Rev. B* **199,** 59, (12), 7852-7855.

35. Xue, Y.; Datta, S.; Hong, S.; Reifenberger, R.; Henderson, J. I.; Kubiak, C. P., Negative differential resistance in the scanning-tunneling spectroscopy of organic molecules. *Phys. Rev. B* **1999,** 59, (12), 7852-7855.

36. Laibinis, P. E.; Whitesides, G. M.; Allara, D. L.; Tao, Y. T.; Parikh, A. N.; Nuzzo, R. G., Comparison of the structures and wetting properties of self-assembled

monolayers of normal-alkanethiols on the coinage metal-surfaces, Cu, Ag, Au. *J. Am. Chem. Soc.* **1991,** 113, (19), 7152-7167.

37. Xiao, X. Y.; Xu, B. Q.; Tao, N. J., Measurement of single molecule conductance: Benzenedithiol and benzenedimethanethiol. *Nano Lett.* **2004,** 4, (2), 267-271.

38. Ferguson, G. S.; Chaudhury, M. K.; Biebuyck, H. A.; Whitesides, G. M., Monolayers on disordered substrates - self-assembly of alkylthrichlorosilanes on surface-modified polyethylene and poly(dimethylsiloxane). *Macromol.* **1993,** 26, (22), 5870-5875.

39. Richter, C. A.; Hacker, C. A.; Richter, L. J.; Kirillov, O. A.; Suehle, J. S.; Vogel, E. M., Interface characterization of molecular-monolayer/SiO2 based molecular junctions. *Solid State Electron.* **2006,** 50, (6), 1088-1096.

40. Wang, D.; Buriak, J. M., Trapping silicon surface-based radicals. *Langmuir* **2006,** 22, (14), 6214-6221.

41. Allongue, P.; Delamar, M.; Desbat, B.; Fagebaume, O.; Hitmi, R.; Pinson, J.; Saveant, J. M., Covalent modification of carbon surfaces by aryl radicals generated from the electrochemical reduction of diazonium salts. *J. Am. Chem. Soc.* **1997,** 119, (1), 201-207.

42. Brooksby, P. A.; Downard, A. J., Multilayer nitroazobenzene films covalently attached to carbon. An AFM and electrochemical study. *J. Phys. Chem. B* **2005,** 109, (18), 8791-8798.

43. Anariba, F.; DuVall, S. H.; McCreery, R. L., Mono- and multilayer formation by diazonium reduction on carbon surfaces monitored with atomic force microscopy "scratching". *Anal. Chem.* **2003,** 75, (15), 3837-3844.

44. Downard, A. J., Electrochemically assisted covalent modification of carbon electrodes. *Electroanal.* **2000,** 12, (14), 1085-1096.

45. Hoekstra, K. J.; Bein, T., Adsorption of zirconium-phosphonate multilayers onto phosphate-derivatized glassy carbon substrates. *Chem. Mater.* **1996,** 8, (8), 1865-1870.

46. Chatgilialoglu, C., (Me3Si)3SiH: twenty years after its discovery as a radical-based reducing agent. *Chem. A* **2008,** 14, 2310-2320.

47. Devaraj, N. K.; Decreau, R. A.; Ebina, W.; Collman, J. P.; Chidsey, C. E. D., Rate of interfacial electron transfer through the 1,2,3-triazole linkage. *J. Phys. Chem. B* **2006,** 110, (32), 15955-15962.

48. Devadoss, A.; Chidsey, C. E. D., Azide-modified graphitic surfaces for covalent attachment of alkyne-terminated molecules by "click" chemistry. *J. Am. Chem. Soc.* **2007,** 129, (17), 5370-+.

49. Bumm, L. A.; Arnold, J. J.; Dunbar, T. D.; Allara, D. L.; Weiss, P. S., Electron transfer through organic molecules. *J. Phys. Chem. B* **1999,** 103, (38), 8122-8127.

50. Datta, S.; Tian, W. D.; Hong, S. H.; Reifenberger, R.; Henderson, J. I.; Kubiak, C. P., Current-voltage characteristics of self-assembled monolayers by scanning tunneling microscopy. *Phys. Rev. Lett.* **1997,** 79, (13), 2530-2533.

51. Tian, W. D.; Datta, S.; Hong, S. H.; Reifenberger, R.; Henderson, J. I.; Kubiak, C. P., Conductance spectra of molecular wires. *J. Chem. Phys.* **1998,** 109, (7), 2874-2882.

52. Donhauser, Z. J.; Mantooth, B. A.; Kelly, K. F.; Bumm, L. A.; Monnell, J. D.; Stapleton, J. J.; Price, D. W.; Rawlett, A. M.; Allara, D. L.; Tour, J. M.; Weiss, P. S., Conductance switching in single molecules through conformational changes. *Science* **2001,** 292, (5525), 2303-2307.

53. Cygan, M. T.; Dunbar, T. D.; Arnold, J. J.; Bumm, L. A.; Shedlock, N. F.; Burgin, T. P.; Jones, L.; Allara, D. L.; Tour, J. M.; Weiss, P. S., Insertion, conductivity, and structures of conjugated organic oligomers in self-assembled alkanethiol monolayers on Au{111}. *J. Am. Chem. Soc.* **1998,** 120, (12), 2721-2732.

54. Wold, D. J.; Frisbie, C. D., Formation of metal-molecule-metal tunnel junctions: Microcontacts to alkanethiol monolayers with a conducting AFM tip. *J. Am. Chem. Soc.* **2000,** 122, (12), 2970-2971.

55. Mantooth, B. A.; Sykes, E. C. H.; Han, P.; Moore, A. M.; Donhauser, Z. J.; Crespi, V. H.; Weiss, P. S., Analyzing the motion of benzene on Au{111}: Single molecule statistics from scanning probe images. *J. Phys. Chem. C* **2007,** 111, (17), 6167-6182.

56. Engelkes, V. B.; Beebe, J. M.; Frisbie, C. D., Analysis of the causes of variance in resistance measurements on metal-molecule-metal junctions formed by conducting-probe atomic force microscopy. *J. Phys. Chem. B* **2005,** 109, (35), 16801-16810.

57. Morita, T.; Lindsay, S., Determination of single molecule conductances of alkanedithiols by conducting-atomic force microscopy with large gold nanoparticles. *J. Am. Chem. Soc.* **2007,** 129, (23), 7262-+.

58. Luo, L.; Frisbie, C. D., Length-dependent conductance of conjugated molecular wires synthesized by stepwise "click" chemistry. *J. Am. Chem. Soc.* **2010,** 132, (26), 8854.

59. Cui, X. D.; Primak, A.; Zarate, X.; Tomfohr, J.; Sankey, O. F.; Moore, A. L.; Moore, T. A.; Gust, D.; Nagahara, L. A.; Lindsay, S. M., Changes in the electronic properties of a molecule when it is wired into a circuit. *J. Phys. Chem. B* **2002,** 106, (34), 8609-8614.

60. Cui, X. D.; Primak, A.; Zarate, X.; Tomfohr, J.; Sankey, O. F.; Moore, A. L.; Moore, T. A.; Gust, D.; Harris, G.; Lindsay, S. M., Reproducible measurement of single-molecule conductivity. *Science* **2001,** 294, (5542), 571-574.

61. Smith, R. K.; Nanayakkara, S. U.; Woehrle, G. H.; Pearl, T. P.; Blake, M. M.; Hutchison, J. E.; Weiss, P. S., Spectral diffusion in the tunneling spectra of ligand-stabilized undecagold clusters. *J. Am. Chem. Soc.* **2006,** 128, (29), 9266-9267.

62. Suzuki, M.; Fujii, S.; Fujihira, M., Measurements of currents through single molecules of alkanedithiols by repeated formation of break junction in scanning tunneling microscopy under ultrahigh vacuum. *Jpn. J. Appl. Phys.* **2006,** 45, (3B), 2041-2044.

63. Xu, B. Q.; Tao, N. J. J., Measurement of single-molecule resistance by repeated formation of molecular junctions. *Science* **2003,** 301, (5637), 1221-1223.

64. Vrouwe, S. A. G.; van der Giessen, E.; van der Molen, S. J.; Dulic, D.; Trouwborst, M. L.; van Wees, B. J., Mechanics of lithographically defined break junctions. *Phys. Rev. B* **2005,** 71, (3).

65. Gonzalez, M. T.; Wu, S. M.; Huber, R.; van der Molen, S. J.; Schonenberger, C.; Calame, M., Electrical conductance of molecular junctions by a robust statistical analysis. *Nano Lett.* **2006,** 6, (10), 2238-2242.

66. Tsutsui, M.; Teramae, Y.; Kurokawa, S.; Sakai, A., High conductance state od single benzenedithiol molecules. *Appl. Phys. Lett.* **2006,** 89, 163111.

67. Strachan, D. R.; Smith, D. E.; Johnston, D. E.; Park, T. H.; Therien, M. J.; Bonnell, D. A.; Johnson, A. T., Controlled fabrication of nanogaps in ambient environment for molecular electronics. *Appl. Phys. Lett.* **2005,** 86, (4), 3.

68. Hadeed, F. O.; Durkan, C., Controlled fabrication of 1-2 nm nanogaps by electromigration in gold and gold-palladium nanowires. *Appl. Phys. Lett.* **2007,** 91, (12), 3.

69. Noguchi, Y.; Nagase, T.; Kubota, T.; Kamikado, T.; Mashiko, S., Fabrication of Au-molecule-Au junctions using electromigration method. *Thin Solid Films* **2006,** 499, (1-2), 90-94.

70. Demarchi, D.; Civera, P.; Piccinini, G.; Cocuzza, M.; Perrone, D., Electrothermal modelling for EIBJ nanogap fabrication. *Electrochim. Acta* **2009,** 54, (25), 6003-6009.

71. Antelmi, D. A.; Connor, J. N.; Horn, R. G., Electrowetting measurements with mercury showing mercury/mica interfacial energy depends on charging. *J. Phys. Chem. B* **2004,** 108, (3), 1030-1037.

72. Nijhuis, C. A.; Reus, W. F.; Whitesides, G. M., Mechanism of rectification in tunneling junctions based on molecules with asymmetric potential drops. *J. Am. Chem. Soc.* **2010,** 132, (51), 18386-18401.

73. Nijhuis, C. A.; Reus, W. F.; Whitesides, G. M., Molecular rectification in metal-sam-metal oxide-metal junctions. *J. Am. Chem. Soc.* **2009,** 131, (49), 17814-17827.

74. Rampi, M. A.; Whitesides, G. M., A versatile experimental approach for understanding electron transport through organic materials. *Chem. Phys.* **2002,** 281, (2-3), 373-391.

75. Akkerman, H. B.; Blom, P. W. M.; de Leeuw, D. M.; de Boer, B., Towards molecular electronics with large-area molecular junctions. *Nature* **2006,** 441, (7089), 69-72.

76. Anariba, F.; McCreery, R. L., Electronic conductance behavior of carbon-based molecular junctions with conjugated structures. *J. Phys. Chem. B* **2002,** 106, (40), 10355-10362.

77. Nowak, A. M.; McCreery, R. L., Characterization of carbon/nitroazobenzene /titanium molecular electronic junctions with photoelectron and Raman spectroscopy. *Anal. Chem.* **2004,** 76, (4), 1089-1097.

78. Richter, C. A.; Hacker, C. A.; Richter, L. J., Electrical and spectroscopic characterization of metal/monolayer/Si devices. *J. Phys. Chem. B* **2005,** 109, (46), 21836-21841.

79. de Boer, B.; Meng, H.; Perepichka, D. F.; Zheng, J.; Frank, M. M.; Chabal, Y. J.; Bao, Z. N., Synthesis and characterization of conjugated mono- and dithiol oligomers and characterization of their self-assembled monolayers. *Langmuir* **2003,** 19, (10), 4272-4284.

80. Jaiswal, A.; Rajagopal, D.; Lakshmikantham, M. V.; Cava, M. P.; Metzger, R. M., Unimolecular rectification of monolayers of CH3C(O)S-C(14)H(28)Q(+)-3CNQ(-) and CH3C(O)S-C(16)H(32)Q(+)-3CNQ(-) organized by self-assembly, Langmuir-Blodgett, and Langmuir-Schaefer techniques. *Phys. Chem. Chem. Phys.* **2007,** 9, (30), 4007-4017.

81. Xu, T.; Morris, T. A.; Szulczewski, G. J.; Metzger, R. M.; Szablewski, M., Current-voltage characteristics of an LB monolayer of didecylammonium tricyanoquinodimethanide measured between macroscopic gold electrodes. *J. Mater. Chem.* **2002,** 12, (10), 3167-3171.

82. Xu, T.; Peterson, I. R.; Lakshmikantham, M. V.; Metzger, R. M., Rectification by a monolayer of hexadecylquinolinium tricyanoquino-dimethanide between gold electrodes. *Angew. Chem. Int. Ed. Engl.* **2001,** 40, (9), 1749-1752.

83. Haick, H.; Cahen, D., Contacting organic molecules by soft methods: Towards molecule-based electronic devices. *Acc. Chem. Res.* **2008,** 41, (3), 359-366.

84. Zhou, C.; Deshpande, R. M.; Reed, M. A.; Jones II, L.; Tour, J. M., Nanoscale metal/self-assembled monolayer/metal heterostructures. *Appl. Phys. Lett.* **1997,** 71, (5), 611-613.

85. Majumdar, N.; Gergel, N.; Routenberg, D.; Bean, J. C.; Harriott, L. R.; Li, B.; Pu, L.; Yao, Y.; Tour, J. M., Nanowell device for the electrical characterization of metal-molecule-metal junctions. *J. Vac. Sci. Technol. B* **2005,** 23, (4), 1417-1421.

86. Kim, T. W.; Wang, G. N.; Lee, H.; Lee, T., Statistical analysis of electronic properties of alkanethiols in metal-molecule-metal junctions. *Nanotechn.* **2007,** 18, (31).

87. Kim, T. W.; Wang, G.; Song, H.; Choi, N. J.; Lee, H.; Lee, T., Charge transport of alkanethiol self-assembled monolayers in micro-via hole devices. *J. Nanosci. Nanotechnol.* **2006,** 6, (11), 3487-3490.

88. Wang, W. Y.; Lee, T.; Kretzschmar, I.; Reed, M. A., Inelastic electron tunneling spectroscopy of an alkanedithiol self-assembled monolayer. *Nano Lett.* **2004,** 4, (4), 643-646.

89. Loo, Y. L.; Lang, D. V.; Rogers, J. A.; Hsu, J. W. P., Electrical contacts to molecular layers by nanotransfer printing. *Nano Lett.* **2003,** 3, (7), 913-917.

90. Niskala, J. R.; You, W., Metal-molecule-metal junctions via PFPE assisted nanotransfer printing (nTP) onto self-assembled monolayers. *J. Am. Chem. Soc.* **2009,** 131, (37), 13202-+.

91. Shimizu, K. T.; Fabbri, J. D.; Jelincic, J. J.; Melosh, N. A., Soft deposition of large-area metal contacts for molecular electronics. *Adv. Mater.* **2006,** 18, (12), 1499-+.

92. Stein, N.; Korobko, R.; Yaffe, O.; Lavan, R. H.; Shpaisman, H.; Tirosh, E.; Vilan, A.; Cahen, D., Nondestructive Contact Deposition for Molecular Electronics: Si-Alkyl//Au Junctions. *J. Phys. Chem. C* 114, (29), 12769-12776.

93. PEDOT:PSS = poly(3,4-ethylenedioxythiophene):poly(styrenesulfonate).

94. Akkerman, H. B.; Naber, R. C. G.; Jongbloed, B.; van Hal, P. A.; Blom, P. W. M.; de Leeuw, D. M.; de Boer, B., Electron tunneling through alkanedithiol self-assembled monolayers in large-area molecular junctions. *Proc. Nat. Acad. Sci. USA* **2007,** 104, (27), 11161-11166.

CHAPTER 3

FABRICATION OF MOLECULAR JUNCTIONS

THROUGH DIRECT EVAPORATION

3.1 INTRODUCTION

Virtually all types of molecular electronic devices depend on electronically addressing a molecule or molecular layer through the formation of a metallic contact. The term "molecular junction" applies to a single-molecule or ensemble of molecules oriented in parallel between conducting contacts, and is the basic component of molecular electronics. Charge transport through single or ensemble molecular junctions has been investigated with techniques such as scanning tunneling microscopy, conducting probe atomic force microscopy, and vapor deposition of top contacts[1-3]. The introduction of molecular devices into integrated circuits will likely depend on contact formation through a vapor deposition technique, but this approach frequently results in the metal atoms penetrating or damaging the molecular layer. This chapter outlines a fabrication paradigm to form many-molecule molecular junctions through direct evaporation of a second electronic contact.

As discussed in Chapter 2, several molecular attachment paradigms have been employed to fabricate molecular junctions, including self-assembled monolayers (SAM), Langmuir-Blodgett films (LB), and the formation of C-C or Si-C irreversible bonds between the contact and molecular layer[4-7]. Irreversible bonding provides structural stability to the molecular layer during subsequent fabrication and characterization processes, thus reducing the likelihood of molecular damage or metal penetration[8]. Although less ordered than to SAMs, irreversible bonding allows the formation of molecular multilayer structures where the thickness can be controlled through the deposition conditions[7, 9]. The irreversible molecular attachment approach used in this

dissertation exploits the inherent stability of the C-C bond to fabricate stable molecular junctions, thus allowing understanding into how molecular structure and electronic coupling between the molecules and substrate influence charge transport through molecular junctions.

Although the field of molecular electronics has achieved significant progress in the fabrication of molecular junctions through vapor deposition techniques, the ability to fabricate robust junctions with high yields has proven experimentally difficult[7]. Contact formation through vapor deposition (e.g. metal evaporation) has several benefits such as parallel fabrication and the ability to form contacts with various work functions. Experimental limitations include metal penetration through the molecular layer and molecular damage resulting in electronic behavior characteristic of electronic shorts. Through spectroscopic techniques, several groups have shown that direct evaporation of reactive metals such as Ti results in significant structural damage to the molecular layer[10, 11]. Direct evaporation of noble metals commonly results in partial molecular damage, molecular displacement at the substrate/molecule interface, or Au penetration between the molecules[12, 13]. These results depended strongly on the substrate/molecule bonding characteristics, type of molecular layer, and terminal groups. Fabrication techniques have been developed to mitigate metal penetration and molecular damage. Examples include spin coating a conducting polymer contact, indirect evaporation, and the evaporation of Cu[1, 14-16].

In this chapter, a paradigm to fabricate large area, many molecule junctions through metal evaporation of the top (second) contact on a molecular layer covalently

attached to an amorphous, mostly sp^2 carbon bottom contact is outlined. This technique has been successfully employed by the McCreery research group. They have definitively shown direct Cu deposition onto irreversibly bonded molecular layers results in robust, highly reproducible molecular junctions without metal penetration or molecular damage[1, 7, 17, 18]. Although Cu deposition has been shown successful for molecular multilayer junctions, fabrication of Au or Pt contacted junctions and junctions consisting of a molecular monolayer remain an experimental challenge. This chapter explores the reason for metal penetration into molecular layers through a relativity simple experimental approach of angled metal evaporation. By simply changing the incident deposition angle, the momentum of the depositing atoms perpendicular to the molecular surface can be reduced. From these experiments, significant insights affecting metal penetration into molecular layers are identified and are employed in Chapter 4 to design a novel molecular junction fabrication paradigm.

3.1 EXPERIMENTAL

3.2.1 Pyrolyzed Photoresist Bottom Electronic Contacts

For all molecular junctions fabricated in Chapter 3 and Chapter 4, the bottom electronic contact consisted of a pyrolyzed photoresist film (PPF), an amorphous, mostly sp^2 hybridized, carbon layer formed through the pyrolysis of photoresist at 1000 °C in a reducing atmosphere[19-21]. The paradigm of employing PPF as an electronic contact for molecular junctions was introduced in 2001 by McCreery, et al. Advantages of this approach include ease of fabrication, low surface roughness, and the attachment of

molecular layers through the irreversible bonding paradigms of diazonium reduction and oxidation of primary amines[19, 21, 22].

The PPF bottom contacts were fabricated on substrates consisting of 13 mm x 18 mm p-Si substrate with a 300 nm thick thermal SiO_2 insulating layer. The substrates were ultrasonically cleaned with sequential immersion in acetone, deionized water (TOC < 3 ppb), and isopropanol for 10 minutes. Following ultrasonic cleaning, the substrates were dried in a dry Ar stream. The substrates were spin coated with photoresist AZ P4330-RS at 6000 rpm for 30 seconds, soft baked at 90°C for 10 minutes, and pyrolyzed in a tube furnace[23]. Prior to pyrolysis, standard lithography was used to pattern the photoresist into four separate 0.5 mm x 18 mm lines. For the pyrolysis process, the temperature ramp rate was 8°C min^{-1} and held at 1000°C for 60 min in the presence of forming gas (5% hydrogen and 95% nitrogen) flowing at 100 cc/min. Metal tubing with brass fittings was used between the forming gas source and tube furnace to ensure the purity and H_2 content of the forming gas. The final thickness of the PPF was between 700-800 nm with a surface root mean square (RMS) roughness determined with AFM of less than 0.5 nm. Conductivity of the PPF layer was measured with a co-linear four-point setup to be 5×10^{-3} $\Omega \cdot cm$. After the pyrolysis process, the PPF was stored under vacuum and used within one week after pyrolysis. A schematic of the PPF fabrication process is shown in Figure 3.1.

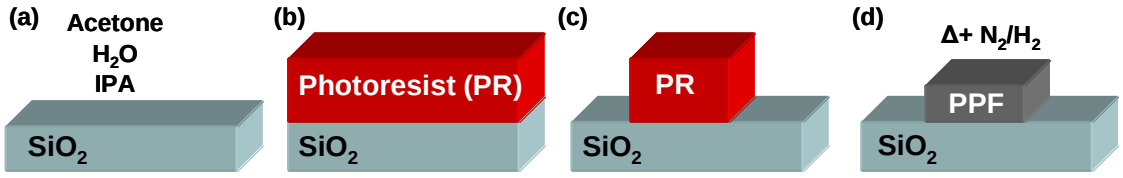

Figure 3.1: Schematic of PPF fabrication. **a,** Substrate ultrasonically cleaned. **b,** Photoresist spin coated onto substrate and soft baked. **c,** Optical lithography used to pattern the photoresist. **d,** Pyrolysis of photoresist at 1000 °C for 1 hour results in the PPF bottom electronic contact.

3.2.2 Molecular Attachment through Diazonium Reduction

For the attachment of aromatic molecular layers, radical attachment to the PPF bottom contact occurred through the electrochemical reduction of a diazonium cation. First introduced by Pinson and coworkers[22, 24], modification of carbon surfaces through the electrochemical reduction of aromatic diazonium cations has been extensively characterized. The standard approach is to synthesize the diazonium cation from the corresponding aromatic amine and then isolate the diazonium salt. Purification of the diazonium salt is achieved during the isolation process. The isolated diazonium salt can be stored in a freezer for a few months without degradation. Although isolation of the diazonium salt is preferred, some diazonium salts cannot be isolated in pure form. For these molecules, aryl diazonium cations are generated and then electrochemically attached in-situ to the PPF surface without isolation of the diazonium salt[25].

Molecular attachment via diazonium reduction is schematically shown in Figure 3.2[26]. First, one electron is transferred from the PPF surface to the diazonium cation causing cleavage of the N_2-C bond to form the aryl radical. Reduction of the diazonium cations occurs at low reduction potentials because of the strong electron-withdrawing

effect of the diazonium group. The generated aryl radicals attach to the PPF surface to form strong covalent C-C bonds.

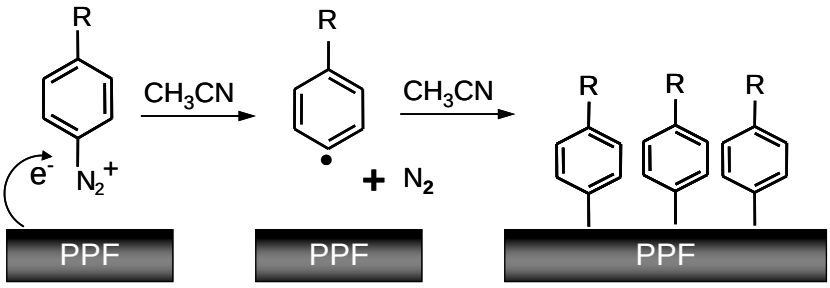

Figure 3.2: Schematic of molecular attachment through diazonium reduction, where aryl radical formation is through a one-electron electrochemical reduction. Attachment occurs through the interaction of the aryl radical and PPF surface resulting in a C-C bond.

Attachment of aromatic molecular multilayers to the PPF bottom contacts was achieved through a cyclic voltammogram method. As shown by several different labs, the molecular multilayers consisted of covalently bonded and conjugated subunits which form from successive attack of the first monolayer by electrogenerated radicals[24,27,28]. For the attachment of 4-nitroazobenzene (NAB) molecular multilayers, the potential of the PPF contact was scanned from + 0.4 V to -0.6 V for four scans in acetonitrile (MeCN) containing 1 mM NAB diazonium salt and 0.1 M n-tetrabutylammonium tetrafluoroborate ($TBABF_4$) as the supporting electrolyte. As shown in Figure 3.3, attachment of NAB occurred when the voltage was swept negative as identified by the presence of a broad, irreversible cathodic peak during the first scan. The height of the voltammetric peak decreases rapidly for additional scans which is indicative of the formation of a passivating molecular layer on the carbon electrode. With the presence of

a molecular layer, charge transfer from the PPF surface to the diazonium cations is less likely leading to the observed decrease in the cathodic peak.

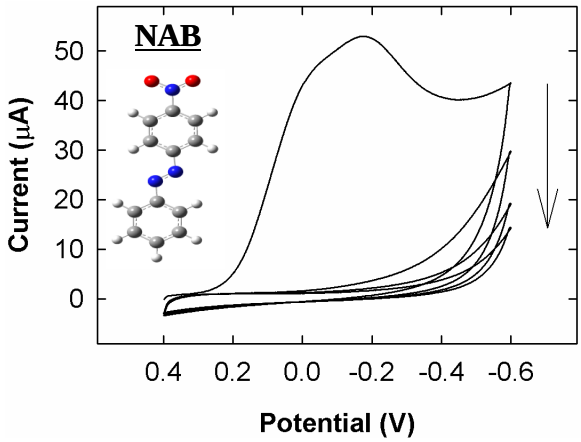

Figure 3.3: Cyclic voltammogram of reduction of 1 mM $NO_2C_6H_4N_2^+$ BF_4^- on a PPF contact resulting in a covalently attached NAB multilayer. Inset is the chemical structure of NAB: nitrogen (blue), carbon (grey), oxygen (red), hydrogen (white).

3.2.3 Molecular Attachment through Oxidation of Primary Amines

For the attachment of aliphatic molecular layers, attachment to the PPF contacts occurred through the electrochemical oxidation of a primary aliphatic amine[29, 30]. The attachment process involves the formation of an aliphatic amine cation radical through a one-electron oxidation of a primary aliphatic amine. Reaction of the cation radial with the PPF surface creates a strong carbon-nitrogen covalent bond. A schematic of the attachment process is shown in Figure 3.4.

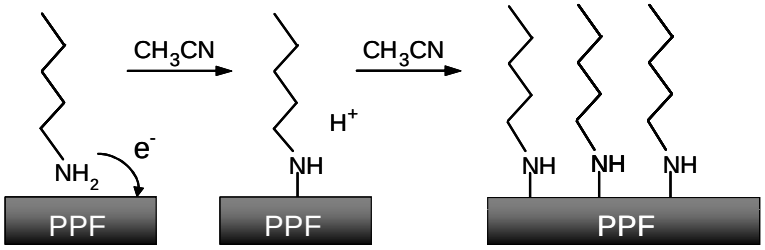

Figure 3.4: Schematic of molecular attachment through oxidation of a primary amine, where radical formation is through one-electron electrochemical oxidation. Attachment occurs through interaction of the radical and the PPF surface resulting in a C-N bond.

In this chapter, the aliphatic molecular monolayers were attached to the PPF contacts through a constant potential electrolysis technique. A constant potential of 0.5 V versus an Ag/Ag^+ electrode was applied to the PPF surface immersed in 5 mM decylamine in MeCN solution containing 0.1 M $TBABF_4$ as the supporting electrolyte. Figure 3.5 shows the measured anodic current versus time for the attachment of a monolayer of decylamine. The decrease in anodic current with time is caused by the passivation of PPF, with the forming decylamine monolayer preventing further oxidation at the PPF/molecule surface.

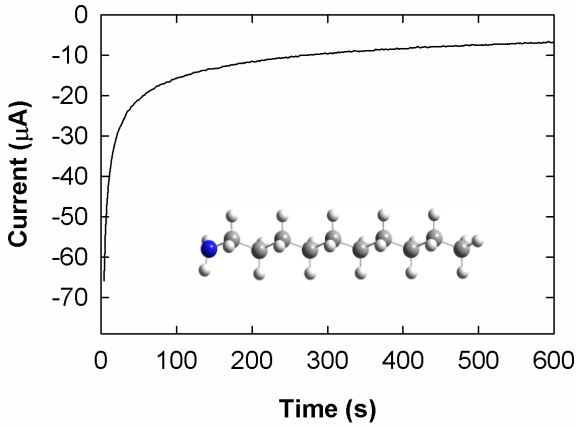

Figure 3.5: Oxidation of PPF contact in decylamine ($C_{10}H_{21}NH_2$) resulting in a covalently attached $C_{10}NH$ monolayer. Inset is the chemical structure of decylamine: nitrogen (blue), carbon (grey), hydrogen (white).

3.2.4 Molecular Layer Thickness

The thickness of the electrochemically attached molecular layers was measured with an AFM "scratching" technique[9]. For this technique, a trench is intentionally scratched into a molecular layer attached to PPF with AFM in contact mode. The AFM tip is loaded with a constant force while the tip is scanned across the molecular surface. The tip force was calibrated to be high enough to completely scratch away the molecular layer but low enough to not scratch into the PPF contact. For all measurements, scratching was performed on a PPF section without a molecule layer to ensure that the tip force did not scratch into the PPF surface. After AFM scratching, the trench and surrounding molecular layer were imaged with AFM tapping mode using the same tip. The thickness of the molecular layer is determined by the difference in the height of the scratched region and the unscratched region, as analyzed by the AFM software.

For all molecular layers in this dissertation, the thickness was measured at atmospheric conditions with a Digital Instruments DI3100 AFM equipped with Si tips

(MicroMasch) with a resonance frequency of ~ 300 kHz. For scratching in contact mode, the voltage set-point was between 0.25 – 0.75 V with a scan rate of 1 Hz. The scratching direction was perpendicular to the cantilever to allow a uniform contact force. For imaging in AFM tapping mode after scratching, the image was acquired at a scan rate of 0.5 Hz. Figure 3.6 shows the final tapping mode image of a scratch trench in a decylamine ($C_{10}H_{21}NH_2$) monolayer. As is apparent, a 4 μm x 4 μm trench was scratched into the monolayer in contact mode followed by imaging a 10 μm x 10 μm area incorporating the trench. To calculate the molecular layer thickness, the z-height scale of the image was determined within the 3 μm x 10 μm dashed box shown in Figure 3.6. For statistical analysis, the average height and standard deviation were calculated from the z-height measured in the scratched trench region and on top of the molecular layer. For the molecular layers investigated in this chapter, the NAB molecular layer was 3.9 ± 0.3 nm and the $C_{10}H_{21}NH_2$ monolayer was 1.2 ± 0.2 nm thick.

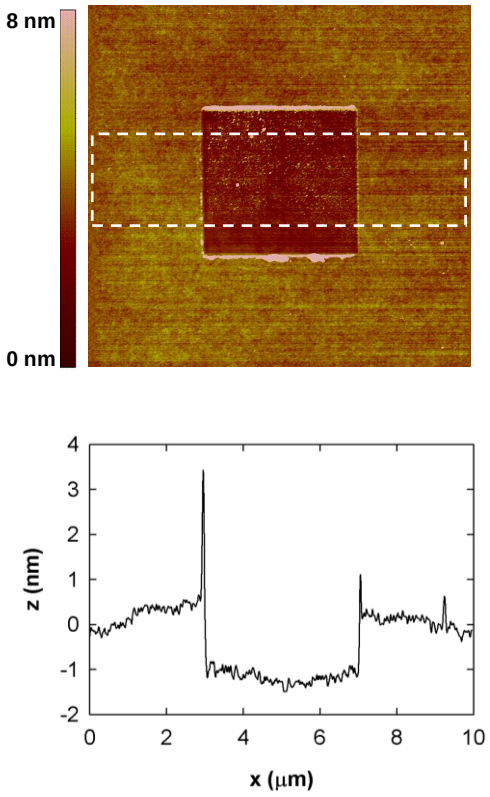

Figure 3.6: Decylamine monolayer thickness measured by AFM scratching technique. The 4 μm x 4 μm trench was scratched in the monolayer with AFM in contact mode. The z-depth of the scratched trench is used to determine the molecular layer thickness.

3.2.5 Characterization of Molecular Layers with Raman Spectroscopy

Raman spectroscopy was used to characterize a NAB multilayer on PPF before and after the evaporation of a 10 nm Au top contact. The thin Au layer allowed sufficient optical transmission for the Raman signal. A custom built spectrometer[31] consisting of an Ar ion laser (514.5 nm), a 50 mm f/1.8 lens, a holographic reflection grating (2000 grove/mm), and an Andor back-thinned CCD detector cooled to -80° C was used to acquire the spectra. The incident laser power was 19 mW with a spot diameter of 17 μm.

The integration time was 30 seconds and the Raman shift was calibrated with naphthalene.

3.2.6 Direct Evaporation of Top Electronic Contacts

For direct evaporation of the top molecular contacts, Au and Cu layers were deposited onto the molecular layer through a shadow mask resulting in a cross-bar geometry with an active area of 0.5 mm^2. Evaporation occurred in a Kurt J. Lesker PVD-75 electron beam evaporation system with a deposition pressure of ~ 2 x 10^{-6} torr. For standard direct evaporation, the deposition angle was at 0° relative to the surface normal of the molecular layer, as shown in Figure 3.7. The deposition rate was 0.2 $Å \cdot s^{-1}$ for the 10 nm Au and Cu top contacts, where an additional 10 nm of Au was deposited on the Cu top contacts to prevent Cu oxidation before and during electronic characterization.

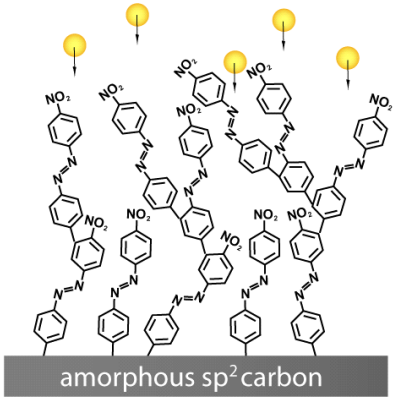

Figure 3.7: Schematic of the direct metal evaporation at 0° deposition angle. Metal penetration has been proposed to be caused by damage to the molecular layer or penetration through defects or spacing between molecules in the molecular layer.

For direct evaporation at different deposition angles (θ), where the angle is relative to the surface normal of the molecular layer, the deposition rate and final thickness (t) was varied according the following equations:

$$rate = \frac{0.2}{\cos(\theta)} \quad \text{Å}\cdot\text{s}^{-1} \qquad \text{Eq. 3.1}$$

$$t = \frac{10}{\cos(\theta)} \quad \text{nm} \qquad \text{Eq. 3.2}$$

By changing the deposition rate and thickness, the resulting contact thickness and the deposition time remained constant for all junctions. The deposition thickness and rate were monitored by a quartz crystal microbalance. The deposition angle was varied by attaching the substrates onto aluminum wedges attached to a standard substrate holder resulting in junctions fabricated at 0°, 45°, 60°, and 70°. Although the total momentum (**p**) of the incident metallic atoms onto the molecular layer is constant at all deposition angles, components of the momentum perpendicular ($\mathbf{p}_{\perp}$) and parallel ($\mathbf{p}_{ll}$) to the molecular layer varied according to:

$$\mathbf{p}_{ll} = \mathbf{p}\sin(\theta) \qquad \text{Eq. 3.3}$$

$$\mathbf{p}_{\perp} = p\cos(\theta) \qquad \text{Eq. 3.4}$$

These equations show that the $\mathbf{p}_\perp$ can be varied by simply controlling the deposition angle, as shown in Figure 3.8. The effect of controlling $\mathbf{p}_\perp$ on the tendency for metal penetration into a molecular layer is discussed in subsequent paragraphs.

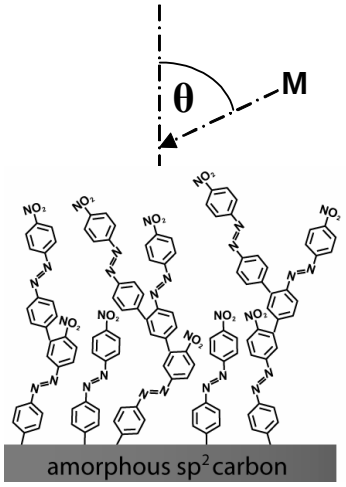

Figure 3.8: Schematic of direct metal evaporation at various deposition angles**.** The momentum (**p**) perpendicular and parallel to the molecular surface follow cosine and sine functions as shown in Eq. 3.3 and 3.4.

3.2.7 Electronic Characterization of Fabricated Molecular Junctions

Electronic characterization was performed in a three probe format allowing for the correction of resistance errors associated with the PPF contact. Current density – voltage (J-V) curves were measured using a custom setup of a National Instruments 6110 data acquisition board and a Stanford Research Systems 570 current amplifier programmed with Labview software[32]. The junction voltage was scanned between 0 to ±1 V with a scan rate of 10 $V \cdot s^{-1}$. Current amplification and signal filtering parameters were carefully selected to reduce noise without affecting the J-V response. *For all*

electronic measurements, the stated voltage is the PPF contact relative to the metallic contact.

For convenience of notation, the fabricated molecular junctions are stated as molecule/contact, where all discussed junctions were fabricated on a PPF bottom contact. For example, a NAB/Au junction describes a 3.9 nm thick NAB multilayer on PPF with an Au top electronic contact. The decylamine monolayer is abbreviated as $C_{10}NH$ in this chapter.

3.3 RESULTS AND DISCUSSION

3.3.1 Characterization of Pyrolyzed Photoresist Electronic Contacts

The structure of the PPF contacts was characterized by X-ray diffraction (XRD), as shown in Figure 3.9 for a PPF contact on a fused silica substrate. Spectra were collected with a Bruker-AXS Discover D8 diffractometer equipped with a 2D x-ray detector. X-rays were generated with a copper target X-ray tube (CuKα, $\lambda = 1.54056$ Å) with a 0.7 mm diameter probe beam. The broad peak centered at $2\theta = 24.6°$ is the (002) diffraction peak, which is consistent with an average intra-plane spacing of 3.6 Å[33]. Compared to the (002) intra-plane spacing in graphite of 3.335 Å, the higher intra-plane spacing and the broad nature of the (002) peak is indicative of a disordered graphitic structure. Considering the photoresist is a type of phenolic resin, a disordered graphitic structure is expected after pyrolysis as side chains along the photoresist backbone limit complete restructuring to graphite.

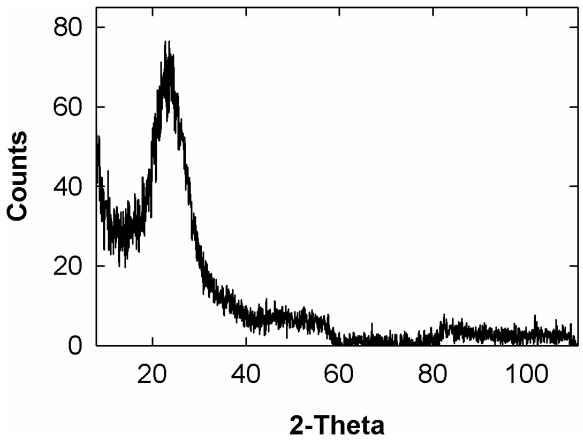

Figure 3.9: XRD pattern for a PPF contact on a fused silica substrate. The broad peak at $2\theta = 24.6°$ corresponds to the (002) planes.

Raman spectroscopy was used to provide additional structural characterization of the PPF contacts. Figure 3.10 shows the Raman spectrum of PPF on a fused silica substrate between 1000 – 1800 wavenumbers (cm^{-1}). The spectrum contains two distinct Raman bands centers at 1350 cm^{-1} and 1600 cm^{-1}. The band at 1600 cm^{-1} is assigned to the G-band and is commonly observed for graphitic structures[34]. The band at 1350 cm^{-1} is assigned to the D-band and is characteristic of disorder in carbon materials[34]. Combined, the presence and relative intensity of the two bands is consistent with the XRD results that the PPF contacts have a disordered graphitic structure (sp^2 hybridized) similar to glassy carbon.

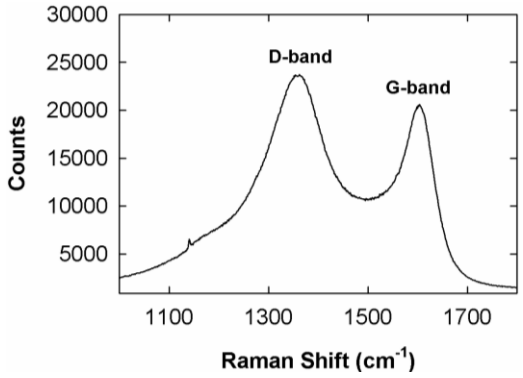

Figure 3.10: Raman spectrum of PPF on a fused silica substrate. The Raman bands at 1350 cm^{-1} and 1600 cm^{-1} are consistent with a disordered graphitic structure.

3.3.2 Determining Molecular Damage with Raman Spectroscopy

Raman spectra for a NAB 3.9 nm thick multilayer on PPF are shown in Figure 3.11 before and after deposition of a 10 nm Au top contact. Comparison of these spectra confirms that structural changes are not observed, providing strong evidence that the NAB layer is not damaged during direct Au evaporation. Since the Raman shift is sensitive to small variations in molecular bonding and structure, changes to the Raman bands are expected if structural changes had occurred in the molecules. The decrease in Raman intensity after Au deposition was caused by the partial transparency of the 10 nm thick Au contact. This result is consistent with previous reports that direct Au evaporation on NAB molecular layers does not result in molecular damage[35]. Although only shown for the NAB layer, molecular damage during direct Au evaporation was not observed for any of the aromatic molecular layers investigated in this dissertation, including azobenzene (AB) and dimethylaminoazobenzene (DAB). Several reasons for the stability of the investigated molecular layers include the strong bonding at the

PPF/molecule interface and the lack of strong chemical interaction between the molecular layer and the noble Au contact.

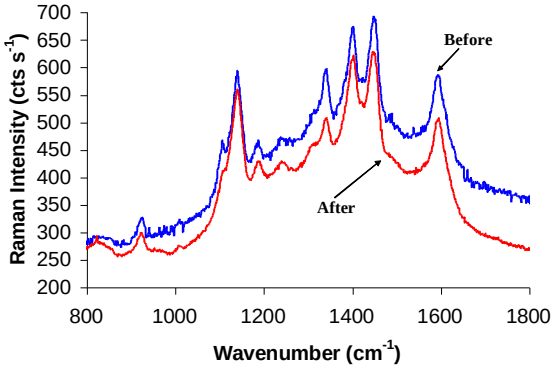

Figure 3.11: Raman spectra for a 3.9 nm NAB multilayer on PPF before and after Au evaporation at 0° relative to the molecular layer surface normal. Direct Au evaporation did not cause observable loss or shift in the NAB Raman bands, showing the absence of molecular damage.

3.3.3 Effect of Evaporation Angle on Junction Electronic Characteristics

The J-V curves for NAB/Au and NAB/Cu junctions formed through direct evaporation at 0° are shown in Figure 3.12. Direct Au evaporation at 0° resulted in linear a J-V response for NAB/Au junctions, which is characteristic of the formation of metal filaments through the molecular layer. For all junctions, the stated voltage is the bottom PPF contact relative to the metallic top contact. Based on the Raman results, the formation of metal filaments most likely occurred by Au atoms penetrating into the molecular layer and depositing on the PPF bottom contact. In contrast, direct Cu evaporation at 0° resulted in a non-linear J-V response which has been attributed to non-resonant tunneling through the NAB layer[1, 17]. As described in the previous references,

the lack of Cu penetration into the molecule layer has been attributed to the higher surface energy of Cu compared to Au, the tendency for bond formation between the Cu and molecular layer, or the formation of oxides or hydroxides at the Cu/molecule interface. Although the formation of molecule/Cu junctions has been shown to result in reproducible J-V curves, the ability to fabricate molecular junctions with additional metallic contacts such as Au and Pt is experimentally desirable.

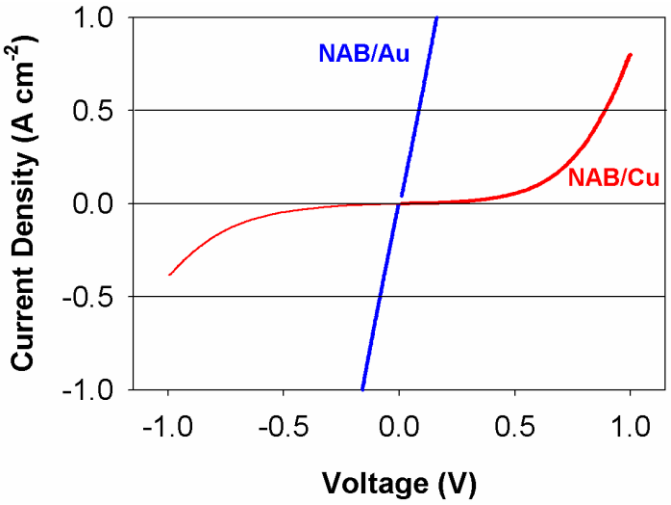

Figure 3.12: J-V curves for NAB/Cu and NAB/Au junctions for direct evaporation at 0° showing a significant difference in the observed current.

The J-V curves for $C_{10}NH$/Au and $C_{10}NH$/Cu junctions formed through direct evaporation at 0° is shown in Figure 3.13. For both top contacts, direct evaporation at 0° resulted in J-V responses characteristic of metal filament formation. Unlike NAB/Cu junctions in Figure 3.12, where the NAB layer consisted of a 3.9 nm thick multilayer, the $C_{10}NH$ layer was measured to be a monolayer about 1.2 nm thick. The thinner monolayer is more likely to have metal filaments as the required penetration depth is less to create metal filaments. Another significant difference between a monolayer and

multilayer is the tendency for defects in the molecular layer. For multilayer formation, defects in the initial monolayer, caused by inactive sites on the PPF contact or surface contamination, are likely to be shadowed or "covered" by the addition of subsequent layers. Although these results do not definitely determine if Au or Cu penetration occurs through defects or between molecules, these results show that metal penetration through aliphatic monolayers during direct evaporation is highly likely.

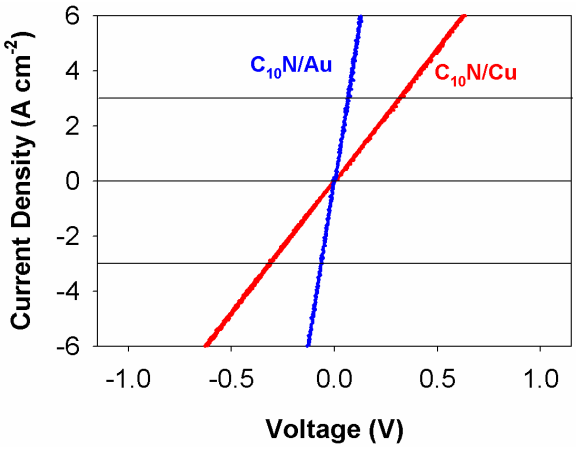

Figure 3.13: J-V curves for C_{10}NH/Cu and C_{10}NH/Au junctions for direct evaporation at 0° showing a linear response characteristic of metal filament formation through the monolayer.

A simple approach to reduce the tendency for Au penetration into a molecular layer is to control the momentum perpendicular ($\mathbf{p}_\perp$) to the surface molecular layer. The $\mathbf{p}_\perp$ of the depositing atoms can be simply controlled by varying the deposition angle. The $\mathbf{p}$ relative to the molecular layer's surface normal is determined with Eq. 3.3 and 3.4. The reduction in $\mathbf{p}_\perp$ with higher deposition angles causes an increase in the $\mathbf{p}_{||}$, which is expected to change the morphology of the contact and potentially reduce the area of the

contact/molecule interface. Although an increase in $\mathbf{p}_{||}$ is not expected to increase the tendency for metal penetration, the increase in lateral mobility of the adatom on the molecular layer would increase the likelihood an adatom can diffuse to a defect in the molecular layer. As previously discussed in Chapter 2, the approach to lower the **p** of the depositing atoms has been demonstrated for molecular junctions fabricated through the indirect evaporation paradigm[14]. For indirect evaporation, the total **p** of the depositing atoms is reduced through intentional collisions with Ar atoms in the evaporation chamber. During the collision event, the **p** of a depositing metal atom is partially lost to an Ar atom. Although both indirect and angled deposition are based on limiting metal penetration by controlling the **p** of the depositing atoms, the total **p** is reduced in the indirect evaporation technique and the $\mathbf{p}_{\perp}$ is reduced in the angled evaporation technique. In regards to the complexity of the paradigms, angled direct evaporation is experimentally more straightforward and cost effective.

The J-V curves for NAB/Au junctions formed through direct Au evaporation at deposition angles of 0°, 45°, 60°, 70° are shown in Figure 3.13. At a deposition angle of 0°, the J-V response for the NAB/Au junctions is the same as observed in Figure 3.12. As the deposition angle increased, and as the corresponding $\mathbf{p}_{\perp}$ decreased, the J-V curves of NAB/Au junctions become increasing non-linear and approach the measured J-V curve for the NAB/Cu junction in Figure 3.12. At 0.2 V, the measured current density of the NAB/Au junctions varied by five orders of magnitude by simply changing the deposition angle. These results give strong evidence that Au penetration into the

molecular layer depends strongly on the $\mathbf{p}_{\perp}$ of the depositing Au atoms as they approach the molecular layer.

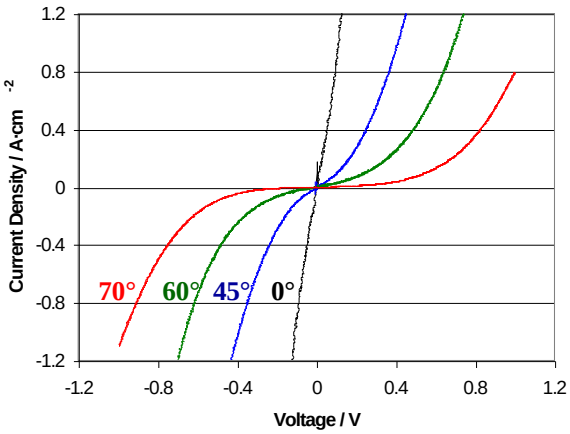

Figure 3.14: J-V curves for NAB/Au junctions for different deposition angles relative to the molecular surface normal showing a strong dependence on deposition angle.

The J-V curves for NAB/Cu junctions after fabrication through direct Au evaporation at deposition angles of 0° and 70° are shown in Figure 3.15. In contrast to the NAB/Au junctions, increasing the deposition angle did not significantly change the observed J-V shape and only caused a slight current reduction of about a factor of 2. These results confirm the previously reported results showing that significant Cu penetration into structurally similar molecular layers does not occur. In addition, the change in molecular contact area associated with a morphology change of the top contact caused by an increase in $\mathbf{p}_{||}$ must be less than a factor of two. This result gives strong evidence that the results in Figure 3.14 were predominately caused by a reduction in the Au penetration depth with increasing deposition angle.

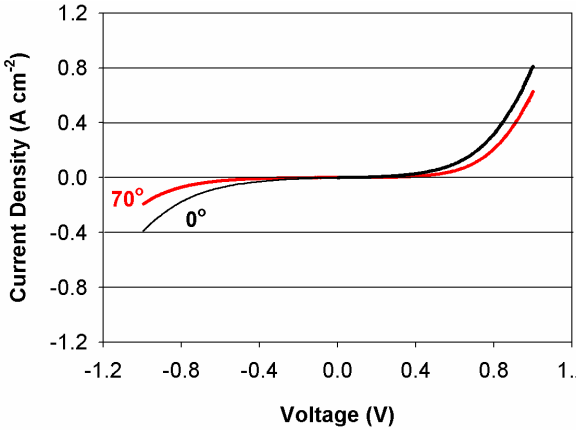

Figure 3.15: J-V curves for NAB/Au junctions at 0° and 70° deposition angles relative to the molecular surface normal showing minimal dependence on deposition angle.

3.3.4 Modeling Au Penetration in NAB Multilayers

This section describes a proposed model for the observed Au penetration through a NAB multilayer, where the Au penetration depth is observed to decrease as the $\mathbf{p}_{\perp}$ of the depositing Au atoms decreases. Conduction through a NAB multilayer has been shown to be consistent with off-resonant tunneling[1,17]. As discussed in Chapter 2, the current density for off-resonant tunneling depends exponentially on the tunneling distance:

$$J \propto \exp(-\beta d_{tunnel}) \qquad \text{Eq. 3.5}$$

where d_{tunnel} is the tunneling distance and β is the tunneling decay constant. For NAB/Cu junctions, β has been measured to be between 2.0 - 2.5 nm^{-1}, as determined by measuring the conductance through NAB/Cu junctions with various NAB thicknesses[1, 17]. For

molecular junctions, the tunneling length is the thickness of the molecular layer (d_{mol}). The simplest approximation for Au penetration is that the penetration depth depends linearly on the $\mathbf{p}_{\perp}$ of the depositing Au atoms. With this approximation, the actual tunneling distance (d^{θ}_{tunnel}) is the molecular layer thickness minus the Au penetration depth, as shown:

$$d^{\theta}_{tunnel} = d_{mol} - \lambda\cos(\theta) \qquad \text{Eq. 3.6}$$

where θ is the deposition angle and λ is the penetration parameter. λ depends on the molecular layer, reactivity of the depositing contact, and the total momentum of the depositing contact. Substituting Eq. 3.6 into Eq. 3.5 results in deposition angle dependent tunneling equations:

$$J \propto J_o \exp\left(-\beta\left(d_{mol} - \lambda\cos(\theta)\right)\right) \qquad \text{Eq. 3.7}$$

$$\ln(J) \propto \ln(J_o) - \beta d_{mol} + \beta\lambda\cos(\theta) \qquad \text{Eq. 3.8}$$

As shown in Eq. 3.8, a plot of the natural logarithm of the measured current density versus the cosine of the deposition angle should be linear with a positive slope, which is observed in Figure 3.16 for the NAB/Au junctions. The linear relationship between the Au penetration depth and $\mathbf{p}_{\perp}$ is consistent with ion implantation techniques where the

implantation depth is linear with the implantation energy[36]. The slope of 7.4 in Figure 3.16 can be used to determine λ for the NAB/Au junctions through the equation:

$$\lambda = \frac{7.4}{\beta} \qquad \text{Eq. 3.9}$$

For the reported β value of 2.1 nm^{-1}, the penetration constant (λ) is determined to be 3.5 nm which is comparable to the NAB thickness of 3.9 nm. This confirms that almost complete penetration of Au through the NAB layer occurs at a deposition angle of 0°, and the resultant J-V response should appear linear. For additional analysis, the minimum deposition angle (θ_{min}) where an increase in deposition angle does not significantly lower the observed current density can be used to calculate the interaction energy (E_b) between the depositing Au atoms and the molecular layer:

$$E_b \approx KE\cos(\theta_{\min}) \qquad \text{Eq. 3.10}$$

Unfortunately for the NAB/Au junctions, 70° was the maximum experimental deposition angle because the Au sticking coefficient rapidly decreased for deposition angles above 70°. Since θ_{min} must be greater or equal to 70°, the upper bound of the NAB-Au E_b is 0.068 eV (1.6 kcal·mol), assuming the **p** of the depositing Au atoms is about 0.2 eV[37]. To put this energy in perspective, thermal energy at 298 K is 0.025 eV. The estimated maximum E_b of 0.68 eV is consistent with the lack of spontaneous physisorption of NAB molecules on Au surfaces.

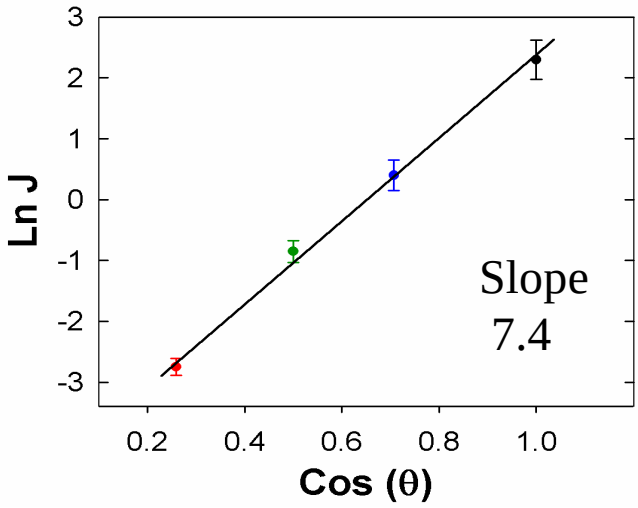

Figure 3.16: Natural logarithm of the current density at 0.2 V versus the cosine of the deposition angle shows a linear relationship consistent with Eq. 3.8.

3.4 CONCLUSIONS AND FUTURE WORK

In this chapter, a general method to fabricate "many-molecule" ensemble molecular junctions through direct metal evaporation is outlined. The bottom contact consisted of a disordered sp^2 hybridized carbon layer, as confirmed by XRD and Raman spectroscopy. The molecular layers for both aromatic and aliphatic molecules were attached to the PPF surface through electrochemical methods and were characterized with Raman spectroscopy and AFM. Fabrication of NAB/Cu junctions through direct Cu evaporation at 0° had electronic characteristics consistent with off resonant tunneling through the NAB layer. For all junctions where Au contacts were directly evaporated at 0°, the measured J-V curves were linear and did not depend on the molecular type or length. These results are consistent with the formation of metal filaments through the

molecular layer. Raman spectra of a NAB multilayer before and after direct evaporation of 10 nm Au contacts at 0° showed no observable structural damage to the molecular layer. Through an experimentally simple approach of controlling the momentum perpendicular to the molecular layer by varying the deposition angle, penetration of Au into an NAB multilayer was shown to depend linearly on the perpendicular momentum. These results provide critical insight into the fabrication of molecular junctions through metal evaporation techniques: the tendency of filament formation through molecular layers can be reduced by controlling the perpendicular momentum of the depositing metal atoms. Based upon these results, a novel evaporation technique to form molecular junctions without damage or metal penetration is introduced and developed in Chapter 4.

Additional work includes broadening the scope of this experiment to include many types of molecular layers and metallic contacts. Brightfield TEM cross section images of fabricated junctions at various angles should provide additional evidence for metal penetration through molecular layers. Also, theoretical modeling of metal penetration into molecular layers will allow additional insight.

3.5 REFERENCES

1. Bergren, A. J.; Harris, K. D.; Deng, F. J.; McCreery, R. L., Molecular electronics using diazonium-derived adlayers on carbon with Cu top contacts: critical analysis of metal oxides and filaments. *J. Phys. Condes. Matter* **2008,** 20, (37), 11.

2. Choi, S. H.; Kim, B.; Frisbie, C. D., Electrical resistance of long conjugated molecular wires. *Science* **2008,** 320, (5882), 1482-1486.

3. Xu, B. Q.; Tao, N. J. J., Measurement of single-molecule resistance by repeated formation of molecular junctions. *Science* **2003,** 301, (5637), 1221-1223.

4. Wang, W.; Scott, A.; Gergel-Hackett, N.; Hacker, C. A.; Janes, D. B.; Richter, C. A., Probing molecules in integrated silicon-molecule-metal junctions by inelastic tunneling spectroscopy. *Nano Lett.* **2008,** 8, (2), 478-484.

5. Richter, C. A.; Stewart, D. R.; Ohlberg, D. A. A.; Williams, R. S., Electrical characterization of Al/AlOx/molecule/Ti/Al devices. *Appl. Phys. A* **2005,** 80, (6), 1355-1362.

6. Love, J. C.; Estroff, L. A.; Kriebel, J. K.; Nuzzo, R. G.; Whitesides, G. M., Self-assembled monolayers of thiolates on metals as a form of nanotechnology. *Chem. Rev.* **2005,** 105, (4), 1103-1169.

7. McCreery, R. L.; Bergren, A. J., Progress with molecular electronic junctions: meeting experimental challenges in design and fabrication. *Adv. Mater.* **2009,** 21, 4303-4322.

8. Walker, A. V.; Tighe, T. B.; Cabarcos, O. M.; Reinard, M. D.; Haynie, B. C.; Uppili, S.; Winograd, N.; Allara, D. L., The Dynamics of Noble Metal Atom Penetration through Methoxy-Terminated Alkanethiolate Monolayers. *J. Am. Chem. Soc.* **2004,** 126, (12), 3954-3963.

9. Anariba, F.; DuVall, S. H.; McCreery, R. L., Mono- and multilayer formation by diazonium reduction on carbon surfaces monitored with atomic force microscopy "scratching". *Anal. Chem.* **2003,** 75, (15), 3837-3844.

10. Richter, C. A.; Hacker, C. A.; Richter, L. J., Electrical and spectroscopic characterization of metal/monolayer/Si devices. *J. Phys. Chem. B* **2005,** 109, (46), 21836-21841.

11. Walker, A. V.; Tighe, T. B.; Haynie, B. C.; Uppili, S.; Winograd, N.; Allara, D., Chemical Pathways in the Interactions of Reactive Metal Atoms with Organic Surfaces: Vapor Deposition of Ca and Ti on a Methoxy-Terminated Alkanethiolate Monolayer on Au. *J. Phys. Chem. B* **2005,** 109, 11263-11272.

12. Haick, H.; Cahen, D., Making contact: Connecting molecules electrically to the macroscopic world. *Prog. Surf. Sci.* **2008,** 83, (4), 217-261.

13. Zhu, Z. H.; Daniel, T. A.; Maitani, M.; Cabarcos, O. M.; Allara, D. L.; Winograd, N., Controlling gold atom penetration through alkanethiolate self-assembled monolayers on Au {111} by adjusting terminal group intermolecular interactions. *J. Amer. Chem. Soc.* **2006,** 128, (42), 13710-13719.

14. Haick, H.; Ambrico, M.; Ghabboun, J.; Ligonzo, T.; Cahen, D., Contacting organic molecules by metal evaporation. *Phys. Chem. Chem. Phys.* **2004,** 6, (19), 4538-4541.

15. Van Hal, P. A.; Smits, E. C. P.; Geuns, T. C. T.; Akkerman, H. B.; De Brito, B. C.; Perissinotto, S.; Lanzani, G.; Kronemeijer, A. J.; Geskin, V.; Cornil, J.; Blom, P. W. M.; De Boer, B.; De Leeuw, D. M., Upscaling, integration and electrical characterization of molecular junctions. *Nat. Nanotechnol.* **2008,** 3, (12), 749-754.

16. Metzger, R. M.; Xu, T.; Peterson, I. R., Electrical rectification by a monolayer of hexadecylquinolinium tricyanoquinodimethanide measured between macroscopic gold electrodes. *J. Phys. Chem. B* **2001,** 105, (30), 7280-7290.

17. Bergren, A. J.; McCreery, R. L.; Stoyanov, S. R.; Gusarov, S.; Kovalenko, A., Electronic characteristics and charge transport mechanisms for large area aromatic molecular junctions. *J. Phys. Chem. C* **2010,** 114, (37), 15806-15815.

18. Anariba, F.; Steach, J. K.; McCreery, R. L., Strong effects of molecular structure on electron transport in carbon/molecule/copper electronic junctions. *J. Phys. Chem. B* **2005,** 109, (22), 11163-11172.

19. Ranganathan, S.; Steidel, I.; Anariba, F.; McCreery, R. L., Covalently bonded organic monolayers on a carbon substrate: A new paradigm for molecular electronics. *Nano Lett.* **2001,** 1, (9), 491-494.

20. Solak, A. O.; Eichorst, L. R.; Clark, W. J.; McCreery, R. L., Modified carbon surfaces as "organic electrodes" that exhibit conductance switching. *Anal. Chem.* **2003,** 75, (2), 296-305.

21. Anariba, F.; DuVall, S. H.; McCreery, R. L., Mono- and multilayer formation by diazonium reduction on carbon surfaces monitored with atomic force microscopy "scratching". *Anal. Chem.* **2003,** 75, (15), 3837-3844.

22. Allongue, P.; Delamar, M.; Desbat, B.; Fagebaume, O.; Hitmi, R.; Pinson, J.; Saveant, J. M., Covalent modification of carbon surfaces by aryl radicals generated from the electrochemical reduction of diazonium salts. *J. Am. Chem. Soc.* **1997,** 119, (1), 201-207.

23. Ranganathan, S.; McCreery, R. L., Electroanalytical performance of carbon films with near-atomic flatness. *Anal. Chem.* **2001,** 73, (5), 893-900.

24. Pinson, J.; Podvorica, F., Attachment of organic layers to conductive or semiconductive surfaces by reduction of diazonium salts. *Chem. Soc. Reviews* **2005,** 34, 429-439.

25. Baranton, S.; Belanger, D., Electrochemical derivatization of carbon surface by reduction of in situ generated diazonium cations. *J. Phys. Chem. B* **2005,** 109, (51), 24401-24410.

26. McCreery, R., Molecular Electronic Junctions. *Chem. Mater.* **2004,** 16, 4477-4496.

27. Brooksby, P. A.; Downard, A. J., Electrochemical and atomic force microscopy study of carbon surface modification via diazonium reduction in aqueous and acetonitrile solutions. *Langmuir* **2004,** 20, 5038-5045.

28. Kariuki, J. K.; McDermott, M. T., Formation of multilayers on glassy carbon electrodes via the reduction of diazonium salts. *Langmuir* **2001,** 17, 5947-5951.

29. Deinhammer, R. S.; Ho, M.; Anderegg, J. W.; Porter, M. D., Electrochemical oxidation of amine-containing coumpounds - a route to the surface modification of glassy-carbon electrodes. *Langmuir* **1994,** 10, (4), 1306-1313.

30. Downard, A. J.; Garrett, D. J.; Tan, E. S. Q., Microscale Patterning of Organic Films on Carbon Surfaces Using Electrochemistry and Soft Lithography. *Langmuir* **2006,** 22, (25), 10739-10746.

31. Ramsey, J.; Ranganathan, S.; McCreery, R. L.; Zhao, J., Performance comparisons of conventional and line-Focused surface Raman spectrometers. *Appl. Spectrosc.* **2001,** 55, (6), 767-773.

32. Anariba, F.; Steach, J.; McCreery, R., Strong Effects of Molecular Structure on Electron Transport in Carbon/molecule/Copper Electronic Junctions. *J. Phys. Chem B* **2005,** 109, 11163-11172.

33. Braun, A.; Bartsch, M.; Schnyder, B.; Kotz, R.; Haas, O.; Haubold, H. G.; Goerigk, G., X-ray scattering and adsorption studies of thermally oxidized glassy carbon. *J. Non-Cryst. Solids* **1999,** 260, (1-2), 1-14.

34. Wang, Y.; Alsmeyer, D. C.; McCreery, R. L., Raman-spectroscopy of caron materials - structural basis of observed spectra. *Chem. Mater.* **1990,** 2, (5), 557-563.

35. Mahmoud, A. M.; Bergren, A. J.; McCreery, R. L., Derivatization of Optically Transparent Materials with Diazonium Reagents for Spectroscopy of Buried Interfaces. *Anal. Chem.* **2009,** 81, (16), 6972-6980.

36. Jaeger, R. C., *Introduction to Microelectronic Fabrication*. 2nd Edition ed.; Prentice-Hall: Upper Saddle River, NJ, 2002.

37. Abelmann, L.; Lodder, C., Oblique evaporation and surface diffusion. *Thin Solid Films* **1997,** 305, (1-2), 1-21.

CHAPTER 4

FABRICATION OF MOLECULAR JUNCTIONS THROUGH SURFACE DIFFUSION MEDIATED DEPOSITION

Sections of this Chapter have been previously published in:

Bonifas, A. P.; McCreery, R. L., 'Soft' Au, Pt and Cu contacts for molecular junctions through surface-diffusion-mediated deposition. *Nat. Nanotech.* **2010,** 5, (8), 612-617.

4.1 INTRODUCTION

4.1.1 Introduction to Surface Diffusion Mediated Deposition

Building upon the results discussed in Chapter 3, this chapter introduces a novel technique for the formation of metallic contacts on molecular layers through surface diffusion mediated deposition (SDMD). Contact formation is achieved by direct electron beam evaporation of a metal (Au, Cu, Pt) layer onto a SiO_2 surface adjacent to and about 50 nm away from the molecular layer. A SiO_2 "overhang" fabricated above the molecular layer protects the molecular layer from direct impingement of the depositing metal atoms and source radiation. Remote deposition allows the momentum and heat of condensation of the depositing metal to be dissipated away from the molecular layer, thus eliminating molecular damage due to heating and metal penetration due to metal atom momentum. Surface diffusion causes the depositing metallic layer to migrate towards and onto the molecular layer to form the second electronic contact. In-situ conductance measurements during the onset of contact formation between the metallic layer and the molecular layer allows molecular junctions containing several to tens of molecules to be measured, where incorporation of individual molecules into the forming junction results in conductance steps equal to the conductance of a single molecule comprising a monolayer. As the deposition time increases, the number of molecules incorporated into the junctions increases, which allows many-molecule "ensemble" junctions to be fabricated and, in the case of this chapter, electronically characterized ex-situ. The ability to measured both single molecule conductance and ensemble conductance with a single

experimental technique represents a significant step forward in the field of molecular electronics.

4.1.2 Inspiration behind Surface Diffusion Mediated Deposition

As identified in Chapter 3, the ability control or limit the momentum of the depositing metal atoms onto a molecular layer is a critical parameter for the fabrication of molecular junctions through physical vapor deposition techniques. Fabrication of molecular junctions by physical vapor deposition has several advantages such as compatibility with standard massively parallel micro-fabrication processes, ability to vary the Fermi energy of the second (top) contact, and the lack of high resolution lithography techniques to fabricate electrodes with a molecular-scaled separation (since the molecular layer defines this separation). For these reasons, the inspiration behind the SDMD technique was to develop a paradigm where molecular contacts can be fabricated on molecular layers through a physical vapor deposition technique. For the SDMD technique, molecular damage and metal penetration is minimized by employing diffusion to control the deposition while still processing all the above stated benefits of physical vapor deposition techniques. Briefly, metal penetration into the molecular layer is prevented because all atoms depositing onto the molecular layer have an internal binding energy (2-3 eV) within the forming metal contact, thus providing a large barrier for adatom dissociation and minimizing metal penetration into the molecular layer[1].

4.1.3 Chapter Overview

This chapter discusses the fabrication process for the SDMD junction architecture, molecular layer formation, and metal evaporation during the SDMD

technique. The fundamental physical principles governing the SDMD technique are identified and discussed. Results from using SDMD to measure molecular conductance are separated into two sections: in-situ conductance measurements of single to several-molecule junctions and ex-situ conductance measurements on "ensemble" molecular junctions containing many molecules. For in-situ conductance measurements, single-molecule conductance is determined through monitoring the conductivity during the onset of electronic contact between the molecular layer and the diffusing contact[2]. For ex-situ conductance measurements, the metal deposition is continued until > 10^3 molecules are contacted and then the sample is removed from the vacuum chamber to be electronically characterized. Results from these experiments demonstrate the effect of both molecular length and molecular energy levels on conduction through aliphatic and aromatic molecules. Combining these two approaches allows insights into in charge transport through a single molecule, several molecules, and many-molecule junctions.

4.2 EXPERIMENTAL

4.2.1 Pyrolyzed Photoresist Sidewall Fabrication

Figure 4.1 shows a schematic of the process flow chart for the fabrication of the PPF sidewall geometry. Substrates consisting of 1 mm thick fused silica microscope slides (G.E. 124, Technical Glass Products) were cleaned in freshly prepared piranha (1:1 H_2SO_4:H_2O_2) for 1 hour, rinsed in deionized water (TOC < 3 ppb), and dried in an Ar stream. *Warning, piranha solution is a powerful oxidant, and contact with organic materials or skin must be prevented.* To form the pyrolyzed photoresist films (PPF),

which consist of amorphous mostly sp^2 carbon, the substrates were spin coated with photoresist AZ P4330-RS at 6000 rpm for 30 seconds, soft baked at 90°C for 10 minutes, and pyrolyzed in a tube furnace[2]. For the pyrolysis process, the temperature ramp rate was 8°C min^{-1} to 1000 ^{o}C, then held at 1000°C for 60 min in the presence of forming gas (5% hydrogen and 95% nitrogen) flowing at 100 cc/min, followed by cooling to room temperature with the gas flow maintained. Metal tubing with brass fittings connected the forming gas source and tube furnace avoided O_2 contamination and maintain the H_2 concentration of the forming gas. The thickness of the PPF was measured with a profilometer to be between 700-800 nm.

Conventional optical lithography (HPR504 photoresist) was used to pattern reactive ion etch (RIE) etch masks on the PPF layer through a lift-off technique (Figure 4.1c). The etch masks were deposited with electron beam evaporation of 3 nm Cr (adhesion layer) and 27 nm SiO_2 followed by lift-off in acetone. Chamber pressure during evaporation was less than 8 x 10^{-8} torr with deposition rates of 0.2 and 0.5 Å·s^{-1} for the Cr and SiO_2 layers respectively. The PPF was etched with an O_2 reactive ion etching (RIE) process to remove the PPF not protected by the Cr/SiO_2 etch mask (Figure 4.1e). The RIE parameters were 200 watt RF plasma, O_2 pressure of 150 x 10^{-3} torr, and substrate DC bias of 360 V for 200 s. The DC bias resulted in an anisotropic etch which forms the near vertical sidewall, where a slight uniform etching beneath the etch mask creates the protective SiO_2 "overhang". Figure 4.2 shows a SEM image of the fabricated PPF sidewall geometry, as schematically shown in Figure 4.1e. PPF was selected as the bottom contact because of the McCreery research group's previous success with

diazonium and primary amine molecular attachment paradigms[3-6] and the ability to create the sidewall geometry with a simple O_2 RIE processing technique.

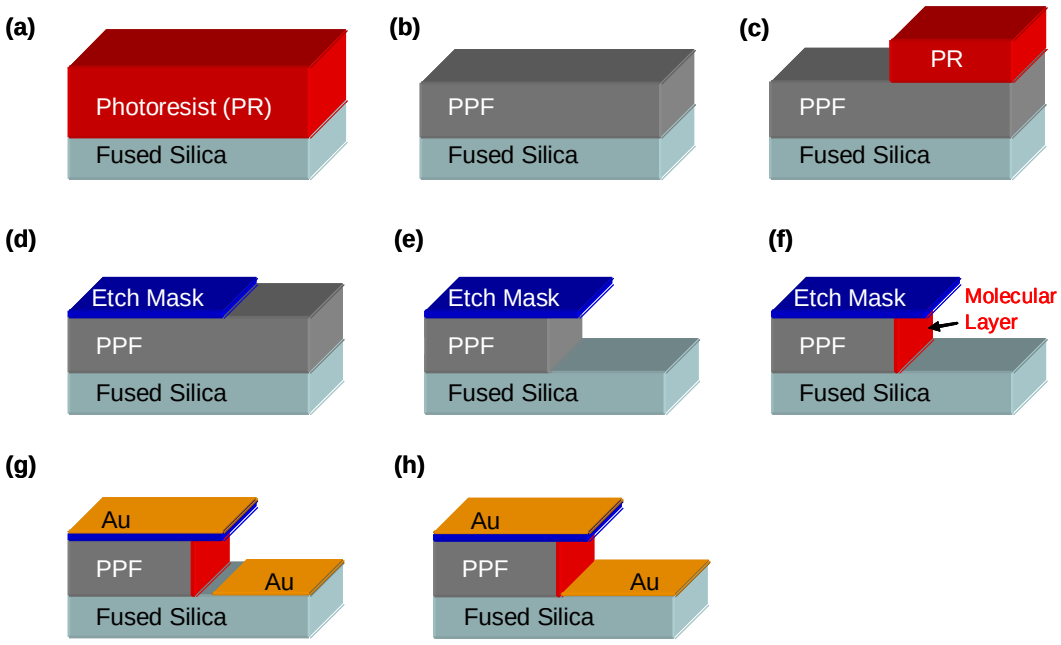

Figure 4.1: Schematic of process flow chart. **a,** Spin coat photoresist. **b,** Pyrolysis of photoresist (PPF). **c,** PPF patterned with photolithography. **d,** Evaporation of Cr/SiO_2 RIE etch mask. **e,** O_2 RIE of PPF. **f,** Molecular monolayer formation. **g,** Deposition of Au electrode. **h,** Au surface diffusion during deposition mediates contact formation.

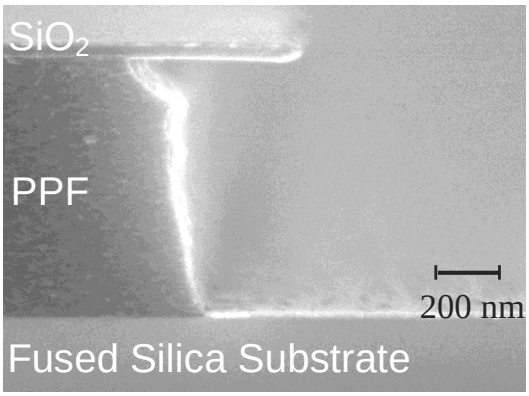

Figure 4.2: Secondary electron SEM image of fabricated PPF sidewall. Image shows the fused silica substrate, PPF sidewall, and the SiO_2 overhang formed during O_2 RIE.

4.2.2 Molecular Layer Attachment and Characterization

4.2.2.1 Molecular Monolayers for Single/Several Molecule Junctions

For attachment of nitroazobenzene (NAB) and azobenzene (AB) monolayers, the corresponding diazonium tetrafluoroborate salt was prepared from the precursors 4-nitro-4'aminoazobenzene (Aldrich, 90%) and 4-Aminoazobenzene (Aldrich, 98%), as previously described[3,4]. The atomic structures of these two molecules are shown in Figure 4.3. The molecular layers were attached to the PPF sidewall through the electrochemical reduction of a 1.0 mM solution of the corresponding diazonium salt in acetonitrile (MeCN) containing 0.1 M n-tetrabutylammonium tetrafluoroborate ($TBABF_4$). For NAB and AB respectively, the electrochemical reduction was performed through an applied constant potential of 0.00 V and 0.10 V versus Ag/Ag^+ for 20 seconds. For dimethylaminoazobenzene (DAB), the attachment was performed in-situ since the diazonium salt could not be isolated. For in-situ generation, a 1.0 mM solution of 4-dimethylamino-4'-aminoazobenzene (Aldrich, 97%) in H_2O containing hydrochloric

acid (pH = 0.5) was prepared. The solution was stirred for 1 hour followed by the addition of 1 molar equivalent of sodium nitrite, which produced a visual color change from transparent to red-orange. After an additional stir time of 30 minutes, the DAB layer was attached to the PPF sidewall with a constant potential of +0.40 V versus Ag/Ag^+ for 20 seconds. To ensure the dimethylamino groups in the monolayer were not protonated, the DAB monolayer was rinsed in 1.0 M NaOH aqueous solution for 1 minute followed by a rinse with deionized water.

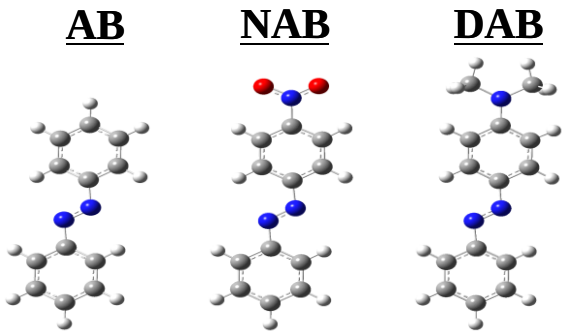

Figure 4.3: Chemical structure of azobenzene (AB), nitroazobenzene (NAB), and dimethylaminoazobenzene (DAB). Color code: nitrogen (blue), carbon (grey), oxygen (red), hydrogen (white).

The aminoalkane monolayers were prepared from the precursors 1-amino-n-butane (TCI America, 99%), 1-amino-n-hexane (TCI America, 99%), 1-amino-n-octane (TCI America, 98%), and 1-amino-n-decane (TCI America, 95%). Solutions of 1.0 mM aminoalkane in MeCN containing 0.1 M $TBABF_4$ were stirred for 30 minutes. The atomic structures of the aliphatic molecules are shown in Figure 4.4. The monolayers were attached to the PPF through electrochemical oxidation at 0.6 V vs Ag/Ag^+ for 5 minutes[5,6]. For all monolayers, the solutions were degassed and blanketed with Ar during

the electrochemical attachment. The monolayers were rinsed with MeCN and dried in an Ar stream.

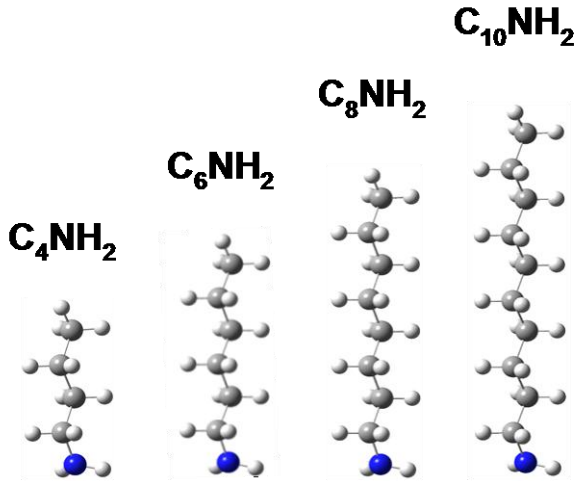

Figure 4.4: Chemical structure of butylamine ($C_4H_9NH_2$), hexylamine ($C_6H_{13}NH_2$), octylamine ($C_8H_{17}NH_2$), decylamine ($C_{10}H_{21}NH_2$). Color code: nitrogen (blue), carbon (grey), hydrogen (white). In this chapter, the above molecules are abbreviated as C_xNH_2 where x in the number of carbons.

For the single molecule conductance measurements, the presence of molecular monolayers (instead of multilayers) for all seven molecules were confirmed by measuring the thickness of the attached layer through an atomic force microscopy scratching technique, as previously described[4]. The thicknesses were measured on a "macro" PPF surface due to the geometric restrictions of the sidewall. The same deposition conditions were used on the "macro" surface as those for the sidewall. The observed AFM thickness and the predicted thickness for a monolayer are listed in Table 4.1. The measured thickness of all seven monolayers confirms the presence of molecular monolayers. The measured layer thickness was 0.83 ± 0.06 times the thickness predicted for a

perpendicular molecular orientation, implying a molecular tilt angle of 34°. This tilt angle is comparable to molecular tilt angles determined previously by FTIR for diazonium-derived monolayers on PPF[7,8]. In addition, the Raman spectra of the NAB, AB, and DAB monolayers were obtained to verify the presence of the molecular layers on the PPF contacts.

Molecule	Calculated Length (Å)[a]	Measured Length (Å)[b]
Butylamine (C_4)	7.3	6.5 ± 1.4
Hexylamine (C_6)	9.9	7.2 ± 1.5
Octylamine (C_8)	12.5	10.0 ± 1.5
Decylamine (C_{10})	14.8	13.0 ± 2.5
Nitroazobenzene (NAB)	12.8	10.5 ± 1.3
Azobenzene (AB)	11.7	10.0 ± 1.6
Dimethylaminoazobenzene (DAB)	14.0	11.3 ± 1.6

[a]Calculated with Gaussian '03 using DFT B3LYP/6-31+g.

[b]Measured with an AFM scratching technique. Length is stated as: average ± 1σ.

Table 4.1: AFM measured and theoretically calculated molecular lengths.

4.2.2.2 Molecular Layers for Many-Molecule "Ensemble" Junctions

For NAB and fluorene (FL) molecular layers, the corresponding diazonium salt was prepared from the precursors 4-4-Nitrophenylazoaniline (Aldrich, 90%) and 2-Aminofluorene (Aldrich, 98%), as previously described[7]. The atomic structure of FL is shown in Figure 4.5. The molecular layers were attached to PPF through the electrochemical reduction of a 1.0 mM solution of the corresponding diazonium salt in acetonitrile (MeCN) containing 0.1 M n-tetrabutylammonium tetrafluoroborate ($TBABF_4$). For the NAB layer, four cyclic voltammetric scans were performed from 0.4

to -0.6 V versus Ag/Ag^+ at 200 $mV \cdot s^{-1}$. For the FL layer, one scan was performed from 0.4 to -0.8 V vs Ag/Ag^+ at 200 $mV \cdot s^{-1}$. Solutions were thoroughly degassed with Ar and blanketed with Ar during electrochemical attachment. After surface modification, the molecular layers were immediately rinsed in MeCN and dried in an Ar stream.

The diaminoalkane monolayers were prepared from the precursors 1,8-diaminoctane (TCI America, 95%), 1,10-diaminodecane (TCI America, 95%), and 1,12-diaminododecane (TCI America, 98%), resulting in monolayers of diaminoctane ($C_8N_2H_4$), diaminodecane ($C_{10}N_2H_4$), and diaminododecane ($C_{12}N_2H_4$). The atomic structure of 1,8-diaminoctane is shown in Figure 4.5. Solutions of 1.0 mM diaminoalkane in MeCN containing 0.1 M $TBABF_4$ were stirred for 1 hour and then filtered through a 0.2 μm filter (Millipore Millex-FG). The monolayers were attached to the PPF through electrochemical oxidation at 0.6 V vs Ag/Ag^+ for 5 minutes. Solutions were degassed and blanketed with Ar during the oxidation process. The monolayers were rinsed with MeCN and dried in an Ar stream.

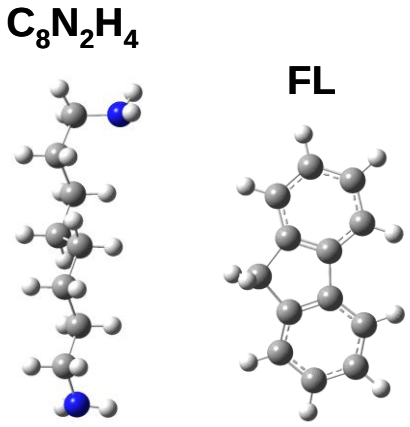

Figure 4.5: Chemical structure of diaminoctane ($H_2NC_8H_{16}NH_2$) and fluorene (FL). Color code: nitrogen (blue), carbon (grey), hydrogen (white). In this chapter, the diaminoalkane monolayers are abbreviated as $C_xN_2H_4$ where x in the number of carbons.

Thicknesses of the molecular layers were measured for similar deposition conditions on a "macro" flat PPF surface using an AFM "scratching" technique because of geometric limitations of the side-wall geometry. Comparing the measured layer thickness to the theoretical calculated molecular length shows that the NAB layer (4.5 ± 0.7 nm) was a multilayer consisting of 3-4 monolayers, and the FL layer (1.7 ± 0.2 nm) consisted of 1-2 monolayers. As shown by several different labs, the multilayer consists of covalently bonded and conjugated subunits which form by successive attack of the first monolayer by electrogenerated radicals[8-10]. The measured thickness of the $C_8N_2H_4$ layer was 1.1 ± 0.2 nm, indicating monolayer formation occurs for the aliphatic monolayers, which is consistent with the results in Table 4.1.

4.2.3 Metal Evaporation for Contact Formation

4.2.3.1 Evaporation for Single/Several Molecule Junctions

For in-situ SDMD, Au second contacts were deposited in a Johnson Ultravac load-locked electron beam evaporation system. A schematic of the in-situ conductance measurements is shown in Figure 4.6. The base pressure of the evaporation chamber was 5×10^{-8} torr , resulting in deposition pressures less than 1×10^{-7} torr. Since surface diffusivity depends on surface contaminants (e.g. O_2, H_2O), the average surface diffusion length and efficiency of the technique is expected to depend on the deposition pressure. For the single/several molecule junctions, Au was used as the contacting metal because surface adsorption of H_2O and O_2 on Au has been shown not to occur at this deposition pressure[9,10]. The Johnson Ultravac system has a metal source to deposition ("throw") distance of 45 cm and a metal source radius of about 8 mm. Since evaporation does not occur from a single point on the metal source, the deposition angle has a range of less than ± 0.5°. It should be noted that the electron beam size was minimized during evaporation resulting in a melted source radius of about 2 mm.

In-situ electronic monitoring during the SDMD process was achieved via a high vacuum electrical pass-through on the chamber of the evaporation system. Conductive Ag epoxy (Chemtronics, CW2400) was used to connect two lead wires to the PPF and Ag epoxy strip shown in blue in Figure 4.6. During Au deposition, the forming Au contact was positioned with a shadow mask to contact the Ag epoxy on the SiO_2 substrate, as shown in Figure 4.6. Conductance was measured with a Keithley 6517B electrometer. For conductance measurement without the presence of a molecular layer, a voltage of 0.2

V was applied during the Au deposition. The measured current was recorded at a rate of 200 measurements per second (5 ms/data point). With the presence of a monolayer, the applied voltage was increased to 1 V with a longer integration time (50 ms/data point) to increase the signal to noise, which was necessary for measuring the low conductance of the aminoalkanes. The applied voltage of 1 V was kept constant for all molecules to allow comparison of the measured molecular conductances. By measuring the entire current-voltage curve for single molecule junctions, the reported molecular conductance can be readily calculated for all voltages between ± 1 V. **For all electronic measurements, the stated voltage is the PPF contact relative to the Au contact.**

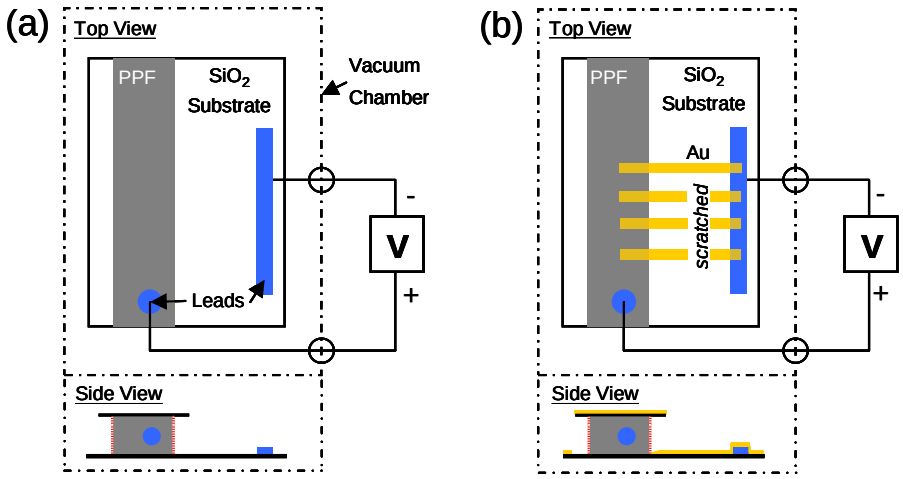

Figure 4.6: Schematic of an in-situ monitored SDMD junction. **a,** Conducting Ag epoxy contact "leads" (in blue) are connected to the PPF and substrate. **b,** Deposition through a shadow mask creates a conductive Au lead which electronically contacts the Ag epoxy prior to Au diffusion onto the molecular layer. Additional in-situ measurements are obtained by scratching the previous Au contact, moving the shadow mask, and depositing a new Au layer.

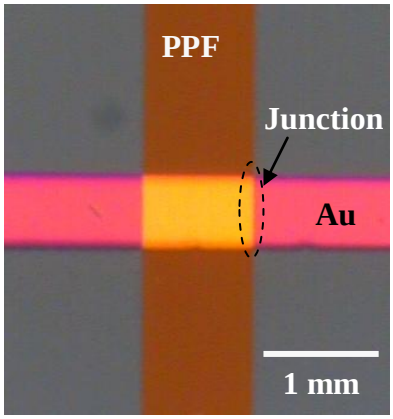

Figure 4.7: A top-view optical image of a molecular junction fabricated with SDMD. Molecular junction is located at the interface between the etched PPF (carbon) and evaporated Au layer, as identified with the dashed line. Both sides of the PPF have the SiO_2 "overhang" projecting to the left and right in the image.

For Au contact formation, Au was evaporated through a shadow mask aligned perpendicular to the etched PPF lines with evaporation rates between 0.01 - 0.5 $Å \cdot s^{-1}$, as measured by a quartz crystal monitor (QCM). The width of the aperture in the shadow mask was 500 µm, and its length bridged the 2-3 mm between the PPF and Ag epoxy lead as shown in Figures 4.6. Prior to the Au layer contacting the sidewall or molecular layer, the deposition rate was 0.5 $Å \cdot s^{-1}$, and at least 10 nm of Au was deposited before the Au contacted the PPF/molecule sidewall to ensure a continuous Au lead up to the sidewall. For the deposition system and fused silica substrate, the Au thickness required for percolation is about 5 nm, as measured by the QCM. A continuous Au lead ensures that the observed conductance steps without or with the presence of a molecular layer are occurring at the Au-sidewall or Au-molecule interface. At the onset of an observed increase in current (about 1% - 5% of the measured molecular conductance), the

deposition rate was decreased and held constant throughout the remaining deposition. The deposition rate was empirically selected with the aim to obtain at least 4000 conductance measurements (one every 50 ms) during the observation of 4 to 10 conductance steps. To ensure adequate sampling to construct the conductance histograms, histograms were constructed with at least 4000 conductance data points.

The Au deposition distance away from the molecular layer was optimized by varying the deposition angle between 3° – 10° relative to the surface normal of the fused silica substrate, with an increase in the deposition angle resulting in Au deposition closer to the molecular layer. For each sample (containing one molecular monolayer type) the deposition angle and rate was optimized to meet the following criteria:

1. All Au was deposited away from and adjacent to the molecule layer. As noted previously, direct Au evaporation onto the molecular layer results in a linear current-voltage response independent of the molecular identity and monolayer thickness.
2. A minimum of 10 nm of Au was deposited at 0.5 $Å \cdot s^{-1}$ prior to the onset of an observable current increase. A maximum Au thickness of 40 nm was selected to minimize Au consumption.
3. Empirical selection of a lower deposition rate (between 0.01 – 0.1 $Å \cdot s^{-1}$) that allowed at least 4000 conductance measurements for 4 to 10 conductance steps. Once the lower deposition rate was obtained, the rate was held constant throughout the deposition process.

In addition to in-situ measuring the junction conductance during contact formation, conductance of the formed junctions was monitored after the electron beam source was turned off and the shutter was closed to stop subsequent Au deposition. After each full deposition process, the Au lead was scratched (electronically isolated) near the Ag epoxy, the shadow mask was moved to an adjacent, pristine section of the sidewall, and the in-situ process was repeated, thus allowing at least 15 individual attempts to measure the conductance per sample chip. A top-view optical image of a completed in-situ SDMD formed junction is shown in Figure 4.7.

4.2.3.2 Evaporation for Many-Molecule "Ensemble" Junctions

For many-molecule "ensemble" junctions the Au, Cu, and Pt contacts were deposited with a base pressure of 5×10^{-8} torr, allowing deposition pressures less than 2×10^{-7}. Metallic contacts, 25 nm thick, were evaporated through a shadow mask aligned perpendicular to the PPF lines with an evaporation rate of 0.5 $Å \cdot s^{-1}$, as measured by QCM. The deposition angle relative to the surface normal of the substrate was varied between 0 - 15°. After deposition, the completed molecular junction was removed from the evaporator chamber before subsequent electronic characterization.

Figure 4.8 shows SEM and TEM images of the cross-section of a fabricated many-molecule junction with an Au contact. Cross-sectional SEM samples were made by cleaving the Si/SiO_2 substrate across the molecular junction. In the secondary electron SEM image, the diffused Au on the PPF sidewall could not be resolved from surface charging on the PPF side-wall. Low acceleration voltages and beam currents (5kV, 5μA) allowed sufficient resolution while minimizing sample charging. TEM lamellae of the

molecular junctions were milled with a Zeiss Nvision focused ion beam (FIB). Prior to milling, the molecular junctions were coated with several micrometers of carbon to minimize sputtering and redeposition during the milling process. For the FIB process, 30 keV Ga ions were used to mill the lamellae to thicknesses below 100 nm and 5 keV Ga ions were used for final polishing. A Jeol 2200FS TEM operating at 200 kV was used to acquire bright field images and diffraction patterns. In the TEM images, the strong atomic number contrast allows the diffused Au onto the PPF/molecule sidewall to be observed. The light region in the TEM image is a void in the TEM lamella.

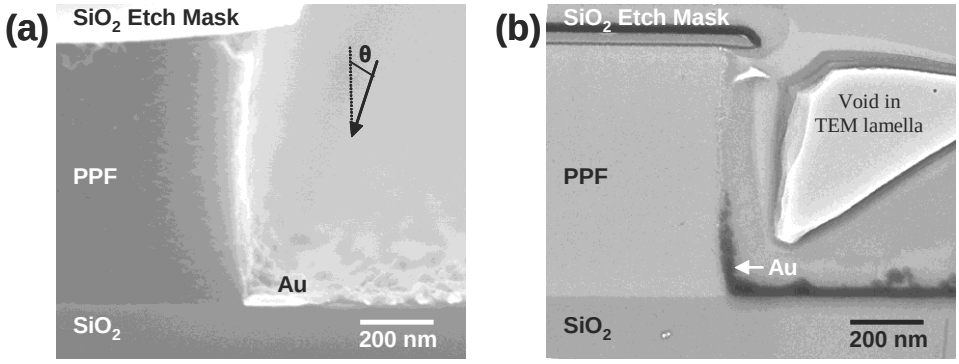

Figure 4.8: Cross-section images of a NAB(4.5)/Au junction. **a,** Secondary electron SEM and **b,** Bright field TEM images show the Cr/SiO_2 "overhang" after O_2 RIE and deposited 25 nm of Au.

SEM micrographs of NAB/Au and NAB/Cr junctions are shown in Figure 4.9. For both junctions, 25 nm of the metal contact was deposited at 5° relative to the surface normal. For the NAB/Au junction, the Au thin film growth mechanism and surface diffusion were sufficient to allow the Au to diffuse onto the PPF/NAB sidewall. For the NAB/Cr junction, the deposited Cr layer did not reach the PPF/NAB sidewall. The

shorter Cr diffusion length could have been caused by a higher diffusion activation energy, parasitic interaction with surface contaminants (e.g. H_2O, O_2) on the SiO_2 substrate[11], or a 3D thin film growth mechanism.

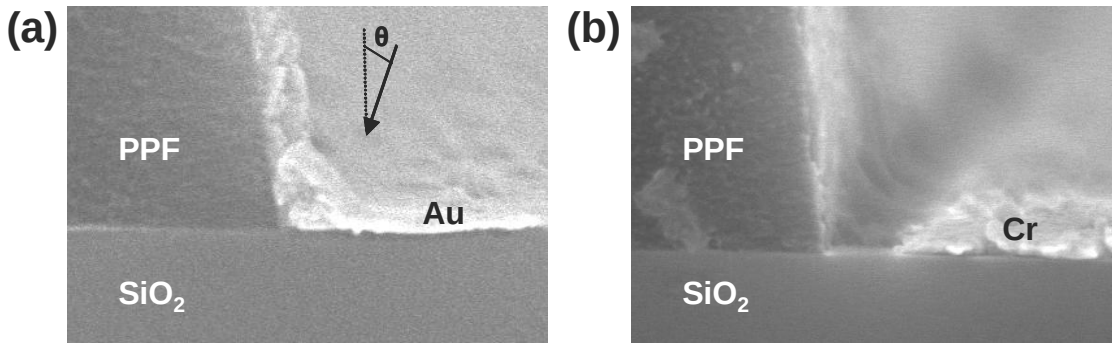

Figure 4.9: Cross-section images of a NAB(4.5)/Au junction. **a,** Deposition of 25 nm Au has adequate surface diffusion to reach the PPF/NAB surface. **b,** 25 nm Cr does not reach the PPF/NAB surface.

Changing the deposition angle relative to the substrate surface normal changed the distance away from the PPF sidewall where metal deposition occurred. To measure if the deposited metallic layer forms electronic contact with the PPF or PPF/molecule sidewall, the resistance of the final junctions were measured at various deposition angles. Resistance measurements were acquired with the same apparatus described in Chapter 3. The measured resistances at 0.8 V for PPF/Au, NAB/Au, and NAB/Cr junctions as a function of the SDMD deposition angle are shown in Table 4.2. For junctions lacking a molecular layer, deposition at 0° resulted in an open circuit between the PPF and Au contacts ($R > 10$ GΩ). Compared to 0°, deposition at 5° caused the Au atoms to land about 50-70 nm closer to the PPF side-wall resulting in electronic contact between the

PPF and Au contacts. At 15°, the depositing Au atoms are directly incident on the PPF side-wall, thus creating immediate electronic contact. For the deposition of Cr at 0° and 5°, the deposited Cr layers did not reach the PPF sidewall, resulting in an open circuit. Unlike Au deposition at 5°, Cr surface diffusion was insufficient to reach the PPF sidewall. Cr deposition at 15° caused direct deposition onto the PPF sidewall, forming electronic contact and showing that the deposited Cr layer was conductive. For junctions containing an NAB layer, deposition at 5° resulted in Au diffusion onto the NAB layer, and produced J-V curves similar to the non-linear J-V curves noted in Chapter 3. Deposition at 15° resulted in shorted junctions with a similar J-V response to the directly evaporated Au junctions reported in Chapter 3.

	θ = 0°	**θ = 5°**	**θ = 15°**
PPF/Au	> 10GΩ	< 100Ω	< 100Ω
PPF/Cr	> 10GΩ	> 10GΩ	< 100Ω
PPF/NAB/Au	> 10GΩ	~ 10MΩ	< 100Ω

Table 4.2: Junction resistance at 0.8 V for SDMD junctions where the deposition angle (θ) relative to the surface normal was 0°, 5°, 15°.

To calculate the current-density, the diffusion length of the metal contact onto the molecular layer was measured. For each test chip, which contained 6 to 9 individual junctions, the fused silica substrates were cleaved perpendicular to the PPF contacts, leaving a cross section of the junction. The diffusion length onto the molecular layer was measured at two locations on the test chip, showing variability less than 20% between individual junctions fabricated during the same deposition process. Backscattered SEM

images were used to determine the diffusion length onto the molecules. Similar to TEM, backscattered SEM images provide strong atomic number contrast. TEM images of a NAB/Au junction were used to confirm the calibration of the SEM images. The areas of the final junctions were between 0.25 um^2 (FL) and 1.5 um^2 (NAB), depending on the molecular layer type and the final deposition thickness. For subsequent sections, the junctions are identified as molecule(thickness)/metal contact with the PPF bottom contact omitted. For example, a NAB(4.5)/Au junction is a 4.5 nm thick NAB layer on PPF with a Au second electronic contact formed through SDMD.

Low temperature electronic characterization was carried out with a Janis ST-500 cryogenic probe station with a Scientific Instruments temperature controller. The junction chamber was pumped to 2 x 10^{-6} torr before collecting J-V curves. The temperature was varied between 300 and 77 K, acquiring J-V curves every 0.001 K^{-1}. The contact resistance of the metallic contact was not corrected during the measurements.

4.2.4 Theoretical Calculations

Gaussian ’03 was used to perform density functional theory (DFT) [B3LYP/6-31+g] calculation of the molecular energy levels of the isolated NAB, AB, and DAB molecules. To estimate of length of the molecular monolayers, DFT was used to calculate the distance between the carbon sidewall to the terminal H (terminal O for NAB) of the end group. The C-C bond length between the molecule and carbon sidewall was determined to be 1.49 Å for the aromatic molecules and 1.47 Å for the aliphatic molecules. The calculated molecular length was taken as the distance from the PPF surface to the nucleus of the terminal atom. Advanced calculations for the free NAB,

AB, and DAB molecules, the PPF contact (modeled as graphene), and the graphene/molecule system were performed with Accelyrys DMol^3/PW91/DNP.

4.1 SURFACE DIFFUSION MEDIATED DEPOSITION

4.1.1 Surface Diffusion Mediated Deposition Mechanism

For the SDMD technique, a physical vapor deposition technique is used to deposit a metallic layer adjacent to and about 10 – 100 nm away from the molecular layer. In this dissertation, electron beam evaporation is used to deposit the metallic contact, although other physical vapor deposition techniques can be used as long as the depositing flux is directional. A schematic of the SDMD mechanism is shown in Figure 4.10. The basic architecture of the SDMD junction involves the fabrication of a vertical PPF sidewall with a SiO_2 layer which overhangs the PPF. The SiO_2 layer physically prevents metal deposition onto the PPF or PPF/molecule sidewall through a "shadowing effect". By varying the deposition angle, commonly between 2° and 10° relative to the surface normal, the distance the metal is deposited away from the PPF/molecule surface is controlled. For example, an increase in deposition angle results in deposition closer to the molecular layer. In addition to shadowing the PPF/molecule sidewall from direct metal deposition, the SiO_2 overhang also shadows the PPF/molecule surface from direct irradiation from the electron beam evaporation source.

During the metal evaporation, surface diffusion of the depositing atoms causes the contact to migrate towards the molecular layer. Migration of the metal contact towards the molecular layer is facilitated by the incorporation of diffusing ad-atoms at the edge of

the contact. With subsequent metal deposition, the contact migrates towards and onto the molecular layer to form the second electronic contact. The growth mechanism of the metallic layer towards to the PPF/molecule surface is controlled by surface energies and diffusion of the depositing metal layer, and is discussed in the subsequent sections. As shown in Figure 4.10c, direct metal evaporation occurs onto the Ag electrode attached to the fused silica substrate. The presence of the Ag electrode allows the depositing metal layer to be electronically addressed during the deposition. If the depositing metal contact is electronically continuous between the Ag electrode and the migrating edge of the contact, then the measured conductivity is controlled by conductivity through the molecular layer on the PPF surface. As discussed in Section 4.2.3.1, the deposition angle was selected to ensure the deposited Au layer thickness was at least 10 nm thick prior to contact formation with the PPF/molecule surface. Since the percolation thickness for deposited Au layers in our evaporation system was about 5 nm, deposition of 10 nm prior to junction formation ensured that the Au contact was continuous between the molecular layer and the Ag electrode.

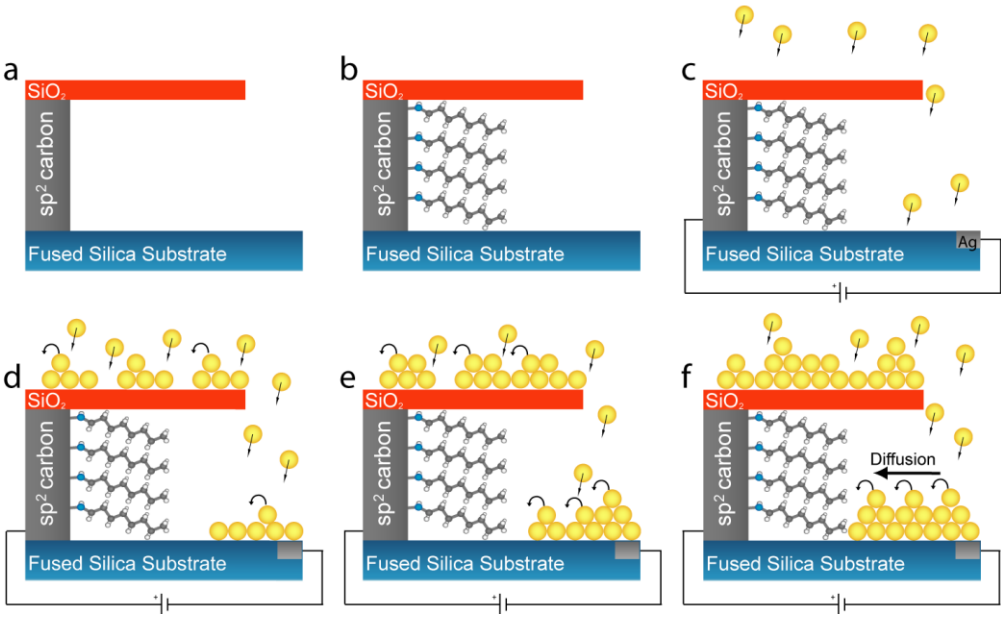

Figure 4.10: Atomistic schematic of in-situ SDMD. **a,** Fabrication of a SiO_2 overhang through O_2 reactive ion etch. **b,** Molecular monolayer attached to the carbon sidewall with electrochemistry. **c,** Attachment of wire leads with Ag epoxy electrodes. **d,** SiO_2 overhang prohibits direct Au impingement onto the molecular layer. **e,** Au adatom surface diffusion during deposition causes the Au layer to migrate toward the molecular layer. **f,** Additional Au deposition allows the deposited Au layer to contact individual molecules comprising the molecular layer.

4.1.2 Thin Film Growth Mechanisms

As noted above, an understanding of thin film grown mechanism is important to understand the migration (or growth) of the depositing metal contact towards the PPF/molecule surface. For metal evaporation techniques, the growth mechanism of a thin film is governed by surface energies and is commonly described through Young's equilibrium equation applied to a deposited film (f) on a substrate (s):

$$\gamma_{sv} = \gamma_{fv} + \gamma_{fs} \qquad \text{Eq. 4.1}$$

where the γ_{sv} is the surface energy of the substrate, γ_{fv} is the surface energy of the deposited film, and γ_{fs} is the interfacial energy between the substrate and deposited film, as shown in Figure 4.11[12]. The growth mechanism observed during metal deposition is based on the inequality between the left and right side of the equation in Eq. 4.1. For 2D growth, commonly called Frank-van der Merwe growth, the film grows only on the surface causing the film to grow layer-by-layer growth[12]. Based on the Eq. 4.1, 2D growth occurs when:

$$\gamma_{sv} \geq \gamma_{fv} + \gamma_{fs} \qquad \text{Eq. 4.2}$$

For 3D growth, commonly referred to as Volmer-Weber growth, the thin film grows in isolated islands where, upon a sufficient deposition thickness, percolation of the islands occurs[12]. 3D growth occurs when:

$$\gamma_{sv} < \gamma_{fv} + \gamma_{fs} \qquad \text{Eq. 4.3}$$

An intermediate growth mechanism is layer plus island, referred to as Stranski-Kastranov grown, where growth through an initial 2D mechanism is followed by 3D growth after the surface is wetted by the film[12]. A schematic of the three thin film growth mechanisms is shown in Figure 4.12.

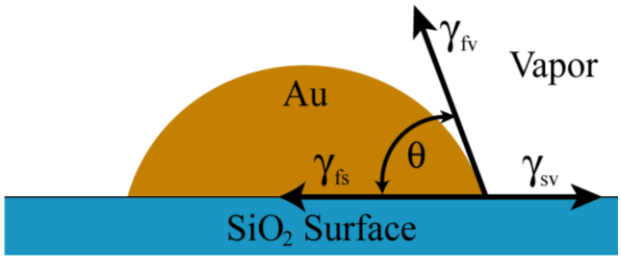

Figure 4.11: Surface energies for the case of Au wetting of a SiO_2 surface.

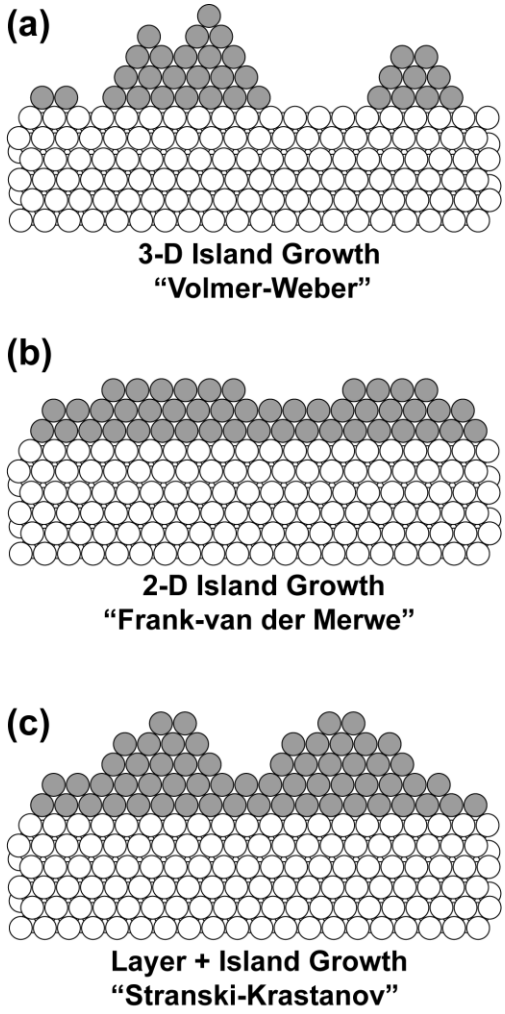

Figure 4.12: Schematic of the three thin film growth mechanisms.

For the case of evaporation at low pressures, an additional term must be added to modify the γ_{fv} term in Eq. 3.1[12]. When a depositing atom is transferred from the gas phase to solid phase, the change in free energy of the system modifies the effective surface energy of the deposited film. The change in free energy (ΔG) associated with the change in the equilibrium partial pressure above the deposited film is:

$$\Delta G = nkT \ln\left(\frac{P}{P_{eq}}\right) \qquad \text{Eq. 4.4}$$

where n is the number of atoms, k is the Boltzmann constant, T is the film temperature, P is the partial film pressure, and P_{eq} is the equilibrium film pressure. The ratio of P/P_{eq} is termed the supersaturation of the system. Taking supersaturation into account and incorporating into Eq. 4.2 and 4.3 results in

$$\text{2D:} \qquad \gamma_{sv} \geq \left(\gamma_{fv} - CnkT \ln\left(\frac{P}{P_{eq}}\right)\right) + \gamma_{fs} \qquad \text{Eq. 4.5}$$

$$\text{3D:} \qquad \gamma_{sv} < \left(\gamma_{fv} - CnkT \ln\left(\frac{P}{P_{eq}}\right)\right) + \gamma_{fs} \qquad \text{Eq. 4.6}$$

where C is a constant. Based on these equations, the growth mechanism for a particular film on a substrate is not a simple material parameter, but the mechanism depends on the temperature and the partial pressure of the depositing film. Although not straightforward,

the partial pressure depends on the deposition rate. The pressure during an evaporation process is the momentum transferred to the depositing surface per area per second. For low equilibrium solids, such as noble metals, during vacuum deposition at room temperature, such as Au, Cu, and Pt, supersaturation can pushed the equilibrium towards 2D growth, where the supersaturation can be as high as 10^{20}.[13-15]

Although Young's equation is a simple and effective approach to understand thin film growth mechanisms, the equation does not fully describe the role of interfacial segregation on wetting phenomena[16]. Since both the substrate and the depositing metal (i.e. the wetting phase) may contain impurities, these impurities can segregate to any of the interfaces and lower their surface energies. As shown in Eq. 4.1, a change in surface energy of an interface can lead to a large change in the observed thin film growth mechanism. For this reason, impurities are commonly added to the depositing system to control the growth mechanism.

For the SDMD technique, the thin growth mechanism must at least follow partial 2D growth, as a 2D growth mechanism would allow the depositing contact to migrate (grow) towards the PPF/molecule surface. Migration of the contact toward the PPF/molecule surface occurs through the incorporation of additional metal atoms at the edge of the contact. For this to occur, two important conditions must be met: the self surface diffusion of the depositing metal must be sufficiently high and there must be an interaction (or bonding) between the depositing metal and the substrate must occur. For a 2D growth mechanism, a closer look at the individual energy terms in Eq. 4.1 is beneficial to determine experimental parameters to optimize the SDMD process. For the

γ_{sv} term, increasing the surface energy of the substrate on which metal deposition occurs would increase wetting and favor 2D growth, although the surface is experimentally limited to an insulator, which typically has low surface energy compared to metals. For the γ_{fv} term, a lower surface energy of the depositing metal would increase wetting but the deposited contact is experimentally limited to noble metals such as Au, Cu, and Pt. The final term of γ_{fs} can be experimentally controlled to increase wetting and cause 2D growth. For example, the formation of self-assembled monolayers of mercaptosilane on a SiO_2 surface has been shown to significantly increase the wetting behavior of Au, thus leading to 2D growth[17].

During the PPF sidewall fabrication process the initial substrate surface is fused silica (SiO_2) as shown in Figure 4.10, but the actual substrate surface on which the SDMD occurs is not SiO_2. Pyrolysis of the photoresist to form PPF resulted in Si – C bond formation at the SiO_2/PPF interface, as determined by XPS[18]. During O_2 RIE, the carbon is not completely removed from the surface of the substrate, resulting in a substrate surface containing various Si, C, and O bonds. The presence of Si-C at the substrate surface complicates the determination of the expected growth mechanism since both γ_{sv} and γ_{sf} are unknown. Also, initial surface contamination and contamination during evaporation are unknown, causing additional uncertainty about determining the growth mechanism. Although these uncertainties exist, the success of the SDMD technique shows that the growth mechanism under the SiO_2 overhang must have at least partial 2D growth behavior. Additional characterization and analysis of the actual growth

mechanism is needed to provide a more complete understanding of the SDMD mechanism.

4.1.3 Surface Diffusion

For the SDMD technique, surface self-diffusion of the depositing metal must be sufficient to allow the deposited metal atoms to diffuse to the edge of the contact. For the metal evaporation process, the momentum of the depositing atoms perpendicular to the surface is lost within several atomic jump distances[19], and the deposited atoms become adatoms. The adatoms are in equilibrium with the film surface and undergo surface diffusion until the adatoms are trapped by chemisorption (e.g. surface kink, reactive functional group) or are buried by newly arriving metal atoms. Surface diffusion of adatoms is characterized by the equations:

$$D_S = \lambda^2 \upsilon_s \exp\left(-\frac{\Delta G_s}{kT}\right) \qquad \text{Eq. 4.7}$$

$$\bar{x} = 2\sqrt{D_s t} \qquad \text{Eq. 4.8}$$

where λ is the hop distance, ν_s is the hop frequency, ΔG_s is the activation energy, k is Boltzmann's constant, T is the temperature, t is the diffusion time, and $\bar{x}$ is the average diffusion length. With a typical Au (or Cu) surface diffusion activation energy of between 0.6 – 0.7 eV, the predicted diffusion length is 50 - 350 nm at 300 K for 500 s (the deposition time)[20, 21], although surface heating caused by radiation and metal

condensation can lead to additional surface diffusion. Since metal deposition occurs about 30-80 nm from the molecular layer, the predicted diffusion length of Au adatoms is sufficient to allow the depositing metal atoms to diffuse from their deposition location to the PPF/molecule surface.

4.1.4 Metal Penetration

The primary benefit and the driving force behind development of the SDMD technique is to minimize metal penetration through the molecular layer during the formation of a metallic second contact. As was demonstrated in Chapter 3, minimizing the momentum of the incident metal atoms onto the molecular layer is critical to reducing the tendency for metal penetration. For the SDMD technique, the influx of metal atoms onto the molecular layer is controlled by surface diffusion. With surface diffusion, all incident atoms onto the molecular layer are coordinated (bonded) with neighboring metal atoms, as shown in Figure 4.13. For a metal atom to dissociate from the metal contact and penetrate into the molecular layer, this binding (coordination) energy (E_B) must be overcome. Figure 4.14 shows the binding energy for Au as a function of its coordination number, showing that even for a coordination number of 1- 2 the binding energy is 1.5 - 2.0 eV[1]. For metal penetration to occur, a binding energy of at least 1.5 eV must be overcome. For direct metal evaporation onto a molecular layer, depositing metals atoms are not coordinated and, in contrast to SDMD, do not have an intrinsic barrier for metal penetration. For the SDMD technique, the momentum of the incident metal atoms onto the molecular layer is controlled by a counter-balancing binding energy within the

forming metal contact, thus providing an insurmountable barrier for metal penetration into the molecular layer.

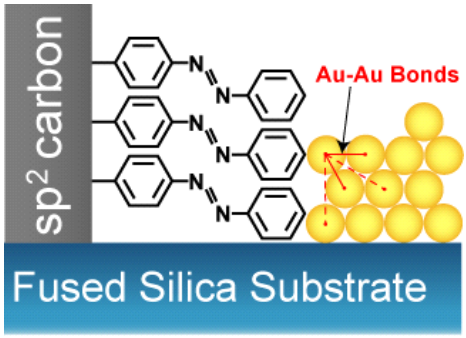

Figure 4.13: Schematic of SDMD contact formation between an Au contact and AB monolayer showing the presence of Au-Au bonding which prevents metal penetration into the molecular layer.

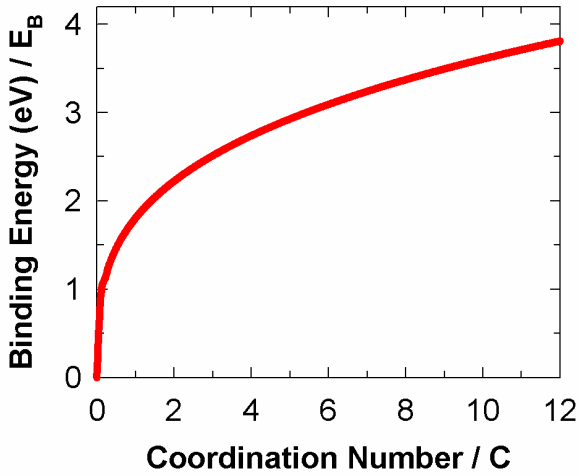

Figure 4.14: Binding energy of a single Au atom in Au as a function of its coordination energy calculated with effective medium theory[1].

4.4 RESULTS AND DISCUSSION

The following sections describe the results of molecular junctions formed through the SDMD technique. The results and discussions are separated in individual sections based on the number of molecules incorporated in the formed molecular junctions: single-several molecule junctions and many-molecule "ensemble" junctions.

4.4.1 Single/Several Molecule Junctions

4.4.1.1 Quantized Conductance

For in-situ SDMD, the junction current was monitored during initial contact formation between the molecular layer and the depositing metal contact, as shown in Figure 4.15. As a control experiment, in-situ SDMD was performed without a molecular layer attached to the conductive carbon sidewall. The measured conductance versus deposition time had observable conductance steps with a magnitude near the quantum of conductance ($G_o=2e^2/h$), as shown for Au deposition in Figure 4.15c. Immediately prior to the observance of the G_o steps (t < 245s), the thickness of the deposited Au contact was 10 nm, which ensured a continuous Au layer leading to the sidewall and that the observed G_o steps were occurring at the sidewall. The G_o steps are caused by the formation of individual contacts between the diffusing Au layer and the carbon sidewall, where the width of conducting channel is on the order of a Fermi wavelength[22-24]. The histogram of conductance versus deposition time shows peaks at near integer intervals of G_o. Substructure within the conductance peaks is likely due to various bonding geometries between the Au and carbon sidewall[25]. The histogram consisted of 20,000 data points, each requiring an acquisition time of 5 msec. The observed $2G_o$ step at about 260 s was

caused by either insufficient measurement resolution (~5 ms) or the presence of diffusing Au dimers[26]. Negative steps, which occur frequently, indicate diffusion away from the sidewall or restructuring within the diffusing Au contact. The observation of G_o steps in the absence of a molecular layer demonstrates individual contact resolution during in-situ SDMD. The presence of G_o steps confirms that PPF/Au contact formed through diffusion onto the PPF sidewall as direct deposition onto the PPF sidewall would not show G_o steps.

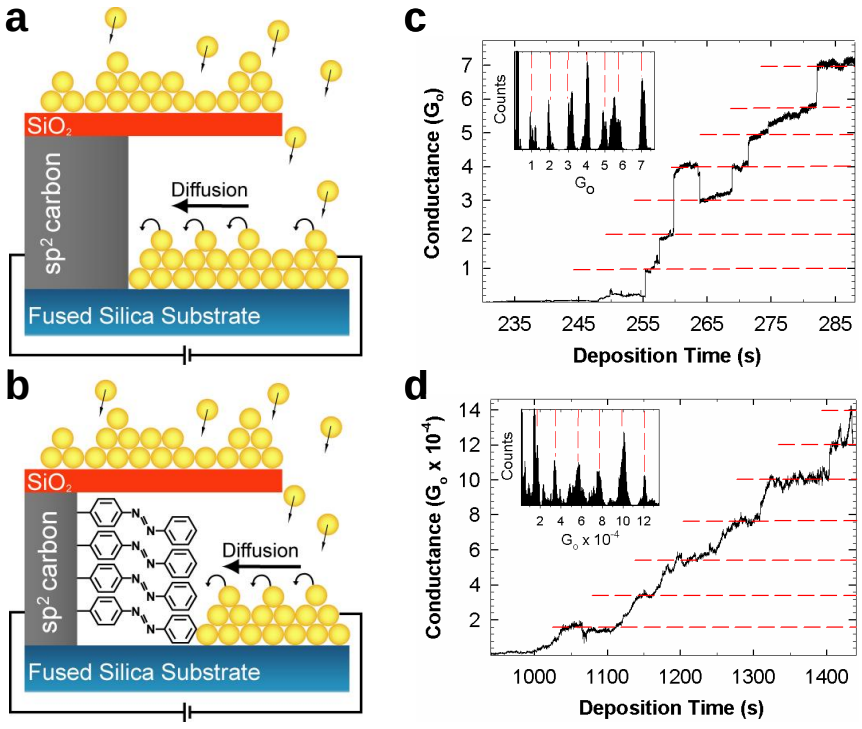

Figure 4.15: a-b, Schematic of the in-situ SDMD technique without and with a molecular monolayer. **c,** Measured conductance vs. deposition time during the deposition of Au without a molecular layer. Inset is the conductance histogram of the conductance vs. deposition time. **d,** Measured conductance vs. deposition time (inset conductance histogram) with an azobenzene monolayer present.

4.4.1.2 Molecular Conductance of Azobenzene

To measure conductance of single molecules within a molecular layer, molecular monolayers were covalently attached to the amorphous, mostly sp^2 carbon sidewall, as shown in Figure 4.15b[27]. Attachment of molecular monolayers was achieved through the oxidation of primary amines for the aliphatic monolayers and diazonium reduction for the aromatic monolayers, as previously described[5, 28]. As shown in Figure 4.15d, the presence of an azobenzene monolayer resulted in much smaller conductance steps than those of Figure 4.15c, with magnitudes equal to 2.0×10^{-4} G_o. These quantized conductance steps are caused by contact formation between the diffusing Au adatoms and individual molecules within the monolayer. Since the molecular conductance is about four orders of magnitude smaller than G_o, resistance within the Au "lead" is negligible. As a guide for the eye, the conductance peaks in the histogram are projected as dashed lines in Figure 4.15d. Each histogram consisted of at least 12,000 data points. As was the case with the molecular layer absent, substructure within each peak is most likely caused by various molecular contact geometries at the molecule/Au interface[29-32].

4.4.1.3 Molecular Conductance of Aliphatic Molecules

For an octylamine (C_8) monolayer, conductance was measured during Au deposition (before 1300 s) and after the electron beam was turned off and deposition stopped, as shown in Figure 4.16a. Focusing on the increase in conductance during Au deposition, conductance steps are observed and highlighted by the dashed lines. The histogram confirms conductance steps with an average spacing of 1.4×10^{-5} G_o, as calculated by fitting Lorentzian distributions to the conductance peaks. After deposition

was stopped, the conductance of the formed C_8/Au junction decreased stepwise from seven contacted molecules to two molecules in about 1300 s, with a similar magnitude of the conductance steps during and after Au deposition. The conductance decrease can be attributed to Au atoms diffusing off the molecular layer toward a lower energy site within the Au lead, presumably due to the weak CH_3 – Au interaction and small barrier for Au diffusion away from the molecular interface. The apparent exponential decrease in conductance is the result of the highest energy (least stable) Au atoms diffusing away first followed by lower energy atoms.

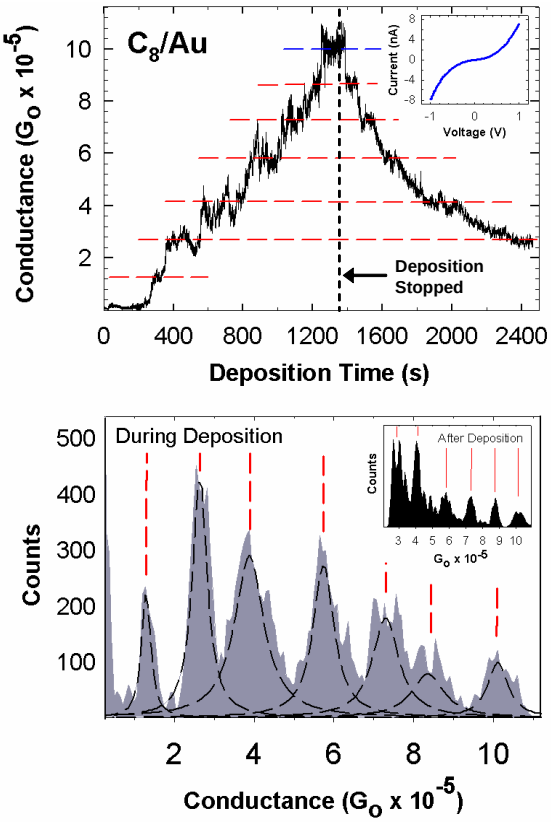

Figure 4.16: a, Conductance vs. Au deposition time for a C_8. The inset shows a current-voltage curve containing seven C_8 molecules, as determined by counting the number of previous conductance steps. **b,** The conductance histogram during formation of the C_8/Au junction. Inset is the conductance histogram after Au deposition. Both histograms contain at least 20,000 data points.

Conductance histograms for a series of C_4 to C_{10} aminoalkanes during Au deposition are shown in Figure 4.17, where the conductance peaks are fit with Lorentzian distributions. The corresponding current versus deposition time for each histogram is shown in Figure 4.18. The conductance exhibits an exponential decrease with molecular length consistent with off-resonant tunneling models[33]. As shown in Figure 4.17d, the tunneling decay constant β (Eq. 2.2) was 0.90 per carbon (0.75 $Å^{-1}$) which is consistent with previously reported values using break junctions, scanning tunneling microscopy, electrochemistry, and large area devices[2, 29, 34-36]. The conductance peaks are nearly equally spaced with no clear trend in the spacing as the number of incorporated molecules increased. Peak broadening in the histograms is the summation of several effects: intrinsic broadening due to electromagnetic noise and thermal vibration at the molecule/Au interface and broadening due to various contact and molecular geometries. Since the measurement time of 5 ms is long compared to Au diffusion steps (~10^{-10} s), it is conceivable that, within a single conductance data point, the number of incorporated molecules could change, which would cause broadening in individual conductance peaks. The absolute value of our measured molecular conductance is within an order of magnitude of the previously reported values for individual alkane molecules[31, 37]. In contrast to most single molecule measurements, our molecules are irreversibly bonded to the bottom contact and incorporated in a monolayer. Additonal experimental results and statistics for aminoalkane/Au juctions are located in Appendix A.

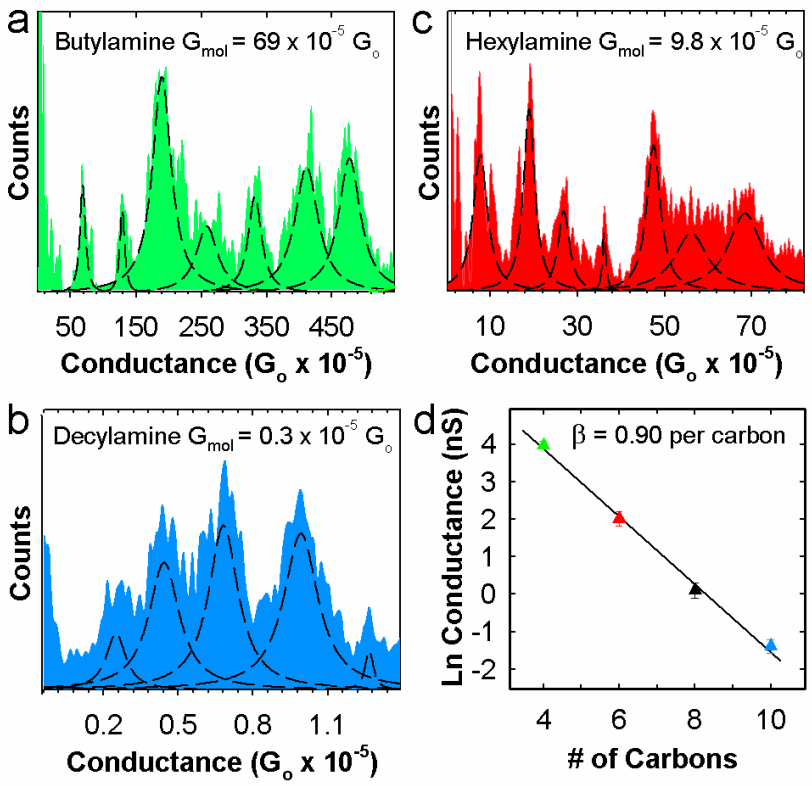

Figure 4.17: a-c, Conductance histograms for C_4, C_6, and C_{10} aminoalkane monolayers attached to the carbon sidewall, fit to Lorentzian distributions. **d,** The single molecule conductance had a tunneling decay constant of $\beta = 0.90$ per carbon (0.75 $Å^{-1}$). All histograms contain at least 8,000 data points.

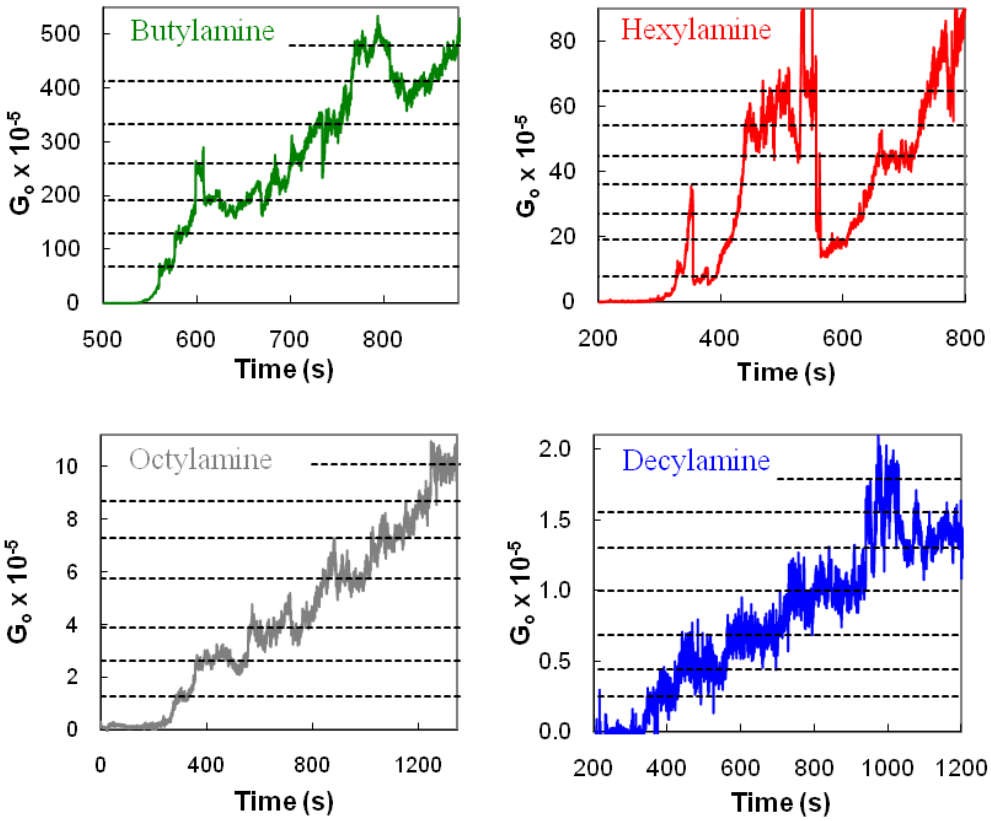

Figure 4.18: In-situ conductance measurements for a series of aminoalkane molecules. The conductance axes have units of 10^{-5} G_o. Dashed horizontal lines are the center of the Lorentzian peaks fitted to the histograms in Figures 4.16 and 4.17.

4.4.1.4 Molecular Conductance for a Series of Azobenzene Molecules

To investigate the effect of molecular energy levels on charge transport, conductance through a series of azobenzene (AB) monolayers with similar lengths but varying orbital energies was measured. The measured conductance versus deposition time curves for the series azobenzene molecules are shown in Figure 4.19 and the corresponding histograms are shown in Figure 4.20. The horizontal dashed lines represent the center of the conductance peaks in their respective conductance histograms. As the number of contacted conducting molecules increased, the noise in the conductance

measurement increased, which limited the maximum number of resolvable conductance steps to be about 6 to 12 depending on the molecular identity. Table 4.3 lists the measured single molecule conductance for the NAB, AB and DAB molecules. Additonal experimental results and statistics for the series of azobenzene/Au juctions are located in Appendix A.

For nitroazobenzene (NAB), the electron withdrawing nitro group lowers the highest occupied molecular orbital (HOMO) energy and decreases the single molecule conductance by a factor of ten compared to AB. The electron donating dimethylamino group in dimethylaminoazobenzene (DAB) raises the HOMO energy and results in a five-fold increase of conductance compared to AB, despite the longer tunneling distance for DAB. This trend of higher conductance when the HOMO energy is closer to the bulk Fermi level (E_F^{bulk} = -4.9 eV) of the carbon sidewall provides strong evidence for HOMO transport through azobenzene molecules and shows that conductance modification through end group tailoring can be achieved, thus providing a critical step toward rational design.

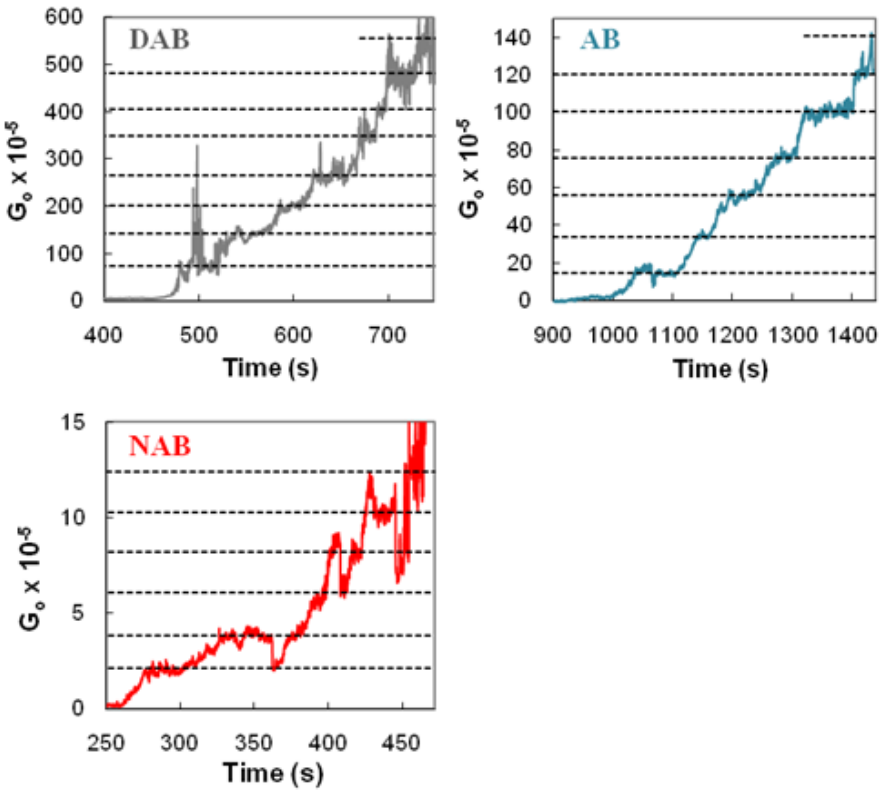

Figure 4.19: In-situ conductance measurements for a series of azobenzene molecules. Numbers on conductance axes have units of 10^{-5} G_o. Dashed horizontal lines were taken from the histograms in Figures 4.20.

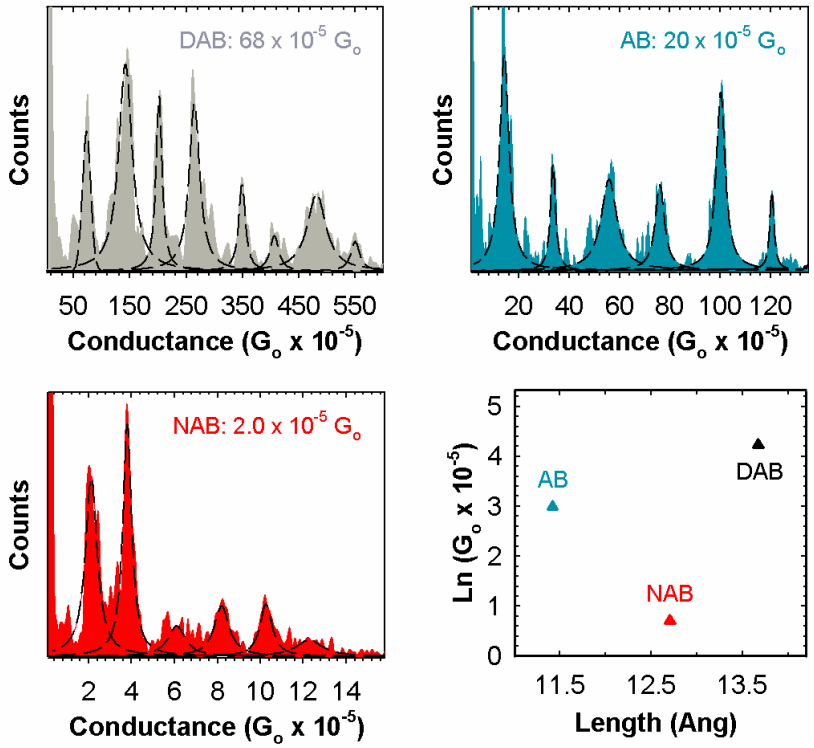

Figure 4.20: Conductance histograms for the conductance vs. time curves of Figure 4.19. Lower right panel is a plot of Ln (G_{mol}) vs. calculated molecular length. Dashed lines in histograms are Lorentzian fits to the experimental data.

Molecule (length, Å)[a]	G_{mol} (G_o x 10^{-5})	Dipole (D)[a]	HOMO (eV)[a]	LUMO (eV)[a]	E_F^{mol} (eV)[b]
NAB (12.8)	2.3 ± 0.4	7.2	-6.9	-3.7	5.1
AB (11.7)	20.4 ± 2.7	0.0	-6.3	-2.6	4.8
DAB (14.0)	73.5 ± 4.0	-4.6	-5.4	-2.1	4.5

[a]Calculated with Gaussian '03 using DFT B3LYP/6-31+g
[b]Measured with ultraviolet photoemission spectroscopy

Table 4.3: Measured and calculated electronic properties for NAB, AB, and DAB molecules.

4.4.1.5 Fitting Single-Molecule Conductance

For off-resonant tunneling through molecules, the molecular conductance (G_{mol}) can be modeled as

$$G_{mol} \propto Ae^{\left(-d\sqrt{\phi}\right)} \qquad \text{Eq. 4.9}$$

where A is a constant, d is the molecule length, and ϕ is the tunneling barrier. A schematic of the energy levels for a molecular junction is shown in Figure 4.21. For HOMO (or hole) tunneling, the tunneling barrier can be approximated by the difference between the molecular HOMO and the Fermi energy (E_F) of the contact electrode. Included in Table 4.3 are the calculated HOMO energies of the free molecules and the interfacial work function (E_F^{mol}) of the carbon contact with its respective bonded monolayer, as determined by ultraviolet photoemission spectroscopy. The change measured in the E_F^{mol} relative to the bulk E_F is consistent with the associated molecular dipole of the monolayer[38]. Plots of the natural logarithm of the observed molecular conductance vs. $d\sqrt{\phi}$ are shown in Figure 4.22a, with the barrier determined either as $E_F^{bulk} - E_{HOMO}$ or $E_F^{mol} - E_{HOMO}$. The slopes in Figure 4.22a differ due to the effect of the molecular dipole on the apparent E_F of the carbon contact, but in both cases there is a linear dependence of ln G_{mol} on $d\sqrt{\phi}$ which is consistent with off-resonant tunneling through the HOMO[33]. The effect of the molecular dipole on the HOMO and interfacial E_F energies are in the same direction, resulting in a lower conductance change than

expected through consideration of the HOMO energy change alone. These results show the importance of the molecular dipole as well as the energetics of the entire system on the molecular conductance.

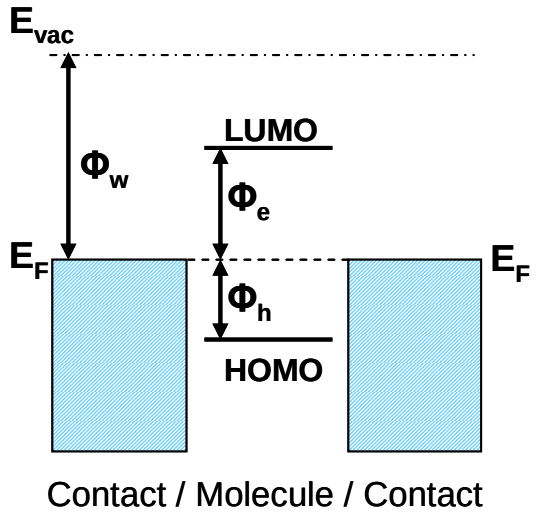

Figure 4.21: Schematic representation of the energy levels for a metal/molecule/metal tunneling junction. For hole tunneling, the tunneling barrier (Φ_h) is the energy offset between Fermi energy (E_F) of the contacts and the HOMO. For electron tunneling, the tunneling barrier (Φ_e) is the energy offset between E_F of the contacts and the LUMO. Additional abbreviations include the vacuum energy level (E_{vac}) and the work function (Φ_w). As shown above, E_F for both contacts are the same resulting in the same tunneling barrier at both interfaces. In cases where the E_F of the contacts are not equal, the tunneling barriers are different at each interface.

\

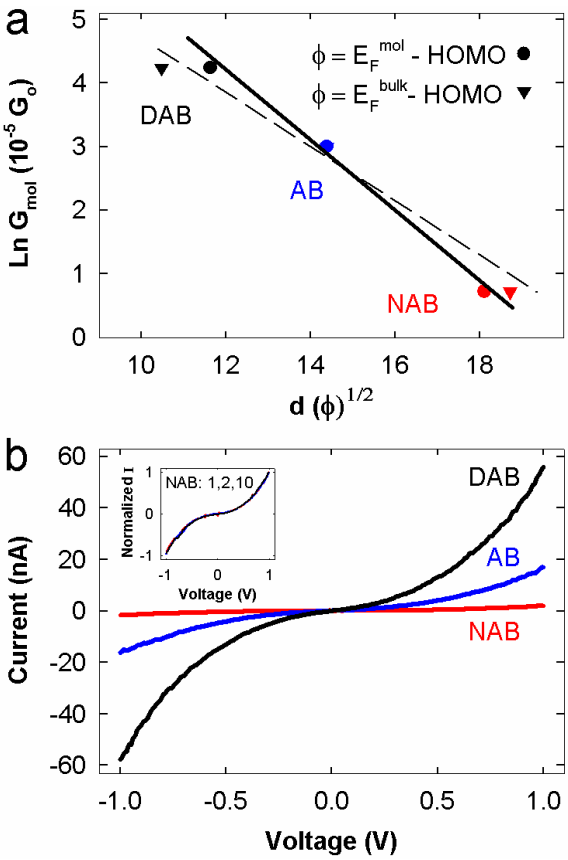

Figure 4.22: a, Plot of the natural logarithm of the molecular conductance vs. $d\sqrt{\phi}$ for three azobenzene molecules. ϕ is calculated from the difference between the calculated HOMO energy and either the bulk E_F or interfacial E_F^{mol}. **b,** I-V curves of junctions containing single NAB, AB, or DAB molecules, determined by counting the conductance steps. Inset shows the normalized I-V curves for 1, 2, and 10 NAB molecules.

In-situ SDMD allows acquisition of current-voltage (I-V) curves at any point during deposition, where the number of incorporated molecules is determined by counting the preceding conductance steps. Figure 4.22b shows I-V curves for molecular junctions containing single NAB, AB, or DAB molecules. The inset in Figure 4.22b shows overlaid I-V curves for junctions containing 1, 2, and 10 NAB molecules normalized to the same maximum current, showing that the curvature of the response does not change with number of conducting molecules. This result is consistent with

equal spacing of conductance steps observed in the histograms, and indicates either that conductance is additive for the increasing number of molecules, or the contacted molecules are widely spaced on the molecular monolayer. This trend was observed for all aliphatic and aromatic molecules studied, suggesting that molecular conductance within a molecular layer is additive with the number of conducting molecules.

The measured I-V curves for single NAB, AB, and DAB junctions were fitted to the Simmons equation over the range of ±0.3 V, as shown in Figure 4.23. The Simmons equation modified to include an effective carrier mass is as follows:

$$I = \frac{qnA}{4\pi^2 \hbar d^2} \left\{ \begin{array}{l} \left(\phi - \frac{qV}{2}\right) \exp\left(-\frac{2d\sqrt{2m_{eff}}}{\hbar}\sqrt{\phi - \frac{qV}{2}}\right) \\ -\left(\phi + \frac{qV}{2}\right) \exp\left(-\frac{2d\sqrt{2m_{eff}}}{\hbar}\sqrt{\phi + \frac{qV}{2}}\right) \end{array} \right\} \qquad \text{Eq. 4.10}$$

where n is the number of conducting molecules, A is the area per molecule, d is the molecular length, m_{eff} is the electron effective mass, ϕ is the effective barrier height, q is the electronic charge, $\hbar$ is the reduced Planck constant, and V is the applied voltage[11,12]. See Figure 2.21 for a schematic of the energy levels for a molecular junction. For single molecule junctions (n = 1), the contact area for each molecule was selected to be held constant at 1 nm^2 , which corresponds to a surface coverage of 1 x 10^{14} molecules cm^{-2} (1.66 x 10^{-10} mol cm^{-2}). Table 4.4 shows the fitted barrier height and effective mass as determined by minimizing the summation of the difference between the nature logarithm

of the current for the experimental and calculated results. As was observed for larger junctions with a higher range of thickness (22-52 Å) [11], the effective mass and apparent barrier height depend on molecular structure and length. The effective mass determined from the Simmons model for the single molecule case is consistent with that reported for large area junctions[11]. Although the apparent barrier height is lower for the single molecules, the single molecule analysis did not include an image charge correction, which predicts a significant decrease in the average barrier height compared to the (E_F – HOMO) offset. The fitted parameters show the same trends in barrier height and molecular conductance shown in Figure 4.22 and give support for HOMO mediated tunneling through the aromatic molecules.

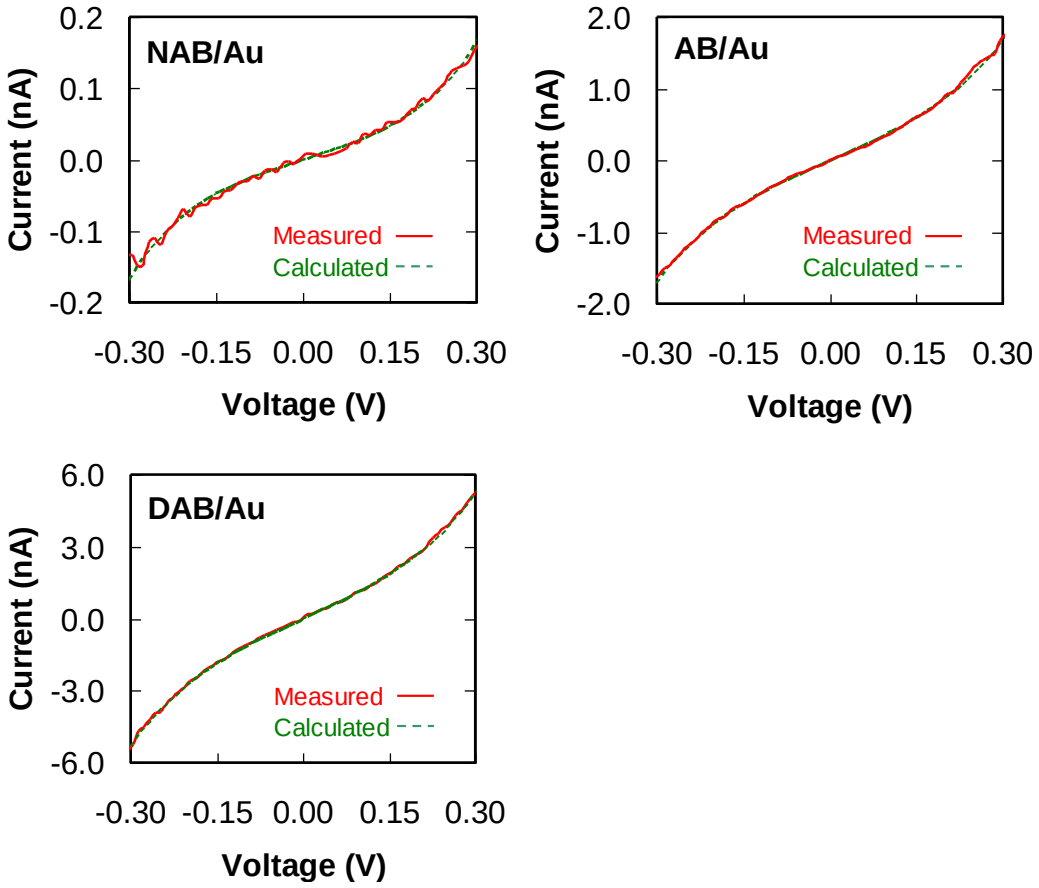

Figure 4.23: Calculated fit of the measure I-V curves for NAB, AB, and DAB junctions containing one molecule over the range of ± 0.3 V**.**

Molecule	Length (Å)	ϕ (eV)[a]	m_{eff}[a]	$\phi * m_{eff}$	G^{mol} (G_o)
NAB	12.8	0.36	2.00	0.71	2.0×10^{-5}
AB	11.7	0.33	1.46	0.48	20×10^{-5}
DAB	14.0	0.23	0.87	0.20	68×10^{-5}

[a]Determined by fitting I-V curves containing one molecule between ± 0.3 V

Table 4.4: Calculated fit parameters from Eq. 4.10 and the measured molecular conductance. The unit of m_{eff} is the free electron rest mass.

4.4.1.6 Advanced Theoretical Modeling of the PPF/Molecule Interaction

As discussed in Section 4.4.1.5, the in-situ SDMD measured single molecule conductance of NAB, AB, and DAB molecules is consistent with off resonant tunneling, where the tunneling barrier can be estimated by the energy offset between the Fermi energy of the PPF and the DFT calculated HOMO of the free molecules. The effect of the molecular dipole on the interfacial Fermi energy of a PPF contact was experimentally measured with UPS. The XPS measured PPF interfacial Fermi energy relative to a bare PPF contact decreased with NAB attachment, remained constant with AB attachment, and increased with DAB attachment. A more complete theoretical model of the PPF/molecule interface would involve calculating the energy levels of the complete PPF/molecule system, not just the individual components. For this investigation, DFT was used to calculate the molecular energies and orbitals for the free molecules, the PPF contact (modeled as graphene), and the PPF/molecule system. Accelyrys DMol^3/PW91/DNP was used for all calculations and was performed by the Kovalenko Research Group at The National Institute for Nanotechnology. The majority of the calculations were performed by Dr. Stanislov Stoyanov. The free molecule energy levels and visualized orbitals are shown in Figure 4.24 for NAB, AB, DAB, and graphene. Graphene was used to model the amorphous sp^2 hybridized structure of the PPF contact. For the molecular HOMO energies in Figure 4.24, the effect of the para-substituted group on the HOMO energies is consistent with the DFT calculated HOMO energies for the free molecules in Table 4.3. As apparent in the orbital distributions shown in Figure 4.24, the molecular HOMOs are localized near the azo group (N=N) of the molecules,

which have been shown in Section 4.4.1.4 to affect the tunneling probability through the series of azobenzene molecules. Interestingly, the HOMO of the graphene and free DAB molecule are within the resonant tunneling criteria although the SDMD measured conductance of a DAB molecule is too low to be consistent with resonant transport. This lack of apparent resonant tunneling through single DAB molecules may be due to the molecular energies of the attached DAB molecule being significantly altered upon molecular attachment to the PPF contact.

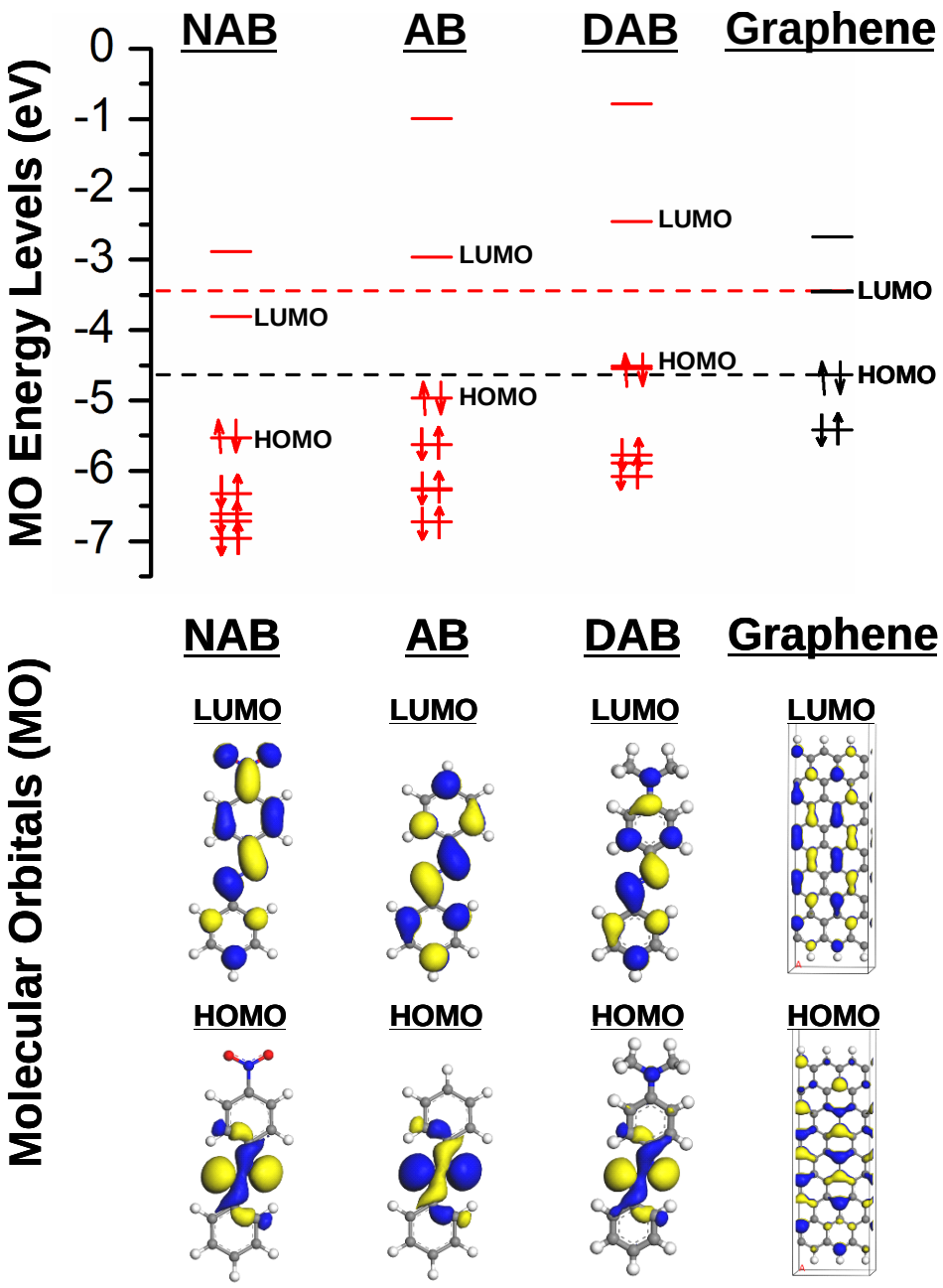

Figure 4.24: Molecular energy levels and visualized molecular orbitals for the free molecules NAB, AB, DAB, and graphene calculated with Accelrys DMol^3/Pw91/DNP. The black and red dashed lines represent the HOMO and LUMO of the graphene respectively.

Figure 4.25 shows the energy levels and associated orbitals for the cases where molecules are covalently bonded to a graphene fragment The red and black dashed lines represent the HOMO and LUMO energy of the graphene prior to molecular attachment. The reported energy levels in Figure 4.25 are the combined energy levels of the graphene with bonded molecules As previously discussed, the expected tunneling barrier through the molecules is the energy offset between the HOMO of the graphene and the HOMO of the molecule. Distinguishing between energy levels localized on the graphene and localized on the molecules is accomplished by visualization of the respective orbitals for each energy level. This approach allows the energy levels to be assigned to the graphene or molecules by their spatial location in the combined system. As shown in Figure 4.25, the energy levels labeled as the HOMO levels of the system have their orbitals localized on the graphene and the energy levels labeled as the HOMO (-1) levels of the system have their orbitals localized on the molecule. As previously discussed, the tunneling barrier is the energy offset between the HOMO of the PPF and the HOMO of the molecule. For all the systems in Figure 4.25, the HOMO of the PPF is the HOMO of the system and the HOMO of the molecules is the HOMO (-1) of the system. For all three molecule/graphene systems, the tunneling barrier associated with HOMO tunneling is calculated from the energy difference between the HOMO and HOMO (-1) energy levels. Comparing this theoretically calculated tunneling barrier (φ) for the graphene/molecule systems shows that $\varphi_{G\text{-}NAB}$ (0.77 eV)> $\varphi_{G\text{-}AB}$ (0.72 eV) > $\varphi_{G\text{-}DAB}$ (0.55 eV), and is consistent with the calculated tunneling barrier in Section 4.4.1.4 and with the SDMD measured single molecule conductance. As previously discussed, the lack of observed

resonant tunneling through the DAB molecules indicates that the molecular energy levels are shifted during attachment to the PPF layer. The shift in the DAB HOMO energy is apparent by comparing Figure 4.24 and 4.25. The free DAB HOMO was -4.4 eV and the graphene/DAB (G-DAB) HOMO was -5.1 eV. This large energy shift of -0.7 eV in the DAB HOMO level is caused by the stabilization of the HOMO level during electronic interaction with the graphene contact. Without considering the electronic interaction between DAB and graphene, resonant tunneling transport would be predicted, but through modeling the combined graphene/DAB system a tunneling barrier of about 0.55 eV is calculated. This calculation is consistent with the lack of resonant tunneling measured through the DAB/Au junctions. For all three molecules, the molecular HOMO was shown to be stabilized upon molecular attachment. In a more general application to molecular electronics, and specifically relevant to rational design attempts, these theoretical calculations show that the interaction between the contact and molecule is critical to understanding and predicting charge transport through molecular electronic systems.

In addition to the effect of the interfacial interaction on the molecular energy levels, the effect of the molecular dipoles on the work function of the PPF (modeled as graphene) is evident in Figure 4.25. The work function measured by UPS is determined by the lowest excitation energy where photoemission occurs. In the case of PPF, the expected change in the interfacial work function is expected to correlate with the HOMO energy of the graphene upon molecular attachment. The HOMO energy level of the bare graphene structure is shown as a black dashed line in Figure 4.25. For an attached AB

molecule, a small change in the graphene HOMO energy is observed and is consistent with the lack of a molecular dipole. For an attached NAB molecule, a -0.5 eV change in the graphene HOMO was calculated. The dipole of a DAB molecule, which is oriented opposite that of the NAB molecule, caused the graphene HOMO to increase upon DAB attachment. Overall, these observed changes in the graphene HOMO level upon attachment of NAB, AB, and DAB is consistent with the UPS measured PPF work function changes shown in Table 4.4.

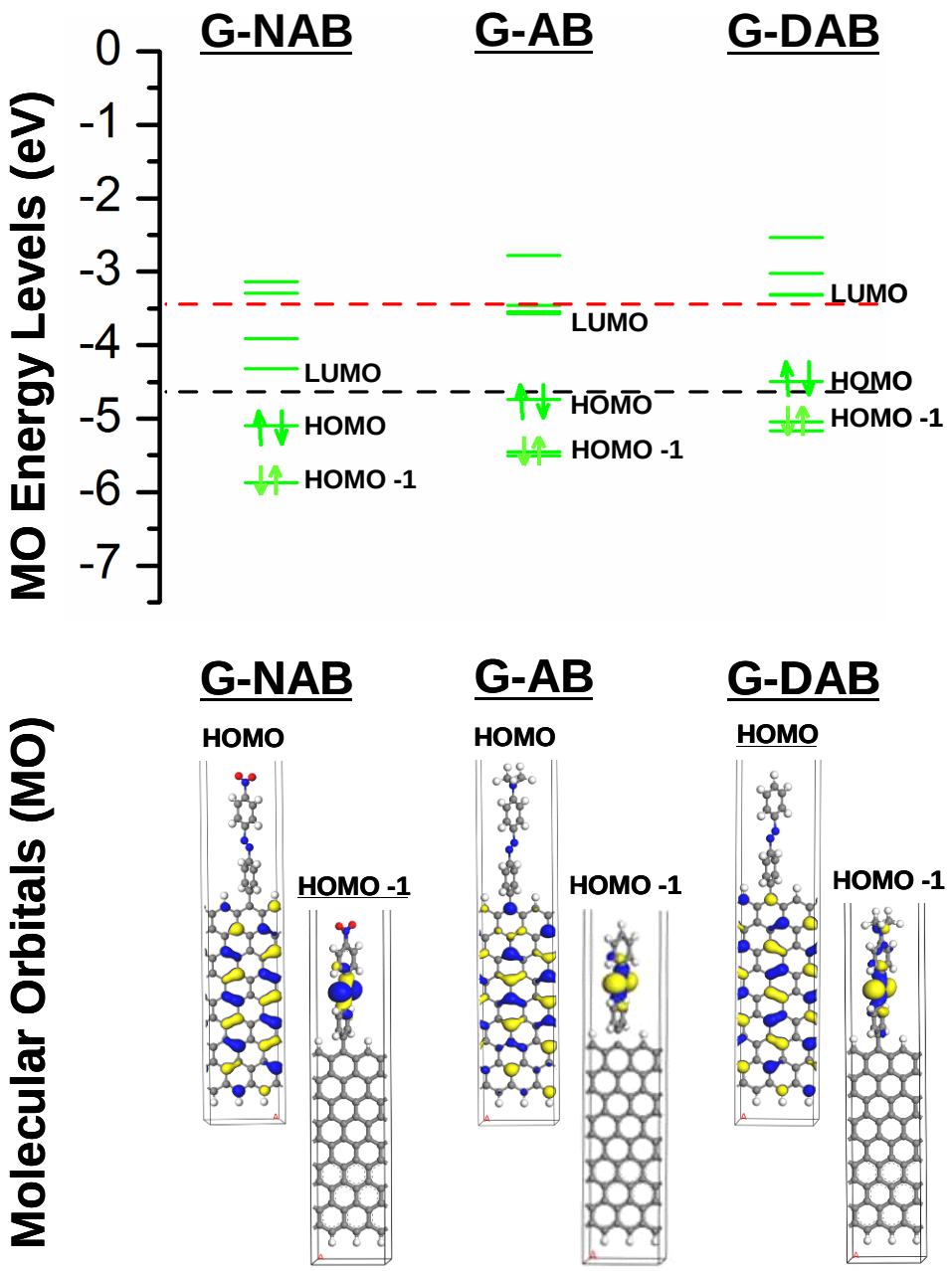

Figure 4.25: Molecular energy levels and visualized molecular orbitals for NAB, AB, DAB covalently attached to graphene calculated with Accelrys DMol^3/Pw91/DNP. The black and red dashed lines represent the HOMO and LUMO of the graphene respectively.

4.4.2 Many-Molecule "Ensemble" Junctions

4.4.2.1 Diaminoalkane/Au Junctions

The J-V characteristics for diaminoalkane/Au many-molecule junctions fabricated with SDMD are shown in Figure 4.26. Using the contact areas of the molecular junctions stated in section 4.2.3.2 and an estimated molecular packing density of 5 x 10^{13} molecules·cm^{-2}, the number of incorporated molecules in the many-molecule junctions discussed in this section is between 10^5 and 10^7 molecules Direct Au evaporation on diaminoalkane monolayers resulted in electronic shorts (inset), demonstrating the "soft" nature of the SDMD technique for fabricating many-molecule junctions. For C_8, C_{10}, and C_{12} diaminoalkane/ Au junctions, the current-density decreases exponentially with molecular length, which is consistent with off-resonant tunneling. As shown in Figure 4.27, the observed decay constant β was 1.1 per carbon atom (0.88 $Å^{-1}$), in agreement with the literature[34, 39], providing strong evidence that the measured current propagates through the molecular layer and is not associated with transport through pin holes or metal filaments. For these results, the aliphatic monolayer consisted of diaminoalkane molecules instead of aminoalkanes because of the stability of the formed junctions. For aminoalkane/Au junctions, the junctions were unstable during the I-V measurements. During measurement, the current suddenly decreased to less than 0.1 nA as the voltage increased above 0.05 V, and remain below 0.1 nA for all subsequent voltage scans. Since minimal interaction at the aminoalkane/Au interface is expected, the most likely reason for the permanent decrease in current was heating during the I-V measurement causing the Au contact to diffuse away from the molecular layer. To provide more

stability, aminoalkane monolayers were replaced with diaminoalkane monolayers, which allowed additional bonding at the diaminoalkane/Au interface through a NH_2/Au interaction. For all the reported diaminoalkane/Au junctions, the J-V measurements were stable between ± 1 V, although higher voltage ranges were not fully investigated.

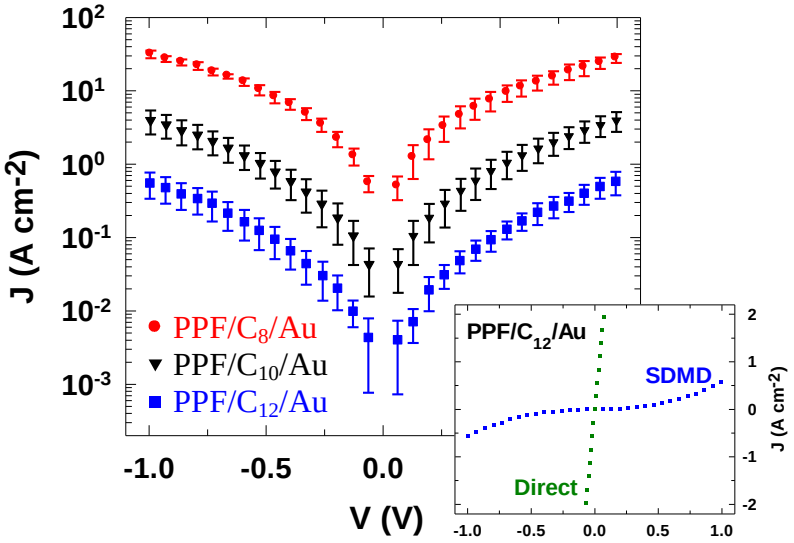

Figure 4.26: J-V measurements for diaminoalkane monolayer junctions. C_8, C_{10}, and C_{12} junctions with Au top contacts were fabricated with the SDMD technique. Error bars represent the standard deviation for a minimum of five junctions on one test chip. Inset: J-V response for direct and SDMD evaporation of Au on C_{12} monolayers plotted on a linear y-axis.

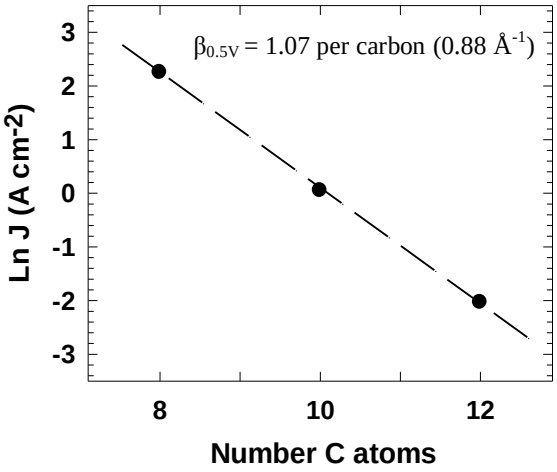

Figure 4.27: Calculation of the decay constant β for the diaminoalkane monolayer junctions at 0.5 V. The dashed line represents the linear regression fit for C_8, C_{10}, C_{12} junctions. Plotted points are the average of at least five junctions for each monolayer length.

4.4.2.2 NAB and FL Junctions with Au, Cu, and Pt Contacts

In addition to electronic characterization of aliphatic monolayers, aromatic multilayers consisting of NAB and FL molecules were electronically characterized, as shown in Figure 4.28 and Figure 4.29. For NAB(4.5)/Au junctions, J-V curves for direct evaporation and SDMD show significant differences in shape and current density. Direct evaporation of Au resulted in a high current density and nearly linear J-V response characteristic of an electronic short between PPF and Au. As discussed in Chapter 3, Raman spectroscopy of the NAB layer before and after direct Au deposition shows no apparent structural changes implying the shorted junctions are caused by Au penetration. In contrast, Au junctions fabricated with SDMD exhibit a nonlinear J-V response similar to reported conductor/molecule/metal junctions[40], and have a similar J-V response for NAB(4.5)/Au junctions fabricated with angled deposition of 70° as shown in Chapter 3.

Although not shown, FL junctions fabricated with direct Au evaporation had linear, non-characteristic I-V curves indicating Au penetration. As shown in Figure 4.28b, deposition of Cu contacts results in similar J-V responses for both direct evaporation and SDMD. This is consistent with previous reports that highly reproducible molecular junctions can be fabricated with direct evaporation of Cu without the presence of observable metal penetration into the molecular layer[3], yielding J-V characteristics with the same shape and magnitude as those obtained with SDMD. Although expected, the overlap in J-V curves for direct and SDMD NAB(4.5)/Cu junctions show that two distinctly different deposition techniques result in junctions with similar electronic behavior. For Pt deposited contacts, the same trend for the NAB and FL junctions was observed, as direct evaporation resulted in Pt filament formation and SDMD resulted in the non-linear response shown in Figure 4.28a. These results show that Au and Pt penetration into the molecular layer can be minimized with SDMD.

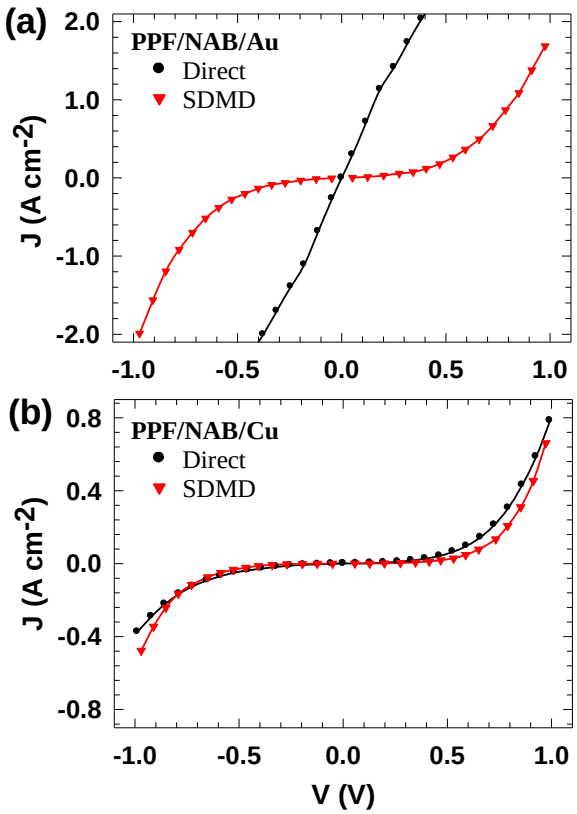

Figure 4.28: J-V measurements for direct deposition and SDMD techniques. Direct evaporation vs. SDMD demonstrates large differences in Au contacted junctions and similar behavior for Cu contacted junctions.

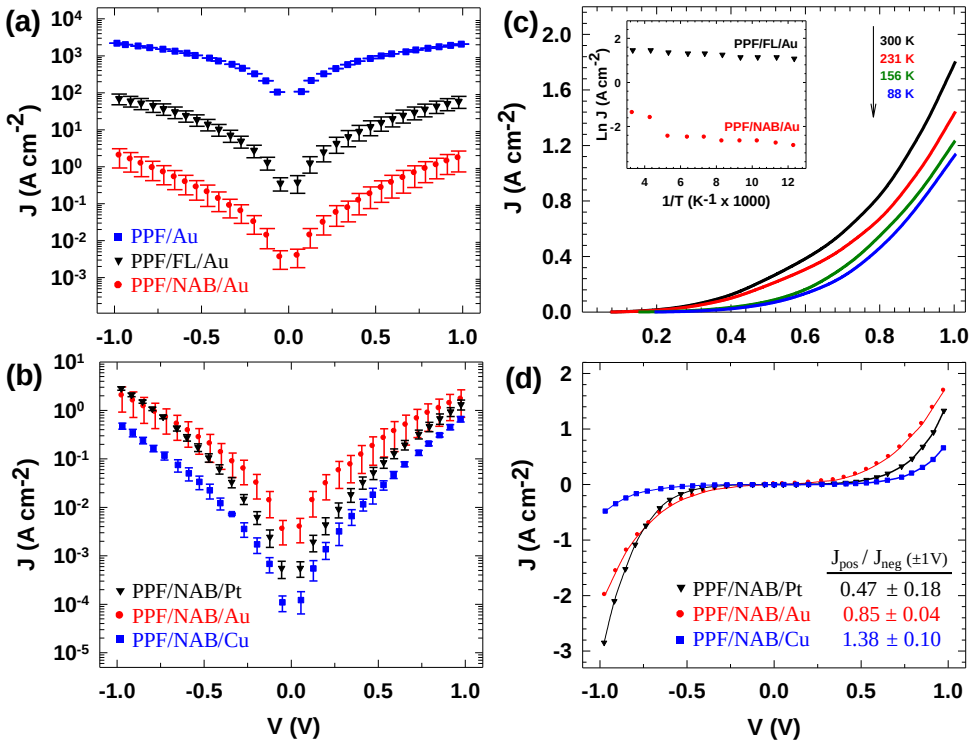

Figure 4.29: a – b, Error bars represent the standard deviation for a minimum of five junctions on one test chip **a,** Current density strongly influenced by the presence of a FL or NAB molecular layer. **b,** J-V curves for NAB(4.5) with Cu, Au, and Pt contacts. **c,** Temperature dependence of the J-V curves for NAB(4.5)/Au. Inset: An Arrhenius plot between 80 and 188 K for NAB and FL junctions. **d,** Same data as 4b but with a linear y-axis to emphasize the asymmetry. Inset: Measured asymmetry ratio at ± 1V.

Figure 4.29 shows J-V curves plotted on a log scale for various junctions, with the standard deviations indicated for at least five different junctions prepared simultaneously. The large decrease in current density with the incorporation of a molecular layer between the PPF and metallic contacts indicates the current is dominated by charge transport through the molecular layer. Comparison between various molecular layers shows that the J-V characteristics depend strongly on the thickness and structure of the molecular layer. Comparison between the current densities of FL (1.7 ± 0.2nm thick) and C_{12} (1.6 ±

0.2 nm thick) junctions shows that the current densities differ by two orders of magnitude although the molecular layers have similar thicknesses, indicating conjugation within the molecular layer strongly affects charge transport. Compared to C_{12}, the conjugated FL layer has molecular energy levels closer to the Fermi energy of the contacts, resulting in higher conductance. Figure 4.29d compares the J-V responses for PPF/NAB(4.5) with Cu, Au, and Pt top contacts; a comparison that cannot be achieved through direct evaporation alone due to Au and Pt penetration. The observed trend in current asymmetry (J_{pos} /J_{neg}) shown in Figure 4.29d and Table 4.5 is consistent with charge transport through the highest occupied molecular orbital (HOMO), which has been suggested by several groups[29,30]. As the work function of a contact increases, the barrier between the HOMO and Fermi energy of the contact decreases, allowing more efficient transport through the HOMO. The work function of the PPF contact is -4.93 eV, and that of e-beam deposited Cu is 4.73, determined with a Kelvin probe [30]. For NAB(4.5)/Cu junctions, the lowest barrier for hole conduction is between the PPF and HOMO resulting in a higher current when the PPF is biased positive. NAB(4.5)/Pt junctions, the lowest barrier is between the HOMO and Pt resulting in a higher current when the PPF is biased negative (Pt biased positive). Although the above model is consistent with the observed asymmetry, unequivocally determining the dominant charge carrier is complicated by the unknown nature of energy level alignment within a molecular layer. Other considerations, although not all inclusive, that need to be accounted for are the effect of interfacial dipoles and molecular energy level broadening. Varying the work function of the second contact by ~ 0.7 eV (for Cu to Pt) resulted in a current-density change of less

than an order of magnitude; a result similar to that observed by Engelkes et al. for the contact resistance of alkanedithiols[31]. A more complete understanding of energy level alignment with a molecular layer is needed to fully understand the work function effect on current density.

	NAB/Cu	NAB/Au	NAB/Pt
J_{pos} [1V]	0.66	1.69	1.33
J_{neg} [-1V]	-0.48	-1.99	-2.85
J_{pos} / J_{neg}	1.38	0.85	0.47
H_o: $J_{pos} = J_{neg}$	$p = 9x10^{-6}$	$p = 7x10^{-8}$	$p = 5x10^{-6}$

Table 4.5: Current density asymmetry at ±1 V for three different metal contacts. Data represents the average data of at least 5 junctions on one test chip. The asymmetry ratios are statistically different and correlate with the work function of the contacts.

Low temperature J-V curves for SDMD junctions were measured in a cryogenic probe station evacuated to 5 x 10^{-6} torr, with the results shown in Figure 4.29c. For the temperature range 81-188 K, the measured activation energies for the NAB(4.5)/Au and FL/Au junctions were less than 0.003 eV, substantially less than expected for activated charge transport mechanisms such as redox exchange or molecular conformation changes. The small activation barrier may originate outside the junction, since correction of lead or contact resistance of the metal contact cannot readily be achieved with the SDMD junctions.

4.4.3 Comparison between Single-Molecule and Many-Molecule Conductance

4.4.3.1 Aliphatic Molecular Junctions

To compare the measured molecular conductance between single/several molecule and many-molecule junctions, the equivalent single molecule current (I_{mol}) is calculated from the measured current density (J_{alkane}) of the diaminoalkane/Au junctions through:

$$I_{mol} = \frac{J_{alkane}}{\rho_{mol}} \qquad \text{Eq. 4.11}$$

where ρ_{mol} is the molecular packing density of the diaminoalkane monolayer. The molecular packing density of molecules attached through oxidation of a primary amine on carbon surfaces has been reported to be $0.5 – 1.0 \times 10^{13}$ molecules·cm^{-2}.[28] From Eq. 4.11, the calculated equivalent single molecule current at ± 1V for the diaminoalkane C_8 and C_{10} is $3 – 6 \times 10^{-12}$ and $2 – 4 \times 10^{-13}$ A·molecule^{-1} respectively. Compared to the measured single molecule current at ± 1 V for monoaminoalkane C_8 and C_{10} of 1.1×10^{-9} and 2.3×10^{-10} A·molecule^{-1} respectively, the measured single molecule conductance is about 2-3 orders of magnitude higher than the calculated equivalent single molecule conduction from many-molecule junctions. Unfortunately, fabricated aminoalkane C_8 and C_{10} many-molecule junctions were unstable during ex-situ electronic measurements, preventing direct comparison. Based on the measured tunneling decay constants of the amino- and diaminoalkane molecules, the aminoalkanes would be expected to have a higher conductance compared to the diaminoalkanes. A significant potential source of

the discrepancy is determination of the contact area for the many-molecule diaminoalkane/Au junctions. If the actual molecular contact area was less than the calculated geometrical contact area, the calculated single molecule conductance from the many-molecule junctions would be lower than their actual conductance. This source of error is not confined to the SDMD technique, but is a source of error for most many-molecule fabrication paradigms.

4.4.3.2 NAB Molecular Layers

To compare the conductance through the single NAB(1.05)/Au junctions and the many molecule NAB(4.5)/Au junctions, the measured current density ($J_{4.5nm}$) for NAB(4.5)/Au junctions was converted to an equivalent single molecule current for an equivalent monolayer thickness. For this conversion, the expected current density ($J_{1.05nm}$) for a monolayer NAB (1.05)/Au junction was calculated using the previously determined $\beta = 2.47\ nm^{-1}$ with the following equations[3, 41].

$$J_{4.5nm} = J_o \exp\left[(-2.47)(4.5)\right] \qquad \text{Eq. 4.12}$$

$$J_{1.05nm} = J_o \exp\left[(-2.47)(1.05)\right] \qquad \text{Eq. 4.13}$$

$$J_{1.05nm} = J_{4.5nm} \exp\left[(-2.47)(1.05-4.5)\right] \qquad \text{Eq. 4.14}$$

For Eq. 4.14, the calculated $J_{1.05nm}$ at ± 1 V for NAB(1.05)/Au is $1.0 \times 10^4\ A \cdot cm^{-2}$, where J_o for both junctions was assumed to be equal. To convert $J_{1.05nm}$ to an equivalent current per NAB molecule (I_{NAB}),

$$I_{NAB} = \frac{J_{1.05nm}}{\rho_{NAB}} \qquad \text{Eq. 4.15}$$

where ρ_{NAB} is the packing density of a NAB monolayer. Molecular monolayers attached through the diazonium reduction paradigm have been reported to have packing density of $1 - 6 \times 10^{13}$ molecules·cm^2.[8, 42] Using Eq. 4.15, the calculated equivalent single NAB molecule current at ± 1 V is between $0.2 - 1.0 \times 10^{-9}$ A per NAB. Compared to the single molecule measured current at ± 1 V of 1.6×10^{-9} A per NAB, the NAB current from single molecule NAB(1.05)/Au and many-molecule NAB(4.5)/Au junctions are within an order of magnitude. This agreement gives evidence that for NAB molecular layers the conductance of a many-molecule junction can be estimated from the measured single NAB conductance through the in-situ SDMD technique.

4.5 CONCLUSIONS AND FUTURE WORK

The guiding principle behind the SDMD technique was to minimize the tendency for metal penetration through a molecular layer during electronic contact formation through a physical vapor deposition technique. As discussed in this chapter, metal penetration into the molecular layer is eliminated through the SDMD technique because the technique ensures all metal atoms arriving at the molecular layer are coordinated with additional metal atoms of the forming contact. The binding energy associated with the coordination acts as an insurmountable barrier for metal penetration. In addition to preventing penetration, in-situ SDMD current measurements during the onset of junction formation allows the conductance of a single molecule comprising a molecular

monolayer to be measured. Incorporation of each individual molecule into the molecular junction resulted in a conductance step observed in the in-situ current measurement. Stepwise incorporation of each molecule allows the exact number of conducting molecules to be known, which, for the first time, allows conductance measurements through both single-molecule and several-molecule junctions during the same experiment on the same molecular layer. The single molecule conductivity measurements obtained through the SDMD technique provide insight into how molecular conductance can be modulated through molecular engineering. Also, these results give evidence that molecular conduction through a molecular junction is additive with the number of conducting molecules incorporated in the junction.

Continuation of the metal deposition allows the fabrication of "ensemble" junctions containing greater than 10^3 molecules, which are more amenable to practical applications. For many-molecule junctions, fabrication of electronic contacts through the SDMD technique resulted in reproducible J-V curves, which depended strongly on the molecular structure. For the case of a Cu top contact, the SDMD current-voltage response agreed quantitatively with those from direct Cu deposition, but Au and Pt deposition was successful only with the SDMD technique. In contrast to direct Au and Pt evaporation, the SDMD technique was shown to prevent metal penetration and results in reproducible molecular junctions with Au, Cu, and Pt contacts. The ability to vary the work function of the second electronic contact provides a crucial experimental tool which permits insight into charge transport mechanisms in molecular junctions.

The SDMD paradigm is amenable to a variety of materials and bonding chemistry, as well as a wide range of molecular structures with different energy levels, dipoles, and conjugation. The ability to monitor conductance in-situ during contact formation with single-molecule resolution suggests additional applications of this technique, such as conductance measurements on biological molecules, fullerenes, and conjugated polymers. Further development of the technique will most likely fuel additional use of the SDMD technique for unforeseen applications.

Future work involving the SDMD technique includes conductance measurements on a wider range of molecules for both single-molecule and many-molecule junctions. Additional molecular conductance measurements will improve our understanding of the role that molecular energy levels play in molecular conductance. Theoretically modeling of the contact/molecule system is needed for a better understanding of the electronic coupling between the molecules and the electronic contacts. A better understanding of this interaction is critical to achieve rational design in future molecular electronic devices. Finally, development of additional SDMD junction designs is needed. Advancements to the technique could include the ability to vary the bottom contact material, improved control of the fabrication process, and a better understanding of the thin film growth mechanism as characterized by ex-situ SEM and TEM.

4.6 REFERENCES

1. Ibach, H., *Physics of Surfaces and Interfaces*. 1st ed.; Springer: New York, 2006.

2. Bonifas, A. P.; McCreery, R. L., 'Soft' Au, Pt and Cu contacts for molecular junctions through surface-diffusion-mediated deposition. *Nat. Nanotech.* **2010,** 5, (8), 612-617.

3. Bergren, A. J.; Harris, K. D.; Deng, F. J.; McCreery, R. L., Molecular electronics using diazonium-derived adlayers on carbon with Cu top contacts: critical analysis of metal oxides and filaments. *J. Phys. Condens. Matter* **2008,** 20, (37), 11.

4. Ranganathan, S.; Steidel, I.; Anariba, F.; McCreery, R. L., Covalently bonded organic monolayers on a carbon substrate: A new paradigm for molecular electronics. *Nano Lett.* **2001,** 1, (9), 491-494.

5. Anariba, F.; DuVall, S. H.; McCreery, R. L., Mono- and multilayer formation by diazonium reduction on carbon surfaces monitored with atomic force microscopy "scratching". *Anal. Chem.* **2003,** 75, (15), 3837-3844.

6. Anariba, F.; McCreery, R. L., Electronic Conductance Behavior of Carbon-Based Molecular Junctions with Conjugated Structures. *J. Phys. Chem. B* **2002,** 106, 10355-10362.

7. Dunker, M. F. W.; Starkey, E. B.; Jenkins, G. L., The preparation of some organic mercurials from diazonium borofluorides. *J. Am. Chem. Soc.* **1936,** 58, 2308-2309.

8. Brooksby, P. A.; Downard, A. J., Electrochemical and atomic force microscopy study of carbon surface modification via diazonium reduction in aqueous and acetonitrile solutions. *Langmuir* **2004,** 20, 5038-5045.

9. Pinson, J.; Podvorica, F., Attachment of organic layers to conductive or semiconductive surfaces by reduction of diazonium salts. *Chem. Soc. Reviews* **2005,** 34, 429-439.

10. Kariuki, J. K.; McDermott, M. T., Formation of multilayers on glassy carbon electrodes via the reduction of diazonium salts. *Langmuir* **2001,** 17, 5947-5951.

11. Racz, Z.; Seabaugh, A., Characterization and control of unconfined lateral diffusion under stencil masks. *J. Vac. Sci. Technol. B* **2007,** 25, (3), 857-861.

12. Ohring, M., *Materials Science of Thin Films Deposition and Structure*. 2nd ed.; Academic Press: 2002.

13. Jaeger, R. C., *Introduction to Microelectronic Fabrication*. 2nd Edition ed.; Prentice-Hall: Upper Saddle River, NJ, 2002.

14. Kaiser, N., Review of the fundamentals of thin-film growth. *Appl. Optics* **2002,** 41, (16), 3053-3060.

15. Markov, I.; Kaischew, R., Influence of supersaturation on mode of crystallization on cyrstalline substrates. *Thin Solid Films* **1976,** 32, (1), 163-167.

16. Wynblatt, P., The effects of interfacial segregation on wetting in solid metal-on-metal and metal-on-ceramic systems. *Acta Mater.* **2000,** 48, (18-19), 4439-4447.

17. Doron-Mor, I.; Barkay, Z.; Filip-Granit, N.; Vaskevich, A.; Rubinstein, I., Ultrathin gold island films on silanized glass. morphology and optical properties. *Chem. Mater.* **2004,** 16, (18), 3476-3483.

18. Du, R. B.; Ssenyange, S.; Aktary, M.; McDermott, M. T., Fabrication and characterization of graphitic carbon nanostructures with controllable size, shape, and position. *Small* **2009,** 5, (10), 1162-1168.

19. Abelmann, L.; Lodder, C., Oblique evaporation and surface diffusion. *Thin Solid Films* **1997,** 305, (1-2), 1-21.

20. Liu, C. L.; Cohen, J. M.; Adams, J. B.; Voter, A. F., EAM Study of Surface Self-Diffusion of Single Adatoms of FCC Metals Ni, Cu, Al, Ag, Au, Pd, and Pt. *Surf. Sci.* **1991,** 253, (1-3), 334-344.

21. Speller, S.; Molitor, S.; Rothig, C.; Bomermann, J.; Heiland, W., Surface Mobility on the Au(110) Surface Observed with Scanning Tunneling Microscopy. *Surf. Sci.* **1994,** 312, (1-2), L748-L752.

22. Bhattacharyya, S.; Henley, S. J.; Mendoza, E.; Gomez-Rojas, L.; Allam, J.; Silva, S. R. P., Resonant tunnelling and fast switching in amorphous-carbon quantum-well structures. *Nat. Mater.* **2006,** 5, (1), 19-22.

23. Ittah, N.; Yutsis, I.; Selzer, Y., Fabrication of highly stable configurable metal quantum point contacts. *Nano Lett.* **2008,** 8, (11), 3922-3927.

24. Li, J. Z.; Kanzaki, T.; Murakoshi, K.; Nakato, Y., Metal-dependent conductance quantization of nanocontacts in solution. *Appl. Phys. Lett.* **2002,** 81, (1), 123-125.

25. Agrait, N.; Yeyati, A. L.; van Ruitenbeek, J. M., Quantum properties of atomic-sized conductors. *Phys. Rep.* **2003,** 377, (2-3), 81-279.

26. Zhuang J; L, L., Exchange mechanism for adatom diffusion on metal fcc(100) surfaces. *Phys. Rev. B* **1998,** 58, (3), 1173-1176.

27. Ranganathan, S.; McCreery, R. L., Electroanalytical performance of carbon films with near-atomic flatness. *Anal. Chem.* **2001,** 73, (5), 893-900.

28. Deinhammer, R. S.; Ho, M.; Anderegg, J. W.; Porter, M. D., Electrochemical oxidation of amine-containing coumpounds - a route to the surface modification of glassy-carbon electrodes. *Langmuir* **1994,** 10, (4), 1306-1313.

29. Xu, B. Q.; Tao, N. J. J., Measurement of single-molecule resistance by repeated formation of molecular junctions. *Science* **2003,** 301, (5637), 1221-1223.

30. Muller, K. H., Effect of the atomic configuration of gold electrodes on the electrical conduction of alkanedithiol molecules. *Phys. Rev. B* **2006,** 73, (4), 6.

31. Venkataraman, L.; Klare, J. E.; Tam, I. W.; Nuckolls, C.; Hybertsen, M. S.; Steigerwald, M. L., Single-molecule circuits with well-defined molecular conductance. *Nano Lett.* **2006,** 6, (3), 458-462.

32. He, J.; Sankey, O.; Lee, M.; Tao, N. J.; Li, X. L.; Lindsay, S., Measuring single molecule conductance with break junctions. *Faraday Discuss.* **2006,** 131, 145-154.

33. Mujica, V.; Ratner, M. A., Current-voltage characteristics of tunneling molecular junctions for off-resonance injection. *Chem. Phys.* **2001,** 264, (3), 365-370.

34. Engelkes, V. B.; Beebe, J. M.; Frisbie, C. D., Length-dependent transport in molecular junctions based on SAMs of alkanethiols and alkanedithiols: Effect of metal work function and applied bias on tunneling efficiency and contact resistance. *J. Am. Chem. Soc.* **2004,** 126, (43), 14287-14296.

35. Liu, B.; Bard, A. J.; Mirkin, M. V.; Creager, S. E., Electron transfer at self-assembled monolayers measured by scanning electrochemical microscopy. *J. Am. Chem. Soc.* **2004,** 126, (5), 1485-1492.

36. Akkerman, H. B.; Blom, P. W. M.; de Leeuw, D. M.; de Boer, B., Towards molecular electronics with large-area molecular junctions. *Nature* **2006,** 441, (7089), 69-72.

37. Li, C.; Pobelov, I.; Wandlowski, T.; Bagrets, A.; Arnold, A.; Evers, F., Charge transport in single Au vertical bar alkanedithiol vertical bar Au junctions: Coordination geometries and conformational degrees of freedom. *J. Am. Chem. Soc.* **2008,** 130, (1), 318-326.

38. Vilan, A.; Shanzer, A.; Cahen, D., Molecular control over Au/GaAs diodes. *Nature* **2000,** 404, (6774), 166-168.

39. Holmlin, R. E.; Haag, R.; Chabinyc, M. L.; Ismagilov, R. F.; Cohen, A. E.; Terfort, A.; Rampi, M. A.; Whitesides, G. M., Electron transport through thin organic films in metal-insulator-metal junctions based on self-assembled monolayers. *J. Am. Chem. Soc.* **2001,** 123, (21), 5075-5085.

40. Haick, H.; Ambrico, M.; Ghabboun, J.; Ligonzo, T.; Cahen, D., Contacting organic molecules by metal evaporation. *Phys. Chem. Chem. Phys.* **2004,** 6, (19), 4538-4541.

41. Bergren, A. J.; McCreery, R. L.; Stoyanov, S. R.; Gusarov, S.; Kovalenko, A., Electronic characteristics and charge transport mechanisms for large area aromatic molecular junctions. In *J. Phys. Chem. C*, 2009; Vol. 114, pp 15806-15815.

42. Downard, A. J., Electrochemically assisted covalent modification of carbon electrodes. *Electroanal.* **2000,** 12, (14), 1085-1096.

CHAPTER 5

IN-SITU OPTICAL ABSORBANCE SPECTROSCOPY OF MOLECULAR LAYERS IN ACTIVE CARBON BASED ELECTRONIC JUNCTIONS

Sections of this Chapter have been previously published in:

Bonifas, A. P.; McCreery, R. L., In-situ optical absorbance spectroscopy of molecular layers in carbon based molecular electronic devices. *Chem. Mat.* **2008,** 20, (12), 3849-3856.

5.1 INTRODUCTION

5.1.1 Motivation behind Spectroscopic Characterization

As the field of molecular electronics matures, additional focus has been placed on understanding the mechanisms behind observed electronic properties of molecular junctions[1-10]. One attractive method to gain additional insight into charge transport through single molecules or molecular layers is optical spectroscopy, such as optical absorbance, Fourier transform infrared (FTIR), Raman, and fluorescence spectroscopy. Optical spectroscopy allows direct, non-destructive characterization of molecular properties such as energy levels, oxidation states, and molecular structure which are difficult to obtain from current-voltage or capacitance-voltage measurements alone. In addition, optical spectroscopy often provides fast time resolution for in-situ monitoring of functioning devices. The well established field of spectroelectrochemistry has exploited optical spectroscopy for monitoring molecules in solution-based electrochemical cells, allowing complementary structural and electrochemical analysis[11, 12]. The current investigation describes the application of some of the principles of spectroelectrochemistry to solid state molecular electronic devices in order to probe the electronic properties of molecular layers only a few nm thick.

In-situ Raman spectroscopy has been previously used to monitor molecular structure of chemisorbed molecular layers on carbon surfaces in both solution and solid state devices[13, 14]. Nitroazobenzene molecules chemisorbed on a carbon electrode in an electrolyte exhibited reversible changes in their Raman spectrum when the electrode was cycled between reducing and oxidizing potentials. Analysis of the Raman spectra and

voltammetry allowed the correlation of the vibrational changes with the reduction and oxidation of the chemisorbed molecular layer. In solid state molecular junctions, consisting of NABTiO_2 layers sandwiched between carbon and Au electrodes, Raman spectroscopy revealed vibrational changes consistent with the reduction and oxidation of the molecular layer during an applied bias. Although Raman provides valuable in-situ structural information, it requires the molecular layer to consist of a strong Raman scatterer and be subjected to prolonged laser exposure. FTIR spectroscopy has been used to characterize molecular devices but in-situ analysis has been limited by long signal acquisition times of several minutes[15-17]. In addition, FTIR has limitations on the substrate material, since the surface selection rules are most pronounced on Au. Optical absorption has previously been used to probe conducting polymers in light emitting diodes and metal/polymer/semiconductor structures, but the polymer layers were much thicker (~100 nm) than those used in molecular electronic devices[18, 19].

The motivation for using optical absorption as a diagnostic tool is threefold. First, since many molecular systems of electronic interest absorb in the ultraviolet-visible region, optical absorption allows for the analysis of a wide range of molecular systems. Metal oxides in molecule/metal oxide "heterojunctions" are also amendable to optical absorption spectroscopy allowing the absorbance changes of both the molecular and oxide layer to be monitored. Second, time resolution of optical absorption may range from femtoseconds to seconds for laser based techniques or microseconds to seconds with broad-band light sources. Considering the speed of most electronic devices, fast time resolution is necessary for in-situ analysis of junction dynamics. Third, optical

absorption gives direct evidence of changes in energy levels within electronically active molecular junctions. By measuring absorption spectra as a function of applied voltage or time, significant insight into electron transfer and energy level alignment between device layers can be obtained. For these reasons, optical absorption spectroscopy will be a useful in-situ probe of molecular electronic devices provided the device structure is amenable to spectroscopy of the "buried interface".

5.1.2 Spectroscopic Characterization Technique

As described in Chapter 2, observed charge transport through molecular layers on the order of 1 – 5 nm thick is consistent with off-resonant tunneling through the highest occupied molecular orbital (HOMO) or lowest unoccupied molecular orbital (LUMO) energy levels. As determined in Chapter 4, charge transport through aliphatic monolayers and aromatic monolayers and multilayers was consistent with off-resonant tunneling through the HOMO energy levels. For charge transport in this regime, the tunneling time (τ_{LB}) calculated with the Landauer-Buttiker equation (Eq. 2.3) is on the order of sub-femtoseconds. The τ_{LB} can be interpreted as the time the tunneling charge resides on a molecule. Since molecular vibrational periods are at least several femtoseconds, redox events and associated structural reorganization within the molecular layer are not expected in the off-resonant tunneling regime. This calculation is consistent with the lack of bias induced in-situ optical absorbance changes for carbon/molecular layer/Cu junctions. For molecular layers operating in the off-resonant tunneling regime, determination of the molecular vibrational bands has been successfully shown with

ineleastic electron tunneling spectroscopy (IETS) and scanning tunneling spectroscopy (STS)[20-22].

For in-situ optical absorbance spectroscopy to be applied to molecular layers, redox events must occur within the molecular layer. This can be accomplished by providing a tunneling barrier in the junction. The presence of a tunneling barrier increases the time the injected charge resides on the molecule, and, if this time is longer than the molecular vibrational period, redox events can occur. In this chapter, the molecular junctions were fabricated with a tunneling barrier layer consisting of SiO_2 or Al_2O_3 added between the molecular layer and top Pt electronic contact. The incorporation of the oxide layer caused the junction to operate in a coulomb blockade (CB) regime. Junctions operating in the CB regime have been experimentally shown and theoretically proposed to exhibit redox reactions analogous to conventional electrochemistry[14, 23-25]. As an additional benefit, the evaporation of a metal oxide between the molecule layer and top metallic contact reduces the tendency for metal filament formation. Although two-terminal junctions operating in the CB regime cannot be used to directly measure molecular conductance since the measured electronic characteristics are dominated by the capacitance and resistance of the oxide layer, several key insights into the redox activity of the molecular layer, molecular energy levels, and charge injection mechanisms can be ascertained. First, understanding redox events within molecular layers in solid state junctions is critical to gauge the potential of using molecules as charge storage devices. Second, absorbance spectra allow insight into the electronic structure of a molecule attached to a conductive surface. Coupled with

ultraviolet photoemission spectroscopy (UPS), absorbance spectra can be used to understand charge transport mechanisms and provide experimental inputs for theoretical calculations. Finally, understanding charge injection into molecular layers is important for both the fields of molecular electronics and the vast field of organic electronics[26, 27].

As required for all spectroscopic experiments, the expected signal or signal change should be determined to ensure that the signal is larger than the limit of detection (LOD) of the technique. As an estimate, the absorbance change associated with a redox reaction is given by a modified Beer-Lambert equation:

$$\Delta A(\lambda) = \sum_{i=1}^{i=n} \varepsilon(\lambda)_i b \Delta C_i = \sum_{i=1}^{i=n} \varepsilon(\lambda)_i \Delta\Gamma_i \qquad \text{Eq. 5.1}$$

where $\varepsilon(\lambda)_i$ is the molar absorptivity at wavelength λ of species i, b is the path length, ΔC_i is the change in concentration, $\Delta\Gamma_i$ is the change in surface concentration, and n is the number of absorbing species . Assuming $\Gamma = 1x10^{-10}$ mol·cm^{-2} and $\varepsilon_{anion} = 1x10^4$ M^{-1}·cm^{-1} ($1x10^7$ cm^2·mol^{-1}), the absorbance change would be $1x10^{-3}$ for complete reduction of a monolayer to its anion, which is higher than the LOD for sensitive optical absorption spectrometers and is discussed in later sections. Although optical absorption is not necessarily linear with the number of chromophores in dense molecular layers, as is the case for dilute solutions, the above calculation gives a rough estimate that the expected absorbance change is indeed higher than the LOD.

5.1.3 Objectives for Spectroscopic Characterization of Molecular Junctions

In this chapter, an in-situ optical absorbance spectroscopy technique is developed and employed to investigate redox events in molecule/oxide junctions. The application of voltage pulses results in reversible absorbance changes that are consistent with changes in the oxidation state of the molecular layer. To our knowledge, these reported in-situ optical absorption spectra are the first reported for a 1-5 nm thick molecular layer in an active solid state molecular junction. These results provide evidence that the electronic state of a molecular layer can be dynamically changed, which is a significant milestone in confirming the molecular influence on our architecture of molecular junctions. Finally, we will discuss the correlation of these results to the single molecule conductance experiments in Chapter 4.

5.2 EXPERIMENTAL

5.2.1 Fabrication of Transparent Molecular Junctions

Transparent electrodes were fabricated on optically transparent fused silica (Q) microscope slides (G.E. 124, Technical Products) allowing the junction absorbance to be monitored in transmission mode. Analysis of absorbance spectra in transmission mode is conceptually more straightforward compared to absorbance spectra acquired in reflection mode. To remove organic contaminants from the fused silica surface, the slides were cleaned in a H_2O_2:H_2SO_4 (piranha) solution for 30 minutes. The transparent bottom contacts consisted of three layers: the Cr layer was used to improve adhesion of the contacts to the fused silica substrates, the Pt layer was employed because it lowered the

resistivity of the contacts, and the amorphous C layer was used to provide a similar electro-active layer compared to the pyrolyzed photoresist films (PPF) described in previous chapters. Au was initially used as the metallic layer in both the bottom and top contacts but Au surface plasmons resulted in bias induced absorbance changes between 300 – 800 nm. To solve this problem, Pt was used for the contacts since it did not have surface plasmons in the spectral region investigated. The transparent contacts were deposited on the fused silica slides (Q) through the successive electron beam evaporation of 2.0 nm Cr, 5.0 nm Pt, and 5.0 nm C (from graphite source) at a deposition pressure < 5.0×10^{-6} torr with a deposition rate of 0.3 $A \cdot sec^{-1}$ for all three layers. The evaporated carbon layer consisted of amorphous, mostly sp^2 hybridized carbon[28]. The final surface roughness of the deposited transparent contacts was measured with atomic force microscopy (AFM) in tapping mode. A Perkin Elmer Lambda 900 UV-Vis-NIR spectrometer was used to record the absorbance of the transparent contacts relative to a reference fused silica slide. Fabricated contacts were stored in a 100 mtorr vacuum chamber with calcium sulfate (DrieriteT) as a desiccant until attachment of the molecular layer and molecular attachment occurred within 7 days after deposition.

Molecular monolayers and multilayers were attached to the transparent contacts through the electrochemical reduction of a corresponding diazonium salt for aromatic molecular layers and electrochemical oxidation of primary amines for aliphatic monolayers. The electro-active C surface of the bottom contacts has been reported to have similar electrochemical properties to PPF and glassy carbon. For 4-nitroazobenzene (NAB), 9,10-anthraquinone (AQ) and fluorene (FL) junctions, molecular layers were

attached through the electrochemical reduction of a 1.0 mM solution of the corresponding diazonium salt in acetonitrile (MeCN) containing 0.1 M n-tetrabutylammonium tetrafluoroborate ($TBABF_4$), as described previously[29, 30]. N-decylamine ($C_{10}N$) molecular layers were attached through electrochemical oxidation of 5 mM n-decylamine in MeCN containing 0.1 M $TBABF_4$ at 1.4 V versus Ag/Ag^+ for 10 minutes[31, 32]. Solutions were thoroughly degassed with Ar before modification and blanketed with Ar during modification. Modified substrates were sonicated in MeCN for 5 minutes to remove physisorbed molecules. Molecular layer thicknesses were measured using a "scratching" technique with AFM, as described previously[33].

Molecular junctions were fabricated from the transparent contacts with an attached molecular layer through electron beam evaporation of an oxide/metal top contact. The top oxide/metal contacts were evaporated on molecular layers through a shadow mask resulting in a cross-bar junction with an active area of 0.16 cm^2. The 10 nm oxide layers were evaporated from a SiO_2 or Al_2O_3 source with an O_2 backpressure of 2×10^{-5} torr. Without breaking the chamber vacuum, Pt was evaporated on top of the oxide layer with a deposition pressure $< 8 \times 10^{-6}$ torr. Molecular damage or metal penetration during the Pt evaporation was prevented by the oxide layer on the molecular layer. For all layers, the deposition rate was 0.3 $A \cdot sec^{-1}$. Fabricated molecular junctions are labeled as "molecule/oxide", with both the substrate/contact and top contact omitted. For example, "NAB/SiO_2" refers to a Q/Cr/Pt/C/NAB/SiO_2/Pt junction. The voltage convention used for all subsequent experiments is the transparent Pt/C electrode relative

to the Pt electrode. A schematic of a molecular junction and an optical image of a NAB/SiO2 junction are shown in Figure 5.1.

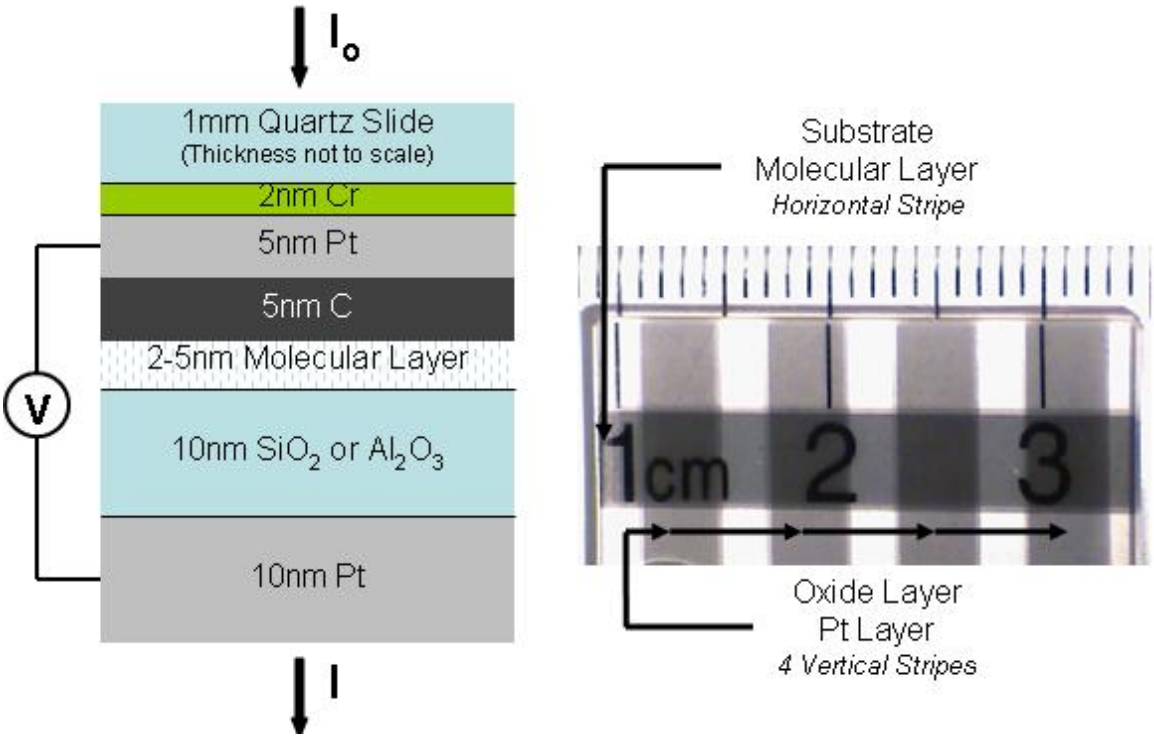

Figure 5.1: Schematic of transparent molecule/oxide junction and image of a NAB/SiO_2 junction. For in-situ absorbance measurements, spectra were acquired after applied voltage pulses between the bottom and top contacts. For the optical image, the junction was placed on top of a scale bar showing both the transparency and scale of the fabricated junction.

5.2.2 Electrochemical Characterization of Molecular Layers in Solution

Solution voltammetry was performed with a BAS/Epsilon potentiostat, Ag/Ag^+ nonaqueous reference electrode, and a platinum counter electrode. The working electrode was a stationary 2 mm^2 Au electrode (BAS, MF-2014) modified by evaporating 5.0 nm of Pt and C on the Au electrode to replicate the transparent substrate. To

minimize effects caused by dissolved oxygen and water in the MeCN solution, the electrochemistry was performed in a dry nitrogen environment. The MeCN solvent was dried, nitrogen purged, and transferred via a Schlenk line into a nitrogen glove box. Voltammetry of free NAB and AQ was performed with 1.0 mM solutions in MeCN containing 1.0 M $TBABF_4$. Voltammetry was performed using NAB, AQ, FL, and $C_{10}N$ modified electrodes as the working electrodes in MeCH containing 1.0 M $TBABF_4$. Electrochemical quasireversible redox events were only observed in the NAB and AQ molecular layers between ± 2 V vs Ag/Ag^+.

5.2.3 Bias Induced Absorbance Measurements: Solid-State Molecular Junctions

Bias induced absorbance spectra of the molecular junctions were measured in the absence of a liquid electrolyte in ambient lab conditions. After mounting a junction in a CCD based spectrometer (see below), a reference spectrum without an applied bias was collected. Response to an applied bias is stated as delta absorbance (ΔA) which is the change in absorbance relative to the reference spectrum. Since the junction absorbance was 2-3 orders of magnitude larger than the observed ΔA ($\sim 1x10^{-3}$), the reference spectrum was set to zero on the ΔA scale to permit the observation of small changes in absorption. With this convention, a positive ΔA identifies an increase and a negative ΔA identifies a decrease in absorbance relative to the reference spectrum.

A custom program in Labview 8.1 (National Instruments) was used to apply voltage pulses to the junctions with the pulse sequence: V=0 for 30 sec; $V=V_{neg}$ for 100 msec; V=0 for 30 sec; $V=V_{pos}$ for 100 msec; V=0 for 30 sec where V_{neg} (V_{pos}) is the magnitude of the negative (positive) voltage pulse. After each voltage pulse, ΔA was

measured while V=0 during a 30 sec period. After each pulse sequence, the capacitance of the junction was measured from a current-voltage curve and compared to the initial junction capacitance to determine if dielectric breakdown or other electronic changes occurred during the in-situ measurements.

In-situ optical absorbance spectra were acquired with a custom built optical absorbance spectrometer. A tungsten-halogen lamp (Sciencetech Inc.) with a very low ripple DC power supply was used as the light source, with quartz optics and apertures to transmit a 2.5 mm diameter light pattern through the cross-bar junctions as indicated in Figure 5.1. Care was taken to restrict the light beam to the active area of the junction. To electrically address the devices in the sample chamber, wires were attached with conducting silver epoxy. Quartz optics were used to match the transmitted light into an f/4 Czerny-Turner spectrograph (Andor, Shamrock SR-303-i-b) with a back-thinned CCD (Andor, Newton DU920N-BU).

Since the expected ΔA is in the $1x10^{-3}$ range, maximizing signal to noise ratio was crucial. The CCD was cooled to -60°C to minimize thermal noise and full vertical binned (FVB) to maximize the number of detected electrons. Since the CCD camera had a very low readout noise (three counts per FVB readout), binning speed was selected to maximize total counts. Readout and shutter speed limited the maximum number of counts to $3x10^{6}$ with a two second integration period at 600 nm. In the shot noise limited regime, the standard deviation of the absorbance is given by modification of an equation presented by Ingle and Crouch[34] in the case where the incident and transmitted intensities are nearly equal:

$$\sigma_A = \sqrt{2}(0.434)\left(\frac{\sqrt{counts}}{counts}\right). \qquad \text{Eq. 5.2}$$

Assigning the limit of detection (LOD) as three times the standard deviation, LOD is

$$LOD = 3\left[\sqrt{2}(0.434)\left(\frac{\sqrt{counts}}{counts}\right)\right] \qquad \text{Eq. 5.3}$$

Using the maximum number of counts measured for a two second integration period, the LOD is 1.1×10^{-3}. Increasing the integration time to 30 seconds causes the LOD to decrease to 2.8×10^{-4}. Superpixel integration was used to increase the LOD by effectively increasing the number of counts while keeping the resulting wavelength resolution (< 4 nm) to be a small fraction of the absorption bandwidth. Superpixel integration was critical in wavelength regions where the counts were below the maximum, which occurred in the blue region of the spectra. With the use of superpixel integration and relatively small dark signal and readout noise, the LOD was 2.0×10^{-4} at all reported wavelengths.

Gaussian '03 was used to perform time dependent density functional theory (TDDFT) to predict total energies, excitation transitions, and orbital energies[35]. Diffuse functions were added to the basis set to describe the Rydberg state correctly, which has been shown necessary for excited state TDDFT calculations[36]. FilmStar, a dielectric thin

film modeling program, was used to calculate the effect of index of refraction changes of the molecular layer on the absorbance spectra of the molecular junctions[37].

5.3 RESULTS

5.3.1 Characterization of Transparent Contacts and Molecular Layers

The resistivity and surface roughness of the Q/Cr/Pt/C substrate before and after the deposition of various substrate layers are listed in Table 5.1.

Layer	Surface Roughness (nm ± σ)	Resistivity (Ω-cm)
Q	1.16 ± 0.18	Insulator
Q/Cr/C	0.98 ± 0.12	1.4×10^{-2}
Q/Cr/Pt	1.08 ± 0.21	8.4×10^{-5}
Q/Cr/Pt/C	0.88 ± 0.10	1.7×10^{-4}

Table 5.1: AFM measured RMS surface roughness and collinear four point resistively measured electrical resistively of electron beam evaporated layers on fused silica (Q) slides.

The resistivity of the Q/Cr/C substrates was three orders of magnitude higher than the Q/Cr/Pt substrates and two orders of magnitude higher than the final transparent contacts of Q/Cr/Pt/C. These results show that using a 5.0 nm thick Pt layer between the Cr adhesion layer and the electro-active carbon layer results in a significant decrease in resistivity of the transparent contacts. Lower resistivity of the contacts is desirable as it reduces the voltage drop along the electrode. The incorporation of the thin 5.0 nm Pt layer resulted in only a minimal decrease in the overall optical transmission through the

layer. For a typical completed junction, the resistance attributable to the substrate and top contact was ~250Ω. As noted in Table 5.1, the roughness of the fused silica slide following deposition of Cr/Pt and Cr/Pt/C did not significantly change compared to the slide itself, implying that the deposited layers were uniform. We reported previously that electron beam deposited carbon was electrochemically similar to glassy carbon and PPF allowing modification of the Q/Cr/Pt/C substrates with diazonium reduction to proceed as expected[28]. Table 5.2 lists the thicknesses of the molecular layers formed on both Q/Cr/Pt/C and PPF substrates showing the resulting layer thicknesses were similar. For all molecules, the molecular layers on the transparent (Q/Cr/Pt/C) electrodes were thinner than on to PPF. Successful modification and high device yield reinforces the conclusion that the transparent junctions are structurally similar to the PPF junctions reported by the McCreery research group.

Molecule	**Q/Cr/Pt/C**	**PPF**
NAB	3.9 ± 0.7	4.5 ± 0.7
AQ	3.6 ± 0.8	3.9± 0.5
FL	1.5 ± 0.7	1.7 ± 0.4
C_{10}	1.4 ± 0.6	2.1 ± 0.5

Thickness (nm) ± σ

Table 5.2: Comparison of the molecular layer thickness on Q/Cr/Pt/C and PPF substrates measured by an AFM "scratching" technique.

Cyclic voltammograms of free and chemisorbed NAB and AQ in electrolytic solution are shown in Figure 5.2. For free NAB, two quasireversible waves centered at -1131 mV (ΔE_p = 81 mV) and -1463 mV (ΔE_p = 112 mV) were observed at 0.1 $V \cdot s^{-1}$. For

chemisorbed NAB, a quasireversible wave was centered at -1082 mV (ΔE_p = 78 mV) for 0.1 $V \cdot s^{-1}$. For free AQ, a quasireversible wave centered at -1220 mV (ΔE_p = 78 mV) was observed for 0.1 $V \cdot s^{-1}$. Chemisorbed AQ showed a quasireversible wave at 1249 mV (ΔE_p = 115 mV) for 0.1 $V \cdot s^{-1}$. Comparing chemisorbed NAB and AQ, the reduction peak for AQ was broadened compared to NAB. These results agree well with previous reports showing that reduction occurs within chemisorbed molecular layers in electrolyte solution[13].

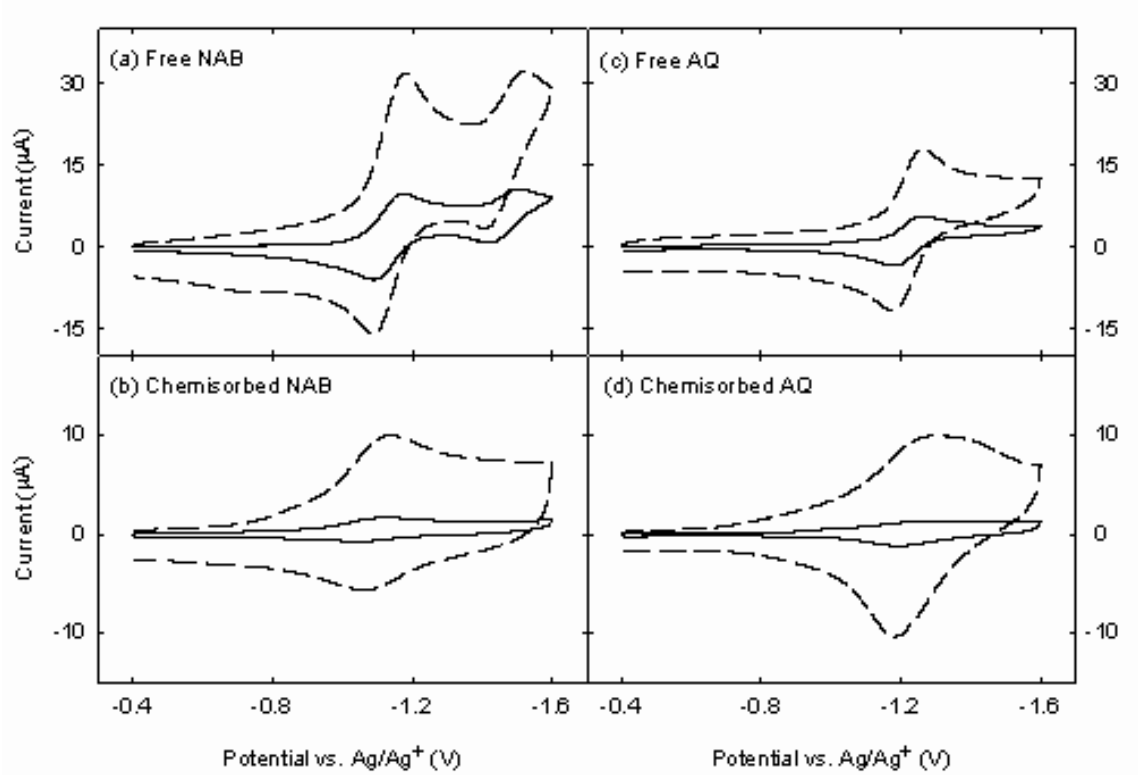

Figure 5.2: Cyclic voltammetry of free and chemisorbed molecules. Voltammetry occurred in MeCN containing 1.0 M $TBABF_4$ versus Ag/Ag^+ reference electrode. **a,** 1 mM free NAB. **b,** 3.9 nm thick chemisorbed NAB layer. **c,** 1 mM free AQ. **d,** 3.6 nm thick chemisorbed AQ layer. For the acquired voltammograms, the scan rates were 0.1 $V \cdot s^{-1}$ (solid) and 1.0 $V \cdot s^{-1}$ (dashed).

5.3.2 Current – Voltage Characterization of Molecule/Oxide Junctions

The measured current-voltage (I-V) curves for several molecular junctions are shown in Figures 5.3, 5.4, and 5.5. For all junctions, the measured I-V curves were dominated by the charging current associated with the capacitance of the metal oxide layer. For an I-V curve of a pure capacitor, the measured current is given by the equation:

$$I = C * \frac{dV}{dt} \qquad \text{Eq. 5.4}$$

where C is the junction capacitance and dV/dt is the scan rate. In Figure 5.3, the I-V curve for the C_{10}/SiO_2 junctions is consistent with a nearly ideal capacitor between ± 1 V. For the NAB/SiO_2, the I-V curve shows additional current, which could be caused by redox events in the molecular layer, voltage dependent capacitance of the molecular layer, or leakage current through the metal oxide layer. The same trend is observed in Figure 5.4 where the incorporation of a redox active AQ molecular layer leads to additional current compared to the redox inactive FL molecular layer. Although the exact nature of the additional current is not fully understood, all the I-V curves were dominated by the capacitance and resistance of the oxide layer. Figure 5.5 shows I-V responses of a NAB/SiO_2 junction before and after the in-situ absorbance measurements showing no observable degradation in the I-V response for 100 ms voltage pulses of ± 4 V. The pulse duration of 100 ms was selected to minimize the potential of breakdown of the molecular layer and oxide layer during the applied voltage pulses. Breakdown was commonly

observed for 1000 ms voltage pulses at ± 4 V. For all reported absorbance changes, the I-V curves of the junctions were measured before and after the measurements to ensure breakdown did not occur.

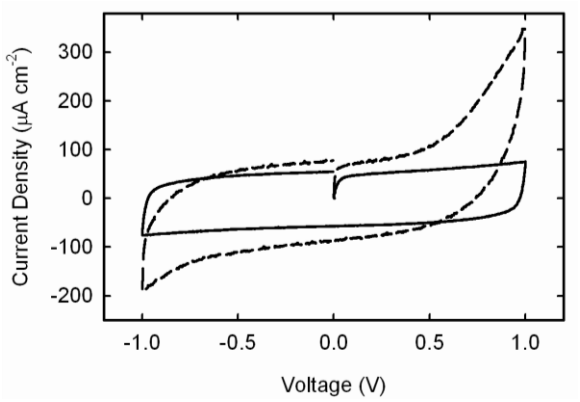

Figure 5.3: Current-voltage curve for $C_{10}N/SiO_2$ (solid) and NAB/SiO_2 (dashed) junctions. The junctions were fabricated on the transparent contact with an area of 0.16 cm^2. The I-V curve was acquired with a 100 $V \cdot s^{-1}$ scan rate.

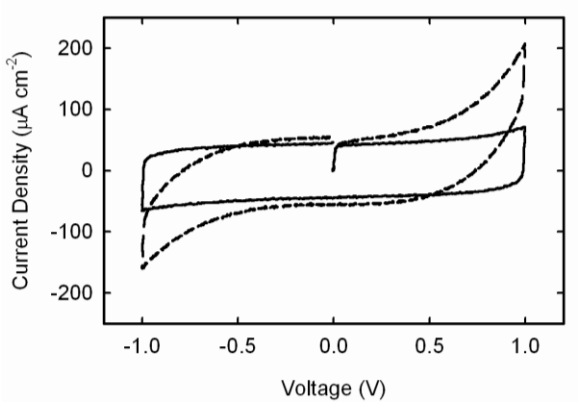

Figure 5.4: Current-voltage curve for FL/SiO_2 (solid) and AQ/SiO_2 (dashed). The junctions were fabricated on the transparent contact with an area of 0.16 cm^2. The I-V curve was acquired with a 100 $V \cdot s^{-1}$ scan rate.

.

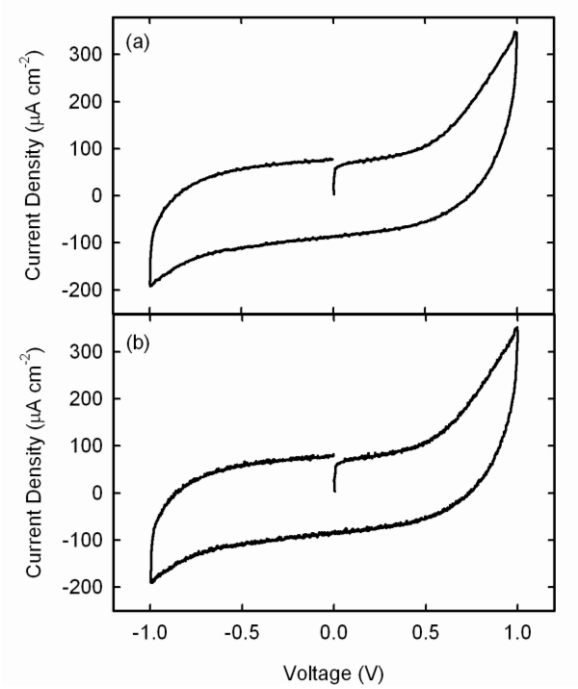

Figure 5.5: Current-voltage curve for a NAB/SiO_2 junction. **a,** I-V curve before in-situ absorbance measurements. **b,** I-V curve after four 100 ms voltage pulses of ± 4V showing that neither dielectric break down nor other electronic changes occurred during the in-situ absorbance measurements.

5.3.3 In-situ Absorbance Changes of Molecule/Oxide Junctions

Optical absorbance spectra of a transparent contact, NAB/SiO_2, and $C_{10}N/SiO_2$ junction are shown in Figure 5.6. The maximum absorbance of all final junctions was below 1 absorbance unit (10% transmission) over the 320 – 820 nm range. A molecular absorbance signature was not observed in Figure 5.3a because the absorbance of the molecular layer is expected to be 2-3 orders of magnitude smaller than the total absorbance of the junction. Absorbance of molecule/Al_2O_3 junctions had similar absorbance magnitudes and characteristics to the molecule/SiO_2 junctions.

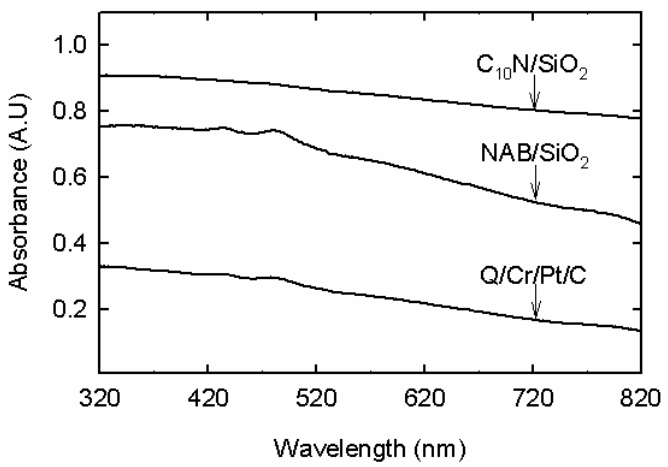

Figure 5.6: Absorbance of a transparent contact, NAB/SiO_2, and $C_{10}N/SiO_2$ junction. Spectra were acquired in transmission mode. For all fabricated junctions, the absorbance was below 1 A.U. allowing sufficient transmitted intensity for in-situ absorbance measurements.

Bias induced absorbance changes for a -4 V, 100 ms voltage pulse for NAB/SiO_2 and $C_{10}N/SiO_2$ junctions are shown in Figure 5.7a. For the $C_{10}N/SiO_2$ junctions, absorbance changes in response to the applied negative bias were below the LOD of the spectrometer. This results shows that bias induced absorbance changes of the transparent electrode, $C_{10}N$, and SiO_2 layers do not contribute to absorbance changes, and allows $C_{10}N$ and SiO_2 layers to be used as optically inert junction layers for subsequent experiments. For the NAB/SiO_2 junctions, an applied -4 V pulse caused an absorbance increase near 410 nm, a decrease in absorbance near 360 nm, and a broad negative ΔA in the 500-800 nm range. These absorbance changes are associated with absorbance and dielectric changes of the NAB molecular layer. The observed absorbance change of about 1 x 10^{-3} absorbance units is similar to the estimated absorbance change previously calculated. The magnitude of the absorbance change depended on the applied negative bias, where an increase in the bias resulted in an increase in the absorbance change as

shown in Figure 5.7b. For NAB/SiO_2 junctions, a threshold (minimum) voltage of 2.5 V was required to observe an absorbance change significantly above the LOD.

Bias induced absorbance changes after a -4V pulse for NAB/Al_2O_3 and $C_{10}N/Al_2O_3$ junctions are shown in Figure 5.7c. For the $C_{10}N/Al_2O_3$ junctions, only a minimal absorption change was observed between 340 – 520 nm. A decrease in absorbance was observed for wavelengths higher than 520 nm. Since the bias induced absorbance changes were not observed in $C_{10}N/SiO_2$ junctions, the absorbance changes were most likely caused by defect states within the Al_2O_3 layer. For NAB/Al_2O_3 junctions, similar absorbance changes to the NAB/SiO_2 junctions were observed between 320-620 nm and an additional absorbance decrease was observed for wavelengths above 620 nm. The additional decrease in absorbance above 620 nm is consistent with the absorbance changes observed in the $C_{10}N/Al_2O_3$ junctions, which suggests this absorbance change was associated with the Al_2O_3 layer.

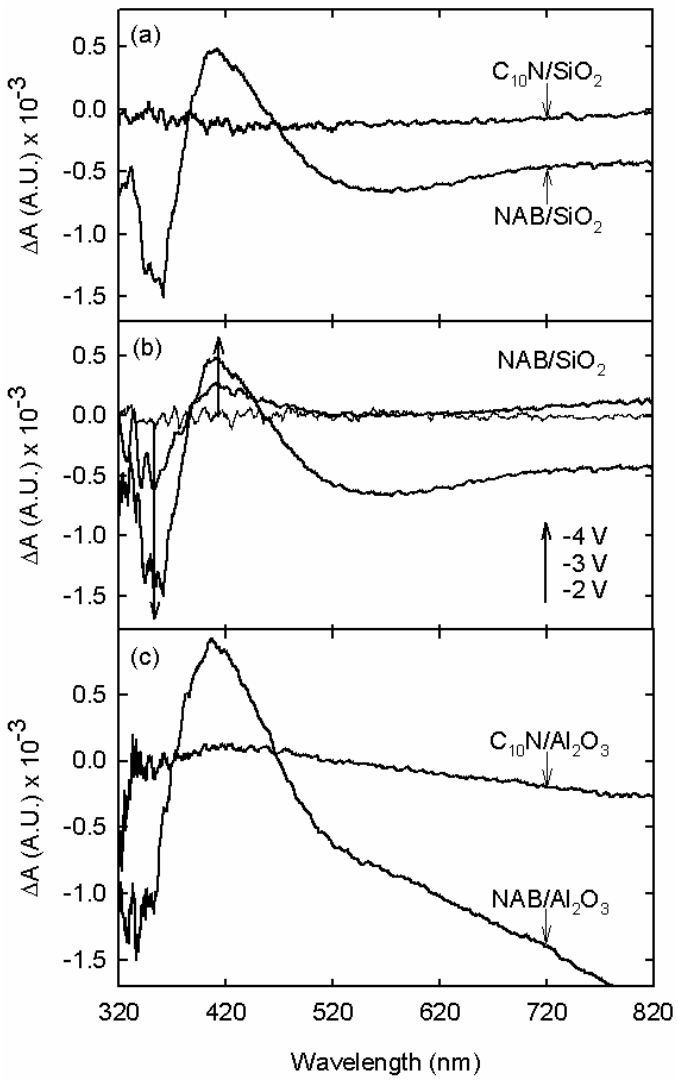

Figure 5.7: In-situ absorbance spectra of molecule junctions. **a,** ΔA for a $C_{10}N/SiO_2$ and NAB/SiO_2 junction after a -4 V pulse. **b,** ΔA for a NAB/SiO_2 junction after a -2 V, -3 V, and -4 V pulse. **c,** ΔA for $C_{10}N/Al_2O_3$ and NAB/Al_2O_3 junctions after a -4 V pulse.

Figure 5.8a shows bias induced absorbance changes for NAB/SiO_2 junctions after a -4 V pulse and subsequent +4 V pulse. For the +4 V pulse, the absorbance changes were almost a mirror image about zero ΔA compared to absorbance changes after a -4 V pulse. The absorbance decreased at 420 nm, increased at 360 nm, and increased between 500 – 800 nm. These absorbance changes can be cycled by changing the polarity of the

applied bias. The absorbance changes can be cycled for at least tens of pulse cycles without degradation of the junction's I-V response or magnitude of the absorbance changes. Higher cycle lifetimes were not studied in this investigation. These results show that the observed absorbance changes in the NAB layer are chemically reversible during the 100 ms voltage pulse. The absorbance changes were stable for at least tens of minutes after the voltage pulse, as shown in Figure 5.8b. The absorbance at 410 nm after a -4 V, 100 ms pulse is stable for tens of minutes with only about a 33% relaxation after 40 minutes.

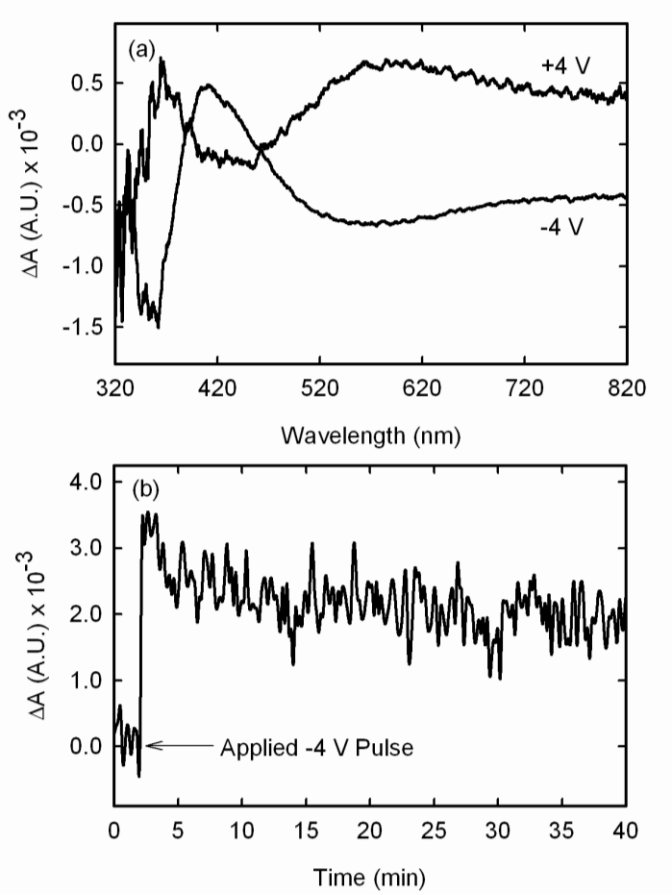

Figure 5.8: In-situ absorbance spectra of a NAB/SiO_2 junction. **a,** ΔA after -4V and subsequent +4V pulse. **b,** ΔA at 410 nm after the -4V pulse at open circuit.

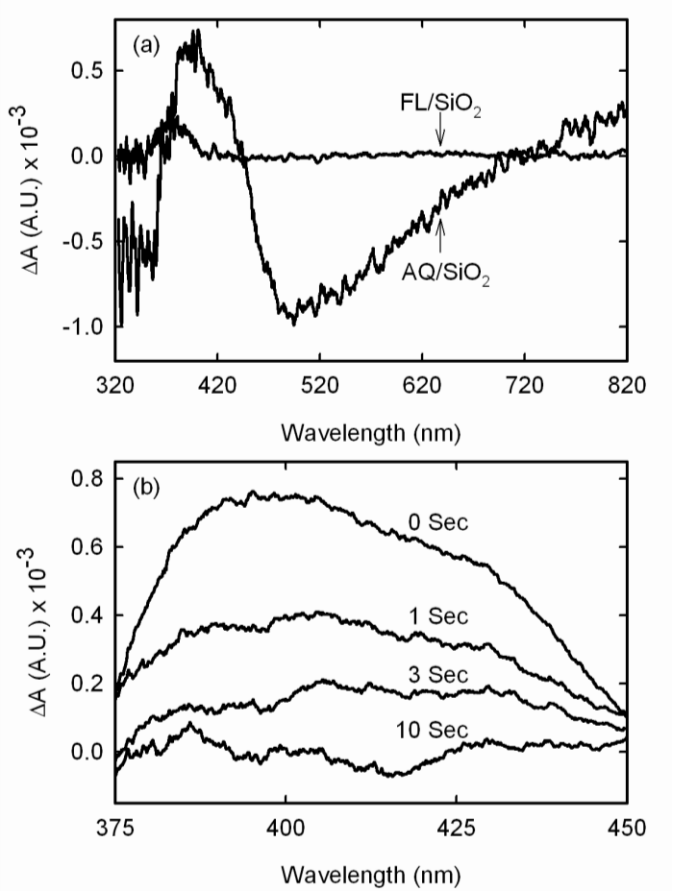

Figure 5.9: In-situ absorbance spectra of an AQ/SiO_2 and FL/SiO_2 junction. **a,** ΔA after an applied -4V pulse. **b,** ΔA for the AQ/SiO_2 junction after a -4V pulse.

Bias induced absorbance changes for AQ/SiO_2 and FL/SiO_2 after a -4 V pulse are shown in Figure 5.9a. Similar to $C_{10}N/SiO_2$ junctions, an absorbance change was not observed for FL/SiO_2 junctions within the applied voltage range of ± 4 V. For AQ/SiO_2 junctions, the absorbance was observed to increase at 395 nm, decrease between 320 – 350 nm, and decrease between 450 – 750 nm. The threshold voltage of -3.25 V was determined for the AQ/SiO_2 junctions, which is about 0.75 V more negative than that for the NAB/SiO_2 junctions. A significant difference between the observed NAB/SiO_2 and AQ/SiO_2 absorbance changes is the stability of the absorbance changes. The AQ/SiO_2

absorbance changes were stable for only a few seconds after the voltage pulse compared to tens of minutes for NAB/SiO_2. Figure 5.9b shows that the absorbance changes for an AQ/SiO_2 junction completely decay within 10 seconds after a -4V, 100 ms pulse. Since the RC time constant of the junctions and voltage pulse length were shorter than the spectrometer's integration time, the observed ΔA was not caused by electroreflectance changes during the voltage pulse.

5.3.4 Theoretical Calculation of Molecular Absorbance

Theoretically (TDDFT) calculated molecular energies, absorption wavelengths and experimentally reported absorption wavelengths for NAB, NAB radical anion, AQ, and AQ radical anion are listed in Tables 5.3 and 5.4. Although the calculated oscillator strengths could be used as an indication of the absorbance strength, correlation between these calculated values and experimental measurements is generally poor, especially for radical anions[38]. Considering the molecules are self-solvated, attached to a surface, and exposed to electric fields of several $MV \cdot cm^{-1}$, the calculated excitation energy should be used as a general indicator. An important conclusion is the calculated absorbance wavelength of the radical anion was red-shifted compared to the neutral species for both NAB and AQ. This conclusion is consistent with previously reported absorption values of NAB and AQ anions in electrolyte[39-41].

Molecule	Energy (E-h)	Calculated Wavelengths, Free Molecule [Oscillator Strength] (nm)	Experimental Wavelengths [Solvent] (nm)
NAB	-777.31	340.2 [0.05]; 343.6 [0.00]; 368.6 [0.83]; 511.3 [0.00]	330 [MeCN][32]
NAB Anion	-777.38	352.0 [0.08]; 408.8 [0.60]; 850.0 [0.32]	490 [MeCN][32]
AQ	-688.82	324.9 [0.12]; 340.5 [0.00]; 384.8 [0.00], 420.13 [0.00]	270, 320 [DMF][30,31]
AQ Anion	-688.87	363.1 [0.02]; 407.7 [0.00]; 568.0 [0.18]	274, 390, 410, 556 [DMF][30,31]

Table 5.3: Calculated gas phase total energy, selected excitation wavelengths, and experimentally measured excitation wavelengths (solution) of NAB, NAB anion, AQ, and AQ anion.

Molecule	Calculated Wavelengths, Free Molecule (nm) [Oscillator Strength]
NAB	218.7 [0.00]; 222.3 [0.08]; 226.2 [0.00]; 227.2 [0.00]; 231.0 [0.08]; 236.1 [0.00]; 242.3 [0.01]; 246.4 [0.00]; 249.5 [0.00]; 254.3 [0.02]; 258.8 [0.00]; 269.7 [0.02]; 290.6 [0.08]; 299.7 [0.00]; 318.9 [0.00]; 319.3 [0.02]; 340.2 [0.05]; 343.6 [0.00]; 368.6 [0.83]; 511.3 [0.00]
NAB Anion	325.7 [0.00]; 330.7 [0.00]; 331.1 [0.00]; 332.7 [0.00]; 342.9 [0.00]; 348.1 [0.02]; 352.0 [0.08]; 353.0 [0.00]; 384.8 [0.00]; 388.0 [0.00]; 408.8 [0.60]; 422.1 [0.00]; 431.9 [0.00]; 435.7 [0.00]; 437.1 [0.00]; 518.4 [0.00]; 550.3 [0.01]; 576.1 [0.01]; 607.2 [0.00]; 851.0 [0.32]
AQ	203.7 [0.00]; 204.4 [0.00]; 210.0 [0.44]; 212.4 [0.00]; 213.5 [0.00]; 216.5 [0.00]; 217.2 [0.00]; 228.0 [0.00]; 236.3 [0.00]; 239.9 [0.00]; 246.6 [0.49]; 246.8 [0.01]; 261.9 [0.00]; 277.3 [0.18]; 279.3 [0.00]; 324.2 [0.00]; 324.9 [0.12]; 340.5 [0.00]; 384.8 [0.00]; 420.1 [0.00]
AQ Anion	311.6 [0.00]; 314.9 [0.00]; 334.9 [0.00]; 336.1 [0.00]; 338.4 [0.00]; 345.1 [0.00]; 345.4 [0.00]; 348.6 [0.00]; 356.2 [0.00]; 363.1 [0.03]; 407.7 [0.00]; 416.2 [0.00]; 438.8 [0.00]; 448.0 [0.06]; 451.6 [0.00]; 541.3 [0.00]; 546.0 [0.00]; 557.0 [0.00]; 568.0 [0.00]; 1086.2 [0.01]

Table 5.4: Complete list of the calculated gas phase molecular excitation wavelengths for NAB, NAB anion, AQ, and AQ anion.

5.4 DISCUSSION

5.4.1 Redox reactions of Molecular Layers in Solution

Cyclic voltammetry was performed on the free molecules and the molecular layers in electrolyte solution to understand their potential redox activity in a solid state molecule/oxide junction. For the C_{10} and FL free molecules and attached molecular layers, reduction or oxidation peaks were not observed in a -3 to +3 V range, showing that redox events are not expected for $C_{10}N$ and FL molecular junctions. Since the LUMO and HOMO energies of the $C_{10}N$ and FL molecules are several eV from the Fermi energy of the C contact, redox activity is not expected for these free molecules or molecular layers. In contrast, NAB and AQ molecules chemisorbed on the transparent contact were shown to undergo electrochemical reduction, and the observed reduction potentials were similar to those of the free molecules in solution. For the NAB molecular layer, only one quasireversible wave was observed compared to two waves for free NAB within the same potential range. The lack of the second quasireversible wave is most likely caused by surface charging within the attached NAB layer. The widths of the reduction peaks are broadened for the NAB and AQ chemisorbed molecules compared to their respective free molecules. Peak broadening has been reported to be an indication that reduction in chemisorbed molecular layers is less stable than that of the free molecule[42-44]. Comparing the observed broadening of the NAB and AQ molecular layer, the increased broadening in the AQ reduction peaks indicates that chemisorbed AQ anions are less stable than chemisorbed NAB anions.

5.4.2 Molecular Redox reactions in Solid State Junctions

For molecular junctions that consisted of a $C_{10}N$ or FL molecular layer, bias induced absorption changes associated with the molecular layer were not observed, which is consistent with the solution electrochemistry results. The lack of redox events in the molecular layer shows that charge transfer into the molecular layer does not occur in $C_{10}N$/oxide or FL/oxide molecular junctions. Considering the large energy gap between the Fermi energy of the C contact (- 4.8 eV) and the molecular LUMO for $C_{10}NH_2$ (0.11 eV) and FL (-1.07 eV), efficient charge injection into the LUMO is not expected in the ±4 V range. Similarly, large charge transfer barriers exist between the contact Fermi energy and the molecular HOMO levels for $C_{10}NH_2$ and FL From these results, $C_{10}N$ and FL molecular layers in molecular junctions are expected to primary behave as tunneling barriers.

The lack of bias induced absorbance changes for $C_{10}N/SiO_2$ and FL/SiO_2 junctions allows several insights into using in-situ absorbance spectroscopy to monitor redox events in active molecular junctions. First, $C_{10}N$, FL, and SiO_2 layers can be used as "controls" that do not exhibit voltage dependent optical responses in the wavelength range investigated. Although the deposited SiO_2 layer was not crystalline, the high O_2 backpressure used during deposition has been shown to create near stochiometric films[45, 46]. Second, changes in optical transmission due to bias induced electroreflectance changes in the contacts were not observed, and therefore are smaller than the LOD. Third, the intensity of the custom built single-beam spectrometer is stable for the several

minutes required for spectrum acquisition, causing only minimal drift in the reference spectra during the voltage pulse cycles.

When the molecular layer in the junction consisted of NAB or AQ, bias induced absorbance changes were observed. For NAB/SiO_2 junctions, a negative voltage pulse resulted in an increase in absorbance at 410 nm which is consistent with injection of electrons into the LUMO resulting in the formation of NAB anions. The decrease in absorbance at 360 nm is consistent with the loss of the neutral NAB absorbance, as expected because the number of NAB molecules within the molecular layer is conserved. The presence of the SiO_2 layer prohibits direct conduction through the junction allowing the injected electron to cause electrochemical reduction. Comparing the absorbance of the neutral and reduced NAB molecules, the observed red-shift upon reduction agrees with the TDDFT calculations. After a positive voltage pulse, the absorbance changes were consistent with the oxidation of the NAB anions back to their neutral state. Interestingly, after the positive voltage pulse the neutral NAB absorbance is higher than the initial neutral NAB absorbance at 360 nm, and the NAB anion absorbance is less than the initial NAB anion absorbance at 410 nm. This observation is consistent with previous Raman spectrometry on similar devices, which implies that the initial NAB layer is partially reduced either during diazonium reduction or deposition of the oxide layer[47]. Comparable absorption changes were observed in NAB/Al_2O_3 junctions, indicating the absorbance changes at 360 nm and 410 nm were not caused by the SiO_2 or Al_2O_3 layers. Since ΔA can be cycled for at least 10's of cycles, the reduction and subsequent oxidation of the NAB layer appears chemically reversible. These results show that a molecular

layer in a solid state junction operating in a coulomb blockade region can undergo redox events. In addition, the observed absorbance changes can be correlated with the reduced and neutral NAB species.

For AQ/SiO_2 junctions, an applied negative voltage pulse results in absorbance changes that are consistent with the electrochemical reduction of the AQ molecular layer. The absorbance change at 420 nm is assigned to the AQ anion and the absorbance change between 320 – 350 nm is assigned to the neutral AQ. The observed absorbance changes were only stable for a few seconds after the voltage pulse, showing that a reduced AQ molecule rapidly undergoes oxidation back to its neutral redox state. This observation is confirmed by the lack of absorbance changes during a positive voltage pulse, as the AQ layer does not contain AQ anions to undergo oxidation. Compared to NAB/SiO_2 junctions, AQ/SiO_2 had a more negative ΔA threshold voltage, and is consistent with the cyclic voltammetric results showing reduction of chemisorbed AQ layers occurred at a more negative potential than the reduction of chemisorbed NAB layers.

For both NAB/SiO_2 and AQ/SiO_2 junctions, an absorbance decrease was observed between 500-800 nm after a negative voltage pulse. Since NAB, AQ, and their respective anions are not expected to absorb in this wavelength region, possible reasons for the absorbance changes include, although not limited to, the formation of energy levels caused by intermolecular interactions, formation of energy levels at the contact/molecule interface, or changes in the dielectric constant of the molecular layer upon reduction. As discussed in Chapter 4, theoretical calculations of the molecular energy levels for a NAB molecule attached to a multilayer graphene substrate do not

show the presence of molecular energy gaps with this spectral range. Besides a change in the molecular absorbance, a change in the dielectric constant of the molecular layer can cause absorbance changes. Using FilmStar software to determine the effect of molecular dielectric changes on the measured absorbance, a broad absorbance decrease would be expected between 600 – 1000 nm if the dielectric constant of the molecular layer increases. The apparent absorbance change is likely caused by increased transmission at the SiO_2/molecule interface because an increase in transmission is expected as the dielectric constants of the SiO_2 and molecule layers become similar. Since NAB and AQ anions have higher molecular polarizabilities compared to their neutral states, an increase in the dielectric constant of the molecular layer upon reduction is likely. Although these results are not conclusive, they do show that dielectric changes of the molecular layer could have caused the observed broad absorbance changes between 500 -800 nm.

5.4.3 Stability of Molecular Redox in Solid State Junctions

Although both NAB/SiO_2 and AQ/SiO_2 junctions showed evidence for solid state reduction, the persistence of the observed absorbance changes after an applied voltage pulse differed by at least two orders of magnitude. For NAB/SiO_2 junctions, bias induced absorbance changes were stable for at least tens of minutes compared to only several seconds for AQ/SiO_2 junctions. According to the TDDFT calculations and solution electrochemistry of the molecular layers, electrochemically formed NAB anions in an NAB layer are more stable than AQ anions in an AQ layer. The stability of an anion in the molecular layer is dependent on the surroundings; including surrounding dielectric medium, presence of charge stabilizing counter ions, or the charge stabilizing defects in

the oxide layer. Since the absorbance changes of the NAB/SiO_2 junctions show that the NAB is initially partially reduced, charge balancing ions or SiO_2 defects were most likely present in the junction. The stable absorbance changes were mostly caused by redistribution of counter-ions or the formation/annilation of defects in the SiO_2 layer. The NAB molecular layer has a NO_2 functional group located at the NAB/SiO_2 interface, which could increase the interaction between NAB and SiO2. For AQ/SiO_2 junctions, the bias induced absorbance changes show that the AQ layer was initially in its neutral redox state. In contrast to NAB, AQ does not have a terminal end group to interact with defects in the SiO_2 layer. Via one or more of the above mechanisms, the persistence of bias induced absorbance change was strongly dependent on the molecule comprising the molecular layer.

5.5 CONCLUSIONS AND FUTURE WORK

Overall, these results provide experimental evidence that molecular energy levels within a carbon/molecule/oxide/Pt junction can be dynamically changed by an applied bias. In-situ optical absorption spectroscopy was shown to be applicable for NAB and AQ molecular junctions. For example, AQ could not be analyzed with Raman spectroscopy because of its weak Raman scattering. As a diagnostic tool, optical absorption spectroscopy can be used in-situ to probe the molecular layer "buried" within a molecular junction. We anticipate that UV-Vis-NIR absorption spectroscopy in both static and transient modes will provide important insights into structural changes and electronic behavior of working molecular junctions under an applied bias. Additional

experiments are needed to more completely identify the following: stability of reduced molecular layers, charge injection mechanisms, and the effect of an applied bias on redox active oxide layers such as TiO_2. These results provide critical insight into the single molecule conductance measured and discussed in Chapter 4. For the NAB molecular layer, the optical absorbance was determined to be 320 nm (3.8 eV) for neutral NAB and 410 nm (3.0 eV) for the NAB anion. These results are critical in comparing the theoretically calculated energy levels of a NAB molecule attached to a carbon surface. Future work includes measuring the bias induced absorbance changes of mixed monolayers. Increasing the intermolecular distance between redox active molecules through dilution with redox inactive molecules or bulky side-groups should provide additional insight into intermolecular interactions. Also, determining the effect of counter ions on the observed absorbance changes would allow a more complete mechanistic view of redox events in solid-state molecular junctions.

4.6 REFERENCES

1. Chen, J.; Reed, M. A.; Rawlett, A. M.; Tour, J. M., Large on-off ratios and negative differential resistance in a molecular electronic device. *Science* **1999,** 286, (5444), 1550-1552.

2. Chen, F.; He, J.; Nuckolls, C.; Roberts, T.; Klare, J. E.; Lindsay, S., A molecular switch based on potential-induced changes of oxidation state. *Nano Lett.* **2005,** 5, (3), 503-506.

3. Kiehl, R. A.; Le, J. D.; Candra, P.; Hoye, R. C.; Hoye, T. R., Charge storage model for hysteretic negative-differential resistance in metal-molecule-metal junctions. *Appl. Phys. Lett.* **2006,** 88, (17).

4. Chen, J.; Wang, W.; Klemic, J.; Reed, M. A.; Axelrod, B. W.; Kaschak, D. M.; Rawlett, A. M.; Price, D. W.; Dirk, S. M.; Tour, J. M.; Grubisha, D. S.; Bennett, D. W., Molecular wires, switches, and memories. In *Molecular Electronics Ii*, New York Acad Sciences: New York, 2002; Vol. 960, pp 69-99.

5. Blum, A. S.; Kushmerick, J. G.; Long, D. P.; Patterson, C. H.; Yang, J. C.; Henderson, J. C.; Yao, Y. X.; Tour, J. M.; Shashidhar, R.; Ratna, B. R., Molecularly inherent voltage-controlled conductance switching. *Nat. Mater.* **2005,** 4, (2), 167-172.

6. Martin, A. S.; Sambles, J. R.; Ashwell, G. J., Molecular Rectifier. *Phys. Rev. Lett.* **1993,** 70, (2), 218-221.

7. Chabinyc, M. L.; Chen, X. X.; Holmlin, R. E.; Jacobs, H.; Skulason, H.; Frisbie, C. D.; Mujica, V.; Ratner, M. A.; Rampi, M. A.; Whitesides, G. M., Molecular rectification in a metal-insulator-metal junction based on self-assembled monolayers. *J. Am. Chem. Soc.* **2002,** 124, (39), 11730-11736.

8. Kalakodimi, R. P.; Nowak, A. M.; McCreery, R. L., Carbon/molecule/metal and carbon/molecule/metal oxide molecular electronic junctions. *Chem. Mat.* **2005,** 17, (20), 4939-4948.

9. Jang, S. S.; Jang, Y. H.; Kim, Y. H.; Goddard, W. A.; Flood, A. H.; Laursen, B. W.; Tseng, H. R.; Stoddart, J. F.; Jeppesen, J. O.; Choi, J. W.; Steuerman, D. W.; DeIonno, E.; Heath, J. R., Structures and properties of self-assembled monolayers of

bistable [2]rotaxanes on Au(111) surfaces from molecular dynamics simulations validated with experiment. *J. Am. Chem. Soc.* **2005,** 127, (5), 1563-1575.

10. Lortscher, E.; Ciszek, J. W.; Tour, J.; Riel, H., Reversible and controllable switching of a single-molecule junction. *Small* **2006,** 2, (8-9), 973-977.

11. Gale, R. J., *Spectroelectrochemistry, Theory and Practice* Plenum Press: New York, 1988.

12. Ruiz, V.; Colina, A.; Heras, M. A.; Lopez-Palacios, J., Potential regulation of the spectroelectrochemical response of monolayer-protected gold cluster films by electrolyte composition. *J. Phys. Chem. C* **2007,** 111, (11), 4277-4284.

13. Itoh, T.; McCreery, R. L., In situ Raman spectroelectrochemistry of electron transfer between glassy carbon and a chemisorbed nitroazobenzene monolayer. *J. Am. Chem. Soc.* **2002,** 124, (36), 10894-10902.

14. Nowak, A. M.; McCreery, R. L., In situ Raman spectroscopy of bias-induced structural changes in nitroazobenzene molecular electronic junctions. *J. Am. Chem. Soc.* **2004,** 126, (50), 16621-16631.

15. de Boer, B.; Meng, H.; Perepichka, D. F.; Zheng, J.; Frank, M. M.; Chabal, Y. J.; Bao, Z. N., Synthesis and characterization of conjugated mono- and dithiol oligomers and characterization of their self-assembled monolayers. *Langmuir* **2003,** 19, (10), 4272-4284.

16. Richter, C. A.; Hacker, C. A.; Richter, L. J., Electrical and spectroscopic characterization of metal/monolayer/Si devices. *J. Phys. Chem. B* **2005,** 109, (46), 21836-21841.

17. Richter, C. A.; Hacker, C. A.; Richter, L. J.; Kirillov, O. A.; Suehle, J. S.; Vogel, E. M., Interface characterization of molecular-monolayer/SiO2 based molecular junctions. *Solid-State Electron.* **2006,** 50, (6), 1088-1096.

18. Brown, T. M.; Kim, J. S.; Friend, R. H.; Cacialli, F.; Daik, R.; Feast, W. J., Built-in field electroabsorption spectroscopy of polymer light-emitting diodes incorporating a doped poly(3,4-ethylene dioxythiophene) hole injection layer. *Appl. Phys. Lett.* **1999,** 75, (12), 1679-1681.

19. Ziemelis, K. E.; Hussain, A. T.; Bradley, D. D. C.; Friend, R. H.; Ruhe, J.; Wegner, G., Optical Spectroscopy of Field-Induced Charge in Poly(3-Hexyl Thienylene) Metal-Insulator-Semiconductor Structures - Evidence for Polarons. *Phys. Rev. Lett.* **1991,** 66, (17), 2231-2234.

20. Stipe, B. C.; Rezaei, M. A.; Ho, W., Single-molecule vibrational spectroscopy and microscopy. *Science* **1998,** 280, (5370), 1732-1735.

21. Palmer, R. E.; Rous, P. J., Resances in electron-scattering by molecules on surfaces. *Rev. Mod. Phys.* **1992,** 64, (2), 383-440.

22. Gimzewski, J. K.; Joachim, C., Nanoscale science of single molecules using local probes. *Science* **1999,** 283, (5408), 1683-1688.

23. Lindsay, S. M.; Ratner, M. A., Molecular transport junctions: Clearing mists. *Adv. Mater.* **2007,** 19, (1), 23-31.

24. Solak, A. O.; Ranganathan, S.; Itoh, T.; McCreery, R. L., A mechanism for conductance switching in carbon-based molecular electronic junctions. *Electrochem. Solid State Lett.* **2002,** 5, (8), E43-E46.

25. McCreery, R. L.; Wu, J.; Kalakodimi, R. P., Electron transport and redox reactions in carbon-based molecular electronic junctions. *Phys. Chem. Chem. Phys.* **2006,** 8, (22), 2572-2590.

26. Facchetti, A.; Mushrush, M.; Yoon, M. H.; Hutchison, G. R.; Ratner, M. A.; Marks, T. J., Building blocks for n-type molecular and polymeric electronics. Perfluoroalkyl-versus alkyl-functionalized oligothiophenes (nT; n=2-6). Systematics of thin film microstructure, semiconductor performance, and modeling of majority charge injection in field-effect transistors. *J. Am. Chem. Soc.* **2004,** 126, (42), 13859-13874.

27. Asadi, K.; Gholamrezaie, F.; Smits, E. C. P.; Blom, P. W. M.; de Boer, B., Manipulation of charge carrier injection into organic field-effect transistors by self-assembled monolayers of alkanethiols. *J. Mater. Chem.* **2007,** 17, (19), 1947-1953.

28. Blackstock, J. J.; Rostami, A. A.; Nowak, A. M.; McCreery, R. L.; Freeman, M. R.; McDermott, M. T., Ultraflat carbon film electrodes prepared by electron beam evaporation. *Anal. Chem.* **2004,** 76, (9), 2544-2552.

29. Allongue, P.; Delamar, M.; Desbat, B.; Fagebaume, O.; Hitmi, R.; Pinson, J.; Saveant, J. M., Covalent modification of carbon surfaces by aryl radicals generated from the electrochemical reduction of diazonium salts. *J. Am. Chem. Soc.* **1997,** 119, (1), 201-207.

30. Brooksby, P. A.; Downard, A. J., Multilayer nitroazobenzene films covalently attached to carbon. An AFM and electrochemical study. *J. Phys. Chem. B* **2005,** 109, (18), 8791-8798.

31. Hoekstra, K. J.; Bein, T., Adsorption of zirconium-phosphonate multilayers onto phosphate-derivatized glassy carbon substrates. *Chem. Mat.* **1996,** 8, (8), 1865-1870.

32. Downard, A. J., Electrochemically assisted covalent modification of carbon electrodes. *Electroanal.* **2000,** 12, (14), 1085-1096.

33. Anariba, F.; DuVall, S. H.; McCreery, R. L., Mono- and multilayer formation by diazonium reduction on carbon surfaces monitored with atomic force microscopy "scratching". *Anal. Chem.* **2003,** 75, (15), 3837-3844.

34. Ingle JR., J. D.; Crouch, S. R., *Spectrochemical Analysis*. Prentice Hall: Englewood Cliffs, 1988.

35. Frisch, M. J. T., G. W.; Schlegel, H. B.; Scuseria, G. E.; Robb, M. A.; Cheeseman, J. R.; Montgomery, Jr., J. A.; Vreven, T.; Kudin, K. N.; Burant, J. C.; Millam, J. M.; Iyengar, S. S.; Tomasi, J.; Barone, V.; Mennucci, B.; Cossi, M.; Scalmani, G.; Rega, N.; Petersson, G. A.; Nakatsuji, H.; Hada, M.; Ehara, M.; Toyota, K.; Fukuda, R.; Hasegawa, J.; Ishida, M.; Nakajima, T.; Honda, Y.; Kitao, O.; Nakai, H.; Klene, M.; Li, X.; Knox, J. E.; Hratchian, H. P.; Cross, J. B.; Bakken, V.; Adamo, C.; Jaramillo, J.; Gomperts, R.; Stratmann, R. E.; Yazyev, O.; Austin, A. J.; Cammi, R.; Pomelli, C.; Ochterski, J. W.; Ayala, P. Y.; Morokuma, K.; Voth, G. A.; Salvador, P.; Dannenberg, J. J.; Zakrzewski, V. G.; Dapprich, S.; Daniels, A. D.; Strain, M. C.; Farkas, O.; Malick, D. K.; Rabuck, A. D.; Raghavachari, K.; Foresman, J. B.; Ortiz, J. V.; Cui, Q.; Baboul, A. G.; Clifford, S.; Cioslowski, J.; Stefanov, B. B.; Liu, G.; Liashenko, A.; Piskorz, P.; Komaromi, I.; Martin, R. L.; Fox, D. J.; Keith, T.; Al-Laham, M. A.; Peng, C. Y.; Nanayakkara, A.; Challacombe, M.; Gill, P. M. W.; Johnson, B.; Chen, W.; Wong, M.

W.; Gonzalez, C.; and Pople, J. A. *Gaussian 03, Revision C.02*, Gaussian, Inc.: Wallingford CT, 2004.

36. Kwasniewski, S. P.; Deleuze, M. S.; Francois, J. P., Optical properties of trans-stilbene using semiempirical and time-dependent density functional theory: A comparative study. *Int. J. Quantum Chem.* **2000,** 80, (4-5), 672-680.

37. FTG Software Associates: Princeton, NJ, www.ftgsoftware.com.

38. DiLabio, G. A.; Litwinienko, G.; Lin, S. Q.; Pratt, D. A.; Ingold, K. U., Revised structure for the diphenylaminyl radical: The importance of theory in the assignment of electronic transitions in Ph2X center dot (X = CH, N) and PhY center dot (Y = CH2, NH, O). *J. Phys. Chem. A* **2002,** 106, (48), 11719-11725.

39. Pedersen, S. U.; Christensen, T. B.; Thomasen, T.; Daasbjerg, K., New methods for the accurate determination of extinction and diffusion coefficients of aromatic and heteroaromatic radical anions in N,N-dimethylformamide. *J. Electroanal. Chem.* **1998,** 454, (1-2), 123-143.

40. Shamsipur, M.; Hemmateenejad, B.; Babaei, A.; Faraj-Sharabiani, L., Use of multivariate curve resolution analysis in the spectroelectrochemistry of 9,10-anthraquinone reduction in dimethylformamide solution. *J. Electroanal. Chem.* **2004,** 570, (2), 227-234.

41. Tian, H.; Bergren, A. J.; McCreery, R. L., UV-vis Spectroelectrochemistry of Chemisorbed Molecular Layers on Optically Transparent Carbon Electrodes. *Appl. Spectrosc.* **2007,** in press.

42. Bard, A. J.; Faulkner, L. R., *Electrochemical Methods Fundamentals and Applications*. 2nd ed.; John Wiley: New York, 2001.

43. Matsuda, H.; Aoki, K.; Tokuda, K., Theory of Electrode-Reactions of Redox Couples Confined to Electrode Surfaces at Monolayer Levels .1. Expression of the Current Potential Relationship for Simple Redox Reactions. *J. Electroanal. Chem.* **1987,** 217, (1), 1-13.

44. Matsuda, H.; Aoki, K.; Tokuda, K., Theory of Electrode-Reactions of Redox Couples Confined to Electrode Surfaces at Monolayer Levels .2. Cyclic Voltammetry and Ac Impedance Measurements. *J. Electroanal. Chem.* **1987,** 217, (1), 15-32.

45. Khodier, S. A.; Sidki, H. M., The effect of the deposition method on the optical properties of SiO2 thin films. *J. Mater. Sci.-Mater. Electron.* **2001,** 12, (2), 107-109.

46. Rao, K. N.; Shivlingappa, L.; Mohan, S., Studies on single layer CeO2 and SiO2 films deposited by rotating crucible electron beam evaporation. *Mater. Sci. Eng. B-Solid State Mater. Adv. Technol.* **2003,** 98, (1), 38-44.

47. Nowak, A. M.; McCreery, R. L., Characterization of carbon/nitroazobenzene/titanium molecular electronic junctions with photoelectron and Raman spectroscopy. *Anal. Chem.* **2004,** 76, (4), 1089-1097.

CHAPTER 6

IN-SITU ABSORBANCE SPECTROSCOPY OF POLYPYRROLE LAYERS IN POLYPYRROLE/OXIDE JUNCTIONS

6.1 INTRODUCTION

6.1.1 Motivation behind Spectroscopic Characterization

In this chapter, the in-situ absorbance spectroscopy technique described in Chapter 5 is used to monitor bias induced electrochemical redox events in "buried" conjugated polymer layers incorporated into polymer/oxide junctions. The fields of molecular electronics and conjugated polymers have similar electronic characteristics and terminology, which make distinguishing between the two fields difficult, especially for the case of conjugated oligomers. For both systems, charge transport depends on the electronic energy levels of the highest occupied molecular orbital (HOMO) for hole transport (p-type) or the lowest unoccupied molecular orbital (LUMO) for electron transport (n-type). The main distinction between the two systems is the relationship between the conjugation or delocalization length within the molecular or polymer layer and the overall charge transport length. The delocalization length depends on several factors including chemical bonding, Fermi energy of the electronic contacts, and the applied electric field. For conjugated polymer systems, the charge transport length (channel length or polymer thickness) is larger than the delocalization length (several monomeric units) allowing injected charge to reside in the polymer layer for sufficient time to cause redox events[1]. Upon a redox event, charge delocalization and structural reorganization around the redox site occurs, where the delocalized charge and the reorganized structures are classified as single entities called polarons[2, 3]. Charge transport is manifested through polaron migration in response to an electrical field. Polaron movement occurs through the movement or "hopping" of the polaron between

neighboring redox sites along the polymer backbone[4]. In contrast, charge transport through molecules is a special case where the conjugation length is shorter than or similar to the charge transport length (molecular length)[5, 6]. In metal/molecule/metal junctions, the charge carrier does not reside on molecules for sufficient time (less than a molecular vibration period) for redox events to occur[7]. With a delocalization length on the order of the charge transport length, quantum mechanical tunneling becomes the most efficient charge transport mechanism.

Conjugated polymers are a versatile class of organic materials that couple chemical structure with electronic properties applicable for a wide range of technological applications[8, 9]. One such system is polypyrrole (PPy), a conjugated polymer that has been employed in a variety of applications including nonvolatile memory, sensors, actuators, and fuel cells[10-17]. The chemical structure of PPy offers a rich electrochemical platform suitable for both polaron doping and proton exchange (acid/base) reactions on the tetrahedral-bonded nitrogen sites on each pyrrole unit. Polaron doping results in increased conductivity and formation of deprotonated imine species results in a lower conductance due to the lack of resonance stabilization of the polaron[11, 18, 19]. The conductivity of PPy depends strongly on doping and hybridization, with typically 8 orders of magnitude increase in conductivity observed upon polaron formation through a one-electron oxidation process. Understanding the dynamic concentration of the chemical species along the PPy backbone is critical to understanding the observed electronic behavior of PPy layers.

In the field of conjugated polymers, a growing pursuit is to exploit observed "resistance switching" phenomena for nonvolatile memory applications, where "resistance switching" indicates the polymer layer has at least two metastable states with different conductivity. Often referred to as "resistance random access memory" (RRAM), these solid state memory devices may be based on inorganic[20] or organic materials[21, 22], and often involve redox reactions. As discussed in the above references, the switching mechanism for a majority of the reported resistance switching devices is not well understood, due in most part to the difficulty to characterization of the thin and often "buried" active polymer layer. Partly for this reason, the only widely used form of RRAM is "flash" memory based on the floating gate Si MOSFET geometry, not based on conjugated polymer devices. Since this type of memory is relatively slow, requires higher voltages compared to most microelectronic devices, and has a limited cycle lifetime, there is a persistent demand for alternative RRAM devices structures[23]. Recently, McCreery et al. have reported two types of RRAM devices based on "dynamic doping", in which the bias induced conductance changes are attributed to the electrochemical modulation between the Ti oxidation state in the case of TiO_2[124-26] or the polaron concentration in polypyrrole layers[10]. In the case of PPy/TiO_2 devices, it was proposed that both layers are cooperatively "doped" during the same bias pulse, which may be reversed by an opposite polarity bias pulse for at least 10^3 cycles[10]. The resistance switching in a PPy/TiO_2 junction is shown in Figure 6.1 where the high conductance "on" state is an order of magnitude more conductive than the "off" state.

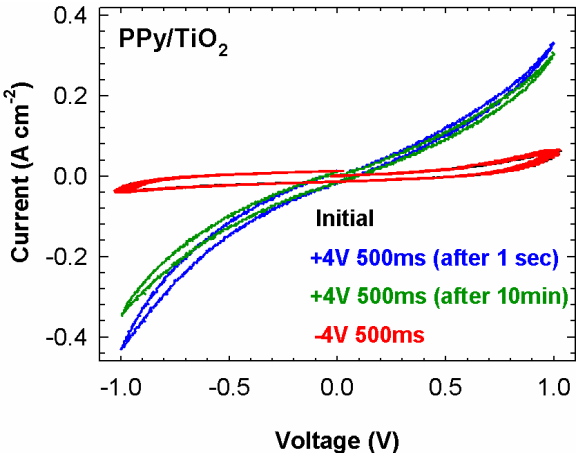

Figure 6.1: Memory cycle of a PPy/TiO_2 junction fabricated on a Pt/carbon contact. Initial low conductance state is switched to a high conductance state with a 100 ms, 4 V pulse. The high conductivity state is shown to be stable for 10 minutes. An applied 100 ms, negative 4 V pulse returns the junction to the low conductance state. For the stated voltages, the voltage convection is the Pt/carbon bottom contact versus the top Pt contact.

A related but more general issue relevant to both RRAM and organic thin film transistors (TFT) is the underlying mechanism behind the observed conductance changes. "Electrostatic" doping refers to a field-induced concentration change in charge carriers where the additional charge carriers are stabilized by an image charge on the gate oxide. Since this type of doping is only present during an applied gate bias, electrostatic doping is utilized for organic TFT operation. "Electrochemical" doping refers to a redox process that involves ion motion where the additional charge carriers are stabilized by a counter ion, and can remain stable after gate bias removal. Stability of electrochemically doping leads to persistent conductance changes suitable for RRAM applications. The relative importance of the two mechanisms is commonly difficult to determine despite their different consequences to the device composition and electronic characteristics[27-30]. In order to understand and control the characteristics of RRAM based on conducting

polymers this chapter discusses a detailed in-situ spectroscopic investigation of PPy/oxide devices, notably their responses to an applied bias and their dependence on device fabrication and operation conditions.

6.1.2 Spectroscopic Characterization Technique

In-situ absorbance spectroscopy is an attractive method to probe chemical states within PPy layers because the UV-Vis-NIR absorbance depends strongly on the oxidation state, conjugation, and chemical bonding along the PPy backbone[31-35]. Optical absorbance spectroscopy allows non-destructive analysis with sufficient time resolution to probe structural changes within functioning PPy devices. The well established field of spectroelectrochemistry has been previously used on PPy layers in an electrolyte, allowing complementary structural and electrochemical analysis[31, 36, 37]. Applying the fundamentals of spectroelectrochemistry to solid-state devices, Chapter 5 showed that in-situ optical absorbance spectroscopy can monitor the chemical structure of a 2-5 nm thick molecular layer incorporated in a solid-state junction. Considering the optical similarities between molecular layers and conjugated polymers, in-situ absorbance spectroscopy should be an excellent probe of "buried" polymer layers in active devices.

6.1.3 Objectives of Spectroscopic Characterization

In this chapter, in-situ optical absorbance is demonstrated as a probe to characterize the chemical structure of PPy layers in active electronic devices. Spectroelectrochemistry combined with multivariate curve resolution (MCR), X-ray photoelectron spectroscopy (XPS), and time dependent density functional theory (TD-DFT) were used to characterize the absorbance spectra of the electropolymerized PPy

layer, allowing the spectra of the chemical species along the PPy backbone to be identified. These absorbance spectra are used to investigate the chemical changes within PPy layers operating in nominal solid-state devices consisting of PPy/oxide junctions. Absorbance changes of the PPy/oxide junctions under an applied bias were correlated with changes in the PPy chemical structure and shown to be influenced by the surrounding environment and chemistry within the junction.

6.2 EXPERIMENTAL

6.2.1 Fabrication of Transparent Polypyrrole/Oxide Junctions

Optically transparent Pt/carbon contacts were fabricated with the same process techniques described in Chapter 5. The surface roughness and the resistivity of the contacts were confirmed to match the previously discussed results.

Polypyrrole (PPy) layers were polymerized on the Pt/carbon contacts through electrochemical oxidation in 0.1 M solution of pyrrole (Py) in acetonitrile (MeCN) containing 0.1 M tetrabutylammonium tetrafluoroborate ($TBABF_4$) as the supporting electrolyte. A constant applied oxidation current of 0.1 $mA \cdot cm^{-2}$ for 200 seconds resulted in ~20 nm thick PPy layers, as determined by a scratching technique with AFM and confirmed with spectroscopic ellipsometry[10, 38]. The potential versus deposition time is shown in Figure 6.2a. The oxidation potential reached a near stable value of about 0.5 V versus the Ag/Ag^+ reference electrode in about 20 seconds. For all fabricated PPy junctions, the PPy layers were electrochemically reduced at -1.0 V vs Ag/Ag^+ in MeCN containing 0.1 M $TBABF_4$ for 100 seconds, and the PPy layer was quickly removed from

the electrolytic solution after the reduction potential was removed. As shown in Figure 6.2b, the reduction current rapidly decreases to below 0.05 $mA \cdot cm^{-2}$ in 20 seconds followed by a gradual decrease to 0.01 $mA \cdot cm^{-2}$ in 100 seconds. This rapid decrease in cathodic current was caused by migration of BF_4^- out of the PPy layer. Redox inactive aliphatic monolayers were attached to the Pt/carbon contacts through the oxidation at 0.6 V vs Ag/Ag^+ for 300 s in a 5 mM solution of ocytlamine in MeCN containing 0.1 M $TBABF_4$[39, 40]. The thickness of the monolayer was measured to be 1.0 ± 0.2 nm, which confirms the presence of an octylamine monolayer. XPS spectra of the PPy layers on the Pt/carbon electrodes were acquired with a Kratos Axis spectrometer with a monochromatic Al K-alpha X-ray source and a residual press of 2 x 10^{-10} torr.

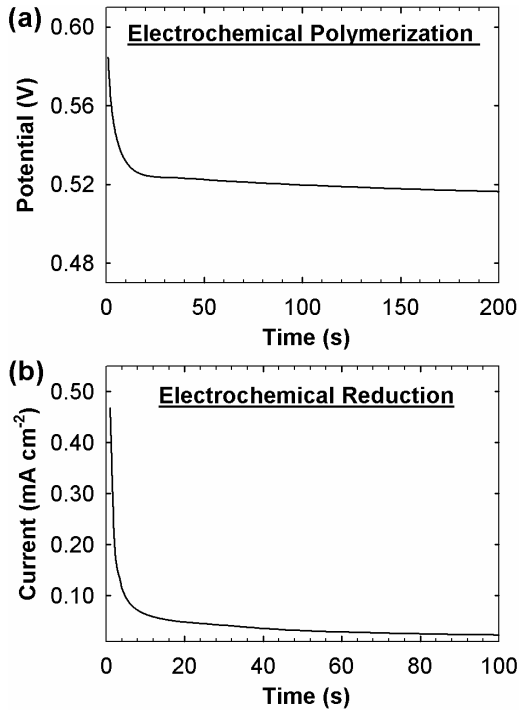

Figure 6.2: Electrochemical polymerization and reduction of a ~ 20 thick PPy layer. **a,** Measured potential versus Ag/Ag^+ reference electrode (0.44 V versus NHE) during the applied oxidation current of 0.1 $mA \cdot cm^{-2}$. **b,** Cathodic current during electrochemical reduction of the formed PPy layer at -1.0 V versus Ag/Ag^+.

The top oxide/metal contacts were evaporated on the PPy layers through a shadow mask resulting in a cross-bar junction with an active area of 0.16 cm^2. The 10 nm oxide layers were evaporated from an Al_2O_3 or TiO_2 source with an O_2 backpressure of 2 x 10^{-5} torr. Without breaking the chamber vacuum, Pt was evaporated on top of the oxide layer with a deposition pressure < 8 x10^{-6} torr. For all deposited layers, the deposition rate was 0.3 A·sec^{-1}. A schematic of a PPy/oxide junction is shown in Figure 6.3. For junctions that contained p-nitrophenol (NP), a 1% w/w solution in MeCN was spin coated at 2000 rpm on the PPy layer prior to the oxide/Pt contact deposition.

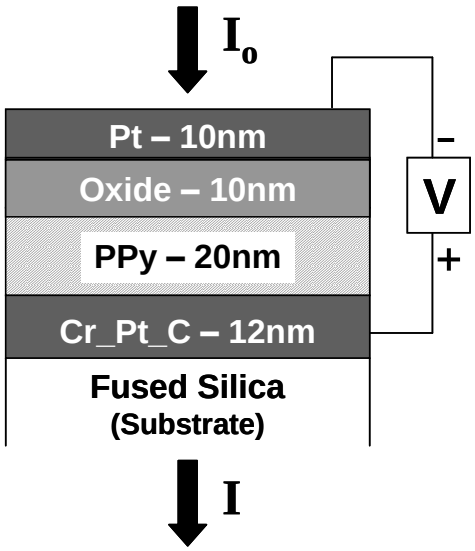

Figure 6.3: Schematic of a PPy/oxide junction during in-situ absorbance spectroscopy. Semi-transparent junction architecture allowed bias induced absorbance changes of PPy/oxide junctions to be monitored in transmission mode.

6.2.2 Spectroelectrochemistry and In-Situ Absorbance Measurements

Spectroelectrochemistry and in-situ absorbance spectra were acquired with a custom built optical absorbance spectrometer equipped with a tungsten-halogen lamp, as

described in Chapter 5. For the spectroelectrochemical experiments in solution, Pt/carbon contacts were placed in a quartz cuvette containing a reference electrode and Pt counter electrode. The cuvette assembly was positioned in the spectrometer and filled with the selected electrolytic solution, as shown in Figure 6.4. Spectra were acquired between 1.5 – 4.0 eV (300 – 850 nm) with a spectrum acquisition time of one second. For spectra collected during PPy polymerization, the measured absorbance is relative to the bare transparent Pt/C bottom contact immersed in the pyrrole solution. For spectroelectrochemistry on the PPy layers, the applied potential was stepped in 0.1 V increments from +0.5 to -0.5 V versus the open circuit potential (OCP) in MeCN containing 0.1 M $TBABF_4$ or H_2O containing 0.1 M NaOH. For the acquired spectra, the reported absorbance change (ΔA) is relative to the initial spectrum of the contact/PPy layers in the respective electrolyte at OCP.

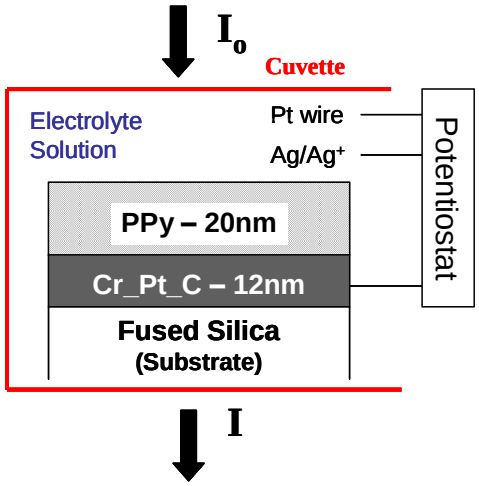

Figure 6.4: Schematic of the spectroscopic experiment during polymerization and electrochemical of PPy. A transparent Pt/carbon electrode allows absorbance spectra to be acquired in transmission mode. Electrochemical setup included a full three electrode cell where the electrochemical polymerization and applied potentials were controlled with a BAS potentiostat.

In-situ absorbance spectra of the PPy/oxide junctions were collected in the absence of an electrolyte. All junctions consisted of PPy layers that were electrochemically reduced prior to junction fabrication. Spectra were collected while bias was applied across the junctions, and after removal of the bias to measure the stability of the absorbance changes. The voltage was controlled by a custom program in Labview 8.2, with a 6111 data acquisition board (National Instruments)[41] connected to the junctions through Ag epoxy attached lead wires. For all spectra, the polarity is stated as the voltage of the Pt/carbon contact (adjacent to the PPy) relative to the Pt top contact, as shown in Figure 6.3. The reported absorbance changes are stated as delta absorbance (ΔA), where ΔA is the change relative to the reference spectrum of the PPy/oxide junction prior to an applied bias. With this convention, a positive ΔA identifies an absorbance increase and a negative ΔA identifies an absorbance decrease relative to the reference spectrum. The advantage of reporting ΔA is the ability to monitor small absorbance changes in the presence of the relatively large total junction absorbance.

All junctions were fabricated on Pt/carbon contacts with a Pt top contact. For brevity, junctions are referred to as "PPy/oxide", with the bottom and top contacts omitted. For example, "PPy/Al_2O_3" refers to a fused silica/Cr/Pt/C/PPy/Al_2O_3/Pt junction.

6.3 RESULTS

6.3.1 Characterization of Polypyrrole Layers

The results are discussed first for the polymerization and electrochemistry of the PPy layers in electrolye, followed by in-situ absorbance of PPy layers incorporated in solid-state PPy/oxide junctions. Figure 6.6 shows the N(1s) XPS peak of an electrochemically polymerized PPy layer on a Pt/carbon contact before and after electrochemical reduction. Analysis of the XPS N(1s) peak has been widely used to determine the nitrogen oxidation state along the PPy backbone[18, 42, 43]. For the as-formed and reduced PPy layers, the N(1s) peaks were deconvoluted into three components centered at 397.8 eV, 399.8 eV, and 402.1 eV, and the molar fractions are identified in Figure 6.6. The peak at 399.8 eV has been identified with the neutral amine-like nitrogen, the peak at 402.1 eV with the positively charged polaron, and the peak at 397.8 eV with the neutral imine-like nitrogen. Imine sites are formed through the deprotonation of an amine-like nitrogen site, where the tendency of deprotonation increases with over-oxidation of the PPy layer[42]. Since the oxidation potential of the polymer is lower than the oxidation potential of the single pyrrole mer unit, electrochemically polymerized PPy layers commonly include a significant fraction of imine species. The expected proton-coupled redox chemistry along the PPy backbone is shown in Figure 6.5.

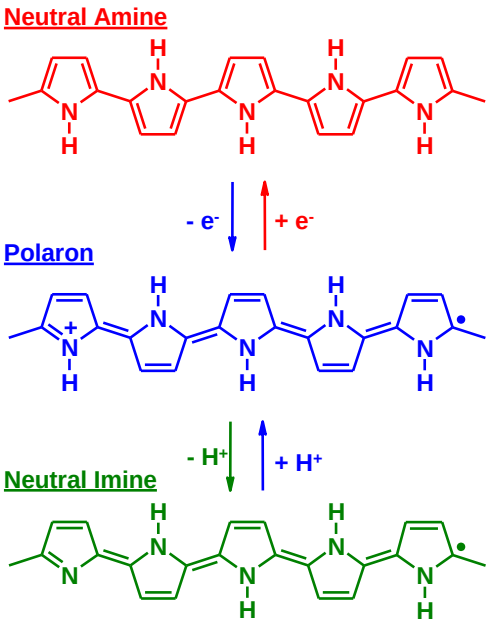

Figure 6.5: Proton-coupled redox chemistry along the PPy backbone[11].

The concentration of BF_4^- incorporated in the PPy layers was determined by the F(1s) XPS spectra, shown as insets in Figure 6.6. For the as grown PPy layer, the F / N ratio was 0.8 corresponding to one BF_4^- counter-ion for every five nitrogen sites along the PPy backbone. After electrochemical reduction, the lack of an observable F(1s) band shows that BF_4^- is removed from the PPy layer. With BF_4^- removed, the polaron concentration is reduced by 5% and the imine concentration increased slightly. In the absence of BF_4^- counter-ions, the remaining polaron concentration (10%) could have been stabilized by charge transfer with the Pt/carbon contact or the generation of counter-ions during PPy exposure to the ambient environment.

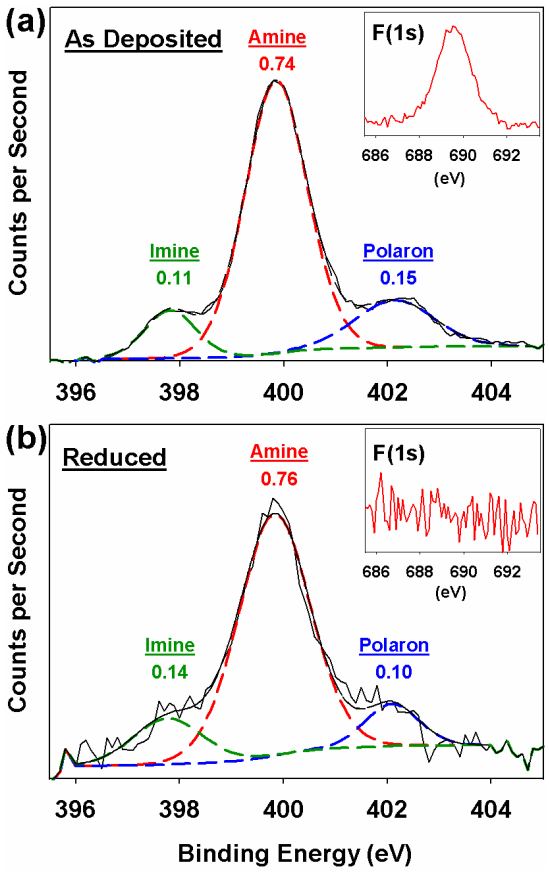

Figure 6.6: XPS N(1s) spectrum of polymerized PPy layer. **a,** PPy N(1s) spectrum before electrochemical reduction. **b,** PPy N(1s) spectrum after electrochemical reduction at 1 V vs. Ag/Ag^{+} for 100 s. Insets in both panels are the F(1s) spectra of the respective PPy layer.

Time dependent density functional theory (TDDFT) was used to optimize the structure and calculate the optical transitions of the neutral amine, neutral imine, and positively charged polaron on a pyrrole pentamer, with the results listed in Table 1. TDDFT was performed with Gaussian '03 using B3LYP/6-31^{+}G(d,p), with diffuse functions added to the basis set to correctly describe the Rydberg state[44, 45]. Modeling PPy with a pentamer allowed an estimation of the expected absorbance trends. Our limited computing capacity prohibited larger PPy units to be studied. For the imine

pentamer, a hydrogen atom was removed from the center nitrogen site on the pentamer. The neutral amine pentamer had the highest excitation energies and the polaron and imine excitations occurred at lower energies. This red-shift in excitation energy is expected as polaron and imine species transition from tetrahedral to a planar triangular structure, allowing increased conjugation and delocalization. As additional confirmation, experimentally measured absorbance spectra of polyaniline show the same trend for similar amine, polaron, and imine structures [46, 47].

Pentamer (charge)	**Calculated Excitation Energies**[a] eV (oscillator strength)
All Amines (0)	3.9 (0.01); 3.6 (0.00); 3.3 (0.01); 2.8 (1.20)
All Amines (+1)	3.6 (0.10); 3.1 (0.07); 2.4 (0.53); 2.3 (0.08)
Single Imine (0)	3.0 (0.40); 2.7 (0.97); 1.9 (0.04); 1.8 (0.02)

[a] top five excitations based on oscillator strength

Table 6.1: TDDFT calculated excitation energies and their oscillator strength. Excitation (absorption) energies for a pentamer containing all amines, a single polaron, or a single imine.

Absorbance spectra were acquired during the electrochemical polymerization of a PPy layer on a transparent contact, as shown in Figure 6.7a. The increase in absorbance is nearly linear with the deposition time indicating a constant polymerization rate and the consistency of the spectra implies that the distribution of PPy species does not significantly change as the thickness of the PPy increases. After electrochemical polymerization ($t > 200s$), the PPy layer was disconnected from the potentiostat and the absorbance spectra were recorded, as shown in Figure 6.7b. Large absorbance changes were observed within 100 seconds after polymerization, and the presence of an

absorbance increase between 3.0-3.6 eV verifies that the absorbance changes cannot be due simply to the loss of PPy at the Pt/carbon surface. Considering polymerization occurred at about 500 mV vs Ag/Ag^{+}, electronic and structural reorganization would be expected as the PPy layer equilibrates within the pyrrole solution. The BF_4^- counter-ion is expected to be at least partially mobile during the observed equilibration, permitting charge balance between the various PPy species.

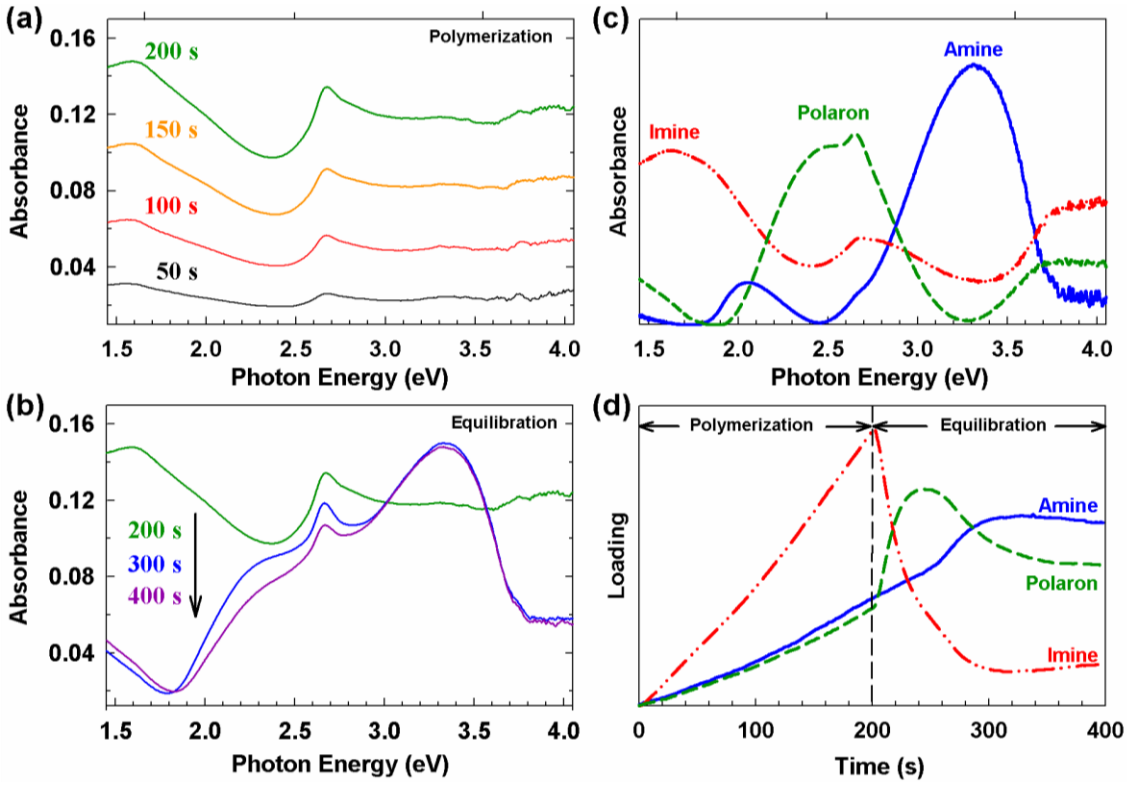

Figure 6.7: In-situ absorbance during polymerization and equilibration of PPy. **a,** Absorbance spectra during electrochemical polymerization of a PPy layer on a Pt/carbon contact. **b,** Absorbance spectra during equilibration of the formed PPy layer after polymerization. **c,** MCR calculated spectra of three components in the PPy layer. Spectra assigned with XPS, theoretical calculations, and spectroelectrochemistry analysis. **d,** MCR calculated loading of the three components during polymerization and equilibration.

Multivariate curve resolution (MCR) analysis using "PLS tool box" from Eigenvector Research was performed on the spectra in Figure 6.7a-b to determine the principal absorbing species and their distributions. For the MCR analysis, 200 spectra obtained during polymerization and 200 spectra obtained during equilibration comprised the input data set. No preprocessing of the raw spectra was performed and no initial absorbance spectra guesses were used. Two physical boundary conditions were imposed on the analysis: each principle component cannot have a negative absorbance value at any absorption energy and the contribution of each principle component cannot be a negative value at any time. The three principle components shown in Figure 6.7c accounted for 98% of the variation in the raw spectra. Combining XPS, TDDFT, and previous experimental reports[19, 35, 48], the neutral amine, neutral imine, and polaron were assigned to the MCR determined spectra, as shown in Figure 6.7c. The spectra loadings (relative species fractions) during polymerization and equilibration are shown in Figure 6.7d, which indicates formation of amine, polaron, and imine species during the electrochemical polymerization and then followed by significant species changes during equilibration at OCP. During the equilibration period, a sharp decrease in the imine concentration followed by an increase in the polaron concentration was observed between 200 and 250 seconds. Interestingly, after 250 seconds a decrease in the polaron concentration and an increase in neutral amine concentration were observed. These dynamics during the equilibration period give strong evidence that the polaron is the intermediate species between the amine and imine equilibrium.

Figure 6.8a shows the MCR analysis on the same 400 spectra in Figure 6.7a-b with four principle components. Four components accounted for 99.5% of the changes observed in Figure 6.7a-b. Compared to the three component MCR results, the absorbance spectra of the additional 4th component is similar to the assigned polaron spectra but red shifted about 0.1 eV. Considering the spectral similarity and the small red-shift, the 4th component spectra is assigned to a PPy bipolaron. Bipolarons are two polarons which are coupled based on spin pairing of the radicals resulting in a lower combined energy[3, 35, 49]. This assignment is consistent with previous experimental results and theoretical calculations on bipolaron formation as a red-shift in the bipolaron absorbance compared to the polaron has been observed[35, 50]. Figure 6.8b shows the spectra loading (relative concentrations) of the 4 components as a function of the polymerization and equilibration showing constant formation of the components during polymerization. During the equilibration period, complex concentrations changes of the four species are observed, and the final changes of the imine and amine concentrations are similar to the three component MCR results. Figure 6.8c shows the spectra loading where the polaron and bipolaron concentration are summed together showing a similar trend to the results in Figure 6.7d and gives evidence that the 4th component is related to a polaron-like species.

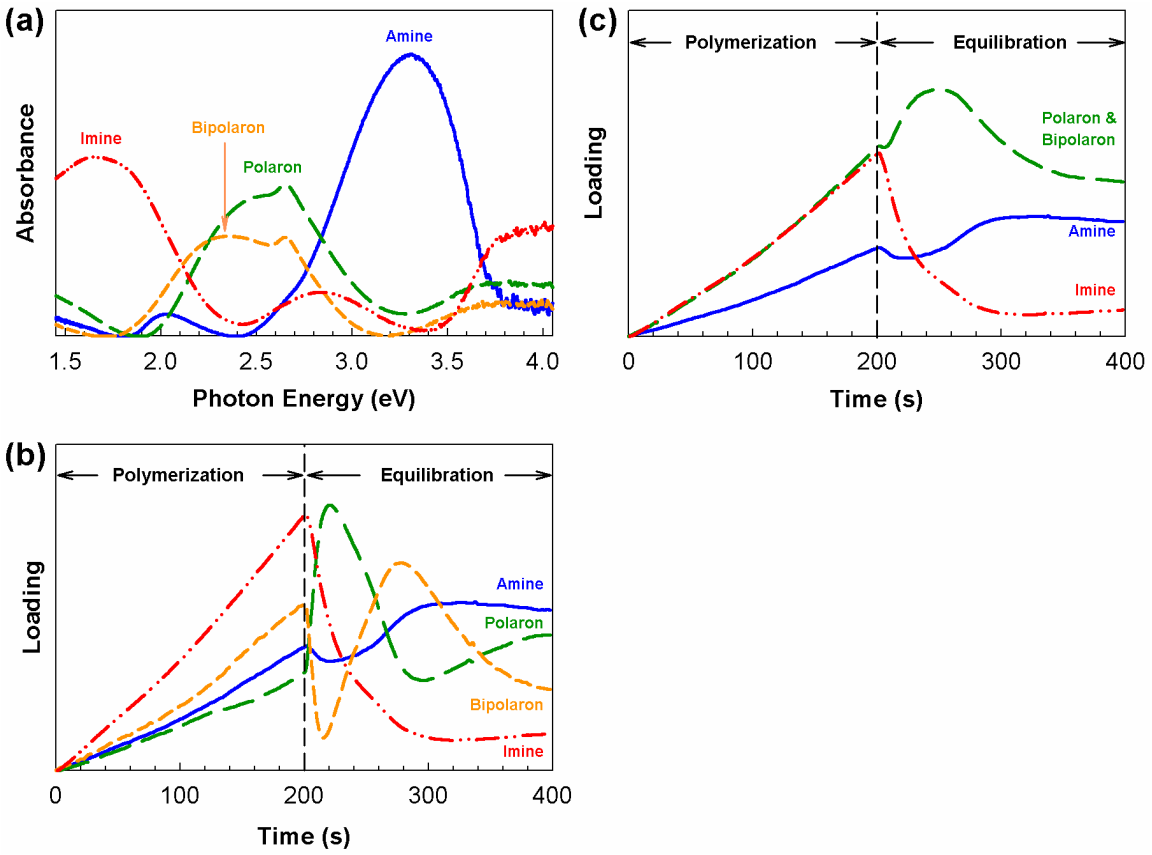

Figure 6.8: Four component MCR analysis on the spectra obtained in Figure 6.7a-b**. a,** MCR determined 4 principle components which account for 99.5% of the absorbance changes observed in Figure 6.7a-b. **b,** Loading of the 4 principle components versus the experiment time. **c,** Loading of the 4 principle components where the polaron and bipolaron loadings were mathematically combined.

6.3.2 Current – Voltage Characterization of Polypyrrole/Oxide Junctions

The current-voltage (I-V) response for a PPy/Al_2O_3 junction is shown in Figure 6.9. The observed response is dominated by the junction capacitance associated with the Al_2O_3 layer. For an applied positive bias, charge is removed from the PPy layer resulting in the formation of positively charged polarons. During the applied bias, a formed polaron can be stabilized by the image charge on the Al_2O_3 layer (electrostatic) or through the presence of negatively charged counter ions (electrochemical). After the

applied bias, an electrostatic stabilized polaron will return to a neutral state within the time constant (RC) of the device, or convert to an electrochemical stabilized polaron by pairing with a counter ion. This conversion from electrostatic to electrochemical doping depends strongly on the concentration and mobility of counter ions in the junctions. For an applied negative bias, electrons are injected into the PPy layer causing reduction of a polaron to the neutral amine. Since the electronic characteristic of a PPy/Al_2O_3 junction is dominated by the capacitance of the Al_2O_3 layer, the I-V response of the junction is mostly invariant to changes in the conductivity of the PPy layer.

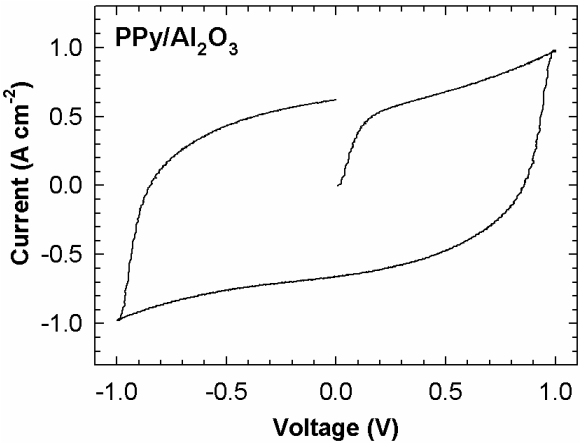

Figure 6.9: Current-voltage (I-V) response of a PPy/Al_2O_3 junction. The PPy layer was electrochemically reduced prior to evaporation of the top oxide/Pt contact. The scan rate of the I-V measurement was 1000 $V \cdot s^{-1}$. The I-V response is characteristic of a "leaky" capacitor.

6.3.3 Bias Induced Absorbance In Polypyrrole Layers in Solution

To estimate the concentration change of the polaron and imine species during electrochemistry of PPy layers in solution and during applied bias excursions on nominal solid-state PPy/oxide junctions, the species absorptivity was calculated from the XPS

analysis (Figure 6.6a), PPy absorbance spectra 400 seconds after the polymerization (Figure 6.7b, violet), and MCR determined absorbance spectra (Figure 6.7c). The procedure amounts to using the XPS results at the end of the equilibration period to determine the relationship between the absorbance and species concentrations, with the assumption that Beer's law applies. As calculated, $\left(\frac{\chi_{species}}{A.U.}\right)_{eV}$ is change in molar fraction of a species ($\chi_{species}$) producing one absorbance unit (A.U.) change at a particular absorption energy:

$$\left(\frac{\chi_{i\min e}}{A.U.}\right)_{eV} = \left(\frac{1}{A_{400s}}\right)_{Fig.6.7b} \times \left(\frac{A_{a\min e} + A_{polaron} + A_{i\min e}}{A_{i\min e}}\right)_{Fig.6.7c} \times \left(\chi_{i\min e}\right)_{Fig.6.6a} \qquad \text{Eq. 6.1}$$

$$\left(\frac{\chi_{polaron}}{A.U.}\right)_{eV} = \left(\frac{1}{A_{400s}}\right)_{Fig.6.7b} \times \left(\frac{A_{a\min e} + A_{polaron} + A_{i\min e}}{A_{polaron}}\right)_{Fig.6.7c} \times \left(\chi_{polaron}\right)_{Fig.6.6a} \qquad \text{Eq. 6.2}$$

where A_{400s} is the absorbance at 400 seconds in Fig. 6.7b, $A_{species}$ is the MCR species absorbance in Fig. 6.7c, and $\chi_{species}$ is the species concentration fraction calculated in Figure 6.6a. For the imine absorbance at 1.8 eV,

$$\left(\frac{\chi_{i\min e}}{A.U.}\right)_{1.8eV} = \left(\frac{1}{0.020}\right)_{Fig.6.7b} \times \left(\frac{0.00 + 0.00 + 0.85}{0.85}\right)_{Fig.6.7c} \times \left(0.11\right)_{Fig.6.6a} = 5.5$$

and for the polaron absorbance at 2.5 eV,

$$\left(\frac{\chi_{polaron}}{A.U.}\right)_{2.5eV} = \left(\frac{1}{0.085}\right)_{Fig.6.7b} \times \left(\frac{0.02+0.93+0.32}{0.93}\right)_{Fig.6.7c} \times (0.15)_{Fig.6.6a} = 2.4$$

To estimate the change in species fraction associated with an absorbance change, the observed absorbance change at 1.8 eV is multiplied by 5.5 for the imine and the absorbance change at 2.5 eV was multiplied by 2.4 for the polaron. At 2.5 eV, the PPy layer in MeCN/TBABF$_4$ had an absorbance change of ± 0.055 at ± 0.5 V versus OCP which is consistent with a polaron fraction change of ± 0.13 (i.e. ± 0.055 x 2.4). For the PPy layer in H_2O/NaOH, the absorbance change at 1.8 eV is associated with the imine absorbance. In this case, the observed absorbance changes depended on the polarity of the applied potential. For positive 0.5 V, the +0.014 absorbance change at 1.8 eV is consistent with an increase of 0.08 imine fraction. For negative 0.5 V, the absorbance change at 1.8 eV is consistent with a decrease of 0.22 imine fraction. Since the initial concentrations of the species are unknown, the concentration changes were reported as the average change during the positive and negative potentials. Estimation of the bias induced concentration change for the PPy layers in PPy/oxide junctions was performed with the same procedure outlined above.

Figure 6.10a shows the affect of an applied potential on the absorbance of PPy layers in an electrolyte absent of the pyrrole monomer. For positive potentials relative to the OCP, an increase in absorbance at 2.2-2.6 eV and a decrease in absorbance at 3.2-3.5 eV were observed. As reported by several groups, oxidation in MeCN results in the formation of polaron species, which is consistent with our assignments in Figure 6.7c as

generated polarons should increase the absorbance between 2.2-2.6 eV[11, 35]. Since the number of nitrogen sites along the PPy backbone is conserved, polaron formation decreases the neutral amine concentration resulting in the absorbance decrease between 3.2-3.5 eV. During an applied reducing potential, the absorbance decrease between 2.2-2.6 eV and increase between 3.2-3.5 eV are consistent with the reduction of the polarons to neutral amines. Increasing the oxidation or reduction potential caused an increase in absorbance changes. Using the XPS and MCR results to estimate the absorbance coefficient of the polaron, the absorbance changes correspond to a change of about ± 0.14 polaron fraction. The polaron fraction modulation of about ± 0.14 is consistent with the initial XPS value of 0.15, as the negative modulation cannot be larger than the initial polaron fraction. The absorbance changes indicate that the polaron fraction can be electrochemically modulated from ~ 0.0 to 0.3 with an applied potential between ± 0.5 V vs OCP.

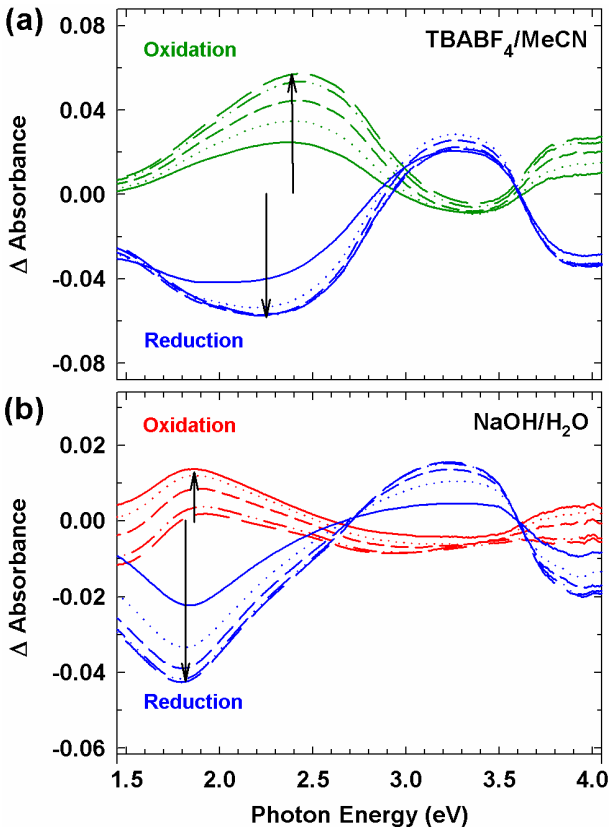

Figure 6.10: Spectroelectrochemistry of PPy layers between ± 500 mV vs. the open circuit potential in 100 mV intervals. **a,** Absorbance spectra in MeCN containing 0.1 M $TBABF_4$. **b,** Absorbance spectra in H_2O containing 0.1 M NaOH. Spectra are referenced to the initial PPy layer on a Pt/carbon contact in their respective electrolytic solution.

Figure 6.10b shows spectra from a similar experiment where the PPy layer was oxidized or reduced in H_2O containing 0.1 M NaOH. For an oxidizing potential, an absorbance increase was observed between 1.7 - 2.1 eV and a decrease between 3.2 - 3.5 eV, which is consistent with the formation of neutral imine species. In basic solution, it has been shown that an oxidizing potential leads to the formation of the imine species. Formation of imines is thought to occur through the deprotonation of a polaron intermediate[19, 51, 52]. The estimated imine fraction change is about ± 0.15, which shows that the imine fraction can be modulated between a fraction of 0.0 – 0.3. This result

indicates the importance of proton exchange along the PPy backbone in determining the equilibrium between polarons and imines during an oxidizing potential, with the redox process in MeCN corresponding to amine/polaron and that in basic solution to amine/imine equilibrium. For both MeCN and H_2O solutions, absorbance modulation could be cycled for at least tens of polarity cycles without significant spectral degradation, indicating a chemically reversible proton-coupled redox process. The observed absorbance changes are consistent with the MCR spectra and show that PPy layers can undergo redox and proton exchange in an electrolyte.

6.3.4 Bias Induced Absorbance Changes in Polypyrrole/Oxide Junctions

As described in the experimental section, PPy/oxide junctions were fabricated from electrochemically reduced PPy layers by evaporation of Al_2O_3/Pt or TiO_2/Pt as the top contacts. Figure 6.11a shows bias induced absorbance changes of solid state PPy/Al_2O_3 and PPy/TiO_2 junctions in ambient laboratory conditions. In contrast to the previous results, the junctions were not immersed in an electrolytic solution. For the PPy/Al_2O_3 junctions, a positive bias caused an increase in absorbance between 1.7 – 1.9 eV and a decrease in absorbance between 2.8 - 3.5 eV, consistent with the formation of neutral imines from neutral amines. With a negative bias, the absorbance changes were consistent with formation of neutral amines, showing the amine/imine equilibrium can be modulated by switching the polarity of the applied bias. The observed absorbance changes correlated to an imine fraction change of about ± 0.12 for ± 4 V bias. For all PPy/oxide junctions studied, the reported absorbance changes were stable after the applied bias was removed for at least 2 hours.

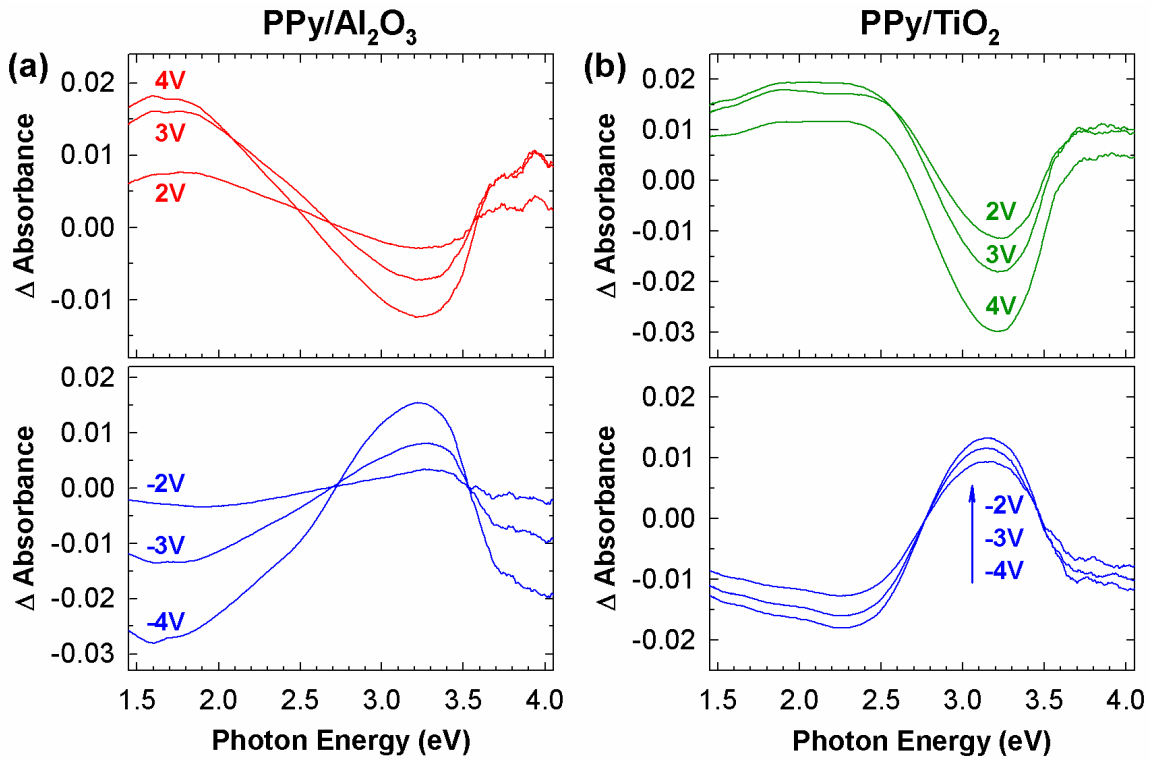

Figure 6.11: In-situ absorbance spectra of PPy junctions during an applied bias at ambient lab conditions. **a,** Absorbance spectra for PPy/Al_2O_3. **b,** Absorbance spectra for PPy/TiO_2. Absorbance changes are referenced to the initial absorbance of the PPy/oxide junctions.

Bias induced absorbance changes of PPy/TiO_2 junctions in ambient conditions are shown in Figure 6.11b. The shape of the ΔA spectra are different for the PPy/TiO_2 compared to PPy/Al_2O_3 junctions, with a larger change observed in the 2.5 eV region corresponding to the polaron. With a positive bias, a broad absorbance increase between 1.7 – 2.6 eV and an absorbance decrease between 3.0 -3.4 eV were observed, consistent with the formation of both polarons and imines from the neutral amine. These absorbance changes correspond to the modulation of ± 0.04 polaron fraction and ± 0.08 imine fraction for an applied ±4 V bias. As was the case for PPy/Al_2O_3, the absorbance changes can be cycled for at least tens of cycles. When the PPy layer was replaced with a

redox-inactive $C_{10}N$ molecular monolayer, absorbance changes were not observed within the limit of detection for the same bias range.

Figure 6.12 shows the effect of the environment on the observed bias induced absorbance changes. When the spectrometer chamber was purged with dry N_2 in the presence of anhydrous calcium sulfate as a desiccant, absorbance changes in response to an applied bias were absent for all junctions types examined. Exposure of the dried junctions to ambient lab conditions for 1 hour restored the bias-induced absorbance changes to responses similar to those shown in Figure 6.11. Absorbance changes for PPy/Al_2O_3 junctions with an applied bias of ± 3 V are shown in Figure 6.12 for a dry environment and exposure to dry N_2 saturated with H_2O or MeCN. For the PPy/Al_2O_3 junctions, bias-induced absorbance changes in the presence of H_2O vapor are similar to absorbance changes at ambient conditions and are consistent with the modulation between the neutral imine and amine. In the presence of MeCN, the bias induced absorbance changes indicate modulation between the polaron and amine species. These results are similar to those reported by Jernigan et al. that a gas phase solvent can be used to induce redox events in a poly($Os(bpy)_2(vpy)_2$)(ClO_4)$_2$ layer sandwiched between two metallic contacts[53].

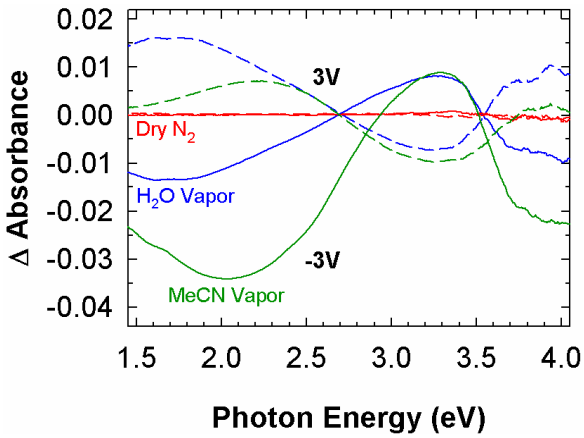

Figure 6.12: Biased induced absorbance changes of PPy/Al_2O_3 junctions in various environments. Absorbance changes in dry N_2 (red), dry N_2 bubbled through H_2O (blue), and dry N_2 bubbled through MeCN (green) under an applied voltage of ± 3V.

Figure 6.13 shows the bias induced absorbance changes at ± 3 V for a PPy/Al_2O_3 junction in which a p-nitrophenol (NP) layer was incorporated between the PPy and Al_2O_3 layer, and the bias was applied at lab ambient conditions. The inset is the spectrum of NP in MeCN and the dashed lines indicate the energies of the maximum absorbance changes for a PPy/Al_2O_3 junction without an included NP layer. In solution, NP is a weak acid with a reported pKa of 7.16 in H_2O and 8.45 in a MeCN/H_2O mixture[54]. The absorbance changes are similar to the PPy/TiO_2 junctions showing that the concentration of both the polarons and imines are modulated with an applied bias. In comparison to the PPy/Al_2O_3 junction, incorporation of the NP layer results in larger bias induced modulation of the polaron concentration.

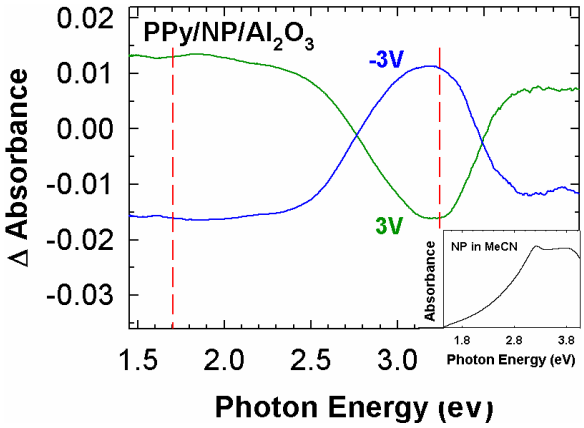

Figure 6.13: Bias induced absorbance changes of a PPy/NP/Al_2O_3 junction at ambient lab conditions. Dashed lines represent the maximum absorbance changes observed in PPy/Al_2O_3 junctions under the same experimental conditions (Fig. 11a). Inset is the solution spectrum of NP in MeCN.

6.4 DISCUSSION

6.4.1 Effect of an Applied Potential on Polypyrrole Layers in Solution

Combining the XPS analysis (Figure 6.6) and the three component MCR analysis (Figure 6.7), concentrations of the neutral amine, neutral imine, and positively charged polaron were monitored during formation and redox processes of a ~20 nm thick PPy film in electrolyte. For a PPy layer in MeCN/$TBABF_4$, the absorbance changes are consistent with electrochemically modulating the polaron fraction from 0.0 and 0.3, where the associated conductance modulation is expected to be at least 8 orders of magnitude[18]. For a PPy layer in H_2O/NaOH, the absorbance changes are consistent with modulating the imine fraction from 0.0 to 0.3. Formation of imine species most likely occurs through the deprotonation of polaron species by OH^- ions. The associated conductivity change associated with imine depends on the transport dimensionality and the concentration of polarons. A significant decrease in the PPy conductivity is expected

for one-dimensional conduction paths and only a small decrease conductivity for conduction paths of higher dimensionalities[55, 56]. For all spectra obtained in solution, the spectra returned to their initial state when the applied potential was removed, indicating the electrochemically formed polaron and imine are not stable at OCP in the electrolytic solution. The lack of stability is most likely the result of sufficient ion mobility in the solvated PPy layer, as ion redistribution with the PPy layer and ion exchange between the PPy layer and the electrolytic solution is required for the large observed absorbance changes. If sufficient ion mobility and ion exchange is present to maintain charge balance, the electrochemically doped PPy layer is expected to return to its initial absorbance after the applied potential is removed. Overall, modulation between the amine and polaron or imine species was strongly influenced by the surrounding environment. The tendency for proton exchange of the polaron appears to be a critical parameter to understand the effect of the surrounding environment.

6.4.2 Effect of an Applied Bias across Polypyrrole/Oxide Junctions

For in-situ spectra of PPy/oxide junctions acquired in a dry N_2 environment, bias-induced absorbance changes were below the detection limit for all junctions tested. The lack of an observable absorbance change indicates charge transfer between the Pt/carbon contact and PPy layer does not occur in a dry N_2 environment. Since the absorbance spectra are sensitive only to concentration changes, bias-induced redistribution of charged polaron species is not expected to result in an absorbance change. The fact that ambient air or H_2O saturated N_2 restore the absorbance changes indicates that H_2O plays a key role in polaron formation, even in nominally solid state PPy/oxide devices. Water

present in the junction likely solvates ions, which greatly increases their mobility and permits charge compensation for formed polarons. Without mobile ions, a space charge would develop in the PPy layer, which would rapidly suppress further oxidation. Water may stabilize the polaron by decreasing the reorganization energy associated with the oxidation of the neutral amine to the polaron species. In addition, reduction of water to OH^- and chemisorbed H at the Pt contact may provide the counter reaction needed to form stable polarons. Under bias, mobile OH^- ions could migrate to the PPy layer to either stabilize the polaron or cause imine formation through polaron deprotonation. The resulting cell reaction is one of the following:

$$PPy + H_2O = H_{ads} + PPy(polaron)^+ + OH^- \quad \text{Eq. 6.3}$$

$$PPy + H_2O = H_{ads} + PPy(imine) + H_2O \quad \text{Eq. 6.4}$$

H_2O is included on both sides of reaction (2) to emphasize that electrochemical reduction of H_2O generates OH^- ions at the Pt contacts that can migrate to the PPy layer and deprotonate the polaron to re-form H_2O. It should be noted that the mobility of charged species can significantly increase in the presence of an electric field (10 MV·cm). A schematic of this mechanism is shown in Figure 6.14. Note that H_2O can serve three roles in the reaction: a counter reaction for PPy oxidation, a solvent to increase ion mobility, and a base to accept protons during imine formation. As shown in Figure 6.13, the addition of p-nitrophenol to the device significantly increases polaron stability since the NP can act as an proton donor or can react with OH^- to reduce the formation of imine.

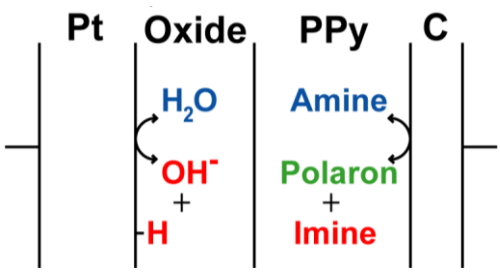

Figure 6.14: Proposed mechanism for observed absorbance changes in PPy/oxide junctions in the presence of water vapor. Positive bias creates mobile OH^- that can either stabilize the polaron or deprotonate the polaron to form the imine. Negative bias causes protonation of imines forming amines and OH^- ions to recombine with the adsorbed H to form H_2O.

6.4.3 Stability of Bias Induced Absorbance Changes

The observed bias induced absorbance changes consistent with the formation of polarons and imines were stable for at least 2 hours after the applied bias for all PPy/oxide junctions investigated. The stability of the polaron species is critical to potential resistance switching applications. The stability indicates that the observed absorbance changes associated with the polaron absorption is caused by electrochemical doping in the PPy layer. The open circuit voltage across the junction after an applied bias quickly decreased to zero volts in less than 60 seconds. For stable absorbance changes and a negligible open circuit voltage, ion migration must have occurred, allowing either charge compensation or deprotonation of the polaron. The stability of the formed polaron and imine species can be explained by low ion mobility in the junction in the absence of an applied bias, low proton mobility caused by chemisorption on the Pt contacts, or large reorganization barriers between the species.

While PPy/Al_2O_3 junctions exhibited modulation of the neutral amine/imine species in the presence of H_2O vapor, bias induced absorbance changes of PPy/Al_2O_3 junctions in MeCN saturated N_2 are consistent with the formation of stable polarons. In contrast to H_2O, MeCN is an aprotic solvent expected to retard deprotonation of a PPy polaron and suppress imine formation. While MeCN should increase ion mobility, it can not be reduced at the Pt surface to generate OH^-. Although the counter reaction in MeCN vapor is not fully understood, the additional absorbance changes associated with the polaron indicates that OH^- migration into the PPy layer is unlikely. Possible stabilizing species include bias-induced point defects in the Al_2O_3 layer or unintentional counter ions in the evaporated Al_2O_3 layer. Significant water is still expected to be chemisorbed in the Al_2O_3 layer that can undergo electrochemical reduction on the Pt contact[57, 58]. To estimate the required amount of chemisorbed H_2O required to stabilize the observed polaron absorbance change, the number density of formed polarons can be calculated from Equations 5.3 and 5.4:

$$\frac{N}{cm^2} = (\rho)\left(\frac{mol(N)}{g(PPy)}\right)(t)(N_A) \qquad \text{Eq. 6.5}$$

$$\frac{N^+}{cm^2} = \frac{N}{cm^2}\left(\frac{N^+}{N_{total}}\right) \qquad \text{Eq. 6.6}$$

where $\left(\frac{N}{cm^2}\right)$ is number of nitrogen (N) sights in a PPy layer per cm^2, $\left(\frac{mol(N)}{g(PPy)}\right)$ is the moles of N per gram of PPy, ρ is the density of the PPy layer, t is the thickness of the PPy

layer, and N_A is Avogadro's number. The number of polarons (N^+) per cm^2 $\left(\frac{N^+}{cm^2}\right)$ is calculated by multiplying the number of N sites per cm^2 by the fraction of polarons. Using $\rho = 1.4\ g \cdot cm^3$ and t = 20 nm, the 20 nm thick PPy layer has about $2.6 \times 10^{16}\ N \cdot cm^{-2}$. At ± 3V, the absorbance change for a PPy/Al_2O_3 junction correlated to an imine fraction change of ± 10%, which is about 2.5×10^{15} imines$\cdot cm^{-2}$. A molar equivalent of chemisorbed H_2O in the Al_2O_3 layer corresponds to about 1.5% H_2O w/w in the Al_2O_3 layer, which is a reasonable value especially for the nanocrystalline Al_2O_3 layer. A problem with this mechanism is the amount of chemisorbed H on the Pt top contacts of $2.5 \times 10^{15}\ cm^{-2}$ is relatively high considering a monolayer of Pt has about 1×10^{15} Pt atoms. Overall, these calculations show that even in the dry N_2/MeCN, sufficient water is presence to allow charge balance, although additional experiments are needed to confirm the actual reactions.

6.4.4 Polaron Stabilization in Polypyrrole/Oxide Junctions

For PPy/TiO_2 junctions, the biased induced absorbance changes are consistent with the generation of both polarons and imines in the presence of H_2O. Under an applied bias, TiO_2 layers have been shown to form intermediate oxidation states[24-26] and negative point defects such as oxygen vacancies and Ti interstitials[25, 59, 60], which could provide charge balance for formed polarons. The additional polaron formation may have been stabilized based the difference in the acid-base properties of the Al_2O_3 and TiO_2 layers in the presence of trace H_2O. Although the observed absorbance changes could have been caused by the TiO_2 layer, the absorbance changes in Figure 6.11b are likely

due to the PPy layer based on the similar changes in the absorbance magnitude observed in PPy/Al_2O_3 devices and that bias induced absorbance changes were absent for octylamine/TiO_2 junctions.

6.5 CONCLUSIONS AND FUTURE WORK

We have used XPS and MCR analysis of electrochemically polymerized PPy layers to determine the individual absorbance spectra of the neutral amine, polaron, and neutral imine species along the PPy backbone. With these results as background, we used in-situ absorbance spectroscopy to monitor bias induced concentration changes in PPy/oxide junctions under various experimental conditions. We showed that the bias induced concentration change along the PPy backbone is strongly influenced by the surrounding environment and oxide composition, as the tendency for polaron deprotonation appears to be a critical parameter. Since commonly applied voltages for organic thin film devices are on the order of several volts, electrochemical redox events in conjugated polymer layers are expected to occur, especially in the presence of residual water. The ability to monitor "buried" organic layers in active devices allows these potential redox events to be monitored, allowing complementary analysis to the observed electronic changes. In addition to Raman spectroscopy, we believe in-situ optical absorbance spectroscopy is a useful method to determined the mechanism of organic RRAM devices and enhance their performance, including direct correlations of absorbance changes with device conductivity.

Future work includes determining the environmental effect on the bias induced absorbance changes and to characterize the counter ions present in the junction. Since UV-Vis absorbance spectroscopy is not sensitive to the absorbance of most counter-ions, additional analytical techniques are required such as XPS, FTIR, or nuclear magnet resonance (NMR). An alternative approach is to intentionally introduce counter ions in the junction layers, although the analysis of the results might be difficult. Determination of ion mobility in the junction layers is critical to understanding which ions play a role in the observed absorbance changes. In addition to ions, additional characterization of the electrochemical polymerized PPy layer is needed to determine the role of the supporting electrolyte, polymerization and reduction potentials, and the work function of the bottom contact. Finally, a comprehensive study is needed to correlate the observed absorbance with changes in the PPy conductance state.

6.6 REFERENCES

1. Pickup, P. G.; Kutner, W.; Leidner, C. R.; Murray, R. W., Redox conduction in single and bilayer films of redox polymers. *J. Am. Chem. Soc.* **1984,** 106, (7), 1991-1998.

2. Karl, N., Charge carrier transport in organic semiconductors. *Synth. Met.* **2003,** 133, 649-657.

3. Bredas, J. L.; Street, G. B., Polarons, bipolarons, and solitons in conducting polymers. *Acc. Chem. Res.* **1985,** 18, (10), 309-315.

4. Zuppiroli, L.; Bussac, M. N.; Paschen, S.; Chauvet, O.; Forro, L., Hopping in disordered conducting polymers. *Phys. Rev. B* **1994,** 50, (8), 5196-5203.

5. Salomon, A.; Cahen, D.; Lindsay, S.; Tomfohr, J.; Engelkes, V. B.; Frisbie, C. D., Comparison of electronic transport measurements on organic molecules. *Adv. Mater.* **2004,** 16, (6), 477-477.

6. Adams, D. M.; Brus, L.; Chidsey, C. E. D.; Creager, S.; Creutz, C.; Kagan, C. R.; Kamat, P. V.; Lieberman, M.; Lindsay, S.; Marcus, R. A.; Metzger, R. M.; Michel-Beyerle, M. E.; Miller, J. R.; Newton, M. D.; Rolison, D. R.; Sankey, O.; Schanze, K. S.; Yardley, J.; Zhu, X. Y., Charge transfer on the nanoscale: current status. *J. Phys. Chem. B* **2003,** 107, (28), 6668-6697.

7. Lindsay, S. M.; Ratner, M. A., Molecular Transport Junctions: Clearing Mists. *Adv. Mat.* **2007,** 19, (1), 23-31.

8. Lee, K.; Cho, S.; Park, S. H.; Heeger, A. J.; Lee, C. W.; Lee, S. H., Metallic transport in polyaniline. *Nature* **2006,** 441, (7089), 65-68.

9. Sugiyasu, K.; Swager, T. M., Conducting-polymer-based chemical sensors: transduction mechanisms. *Bull. Chem. Soc. Jpn.* **2007,** 80, (11), 2074-2083.

10. Barman, S.; Deng, F. J.; McCreery, R. L., Conducting polymer memory devices based on dynamic doping. *J. Am. Chem. Soc.* **2008,** 130, (33), 11073-11081.

11. Lee, D.; Swager, T. M., Toward isolated molecular wires: a ph-responsive canopied polypyrrole. *Chem. Mater.* **2005,** 17, (18), 4622-4629.

12. Janata, J.; Josowicz, M., Conducting polymers in electronic chemical sensors. *Nat. Mater.* **2003,** 2, (1), 19-24.

13. Ramanavicius, A.; Ramanaviciene, A.; Malinauskas, A., Electrochemical sensors based on conducting polymer- polypyrrole. *Electrochim. Acta* **2006,** 51, (27), 6025-6037.

14. Zhao, J. H.; Thomson, D. J.; Pilapil, M.; Pillai, R. G.; Rahman, G. M. A.; Freund, M. S., Field enhanced charge carrier reconfiguration in electronic and ionic coupled dynamic polymer resistive memory. *Nanotechnology* **2010,** 21, (13), 134003.

15. Lu, W.; Fadeev, A. G.; Qi, B. H.; Smela, E.; Mattes, B. R.; Ding, J.; Spinks, G. M.; Mazurkiewicz, J.; Zhou, D. Z.; Wallace, G. G.; MacFarlane, D. R.; Forsyth, S. A.; Forsyth, M., Use of ionic liquids for pi-conjugated polymer electrochemical devices. *Science* **2002,** 297, (5583), 983-987.

16. Berdichevsky, Y.; Lo, Y. H., Polypyrrole nanowire actuators. *Adv. Mater.* **2006,** 18, (1), 122-125.

17. Xu, L.; Wang, J. X.; Song, Y. L.; Jiang, L., Electrically tunable polypyrrole inverse opals with switchable stopband, conductivity, and wettability. *Chem. Mater.* **2008,** 20, (11), 3554-3556.

18. Saunders, B. R.; Fleming, R. J.; Murray, K. S., Recent advances in the physical and spectroscopic properties of polypyrrole films, particularly those containing transition-metal complexes as counterions. *Chem. Mater.* **1995,** 7, (6), 1082-1094.

19. Neoh, K. G.; Lau, K. K. S.; Wong, V. V. T.; Kang, E. T.; Tan, K. L., Structure and degradation behavior of polypyrrole doped with sulfonate anions of different sizes subjected to undoping redoping cycles. *Chem. Mater.* **1996,** 8, (1), 167-172.

20. Waser, R.; Dittmann, R.; Staikov, G.; Szot, K., Redox-based resistive switching memories - nanoionic mechanisms, prospects, and challenges. *Adv. Mater.* **2009,** 21, (25-26), 2632-2663.

21. Scott, J. C.; Bozano, L. D., Nonvolatile memory elements based on organic materials. *Adv. Mater.* **2007,** 19, (11), 1452-1463.

22. Heremans, P.; Gelinck, G. H.; MuÌˆller, R.; Baeg, K.-J.; Kim, D.-Y.; Noh, Y.-Y., Polymer and Organic Nonvolatile Memory Devices *Chem. Mater.* **2010,** 23, (3), 341-358.

23. Chih-Yuan, L.; Kuan, H., Nonvolatile semiconductor memory revolutionizing information storage. *Nanotechnol. Mag. IEEE* **2009,** 3, (4), 4-9.

24. Nowak, A. M.; McCreery, R. L., Characterization of carbon/nitroazobenzene /titanium molecular electronic junctions with photoelectron and raman spectroscopy. *Anal. Chem.* **2004,** 76, 1089.

25. Wu, J.; Mobley, K.; McCreery, R., Electronic characteristics of fluorene/tiO2 molecular heterojunctions. *J. Chem. Phys.* **2007,** 126, 24704.

26. Wu, J.; McCreery, R. L., Solid-state electrochemistry in molecule/tio2 molecular heterojunctions as the basis of the tio2 ``memristor''. *J. Electrochem. Soc.* **2009,** 156, (1), P29-P37.

27. Panzer, M. J.; Frisbie, C. D., Polymer electrolyte gate dielectric reveals finite windows of high conductivity in organic thin film transistors at high charge carrier densities. *J. Am. Chem. Soc.* **2005,** 127, (19), 6960 - 6961.

28. Panzer, M. J.; Frisbie, C. D., High carrier density and metallic conductivity in poly(3-hexylthiophene) achieved by electrostatic charge injection. *Adv. Funct. Mater.* **2006,** 16, (8), 1051-1056.

29. Panzer, M. J.; Frisbie, C. D., Polymer electrolyte-gated organic field-effect transistors: low-voltage, high-current switches for organic electronics and testbeds for

probing electrical transport at high charge carrier density. *J. Am. Chem. Soc.* **2007,** 129, (20), 6599-6607.

30. Kaake, L. G.; Zou, Y.; Panzer, M. J.; Frisbie, C. D.; Zhu, X. Y., Vibrational spectroscopy reveals electrostatic and electrochemical doping in organic thin film transistors gated with a polymer electrolyte dielectric. *J. Am. Chem. Soc.* **2007,** 129, (25), 7824-7830.

31. Skaarup, S.; West, K.; Zachauchristiansen, B.; Jacobsen, T., Insitu spectroscopy of electrochemical doping of polypyrrole. *Synth. Met.* **1992,** 51, (1-3), 267-275.

32. Christensen, P. A.; Hamnett, A., Insitu spectroscopic investigations of the growth, electrocehmical cycling and overoxidation of polyrrole in aqueous-solution. *Electrochim. Acta* **1991,** 36, (8), 1263-1286.

33. Okur, S.; Salzner, U., Theoretical modeling of the doping process in polypyrrole by calculating uv/vis absorption spectra of neutral and charged oligomers. *J. Phys. Chem. A* **2008,** 112, (46), 11842-11853.

34. Turcu, R.; Brie, M.; Leising, G.; Niko, A., Reflection and absorption studies on polypyrrole films electrochemically prepared with different electrolyte types. *Synth. Met.* **1999,** 100, (2), 217-221.

35. Bredas, J. L.; Scott, J. C.; Yakushi, K.; Street, G. B., Polarons and bipolarons in polypyrrole - evolution of the band-structure and optical-spectrum upon doping. *Phys. Rev. B* **1984,** 30, (2), 1023-1025.

36. Genies, E. M.; Pernaut, J. M., Characterization of the radical cation and the dication species of polypyrrole by spectroelectrochemistry - kinetics, redox properties,

and strucutral-changes upon electrochemical cycling. *J. Electroanal. Chem.* **1985,** 191, (1), 111-126.

37. Kim, Y. T.; Collins, R. W.; Vedam, K.; Allara, D. L., Real-time spectroscopic ellipsometry - insitu characterization of pyrrole electropolymerization. *J. Electrochem. Soc.* **1991,** 138, (11), 3266-3275.

38. Anariba, F.; DuVall, S. H.; McCreery, R. L., Mono- and multilayer formation by diazonium reduction on carbon surfaces monitored with atomic force microscopy "scratching". *Anal. Chem.* **2003,** 75, (15), 3837-3844.

39. Deinhammer, R. S.; Ho, M.; Anderegg, J. W.; Porter, M. D., Electrochemical oxidation of amine-containing compounds - a route to the surface modification of glassy-carbon electrodes. *Langmuir* **1994,** 10, (4), 1306-1313.

40. Bonifas, A. P.; McCreery, R. L., 'Soft' Au, Pt and Cu contacts for molecular junctions through surface-diffusion-mediated deposition. *Nat. Nanotechnol.* **2010,** 5, (8), 612-617.

41. Anariba, F.; Steach, J.; McCreery, R., Strong effects of molecular structure on electron transport in carbon/molecule/copper electronic junctions. *J. Phys. Chem. B* **2005,** 109, 11163-11172.

42. Jaramillo, A.; Spurlock, L. D.; Young, V.; Brajter-Toth, A., XPS characterization of nanosized overoxidized polypyrrole films on graphite electrodes. *Analyst* **1999,** 124, (8), 1215-1221.

43. Kim, D. Y.; Lee, J. Y.; Kim, C. Y.; Kang, E. T.; Tan, K. L., Difference in doping behavior between polypyrrole films and powders. *Synth. Met.* **1995,** 72, (3), 243-248.

44. Kwasniewski, S. P.; Deleuze, M. S.; Francois, J. P., Optical properties of trans-stilbene using semiempirical and time-dependent density functional theory: a comparative study. *Int. J. Quantum Chem.* **2000,** 80, (4-5), 672-680.

45. DiLabio, G. A.; Litwinienko, G.; Lin, S. Q.; Pratt, D. A.; Ingold, K. U., Revised structure for the diphenylaminyl radical: the importance of theory in the assignment of electronic transitions in Ph2X center dot (X = CH, N) and PhY center dot (Y = CH2, NH, O). *J. Phys. Chem. A* **2002,** 106, (48), 11719-11725.

46. Nekrasov, A. A.; Ivanov, V. F.; Vannikov, A. V., Analysis of the structure of polyaniline absorption spectra based on spectroelectrochemical data. *J. Electroanal. Chem.* **2000,** 482, (1), 11-17.

47. Malinauskas, A.; Holze, R., Cyclic uv-vis spectrovoltammetry of polyaniline. *Synth. Met.* **1998,** 97, (1), 31-36.

48. Cabala, R.; Skarda, J.; Potje-Kamloth, K., Spectroscopic investigation of thermal treatment of doped polypyrrole. *Phys. Chem. Chem. Phys.* **2000,** 2, (14), 3283-3291.

49. Chakrabarti, S.; Das, B.; Banerji, P.; Banerjee, D.; Bhattacharya, R., Bipolaron saturation in polypyrrole. *Phys. Rev. B* **1999,** 60, (11), 7691-7694.

50. Kaufman, J. H.; Colaneri, N.; Scott, J. C.; Street, G. B., Evolution of Polaron States into Bipolarons in Polypyrrole. *Phys. Rev Lett.* **1984,** 53, 1005-1008.

51. Lee, D.; Swager, T. M., Defining space around conducting polymers: reversible protonic doping of a canopied polypyrrole. *J. Am. Chem. Soc.* **2003,** 125, (23), 6870-6871.

52. Li, Y. F.; Qian, R. Y., Studies on the chemical compensation of conducting polypyrrole by naoh solution. *Synth. Met.* **1988,** 26, (2), 139-151.

53. Jernigan, J. C.; Chidsey, C. E. D.; Murray, R. W., Electrochemistry of polymer-films not immersed in solution - electron-transfer on an ion budget. *J. Am. Chem. Soc.* **1985,** 107, (9), 2824-2826.

54. Saraji, M.; Bakhshi, M., Determination of phenols in water samples by single-drop microextraction followed by in-syringe derivatization and gas chromatography-mass spectrometric detection. *J. Chromatogr. A* **2005,** 1098, (1-2), 30-36.

55. Swager, T. M., The molecular wire approach to sensory signal amplification. *Acc. Chem. Res.* **1998,** 31, (5), 201-207.

56. Lee, D. W.; Swager, T. M., Defining space around conjugated polymers: new vistas in self-amplifying sensory materials. *Synlett* **2004**, (1), 149-154.

57. Hass, K. C.; Schneider, W. F.; Curioni, A.; Andreoni, W., The chemistry of water on alumina surfaces: reaction dynamics from first principles. *Science* **1998,** 282, (5387), 265-268.

58. McHale, J. M.; Auroux, A.; Perrotta, A. J.; Navrotsky, A., Surface energies and thermodynamic phase stability in nanocrystalline aluminas. *Science* **1997,** 277, (5327), 788-791.

59. Kwon, D. H.; Kim, K. M.; Jang, J. H.; Jeon, J. M.; Lee, M. H.; Kim, G. H.; Li, X. S.; Park, G. S.; Lee, B.; Han, S.; Kim, M.; Hwang, C. S., Atomic structure of conducting nanofilaments in TiO2 resistive switching memory. *Nat. Nanotechnol.* **2010,** 5, (2), 148-153.

60. Kim, S.; Choi, Y. K., A comprehensive study of the resistive switching mechanism in Al/TiOx/TiO2/Al-structured RRAM. *IEEE Trans. Electr. Dev.* **2009,** 56, (12), 3049-3054.

CHAPTER 7

THERMAL OXIDATION AS A SIMPLE METHOD TO INCREASE RESOLUTION IN NANOIMPRINT LITHOGRAPHY AND MOLECULAR-SCALED ELECTRODES

.

7.1 INTRODUCTION

7.1.1 Nano-gap Electrodes For Molecular Electronics

As described in Chapter 2, a common paradigm to form molecular junctions involves suspending molecules across a fabricated nano-gap electrode. The width of the fabricated gap needs to be similar to the length of the investigated molecules. Although this approach appears straightforward, fabrication of gaps on the molecular length scale with traditional lithographic techniques is difficult to achieve. To circumnavigate this limitation, standard lithography techniques such as optical, electron beam (EBL), and nanoimprint lithography (NIL) have been used in conjunction with additional etching, deposition, or "breaking" techniques to form molecular-scaled gaps. Electromigration, mechanical break junctions, scanning tunneling break junctions, oxidative "cutting" of carbon nanotubes, and controlled metal deposition techniques have been successfully demonstrated to fabricate electrodes with a molecular-scaled gap[1-5]. Although demonstrated in practice, these techniques have limitations that include difficulty to scale for parallel fabrication, local electric field enhancements caused by edge roughness, and poor reproducibility or experimental control. In Chapter 4, SDMD was introduced and discussed as a novel technique to fabricate molecular junctions with both single molecule resolution and the ability to fabricate many-molecule junctions without the requirement to fabricate molecular-scale electrodes. Although SDMD was shown to provide critical insight into molecular charge transport, development of additional techniques to fabricate molecular electronic junctions is critical to allow cross-paradigm comparison of observed molecular conductance. Cross-paradigm comparison allows charge transport phenomena

that might be artifacts of the paradigm to be identified, allowing the inherent molecular charge transport mechanism to be correctly characterized. For this reason, this chapter discusses a novel technique to fabricate electrodes with molecular-scaled spacing.

7.1.2 Nanoimprint Lithography

A promising technique to fabricate electrodes with molecular-scaled spacing is nanoimprint lithography (NIL). NIL is a conceptually simple method for patterning high resolution features on a substrate[6]. For pattern transfer with the NIL technique, a rigid master with patterned surface relief features is pressed into a soft "resist", which assumes the negative of the master's pattern. The resist usually consists of small molecules or polymers, which are spin coated onto the substrate prior to the imprinting process. In this chapter, the pattern is transferred into the resist through a thermoplastic NIL process, where a thermoplastic resist is imprinted at a temperature above its glass transition temperature (T_g) followed by removal of the NIL master at a temperature below T_g. To optimize the process, the imprint pressure, time, and temperature are controlled parameters. The patterned resist can be used as a mask for subsequent fabrication processes or as a final patterned surface. A schematic of the process flow diagram for NIL pattern transfer is shown in Figure 7.1. With NIL, high throughput patterning has been shown, and features with resolution as low as 5 nm have been successfully demonstrated[7-10]. Due to these attributes, the International Technology Roadmap for Semiconductors (ITRS), the key reference document of the semiconductor industry, has begun to include NIL among the possible methods for reaching the sub-22 nm technology nodes beyond the range of conventional photolithographic techniques[11]. In addition to

conventional microelectronics, applications with less stringent process requirements also exist, as demonstrated by reports detailing the application of NIL to solar cells[12-15], lighting[16, 17], and displays[18]. As a result, NIL is expected to become an increasingly prominent tool in the field of molecular electronics.

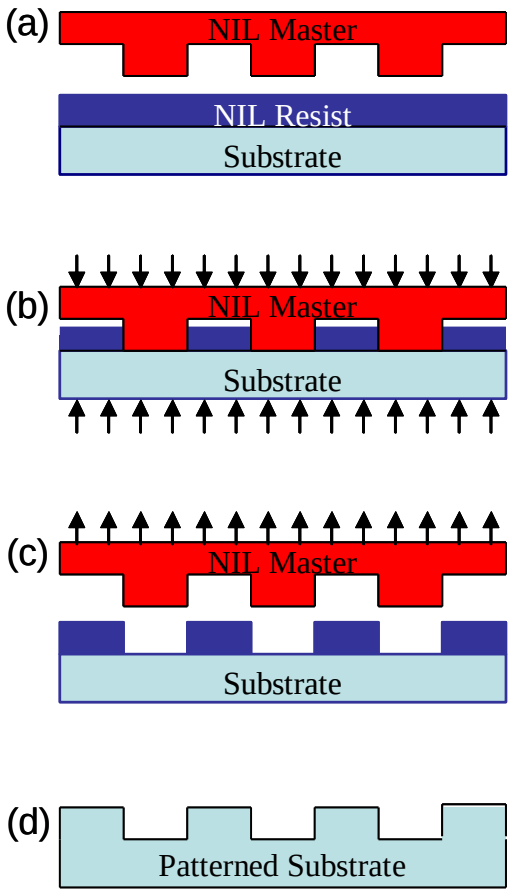

Figure 7.1: Process flow chart for pattern transfer with thermal nanoimprint lithography. **a,** NIL thermal resist is spin coated onto the substrate. **b,** Substrate is heated above the T_g of the NIL resist and then the NIL master is pressed into the resist with a uniform pressure. **c,** Substrate is cooled below T_g and then the NIL master is removed from the substrate. **d,** Subsequent etching or deposition techniques are used to transfer the resist pattern onto the substrate and the resist is removed from the substrate.

Since the NIL process involves one-to-one pattern transfer, the ultimate resolution is limited by that of the master, and improvements made to the master can be expected to lead to improvements in the imprinted substrates. Commonly, NIL master fabrication is performed through high resolution electron beam lithography (EBL) followed by reactive ion etching (RIE)[6]. Figure 7.2 shows the general process flow chart for the fabrication of a NIL master. For EBL, fabrication of dense or large area patterns becomes difficult at sub-20 nm resolution due to surface charging, electron scattering in the resist, and aberrations in the electron optics[19-21]. In addition, high aspect ratio etching to form the master relief pattern becomes increasing difficult with smaller features, leading to limiting phenomena such as aspect ratio dependent etching (ARDE)[22].

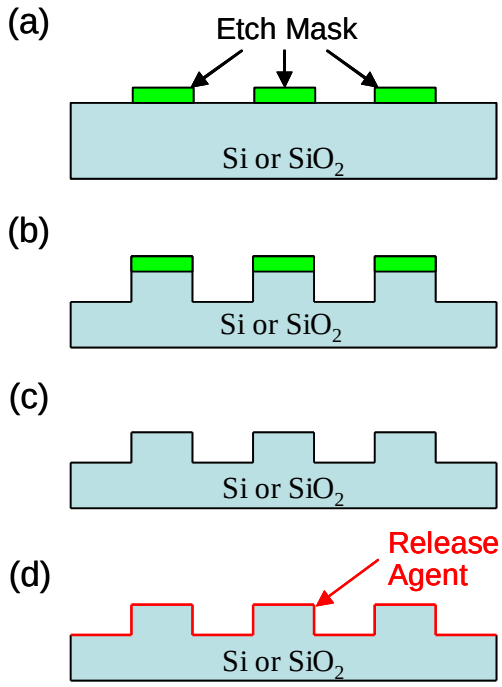

Figure 7.2: Process flow chart for fabrication of a NIL master. **a,** Etch mask is defined onto the Si or SiO_2 substrate; commonly achieved through electron beam lithography. **b,** RIE of the pattern substrate results in patterned surface relief features defined by the etch mask. **c,** Etch mask is removed from the NIL master. **d,** Release agent is attached to the NIL master to reduce adhesion between the resist and master.

7.1.3 Thermal Oxidation for Nanoimprint Lithography and Nanogap Fabrication

In this chapter, a simple thermal oxidation technique is outlined which circumvents the scaling issues associated with the EBL/RIE fabrication route and allows improved resolution of fabricated NIL masters. Employing thermal Si oxidation to vary dimensions in different applications has been previously described in the literature[23-29], but this chapter is the first demonstration of thermal oxidation to increase the resolution of NIL. To demonstrate this technique, a series of Si masters in which the minimum feature size is successively reduced through thermal oxidation are shown, and then these

oxidized masters are shown to be suitable for pattern transfer in an otherwise standard NIL process. With this technique, increased resolution of NIL masters is shown for both negative (e.g., gaps) and positive (e.g., lines) features. The increased resolution of positive features is obtained through an additional simple wet SiO_2 etching process. In addition to the application to NIL, the thermal oxidation technique is shown applicable for increased resolution in direct fabrication of electrodes with molecular-scaled spacing. Several advantages of thermal oxidation are also discussed including the reduction of line edge roughness[30-32], and the provision of an OH-rich surface for easy attachment of common release agents[33]. Since the growth of SiO_2 is highly controllable through thermal oxidation[34-36], reduction in feature sizes is achieved with a high degree of precision. Thermal oxidation is demonstrated to be an inexpensive technique to significantly ease the design constraints for the fabrication of high resolution, high density NIL masters.

7.2 EXPERIMENTAL

7.2.1 Fabrication of Nanoimprint Lithography Masters

The process flow chart for fabrication of an NIL master is shown in Figure 7.3. A highly doped, 100 mm, p-type Si wafer (0.005 Ω·cm) was cleaned in piranha (1:1 H_2O_2:H_2SO_4), and the native oxide was removed in buffered oxide etchant (BOE). Poly(methylmethacrylate) (950 kg/mol, 2 wt% in anisole) was spin coated onto the wafer at 4000 rpm and soft baked at 170°C for 5 minutes at atmospheric conditions, resulting in a 90 nm thick resist layer. EBL was used to pattern the resist with features in the 70 –

500 nm range. The resist was exposed at 100 $\mu C \cdot cm^{-2}$ at 10 keV, then developed in 1:3 methyl isobutyl ketone:isopropanol at 293° C. Etch masks were deposited with electron beam evaporation of 2 nm Cr and 15 nm SiO_2 with a deposition rate of 0.3 $Å \cdot s^{-1}$ at a chamber pressure less than 1 x 10^{-6} torr. The EBL-patterned resist was removed from the substrate by lift-off in dichloromethane. Features larger than 2 μm, such as 200 x 200 μm contact pads, were patterned with traditional optical lithography after the EBL patterning. The etch mask pattern was transferred into the Si substrate by etching with an inductively-coupled plasma reactive ion etcher (ICP-RIE). ICP-RIE was used in a continuous flow or "unswitched" method with a constant flow of C_4F_8 (60 sccm) and SF_6 (80 sccm) with a constant RF power of 750 W. The final etch depth was 300 nm with an etch rate of 10 $nm \cdot s^{-1}$, resulting in a slightly positive etch profile of 88°. Following the Si etch, the Cr/SiO_2 etch mask was removed with BOE and chrome etch (Anachemia Science, #0906015). The Si NIL masks were rinsed in deionized water (DI) for 30 seconds and dried in a N_2 stream. The etch profile and feature sizes of the NIL masters were determined by scanning electron microscopy (SEM, Hitachi S-4800).

7.2.2 Thermal Oxidation Technique

Thermal oxidation of the Si NIL masters was accomplished with a Jipelec Jetfirst Rapid Thermal Annealer (RTA). For all oxidations, the RTA chamber had a constant dry O_2 flow rate with an oxidation temperature of 1000 °C. The fast ramp rates allowed precise control of the oxidation time. The change in the selected feature size versus oxidation time was determined *ex situ* by SEM. For the reduction of positive features

(i.e., to reduce line width), the Si NIL master was thermally oxidized and then etched in BOE to remove the SiO_2 layer.

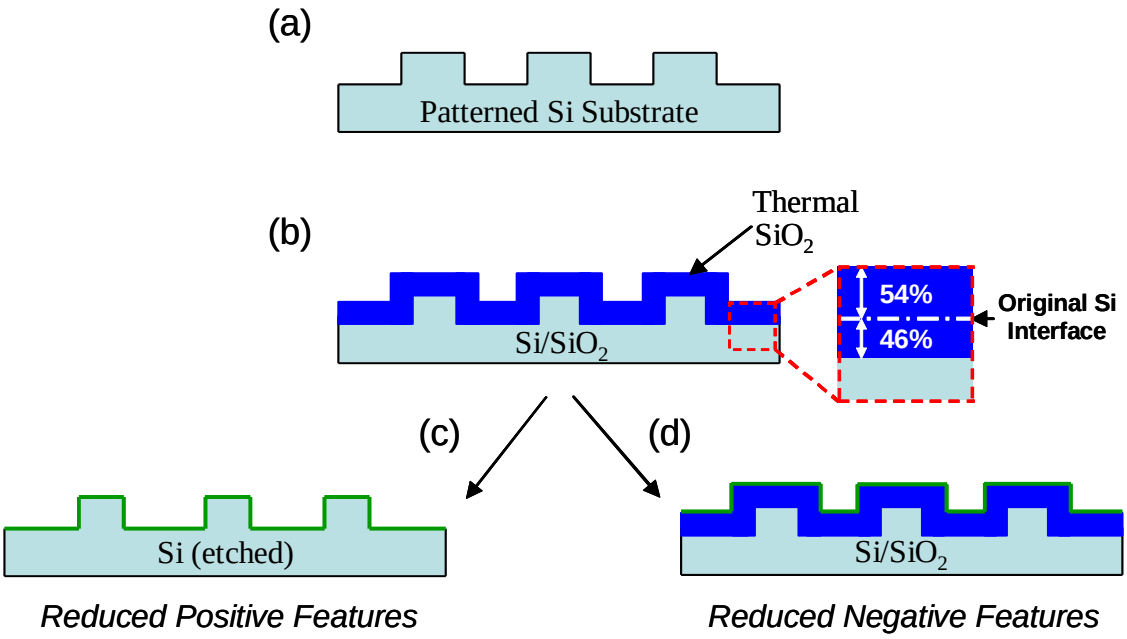

Figure 7.3: a, Si NIL master is fabricated with EBL/RIE techniques. **b,** Thermal oxidation of the Si master reduces the size of negative features. Inset show the percentage of thermal SiO_2 layer grown from the original Si interface. **c,** Removal of the 46% of the thermal oxide grown beneath the original Si with BOE reduces the size of positive features. **d,** The 54% of the thermal oxide grown beyond the original interface reduces the size of negative features.

7.2.3 Pattern Transfer with Nanoimprint Lithography

A Nanonex 2500 imprinter was used for thermal NIL. A 100 mm Si wafer was cleaned in piranha solution and spin coated with 100 nm of NXR1025 thermal resist. The thickness of the resist should be less than the depth of the 300 nm relief features patterned in the NIL master. To reduce the adhesion between the NIL master and resist during the demolding process (removal of the master at $T < T_g$), the master was modified by

immersion in a 2% (w/w) solution of trichloro-(1H,1H,2H,2H-perfluoroctyl)silane (Aldrich, 97%) in toluene for 30 minutes. Since trichlorosilane compounds react with moisture in ambient air, the complete modification process was performed in a dry N_2 glove box. After the surface modification, the NIL masters were rinsed in toluene and dried in an N_2 stream and stored in the glove box until the NIL process. NIL imprinting occurred at 130°C and 200 psi for 2 minutes, followed by demolding at room temperature. The demolding process is non-trivial with the Nanonex 2500 imprinter, as the NIL masters were removed by prying the NIL masters off the patterned surface with a razor blade and a N_2 blow gun. Extreme care should be taken to reduce shear stress between the master and substrate during the demolding process. After imprint, the resist pattern was transferred into the Si wafer using an ICP-RIE process identical to that stated above.

7.2.4 Fabrication of Au Nanogap Electrodes

For direct fabrication of Au electrodes with molecular-scaled spacing, a Si surface was patterned with the same techniques used for the NIL masters. Thermal oxidation of the patterned Si surface resulted in the reduction of the negative "gap" features. To form the Au electrodes, electron beam evaporation was used to deposit 2 nm Cr and 10 nm of Au directly onto the oxidized patterned Si substrates. Since the surface features are about 300 nm above the etched regions, deposition of the Au layer resulted in electrical isolation between the Au deposited on top of the positive features and the Au deposited in the etched regions. The electrical resistance between the resulting Au electrodes was measured with a Keithley 2517B electrometer.

7.3 RESULTS AND DISCUSSION

7.3.1 Resolution Increase with Thermal Oxidation Technique

For dry thermal oxidation of Si, oxidation proceeds by diffusion of O_2 through the forming SiO_2 to the Si/SiO_2 interface. O_2 reaction at the Si/SiO_2 interface follows the simple reaction shown below:

$$Si + O_2 = SiO_2 \qquad \text{Eq. 7.1}$$

Since the density of SiO_2 is less than the density of Si, the growing SiO_2 layer extends beyond the original Si surface. Using this original Si surface as a reference, 54% of the thermally-grown oxide extends outward (i.e., beyond the original dimensions of the Si), while 46% extends inward[37], as shown in Figure 7.3. The 54% of the SiO_2 thickness that extends outward from the original surfaces reduces the size of negative features such as gaps or increases the size of positive features such as lines. The final dimensions of these features are controlled by growing the SiO_2 to a predetermined thickness; a process made straightforward by advanced Si oxidation models[34-36, 38]. Precise control of the grown SiO_2 thickness is obtained by rationally selecting an oxidation temperature that allows the targeted SiO_2 thickness to occur during a constant oxidation rate period. For all oxidations in this chapter 1000 °C was chosen, and in each case, this corresponded to a constant oxidation rate near the target thickness. Although not employed here, *in situ* ellipsometry can also be used to gain additional control of the final oxide thickness. As

noted in the introduction of this chapter, the highly controllable growth rate of the SiO_2 layer provides a wide process window.

The use of thermal oxidation to reduce a negative feature in a Si master is shown in Figure 7.4, where the width of an initial 70 nm gap (Fig. 2a) is reduced to less than 10 nm (Fig. 4b). By comparison of the gap dimensions before and after oxidation, the gap reduction from 70 nm to 10 nm indicates that 30 nm of SiO_2 was grown outward from the initial Si surfaces on each side of the gap, which correlates to a total SiO_2 thickness of 54.5 nm. In an un-patterned region of the master, the total SiO_2 thickness was explicitly measured by ellipsometry, and a value of 55 nm was recorded. This matches well with calculated SiO_2 thickness based on the final gap dimensions. The oxidized 10 nm gap is ~40 times smaller than the length of the feature, which is generally considered difficult to achieve with direct EBL. While EBL can be used to reach this ratio, a delicate balance of several interrelated process parameters (such as electron dose, write speed, resist thickness and uniformity, developer concentration and time, etc) must be carefully maintained, and the requirements generally become more stringent with increasing resolution. Tighter process control and increased EBL write times tend to be required as resolution targets are reduced, which significantly increases fabrication costs. In addition, the oxidized 10 nm gap has a large height to gap width ratio (~30:1) which is difficult to obtain through RIE etching of an initial 10 nm gap feature, as diffusion of the etchant and product gases is limited in narrow features significantly decreasing the etch rate. Improved process control during the thermal oxidation should allow even higher aspect ratios than reported in this dissertation.

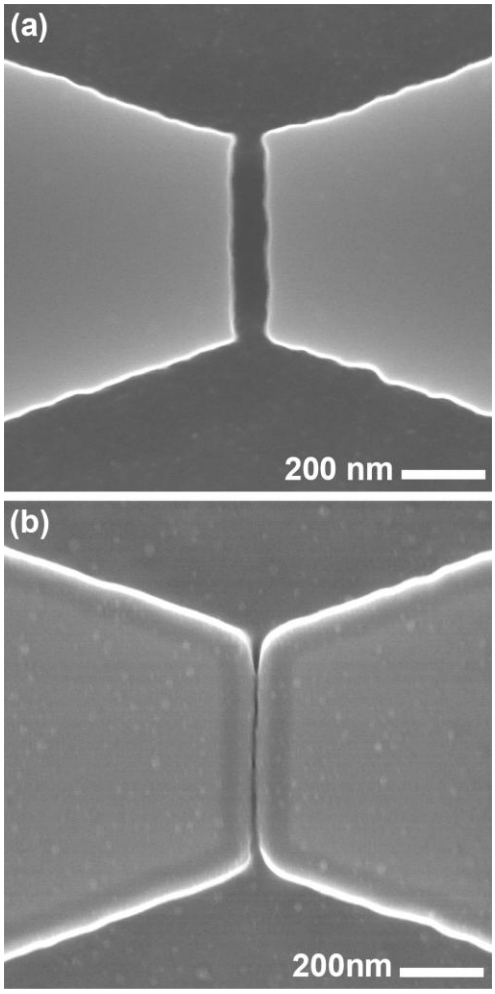

Figure 7.4: SEM images of Si master features before and after thermal oxidation**. a,** Initial 70 nm gap in a Si master formed by EBL/ICR-RIE. **b,** Thermal oxidation resulted in the growth of 55 nm SiO_2 causing the 70 nm gap to be reduced to 10 nm.

Figure 7.5 shows that the thermal oxidation technique can also be used to reduce the size of positive features such as lines. Since 46% of the grown SiO_2 layer forms beneath the original Si surface, thermal oxidation followed by removal of the SiO_2 with a BOE etch results in the reduction of positive feature dimensions. In Figure 7.5, a 225 nm Si line was thermally oxidized to 350 nm then etched in BOE, resulting in a 55 nm Si

line. As observed in Figure 7.5, the edge roughness of the oxidized/etched features is less than the edge roughness of the initial features. One key benefit of this method is the edge roughness of both positive and negative features become smoother during a thermal oxidation or wet etching processes. The equilibrium roughness of initially rough and smooth Si surfaces after thermal oxidation has been previously shown to be 0.3 – 0.5 nm[30-32]. During thermal oxidation, the surface or edge roughness of an initial Si surface is expected to become smoother, where the smoothening effect is caused by higher oxidation rates of the sharp or rough features. The surface free energy (ΔG) is directly proportional to the principle curvatures according the Gibbs-Thompson equation:

$$\Delta G = 2V\gamma\left(k_1 + k_2\right) \qquad \text{Eq. 7.2}$$

where V is molar volume, γ is the surface energy, and k_1 and k_2 are the principle curvatures[30]. For the system to reduce its free energy during thermal oxidation, the principle curvatures must trend towards zero resulting in a smoother (flat) surface. This smoothing process is also observed for wet etching process of SiO_2, since the etching rate is higher for sharp surface features. For application to molecular electronics, edge roughness is critical since molecular lengths are on the 1 – 5 nm scale. Overall, thermal oxidation of patterned Si surfaces is an ideal method to fabricate uniform gaps for electrodes with molecular-scale separation.

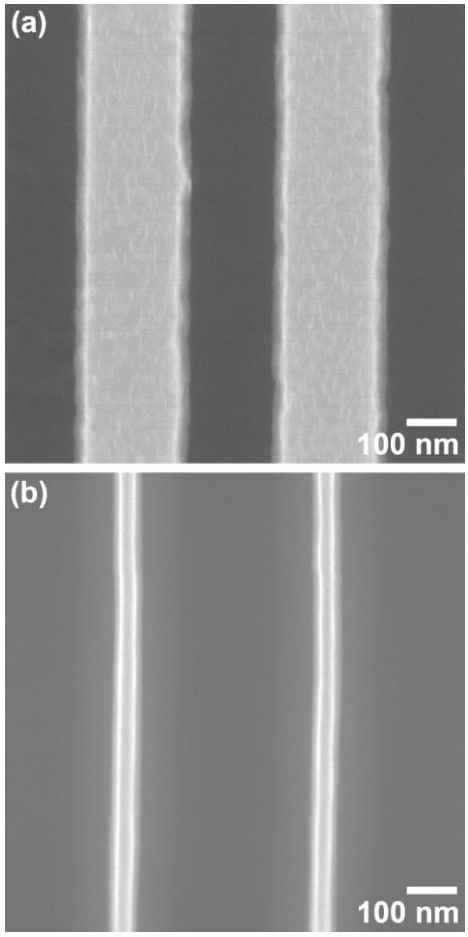

Figure 7.5: SEM images of positive line features reduced through thermal oxidation and subsequent BOE etching processes. **a,** Initial 225 nm wide Si lines fabricated by EBL/ICP-RIE. **b,** Resultant 55 nm Si line features after thermal oxidation to a width of 350 nm (not shown) and then etched in BOE to remove the grown SiO_2 layer.

7.3.2 Resolution Increase for Oxidized Nanoimprint Lithography Masters and Transferred Patterns

To demonstrate NIL pattern transfer with an oxidized master, an interdigitated array was used as the NIL master. As shown in Figure 7.6a, the array originally consisted of 500 nm lines separated

by 180 nm gaps. With successive thermal oxidations, the initial 180 nm gap width was thinned to 100 nm with a 35 minute oxidation (shown in Figure 7.6b), 75 nm with a 135 minute oxidation (Figure 7.6c) and 40 nm with a 205 minute oxidation (Figure 7.6d). In the process, the gap width is reduced, while the pitch of the interdigitated array remained constant. Since the oxidized surface is OH-rich, attachment of a silane-based release agent was trivial. The oxidized features were then transferred into the NIL resist by thermal NIL: the 180 nm and 40 nm features in Figures 7.7a and 7.7b were transferred from the original and oxidized NIL masters in Figures 7.6a and 7.6d, respectively. Qualitatively, the roughness of the transferred patterns is approximately equivalent to that of the corresponding master, although assigning edge roughness contributions to either the NIL or ICP-RIE etch processes is difficult. One potential issue affecting pattern transfer fidelity is corner rounding of the features during the oxidation process. The rounded edge profiles can be observed in Figure 7.6b-d, and this profile is transferred to the NIL resist at the resist/wafer interface during the NIL process. Ideally, the final radius at the corners of an oxidized master is a small fraction of the imprinted resist thickness. To minimize this effect, the required oxidative resizing should be minimized by using the highest initial EBL resolution reasonably achievable, or alternatively, an anisotropic RIE could be performed post-oxidation to decrease the corner radii at all SiO_2 edges.

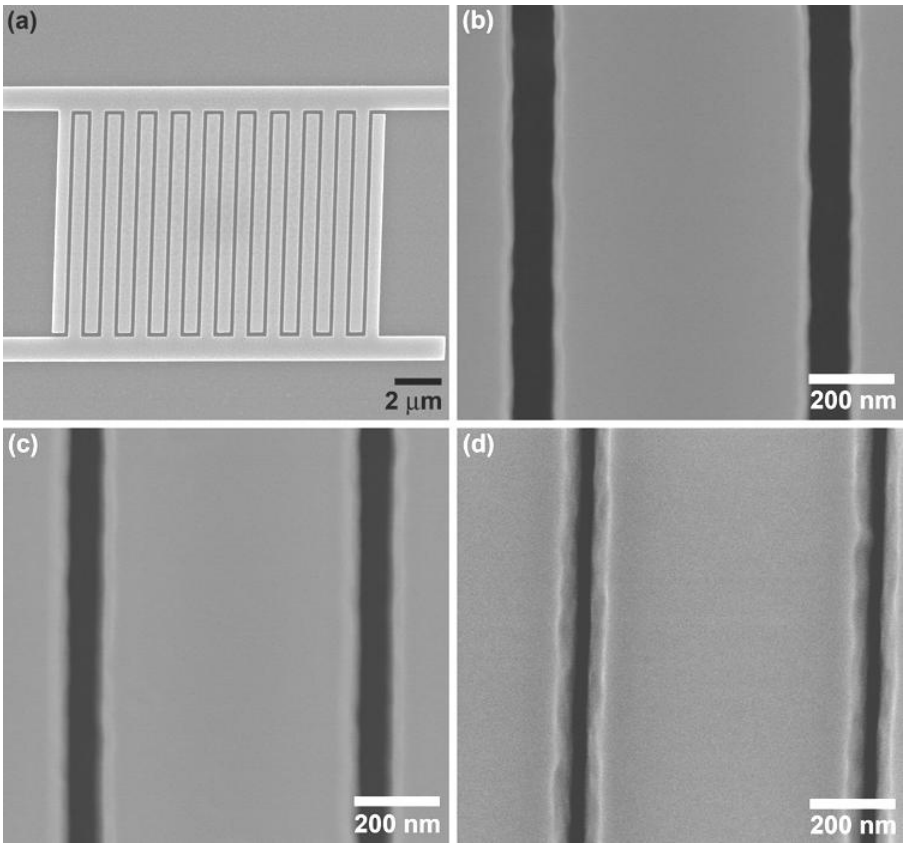

Figure 7.6: SEM images of the NIL master after progressive thermal oxidations. **a,** Original Si interdigitated array master with 500 nm line widths and 180 nm gaps. The gaps are reduced to 100 nm **b**, 75 nm **c**, and 40 nm **d** through successive thermal oxidation processes.

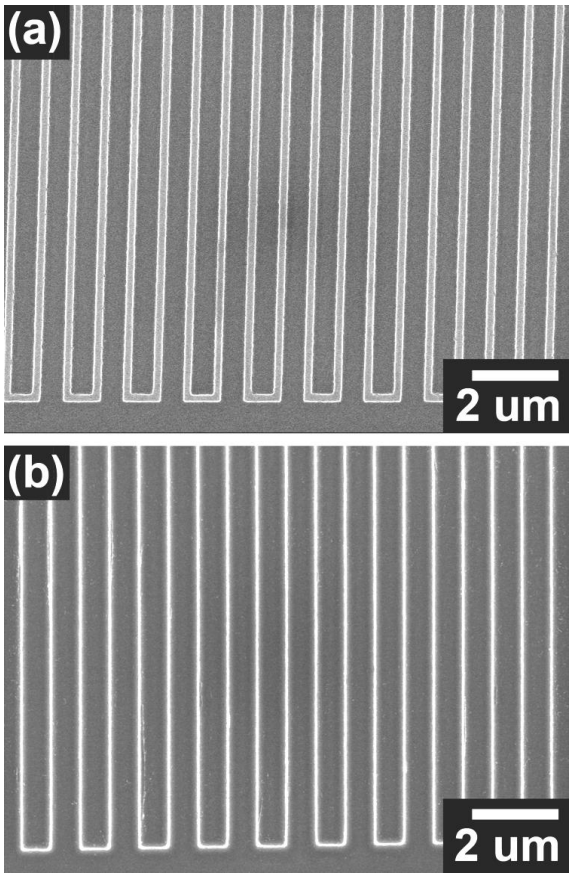

Figure 7.7: SEM images of transferred patterns with the initial and oxidized NIL masters. **a,** 180 nm features transferred from the NIL master in Fig. 4a. **b,** 40 nm features transferred from the oxidized Ni master in Fig. 4d.

7.3.3 Fabrication of 10 nm Au Nanogap Electrodes

Direct fabrication of Au electrodes with ~10 nm gaps was accomplished through the deposition of a Cr adhesion layer (2 nm) and Au layer (10 nm) directly on an oxidized patterned Si surface. In contrast to the fabrication of NIL masters, the oxidized patterned surface is used directly as the final electrode structure. As shown in Figure 7.8, deposition of the Cr/Au layer on an interdigitated oxidized master with an initial 20 nm gap resulted in Au electrodes with a spacing of less than 10 nm. The additional increase

in resolution was caused by the build-up of the deposited Au layer on the SiO_2 surface. Additional increase in resolution could be obtained with a thicker deposited Au layer. The Au deposited on the positive features are electronically isolated from the Au deposited in the 300 nm deep features because minimal Au deposition occurs on the sidewalls, leading to a discontinuous, nonconductive sidewall layer. To confirm the electrical isolation between the Au electrodes, the resistance across the gap was measured to be greater than 100 GΩ. Described as a disadvantage for the fabrication of NIL masters, the loss of sharp edge features upon oxidation is beneficial for the fabrication of electronic gaps intended to be bridged by molecules. Rounding of the edges during oxidation yields a range of gap lengths, allowing bridging molecules to find and attach to the gap region with an identical length to the molecular length.

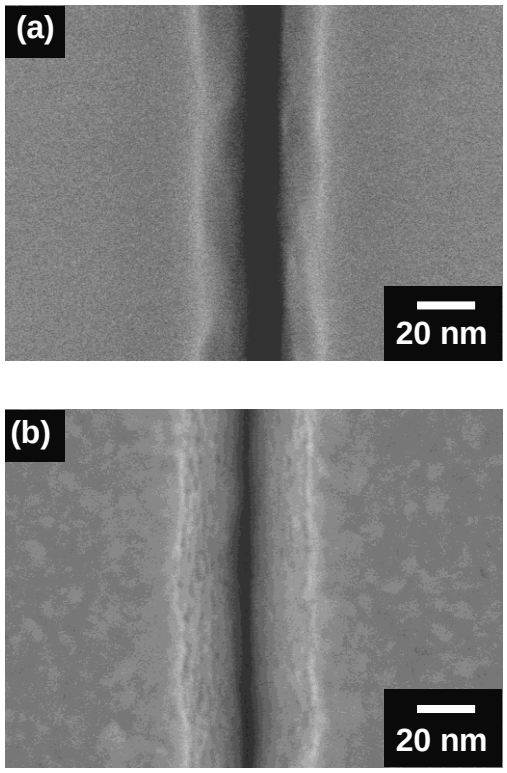

Figure 7.8: SEM images of an oxidized patterned Si surface before and after Au deposition. **a,** Thermally oxidized Si master resulting in a 20 nm gap. **b,** After deposition of 2 nm Cr and 10 nm Au, the Au electrodes have a separation of less than 10 nm and are electronically isolated.

7.4 CONCLUSIONS AND FUTURE WORK

In this Chapter, thermal oxidation as a simple approach is introduced to reduce the feature size of both positive and negative features on a patterned Si surfaces. For isolated negative features, initial gaps of 70 nm were successfully reduced to 10 nm, while positive features were reduced from 225 nm to 55 nm. Since the oxidation parameters were not fully optimized, this technique should be capable of fabricating features with additional resolution enhancements. As a general approach, thermal oxidation to reduce

a feature size is envisioned to be supplemental method to increase the ultimate resolution of standard lithography techniques such as EBL. For example, thermal oxidation would be an ideal technique to produce sub-10 nm features. Careful selection of the oxidation temperature should allow precise control of the final oxide thickness and the final feature dimensions. As identified in the above discussion, methods to improve this technique include *in situ* monitoring of SiO_2 growth, developing post-oxidation techniques to obtain sharper edge profiles, and advanced modeling of O_2 diffusion and SiO_2 growth rate in sub-10 nm trenches. The greatest NIL advantage inherent to the technique is from a fabrication perspective: the ability to employ simple, fast and reliable EBL techniques which are normally confined to modest resolutions, followed by a fast, simple, post-process oxidation to create high resolution masters. For molecular applications, this technique can employed to increase the resolution of standard EBL techniques allowing fabrication of electrodes with molecular-scaled separation.

Suggested future work includes determination of the ultimate resolution achievable with this technique, in regards to the minimal positive and negative features achievable on a NIL master and in NIL pattern transfer. Detailed analysis of the thermal oxidation rate as a function of the (gap) feature size would be insightful in determining the ultimate resolution of the technique. In addition to thermal oxidation, solution based or electrochemical oxidation techniques should be investigated to determine the advantages and disadvantages of the different oxidation methods. For NIL masters, improving the edge profile through subsequent etching techniques should lead to improved fidelity of the transferred patterns, which is expected to be critical on the

nanometer scale. Although successfully demonstrated, improved process control throughout all fabrication stages of the NIL masters should result in improved resolution for NIL pattern transfer.

7.5 REFERENCES

1. Li, T.; Hu, W. P.; Zhu, D. B., Nanogap electrodes. *Adv. Mater.* **2010,** 22, (2), 286-300.

2. Reed, M. A.; Zhou, C.; Muller, C. J.; Burgin, T. P.; Tour, J. M., Conductance of a molecular junction. *Science* **1997,** 278, (5336), 252-254.

3. Xiao, X. Y.; Xu, B. Q.; Tao, N. J., Measurement of single molecule conductance: benzenedithiol and benzenedimethanethiol. *Nano Lett.* **2004,** 4, (2), 267-271.

4. Guo, X. F.; Myers, M.; Xiao, S. X.; Lefenfeld, M.; Steiner, R.; Tulevski, G. S.; Tang, J. Y.; Baumert, J.; Leibfarth, F.; Yardley, J. T.; Steigerwald, M. L.; Kim, P.; Nuckolls, C., Chemoresponsive monolayer transistors. *Proc. Natl. Acad. Sci. U. S. A.* **2006,** 103, (31), 11452-11456.

5. Strachan, D. R.; Smith, D. E.; Johnston, D. E.; Park, T. H.; Therien, M. J.; Bonnell, D. A.; Johnson, A. T., Controlled fabrication of nanogaps in ambient environment for molecular electronics. *Appl. Phys. Lett.* **2005,** 86, (4), 3.

6. Guo, L. J., Nanoimprint lithography: Methods and material requirements. *Adv. Mater.* **2007,** 19, (4), 495-513.

7. Austin, M. D.; Ge, H. X.; Wu, W.; Li, M. T.; Yu, Z. N.; Wasserman, D.; Lyon, S. A.; Chou, S. Y., Fabrication of 5 nm linewidth and 14 nm pitch features by nanoimprint lithography. *Appl. Phys. Lett.* **2004,** 84, (26), 5299-5301.

8. Austin, M. D.; Zhang, W.; Ge, H. X.; Wasserman, D.; Lyon, S. A.; Chou, S. Y., 6 nm half-pitch lines and 0.04 mu m(2) static random access memory patterns by nanoimprint lithography. *Nanotechnology* **2005,** 16, (8), 1058-1061.

9. Chou, S. Y.; Krauss, P. R., Imprint lithography with sub-10 nm feature size and high throughput. *Microelectron. Eng.* **1997,** 35, (1-4), 237-240.

10. Jung, G. Y.; Johnston-Halperin, E.; Wu, W.; Yu, Z. N.; Wang, S. Y.; Tong, W. M.; Li, Z. Y.; Green, J. E.; Sheriff, B. A.; Boukai, A.; Bunimovich, Y.; Heath, J. R.; Williams, R. S., Circuit fabrication at 17 nm half-pitch by nanoimprint lithography. *Nano Lett.* **2006,** 6, (3), 351-354.

11. *International Technology Roadmap for Semiconductors, 2010 Edition*. Semiconductor Industry Association: San Jose, CA, 2010.

12. Aryal, M.; Buyukserin, F.; Mielczarek, K.; Zhao, X. M.; Gao, J. M.; Zakhidov, A.; Hu, W. C., Imprinted large-scale high density polymer nanopillars for organic solar cells. *J. Vac. Sci. & Technol. B* **2008,** 26, (6), 2562-2566.

13. Aryal, M.; Trivedi, K.; Hu, W. C., Nano-confinement induced chain alignment in ordered P3HT nanostructures defined by nanoimprint lithography. *ACS Nano* **2009,** 3, (10), 3085-3090.

14. Cheyns, D.; Vasseur, K.; Rolin, C.; Genoe, J.; Poortmans, J.; Heremans, P., Nanoimprinted semiconducting polymer films with 50 nm features and their application to organic heterojunction solar cells. *Nanotechnology* **2008,** 19, (42), -.

15. Kim, M. S.; Kim, J. S.; Cho, J. C.; Shtein, M.; Guo, L. J.; Kim, J., Flexible conjugated polymer photovoltaic cells with controlled heterojunctions fabricated using nanoimprint lithography. *Appl. Phys. Lett.* **2007,** 90, (12), -.

16. Ishihara, K.; Fujita, M.; Matsubara, I.; Asano, T.; Noda, S.; Ohata, H.; Hirasawa, A.; Nakada, H.; Shimoji, N., Organic light-emitting diodes with photonic crystals on glass substrate fabricated by nanoimprint lithography. *Appl. Phys. Lett.* **2007,** 90, (11), -.

17. Jeon, S.; Kang, J. W.; Park, H. D.; Kim, J. J.; Youn, J. R.; Shim, J.; Jeong, J. H.; Choi, D. G.; Kim, K. D.; Altun, A. O.; Kim, S. H.; Lee, Y. H., Ultraviolet nanoimprinted polymer nanostructure for organic light emitting diode application. *Appl. Phys. Lett.* **2008,** 92, (22), -.

18. Kim, J. G.; Sim, Y.; Cho, Y.; Seo, J. W.; Kwon, S.; Park, J. W.; Choi, H. G.; Kim, H.; Lee, S., Large area pattern replication by nanoimprint lithography for LCD-TFT application. *Microelectron. Eng.* **2009,** 86, (12), 2427-2431.

19. Broers, A. N.; Hoole, A. C. F.; Ryan, J. M., Electron beam lithography - resolution limits. *Microelectron. Eng.* **1996,** 32, (1-4), 131-142.

20. Cord, B.; Yang, J.; Duan, H. G.; Joy, D. C.; Klingfus, J.; Berggren, K. K., Limiting factors in sub-10 nm scanning-electron-beam lithography. *J. Vac. Sci. & Technol. B* **2009,** 27, (6), 2616-2621.

21. Vieu, C.; Carcenac, F.; Pepin, A.; Chen, Y.; Mejias, M.; Lebib, A.; Manin-Ferlazzo, L.; Couraud, L.; Launois, H., Electron beam lithography: resolution limits and applications. *Appl. Surf. Sci.* **2000,** 164, 111-117.

22. Gottscho, R. A.; Jurgensen, C. W.; Vitkavage, D. J., Microscopic uniformity in plasma-etching. *J. Vac. Sci. & Technol. B* **1992,** 10, (5), 2133-2147.

23. Nakamura, T.; Ogawa, T.; Hosoya, N.; Adachi, S., Effects of thermal oxidation on the photoluminescence properties of porous silicon. *J. Lumin.* **2010,** 130, (4), 682-687.

24. Summers, M. A.; Brett, M. J., Thermal oxidation of periodically aligned silicon square-spirals. *Microelectron. Eng.* **2008,** 85, (5-6), 1222-1224.

25. Sofield, C. J.; Stoneham, A. M., Oxidation of silicon - the Vlsi gate dielectric. *Semiconduct. Sci. Tech.* **1995,** 10, (3), 215-244.

26. Zhang, D.; Kolbas, R. M.; Milewski, P. D.; Lichtenwalner, D. J.; Kingon, A. I.; Zavada, J. M., Light-Emission from Thermally Oxidized Silicon Nanoparticles. *Appl. Phys. Lett.* **1994,** 65, (21), 2684-2686.

27. Sasaki, M.; Kimura, T., The impact of oxidation of channel polysilicon on the trap-density of submicron bottom-gate tfts. *Ieee Electron Dev. Lett.* **1994,** 15, (1), 1-3.

28. Yaung, D. N.; Fang, Y. K.; Chen, C. H.; Hung, C. C.; Tsao, F. C.; Wuu, S. G.; Liang, M. S., To suppress photoexcited current of hydrogenated polysilicon TFTs with low temperature oxidation of polychannel. *Ieee Electron Dev. Lett.* **2001,** 22, (1), 23-25.

29. Hug, T. S.; de Rooij, N. F.; Staufer, U., Fabrication and electroosmotic flow measurements in micro- and nanofluidic channels. *Microfluid. Nanofluid.* **2006,** 2, (2), 117-124.

30. Lai, L.; Irene, E. A., Limiting Si/SiO2 interface roughness resulting from thermal oxidation. *J. Appl. Phys.* **1999,** 86, (3), 1729-1735.

31. Juan, W. H.; Pang, S. W., Control of etch profile for fabrication of Si microsensors. *J. Vac. Sci. & Technol. A* **1996,** 14, (3), 1189-1193.

32. Lee, K. K.; Lim, D. R.; Kimerling, L. C.; Shin, J.; Cerrina, F., Fabrication of ultralow-loss Si/SiO2 waveguides by roughness reduction. *Op. Lett.* **2001,** 26, (23), 1888-1890.

33. Jung, G. Y.; Li, Z. Y.; Wu, W.; Chen, Y.; Olynick, D. L.; Wang, S. Y.; Tong, W. M.; Williams, R. S., Vapor-phase self-assembled monolayer for improved mold release in nanoimprint lithography. *Langmuir* **2005,** 21, (4), 1158-1161.

34. Deal, B. E.; Grove, A. S., General relationship for thermal oxidation of silicon. *J. Appl. Phys.* **1965,** 36, (12), 3770-&.

35. Massoud, H. Z.; Plummer, J. D.; Irene, E. A., Thermal-oxidation of silicon in dry oxygen growth-rate enhancement in the thin regime .1. experimental results. *J. Electrochem. Soc.* **1985,** 132, (11), 2685-2693.

36. Massoud, H. Z.; Plummer, J. D.; Irene, E. A., Thermal-oxidation of silicon in dry oxygen - accurate determination of the kinetic rate constants. *J. Electrochem. Soc.* **1985,** 132, (7), 1745-1753.

37. Jaeger, R. C., *Introduction to Microelectronic Fabrication*. 2nd Edition ed.; Prentice-Hall: Upper Saddle River, NJ, 2002.

38. Massoud, H. Z.; Plummer, J. D.; Irene, E. A., Thermal-oxidation of silicon in dry oxygen - growth-rate enhancement in the thin regime .2. physical-mechanisms. *J. Electrochem. Soc.* **1985,** 132, (11), 2693-2700.

CHAPTER 8

CONCLUSIONS AND FINAL THOUGHTS

The excitement surrounding the field of molecular electronics is the potential to fabricate molecular based electronics with novel electronic characteristics suitable for technological applications. The incorporation of molecules as electronic components into integrated circuits will most likely occur through the formation of molecular contacts with a physical vapor technique, as described in Chapter 2. As proposed and experimentally shown in Chapter 3, metal penetration into molecular layers formed through radical molecular attachment paradigms on carbon contacts depends on the momentum of the depositing metal atoms perpendicular to the molecular layer. In the attempt to fabricate molecular junctions without metal penetration, a novel fabrication technique was conceived, developed, and experimentally shown to minimize the tendency for metal penetration. Through surface diffusion mediated deposition (SDMD), the momentum of depositing metal atoms on the molecular layer is minimized, allowing molecular junctions to be fabricated without molecular damage or metal penetration with a standard metal evaporation technique. The development of the SDMD technique is an excellent example of the how an improved understanding of a failure mechanism, such as metal penetration during metal deposition on a molecular layer, can allow novel fabrication techniques to be developed and successfully employed. SDMD can be used to measure the conductance of a single molecule incorporated in a molecular monolayer or the conductance through "ensemble" junctions containing many molecules. The SDMD technique is the first technique developed with the experimental flexibility to measure and compared molecular conductance through single and many-molecule junctions. As a complementary approach to the study of electronic properties of

molecular layers, in-situ optical absorbance spectroscopy was used to characterize redox events in molecular and polymeric electronic layers. To provide cross paradigm comparison between platforms used to fabricate molecular junctions, a simple oxidation technique was introduced and used to fabricate molecular-scaled electrodes for molecular nanogap junctions. Although the SDMD technique was shown to be an excellent approach to measure molecular conductance, development of a second technique is critical to eliminate artifacts associated with individual experimental platforms.

For all metal/molecule/metal junctions fabricated and characterized in this dissertation, the observed charge transport mechanism was consistent with off-resonant HOMO tunneling. With off-resonant tunneling, the uniqueness of the molecular energy levels is "washed" into an average barrier height, which results in a significant change in the magnitude of the tunneling current but only minor changes in the shape of the J-V response. Unfortunately, the sigmoidal J-V curves associated with off-resonant tunneling is difficult to imagine having technological importance, at least for two terminal electronic devices. Moving beyond off-resonant tunneling regimes, a hot topic of interest is to engineer molecular energy levels within molecular junctions to align with the Fermi energy of the electronic contacts, resulting in resonant transport through molecular junctions. Although resonant tunneling through molecules has been proposed for over 20 years, robust examples of molecular junctions operating in a resonant tunneling regime are not apparent in the literature. The likely reason for the absence of resonant transport is molecular level broadening or high electron charging energy of molecular energy levels preventing alignment of molecular energy levels with the Fermi energies of the

contacts. As shown in Chapter 4, the HOMO of a free DAB molecular appears to be in resonant with the Fermi energy of a graphene contact but when DAB is covalently bonded to the graphene contact the molecular energy levels are modified to an off-resonant condition. At this point, it appears that resonant transport through a molecule with a low density of states attached to an electronic contact with a high density of states would be difficult to achieve, if not impossible, at least with the experimental approaches currently used. Although difficult, solving the issues with energy alignment between the contacts and molecules will undoubtedly lead to new science and technological applications.

Like many scientific or engineering pursuits, the techniques and fundamental science learned during the pursuit of a goal are just as important as the initial goal. For this reason, the effort over the past 37 years to incorporate molecular components into integrated circuits has provided invaluable scientific insights and engineering approaches valuable for the future generation of electronics, even if molecular electronics does not develop into commercial applications. All though not directly discussed in this dissertation, the techniques developed and fundamental science learned in this dissertation is applicable to many fields of research beyond the scope of molecular electronics. Hopefully one day the goal of integrated circuits based on molecular components is reached, but most importantly, the science learned and techniques developed will aid the development of the next generations of electronics.

CHAPTER 9

REFERENCES

CHAPTER 1

1. Aviram, A.; Ratner, M. A., Molecular rectifiers. *Chem. Phys. Lett.* **1974,** 29, (2), 277-283.

2. Adams, D. M.; Brus, L.; Chidsey, C. E. D.; Creager, S.; Creutz, C.; Kagan, C. R.; Kamat, P. V.; Lieberman, M.; Lindsay, S.; Marcus, R. A.; Metzger, R. M.; Michel-Beyerle, M. E.; Miller, J. R.; Newton, M. D.; Rolison, D. R.; Sankey, O.; Schanze, K. S.; Yardley, J.; Zhu, X. Y., Charge transfer on the nanoscale: current status. *J. Phys. Chem. B* **2003,** 107, (28), 6668-6697.

3. Akkerman, H. B.; de Boer, B., Electrical conduction through single molecules and self-assembled monolayers. *J.Phys. Conden. Mat.* **2008,** 20, (1), 20.

4. James, D. K.; Tour, J. M., Electrical measurements in molecular electronics. *Chem. Mater.* **2004,** 16, (23), 4423-4435.

5. McCreery, R. L., Molecular electronic junctions. *Chem. Mater.* **2004,** 16, (23), 4477-4496.

6. McCreery, R. L., Advanced carbon electrode materials for molecular electrochemistry. *Chem. Rev.* **2008,** 108, (7), 2646-2687.

7. Mirkin, C. A.; Ratner, M. A., Molecular Electronics. *Ann. Rev. Phys. Chem.* **1992,** 43, 719-754.

8. McCreery, R. L.; Bergren, A. J., Progress with molecular electronic junctions: meeting experimental challenges in ddesign and fabrication. *Adv. Mater.* **2009,** 21, (43), 4303-4322.

CHAPTER 2

1. Aviram, A.; Ratner, M. A., Molecular Rectifiers *Chem. Phys. Lett.* **1974,** 29, (2), 277-283.

2. Martin, A. S.; Sambles, J. R.; Ashwell, G. J., Molecular Rectifier. *Phys. Rev. Lett.* **1993,** 70, (2), 218-221.

3. Chabinyc, M. L.; Holmlin, R. E.; Haag, R.; Chen, X. X.; Ismagilov, R. F.; Rampi, M. A.; Whitesides, G. M., Molecular electronics with a metal-insulator-metal junction based on self-assembled monolayers. *ACS Sym. Ser.* **2003,** 844, 16-35.

4. Chen, J.; Wang, W.; Klemic, J.; Reed, M. A.; Axelrod, B. W.; Kaschak, D. M.; Rawlett, A. M.; Price, D. W.; Dirk, S. M.; Tour, J. M.; Grubisha, D. S.; Bennett, D. W., Molecular wires, switches, and memories. In *Molecular Electronics Ii*, New York Acad Sciences: New York, 2002; Vol. 960, pp 69-99.

5. Blum, A. S.; Kushmerick, J. G.; Long, D. P.; Patterson, C. H.; Yang, J. C.; Henderson, J. C.; Yao, Y. X.; Tour, J. M.; Shashidhar, R.; Ratna, B. R., Molecularly inherent voltage-controlled conductance switching. *Nat. Mater.* **2005,** 4, (2), 167-172.

6. Chen, F.; He, J.; Nuckolls, C.; Roberts, T.; Klare, J. E.; Lindsay, S., A molecular switch based on potential-induced changes of oxidation state. *Nano Let.* **2005,** 5, (3), 503-506.

7. Kiehl, R. A.; Le, J. D.; Candra, P.; Hoye, R. C.; Hoye, T. R., Charge storage model for hysteretic negative-differential resistance in metal-molecule-metal junctions. *Appl. Phys. Lett.* **2006,** 88, (17).

8. Lortscher, E.; Ciszek, J. W.; Tour, J.; Riel, H., Reversible and controllable switching of a single-molecule junction. *Small* **2006,** 2, (8-9), 973-977.

9. Jang, S. S.; Jang, Y. H.; Kim, Y. H.; Goddard, W. A.; Flood, A. H.; Laursen, B. W.; Tseng, H. R.; Stoddart, J. F.; Jeppesen, J. O.; Choi, J. W.; Steuerman, D. W.; DeIonno, E.; Heath, J. R., Structures and properties of self-assembled monolayers of bistable [2]rotaxanes on Au(111) surfaces from molecular dynamics simulations validated with experiment. *J. Am. Chem. Soc.* **2005,** 127, (5), 1563-1575.

10. Piva, P. G.; DiLabio, G. A.; Pitters, J. L.; Zikovsky, J.; Rezeq, M.; Dogel, S.; Hofer, W. A.; Wolkow, R. A., Field regulation of single-molecule conductivity by a charged surface atom. *Nature* **2005,** 435, (7042), 658-661.

11. Song, H.; Kim, Y.; Jang, Y. H.; Jeong, H.; Reed, M. A.; Lee, T., Observation of molecular orbital gating. *Nature* **2009,** 462, (7276), 1039-1043.

12. Osorio, E. A.; O'Neill, K.; Wegewijs, M.; Stuhr-Hansen, N.; Paaske, J.; Bjornholm, T.; van der Zant, H. S. J., Electronic excitations of a single molecule contacted in a three-terminal configuration. *Nano Lett.* **2007,** 7, (11), 3336-3342.

13. Akkerman, H. B.; de Boer, B., Electrical conduction through single molecules and self-assembled monolayers. *J. Phys. Condens. Matter.* **2008,** 20, (1), 013001-013001.

14. Weiss, E. A.; Kriebel, J. K.; Rampi, M. A.; Whitesides, G. M., The study of charge transport through organic thin films: mechanism, tools and applications. *Phil. Trans. Math. Phys. Eng. Sci.* **2007,** 365, (1855), 1509-1537.

15. McCreery, R. L., Molecular electronic junctions. *Chem. Mater* **2004,** 16, (23), 4477-4496.

16. Datta, S., *Quantum transport atom to transistor*. Cambridge University Press: Cambridge, UK, 2005.

17. Engelkes, V. B.; Beebe, J. M.; Frisbie, C. D., Length-dependent transport in molecular junctions based on SAMs of alkanethiols and alkanedithiols: effect of metal work function and applied bias on tunneling efficiency and contact resistance. *J. Am. Chem. Soc.* **2004,** 126, (43), 14287-14296.

18. Bergren, A. J.; McCreery, R. L.; Stoyanov, S. R.; Gusarov, S.; Kovalenko, A., Electronic characteristics and charge transport mechanisms for large area aromatic molecular junctions. *J. Phys. Chem. C* 114, (37), 15806-15815.

19. Harrison, W. A., *Electronic Structure and the Properties of Solids: The Physics of the Chemical Bond*. Dover: 1989.

20. Bergren, A. J.; McCreery, R. L.; Stoyanov, S. R.; Gusarov, S.; Kovalenko, A., Electronic characteristics and charge transport mechanisms for large area aromatic molecular junctions. *J. Phys. Chem. C* **2009,** 114, (37), 15806-15815.

21. Galperin, M.; Ratner, M. A.; Nitzan, A., Molecular transport junctions: vibrational effects. *J. Phys. Condens. Matter* **2007,** 19, (10), 103201 (81pp).

22. Flood, A. H.; Wong, E. W.; Stoddart, J. F., Models of charge transport and transfer in molecular switch tunnel junctions of bistable catenanes and rotaxanes. *Chem. Phys.* **2006,** 324, (1), 280-290.

23. Buttiker, M., Coherent and sequential tunneling in series barriers. *IBM J. Res. Develop.* **1988,** 132, (1), 63-75.

24. Zhang, H. Y.; Li, X. Q.; Han, P.; Yu, X. Y.; Yan, Y. J., A partially incoherent rate theory of long-range charge transfer in deoxyribose nucleic acid. *J. Chem. Phys.* **2002,** 117, (9), 4578-4584.

25. Nitzan, A.; Jortner, J.; Wilkie, J.; Burin, A. L.; Ratner, M. A., Tunneling time for electron transfer reactions. *J. Phys. Chem. B* **2000,** 104, (24), 5661-5665.

26. Barman, S.; Deng, F. J.; McCreery, R. L., Conducting polymer memory devices based on dynamic doping. *J. Am. Chem. Soc.* **2008,** 130, (33), 11073-11081.

27. Lee, D.; Swager, T. M., Toward isolated molecular wires: A pH-responsive canopied polypyrrole. *Chem. Mater.* **2005,** 17, (18), 4622-4629.

28. Collier, C. P.; Wong, E. W.; Belohradsky, M.; Raymo, F. M.; Stoddart, J. F.; Kuekes, P. J.; Williams, R. S.; Heath, J. R., Electronically configurable molecular-based logic gates. *Science* **1999,** 285, (5426), 391-394.

29. Metzger, R. M.; Baldwin, J. W.; Shumate, W. J.; Peterson, I. R.; Mani, P.; Mankey, G. J.; Morris, T.; Szulczewski, G.; Bosi, S.; Prato, M.; Comito, A.; Rubin, Y., Electrical rectification in a Langmuir-Blodgett monolayer of dimethyanilinoazafullerene sandwiched between gold electrodes. *J. Phys. Chem. B* **2003,** 107, (4), 1021-1027.

30. Zasadzinski, J. A.; Viswanathan, R.; Madsen, L.; Garnaes, J.; Schwartz, D. K., Langmuir-Blodgett films. *Science* **1994,** 263, (5154), 1726-1733.

31. Peterson, I. R., Langmuir-blodgett films. *J. Phys. D-Appl. Phys.* **1990,** 23, (4), 379-395.

32. Kraack, H.; Ocko, B. M.; Perhan, P. S.; Sloutskin, E.; Deutsch, M., Structure of a Langmuir Film on a Liquid Metal. *Science* **2002,** 298, 1404-1407.

33. Porter, M. D.; Bright, T. B.; Allara, D. L.; Chidsey, C. E. D., Spontaneously organized molecular assemblies. 4 Structural characterization of normal-alkyl thiol monolayers on gold by optical ellipsometry, infrared-spectroscopy, and electrochemistry. *J. Am. Chem. Soc.* **1987,** 109, (12), 3559-3568.

34. Xue, Y.; Datta, S.; Hong, S.; Reifenberger, R.; Henderson, J. I.; Kubiak, C. P., Negative differential resistance in the scanning-tunneling spectroscopy of organic molecules. *Phys. Rev. B* **199,** 59, (12), 7852-7855.

35. Xue, Y.; Datta, S.; Hong, S.; Reifenberger, R.; Henderson, J. I.; Kubiak, C. P., Negative differential resistance in the scanning-tunneling spectroscopy of organic molecules. *Phys. Rev. B* **1999,** 59, (12), 7852-7855.

36. Laibinis, P. E.; Whitesides, G. M.; Allara, D. L.; Tao, Y. T.; Parikh, A. N.; Nuzzo, R. G., Comparison of the structures and wetting properties of self-assembled

monolayers of normal-alkanethiols on the coinage metal-surfaces, Cu, Ag, Au. *J. Am. Chem. Soc.* **1991,** 113, (19), 7152-7167.

37. Xiao, X. Y.; Xu, B. Q.; Tao, N. J., Measurement of single molecule conductance: Benzenedithiol and benzenedimethanethiol. *Nano Lett.* **2004,** 4, (2), 267-271.

38. Ferguson, G. S.; Chaudhury, M. K.; Biebuyck, H. A.; Whitesides, G. M., Monolayers on disordered substrates - self-assembly of alkylthrichlorosilanes on surface-modified polyethylene and poly(dimethylsiloxane). *Macromol.* **1993,** 26, (22), 5870-5875.

39. Richter, C. A.; Hacker, C. A.; Richter, L. J.; Kirillov, O. A.; Suehle, J. S.; Vogel, E. M., Interface characterization of molecular-monolayer/SiO2 based molecular junctions. *Solid State Electron.* **2006,** 50, (6), 1088-1096.

40. Wang, D.; Buriak, J. M., Trapping silicon surface-based radicals. *Langmuir* **2006,** 22, (14), 6214-6221.

41. Allongue, P.; Delamar, M.; Desbat, B.; Fagebaume, O.; Hitmi, R.; Pinson, J.; Saveant, J. M., Covalent modification of carbon surfaces by aryl radicals generated from the electrochemical reduction of diazonium salts. *J. Am. Chem. Soc.* **1997,** 119, (1), 201-207.

42. Brooksby, P. A.; Downard, A. J., Multilayer nitroazobenzene films covalently attached to carbon. An AFM and electrochemical study. *J. Phys. Chem. B* **2005,** 109, (18), 8791-8798.

43. Anariba, F.; DuVall, S. H.; McCreery, R. L., Mono- and multilayer formation by diazonium reduction on carbon surfaces monitored with atomic force microscopy "scratching". *Anal. Chem.* **2003,** 75, (15), 3837-3844.

44. Downard, A. J., Electrochemically assisted covalent modification of carbon electrodes. *Electroanal.* **2000,** 12, (14), 1085-1096.

45. Hoekstra, K. J.; Bein, T., Adsorption of zirconium-phosphonate multilayers onto phosphate-derivatized glassy carbon substrates. *Chem. Mater.* **1996,** 8, (8), 1865-1870.

46. Chatgilialoglu, C., (Me3Si)3SiH: twenty years after its discovery as a radical-based reducing agent. *Chem. A* **2008,** 14, 2310-2320.

47. Devaraj, N. K.; Decreau, R. A.; Ebina, W.; Collman, J. P.; Chidsey, C. E. D., Rate of interfacial electron transfer through the 1,2,3-triazole linkage. *J. Phys. Chem. B* **2006,** 110, (32), 15955-15962.

48. Devadoss, A.; Chidsey, C. E. D., Azide-modified graphitic surfaces for covalent attachment of alkyne-terminated molecules by "click" chemistry. *J. Am. Chem. Soc.* **2007,** 129, (17), 5370-+.

49. Bumm, L. A.; Arnold, J. J.; Dunbar, T. D.; Allara, D. L.; Weiss, P. S., Electron transfer through organic molecules. *J. Phys. Chem. B* **1999,** 103, (38), 8122-8127.

50. Datta, S.; Tian, W. D.; Hong, S. H.; Reifenberger, R.; Henderson, J. I.; Kubiak, C. P., Current-voltage characteristics of self-assembled monolayers by scanning tunneling microscopy. *Phys. Rev. Lett.* **1997,** 79, (13), 2530-2533.

51. Tian, W. D.; Datta, S.; Hong, S. H.; Reifenberger, R.; Henderson, J. I.; Kubiak, C. P., Conductance spectra of molecular wires. *J. Chem. Phys.* **1998,** 109, (7), 2874-2882.

52. Donhauser, Z. J.; Mantooth, B. A.; Kelly, K. F.; Bumm, L. A.; Monnell, J. D.; Stapleton, J. J.; Price, D. W.; Rawlett, A. M.; Allara, D. L.; Tour, J. M.; Weiss, P. S., Conductance switching in single molecules through conformational changes. *Science* **2001,** 292, (5525), 2303-2307.

53. Cygan, M. T.; Dunbar, T. D.; Arnold, J. J.; Bumm, L. A.; Shedlock, N. F.; Burgin, T. P.; Jones, L.; Allara, D. L.; Tour, J. M.; Weiss, P. S., Insertion, conductivity, and structures of conjugated organic oligomers in self-assembled alkanethiol monolayers on Au{111}. *J. Am. Chem. Soc.* **1998,** 120, (12), 2721-2732.

54. Wold, D. J.; Frisbie, C. D., Formation of metal-molecule-metal tunnel junctions: Microcontacts to alkanethiol monolayers with a conducting AFM tip. *J. Am. Chem. Soc.* **2000,** 122, (12), 2970-2971.

55. Mantooth, B. A.; Sykes, E. C. H.; Han, P.; Moore, A. M.; Donhauser, Z. J.; Crespi, V. H.; Weiss, P. S., Analyzing the motion of benzene on Au{111}: Single molecule statistics from scanning probe images. *J. Phys. Chem. C* **2007,** 111, (17), 6167-6182.

56. Engelkes, V. B.; Beebe, J. M.; Frisbie, C. D., Analysis of the causes of variance in resistance measurements on metal-molecule-metal junctions formed by conducting-probe atomic force microscopy. *J. Phys. Chem. B* **2005,** 109, (35), 16801-16810.

57. Morita, T.; Lindsay, S., Determination of single molecule conductances of alkanedithiols by conducting-atomic force microscopy with large gold nanoparticles. *J. Am. Chem. Soc.* **2007,** 129, (23), 7262-+.

58. Luo, L.; Frisbie, C. D., Length-dependent conductance of conjugated molecular wires synthesized by stepwise "click" chemistry. *J. Am. Chem. Soc.* **2010,** 132, (26), 8854.

59. Cui, X. D.; Primak, A.; Zarate, X.; Tomfohr, J.; Sankey, O. F.; Moore, A. L.; Moore, T. A.; Gust, D.; Nagahara, L. A.; Lindsay, S. M., Changes in the electronic properties of a molecule when it is wired into a circuit. *J. Phys. Chem. B* **2002,** 106, (34), 8609-8614.

60. Cui, X. D.; Primak, A.; Zarate, X.; Tomfohr, J.; Sankey, O. F.; Moore, A. L.; Moore, T. A.; Gust, D.; Harris, G.; Lindsay, S. M., Reproducible measurement of single-molecule conductivity. *Science* **2001,** 294, (5542), 571-574.

61. Smith, R. K.; Nanayakkara, S. U.; Woehrle, G. H.; Pearl, T. P.; Blake, M. M.; Hutchison, J. E.; Weiss, P. S., Spectral diffusion in the tunneling spectra of ligand-stabilized undecagold clusters. *J. Am. Chem. Soc.* **2006,** 128, (29), 9266-9267.

62. Suzuki, M.; Fujii, S.; Fujihira, M., Measurements of currents through single molecules of alkanedithiols by repeated formation of break junction in scanning tunneling microscopy under ultrahigh vacuum. *Jpn. J. Appl. Phys.* **2006,** 45, (3B), 2041-2044.

63. Xu, B. Q.; Tao, N. J. J., Measurement of single-molecule resistance by repeated formation of molecular junctions. *Science* **2003,** 301, (5637), 1221-1223.

64. Vrouwe, S. A. G.; van der Giessen, E.; van der Molen, S. J.; Dulic, D.; Trouwborst, M. L.; van Wees, B. J., Mechanics of lithographically defined break junctions. *Phys. Rev. B* **2005,** 71, (3).

65. Gonzalez, M. T.; Wu, S. M.; Huber, R.; van der Molen, S. J.; Schonenberger, C.; Calame, M., Electrical conductance of molecular junctions by a robust statistical analysis. *Nano Lett.* **2006,** 6, (10), 2238-2242.

66. Tsutsui, M.; Teramae, Y.; Kurokawa, S.; Sakai, A., High conductance state od single benzenedithiol molecules. *Appl. Phys. Lett.* **2006,** 89, 163111.

67. Strachan, D. R.; Smith, D. E.; Johnston, D. E.; Park, T. H.; Therien, M. J.; Bonnell, D. A.; Johnson, A. T., Controlled fabrication of nanogaps in ambient environment for molecular electronics. *Appl. Phys. Lett.* **2005,** 86, (4), 3.

68. Hadeed, F. O.; Durkan, C., Controlled fabrication of 1-2 nm nanogaps by electromigration in gold and gold-palladium nanowires. *Appl. Phys. Lett.* **2007,** 91, (12), 3.

69. Noguchi, Y.; Nagase, T.; Kubota, T.; Kamikado, T.; Mashiko, S., Fabrication of Au-molecule-Au junctions using electromigration method. *Thin Solid Films* **2006,** 499, (1-2), 90-94.

70. Demarchi, D.; Civera, P.; Piccinini, G.; Cocuzza, M.; Perrone, D., Electrothermal modelling for EIBJ nanogap fabrication. *Electrochim. Acta* **2009,** 54, (25), 6003-6009.

71. Antelmi, D. A.; Connor, J. N.; Horn, R. G., Electrowetting measurements with mercury showing mercury/mica interfacial energy depends on charging. *J. Phys. Chem. B* **2004,** 108, (3), 1030-1037.

72. Nijhuis, C. A.; Reus, W. F.; Whitesides, G. M., Mechanism of rectification in tunneling junctions based on molecules with asymmetric potential drops. *J. Am. Chem. Soc.* **2010,** 132, (51), 18386-18401.

73. Nijhuis, C. A.; Reus, W. F.; Whitesides, G. M., Molecular rectification in metal-sam-metal oxide-metal junctions. *J. Am. Chem. Soc.* **2009,** 131, (49), 17814-17827.

74. Rampi, M. A.; Whitesides, G. M., A versatile experimental approach for understanding electron transport through organic materials. *Chem. Phys.* **2002,** 281, (2-3), 373-391.

75. Akkerman, H. B.; Blom, P. W. M.; de Leeuw, D. M.; de Boer, B., Towards molecular electronics with large-area molecular junctions. *Nature* **2006,** 441, (7089), 69-72.

76. Anariba, F.; McCreery, R. L., Electronic conductance behavior of carbon-based molecular junctions with conjugated structures. *J. Phys. Chem. B* **2002,** 106, (40), 10355-10362.

77. Nowak, A. M.; McCreery, R. L., Characterization of carbon/nitroazobenzene /titanium molecular electronic junctions with photoelectron and Raman spectroscopy. *Anal. Chem.* **2004,** 76, (4), 1089-1097.

78. Richter, C. A.; Hacker, C. A.; Richter, L. J., Electrical and spectroscopic characterization of metal/monolayer/Si devices. *J. Phys. Chem. B* **2005,** 109, (46), 21836-21841.

79. de Boer, B.; Meng, H.; Perepichka, D. F.; Zheng, J.; Frank, M. M.; Chabal, Y. J.; Bao, Z. N., Synthesis and characterization of conjugated mono- and dithiol oligomers and characterization of their self-assembled monolayers. *Langmuir* **2003,** 19, (10), 4272-4284.

80. Jaiswal, A.; Rajagopal, D.; Lakshmikantham, M. V.; Cava, M. P.; Metzger, R. M., Unimolecular rectification of monolayers of CH3C(O)S-C(14)H(28)Q(+)-3CNQ(-) and CH3C(O)S-C(16)H(32)Q(+)-3CNQ(-) organized by self-assembly, Langmuir-Blodgett, and Langmuir-Schaefer techniques. *Phys. Chem. Chem. Phys.* **2007,** 9, (30), 4007-4017.

81. Xu, T.; Morris, T. A.; Szulczewski, G. J.; Metzger, R. M.; Szablewski, M., Current-voltage characteristics of an LB monolayer of didecylammonium tricyanoquinodimethanide measured between macroscopic gold electrodes. *J. Mater. Chem.* **2002,** 12, (10), 3167-3171.

82. Xu, T.; Peterson, I. R.; Lakshmikantham, M. V.; Metzger, R. M., Rectification by a monolayer of hexadecylquinolinium tricyanoquino-dimethanide between gold electrodes. *Angew. Chem. Int. Ed. Engl.* **2001,** 40, (9), 1749-1752.

83. Haick, H.; Cahen, D., Contacting organic molecules by soft methods: Towards molecule-based electronic devices. *Acc. Chem. Res.* **2008,** 41, (3), 359-366.

84. Zhou, C.; Deshpande, R. M.; Reed, M. A.; Jones II, L.; Tour, J. M., Nanoscale metal/self-assembled monolayer/metal heterostructures. *Appl. Phys. Lett.* **1997,** 71, (5), 611-613.

85. Majumdar, N.; Gergel, N.; Routenberg, D.; Bean, J. C.; Harriott, L. R.; Li, B.; Pu, L.; Yao, Y.; Tour, J. M., Nanowell device for the electrical characterization of metal-molecule-metal junctions. *J. Vac. Sci. Technol. B* **2005,** 23, (4), 1417-1421.

86. Kim, T. W.; Wang, G. N.; Lee, H.; Lee, T., Statistical analysis of electronic properties of alkanethiols in metal-molecule-metal junctions. *Nanotechn.* **2007,** 18, (31).

87. Kim, T. W.; Wang, G.; Song, H.; Choi, N. J.; Lee, H.; Lee, T., Charge transport of alkanethiol self-assembled monolayers in micro-via hole devices. *J. Nanosci. Nanotechnol.* **2006,** 6, (11), 3487-3490.

88. Wang, W. Y.; Lee, T.; Kretzschmar, I.; Reed, M. A., Inelastic electron tunneling spectroscopy of an alkanedithiol self-assembled monolayer. *Nano Lett.* **2004,** 4, (4), 643-646.

89. Loo, Y. L.; Lang, D. V.; Rogers, J. A.; Hsu, J. W. P., Electrical contacts to molecular layers by nanotransfer printing. *Nano Lett.* **2003,** 3, (7), 913-917.

90. Niskala, J. R.; You, W., Metal-molecule-metal junctions via PFPE assisted nanotransfer printing (nTP) onto self-assembled monolayers. *J. Am. Chem. Soc.* **2009,** 131, (37), 13202-+.

91. Shimizu, K. T.; Fabbri, J. D.; Jelincic, J. J.; Melosh, N. A., Soft deposition of large-area metal contacts for molecular electronics. *Adv. Mater.* **2006,** 18, (12), 1499-+.

92. Stein, N.; Korobko, R.; Yaffe, O.; Lavan, R. H.; Shpaisman, H.; Tirosh, E.; Vilan, A.; Cahen, D., Nondestructive Contact Deposition for Molecular Electronics: Si-Alkyl//Au Junctions. *J. Phys. Chem. C* 114, (29), 12769-12776.

93. PEDOT:PSS = poly(3,4-ethylenedioxythiophene):poly(styrenesulfonate).

94. Akkerman, H. B.; Naber, R. C. G.; Jongbloed, B.; van Hal, P. A.; Blom, P. W. M.; de Leeuw, D. M.; de Boer, B., Electron tunneling through alkanedithiol self-assembled monolayers in large-area molecular junctions. *Proc. Nat. Acad. Sci. USA* **2007,** 104, (27), 11161-11166.

CHAPTER 3

1. Bergren, A. J.; Harris, K. D.; Deng, F. J.; McCreery, R. L., Molecular electronics using diazonium-derived adlayers on carbon with Cu top contacts: critical analysis of metal oxides and filaments. *J. Phys. Condes. Matter* **2008,** 20, (37), 11.

2. Choi, S. H.; Kim, B.; Frisbie, C. D., Electrical resistance of long conjugated molecular wires. *Science* **2008,** 320, (5882), 1482-1486.

3. Xu, B. Q.; Tao, N. J. J., Measurement of single-molecule resistance by repeated formation of molecular junctions. *Science* **2003,** 301, (5637), 1221-1223.

4. Wang, W.; Scott, A.; Gergel-Hackett, N.; Hacker, C. A.; Janes, D. B.; Richter, C. A., Probing molecules in integrated silicon-molecule-metal junctions by inelastic tunneling spectroscopy. *Nano Lett.* **2008,** 8, (2), 478-484.

5. Richter, C. A.; Stewart, D. R.; Ohlberg, D. A. A.; Williams, R. S., Electrical characterization of Al/AlOx/molecule/Ti/Al devices. *Appl. Phys. A* **2005,** 80, (6), 1355-1362.

6. Love, J. C.; Estroff, L. A.; Kriebel, J. K.; Nuzzo, R. G.; Whitesides, G. M., Self-assembled monolayers of thiolates on metals as a form of nanotechnology. *Chem. Rev.* **2005,** 105, (4), 1103-1169.

7. McCreery, R. L.; Bergren, A. J., Progress with molecular electronic junctions: meeting experimental challenges in design and fabrication. *Adv. Mater.* **2009,** 21, 4303-4322.

8. Walker, A. V.; Tighe, T. B.; Cabarcos, O. M.; Reinard, M. D.; Haynie, B. C.; Uppili, S.; Winograd, N.; Allara, D. L., The Dynamics of Noble Metal Atom Penetration

through Methoxy-Terminated Alkanethiolate Monolayers. *J. Am. Chem. Soc.* **2004,** 126, (12), 3954-3963.

9. Anariba, F.; DuVall, S. H.; McCreery, R. L., Mono- and multilayer formation by diazonium reduction on carbon surfaces monitored with atomic force microscopy "scratching". *Anal. Chem.* **2003,** 75, (15), 3837-3844.

10. Richter, C. A.; Hacker, C. A.; Richter, L. J., Electrical and spectroscopic characterization of metal/monolayer/Si devices. *J. Phys. Chem. B* **2005,** 109, (46), 21836-21841.

11. Walker, A. V.; Tighe, T. B.; Haynie, B. C.; Uppili, S.; Winograd, N.; Allara, D., Chemical Pathways in the Interactions of Reactive Metal Atoms with Organic Surfaces: Vapor Deposition of Ca and Ti on a Methoxy-Terminated Alkanethiolate Monolayer on Au. *J. Phys. Chem. B* **2005,** 109, 11263-11272.

12. Haick, H.; Cahen, D., Making contact: Connecting molecules electrically to the macroscopic world. *Prog. Surf. Sci.* **2008,** 83, (4), 217-261.

13. Zhu, Z. H.; Daniel, T. A.; Maitani, M.; Cabarcos, O. M.; Allara, D. L.; Winograd, N., Controlling gold atom penetration through alkanethiolate self-assembled monolayers on Au {111} by adjusting terminal group intermolecular interactions. *J. Amer. Chem. Soc.* **2006,** 128, (42), 13710-13719.

14. Haick, H.; Ambrico, M.; Ghabboun, J.; Ligonzo, T.; Cahen, D., Contacting organic molecules by metal evaporation. *Phys. Chem. Chem. Phys.* **2004,** 6, (19), 4538-4541.

15. Van Hal, P. A.; Smits, E. C. P.; Geuns, T. C. T.; Akkerman, H. B.; De Brito, B. C.; Perissinotto, S.; Lanzani, G.; Kronemeijer, A. J.; Geskin, V.; Cornil, J.; Blom, P. W. M.; De Boer, B.; De Leeuw, D. M., Upscaling, integration and electrical characterization of molecular junctions. *Nat. Nanotechnol.* **2008,** 3, (12), 749-754.

16. Metzger, R. M.; Xu, T.; Peterson, I. R., Electrical rectification by a monolayer of hexadecylquinolinium tricyanoquinodimethanide measured between macroscopic gold electrodes. *J. Phys. Chem. B* **2001,** 105, (30), 7280-7290.

17. Bergren, A. J.; McCreery, R. L.; Stoyanov, S. R.; Gusarov, S.; Kovalenko, A., Electronic characteristics and charge transport mechanisms for large area aromatic molecular junctions. *J. Phys. Chem. C* **2010,** 114, (37), 15806-15815.

18. Anariba, F.; Steach, J. K.; McCreery, R. L., Strong effects of molecular structure on electron transport in carbon/molecule/copper electronic junctions. *J. Phys. Chem. B* **2005,** 109, (22), 11163-11172.

19. Ranganathan, S.; Steidel, I.; Anariba, F.; McCreery, R. L., Covalently bonded organic monolayers on a carbon substrate: A new paradigm for molecular electronics. *Nano Lett.* **2001,** 1, (9), 491-494.

20. Solak, A. O.; Eichorst, L. R.; Clark, W. J.; McCreery, R. L., Modified carbon surfaces as "organic electrodes" that exhibit conductance switching. *Anal. Chem.* **2003,** 75, (2), 296-305.

21. Anariba, F.; DuVall, S. H.; McCreery, R. L., Mono- and multilayer formation by diazonium reduction on carbon surfaces monitored with atomic force microscopy "scratching". *Anal. Chem.* **2003,** 75, (15), 3837-3844.

22. Allongue, P.; Delamar, M.; Desbat, B.; Fagebaume, O.; Hitmi, R.; Pinson, J.; Saveant, J. M., Covalent modification of carbon surfaces by aryl radicals generated from the electrochemical reduction of diazonium salts. *J. Am. Chem. Soc.* **1997,** 119, (1), 201-207.

23. Ranganathan, S.; McCreery, R. L., Electroanalytical performance of carbon films with near-atomic flatness. *Anal. Chem.* **2001,** 73, (5), 893-900.

24. Pinson, J.; Podvorica, F., Attachment of organic layers to conductive or semiconductive surfaces by reduction of diazonium salts. *Chem. Soc. Reviews* **2005,** 34, 429-439.

25. Baranton, S.; Belanger, D., Electrochemical derivatization of carbon surface by reduction of in situ generated diazonium cations. *J. Phys. Chem. B* **2005,** 109, (51), 24401-24410.

26. McCreery, R., Molecular Electronic Junctions. *Chem. Mater.* **2004,** 16, 4477-4496.

27. Brooksby, P. A.; Downard, A. J., Electrochemical and atomic force microscopy study of carbon surface modification via diazonium reduction in aqueous and acetonitrile solutions. *Langmuir* **2004,** 20, 5038-5045.

28. Kariuki, J. K.; McDermott, M. T., Formation of multilayers on glassy carbon electrodes via the reduction of diazonium salts. *Langmuir* **2001,** 17, 5947-5951.

29. Deinhammer, R. S.; Ho, M.; Anderegg, J. W.; Porter, M. D., Electrochemical oxidation of amine-containing coumpounds - a route to the surface modification of glassy-carbon electrodes. *Langmuir* **1994,** 10, (4), 1306-1313.

30. Downard, A. J.; Garrett, D. J.; Tan, E. S. Q., Microscale Patterning of Organic Films on Carbon Surfaces Using Electrochemistry and Soft Lithography. *Langmuir* **2006,** 22, (25), 10739-10746.

31. Ramsey, J.; Ranganathan, S.; McCreery, R. L.; Zhao, J., Performance comparisons of conventional and line-Focused surface Raman spectrometers. *Appl. Spectrosc.* **2001,** 55, (6), 767-773.

32. Anariba, F.; Steach, J.; McCreery, R., Strong Effects of Molecular Structure on Electron Transport in Carbon/molecule/Copper Electronic Junctions. *J. Phys. Chem B* **2005,** 109, 11163-11172.

33. Braun, A.; Bartsch, M.; Schnyder, B.; Kotz, R.; Haas, O.; Haubold, H. G.; Goerigk, G., X-ray scattering and adsorption studies of thermally oxidized glassy carbon. *J. Non-Cryst. Solids* **1999,** 260, (1-2), 1-14.

34. Wang, Y.; Alsmeyer, D. C.; McCreery, R. L., Raman-spectroscopy of caron materials - structural basis of observed spectra. *Chem. Mater.* **1990,** 2, (5), 557-563.

35. Mahmoud, A. M.; Bergren, A. J.; McCreery, R. L., Derivatization of Optically Transparent Materials with Diazonium Reagents for Spectroscopy of Buried Interfaces. *Anal. Chem.* **2009,** 81, (16), 6972-6980.

36. Jaeger, R. C., *Introduction to Microelectronic Fabrication*. 2nd Edition ed.; Prentice-Hall: Upper Saddle River, NJ, 2002.

37. Abelmann, L.; Lodder, C., Oblique evaporation and surface diffusion. *Thin Solid Films* **1997,** 305, (1-2), 1-21.

CHAPTER 4

1. Ibach, H., *Physics of Surfaces and Interfaces*. 1st ed.; Springer: New York, 2006.

2. Bonifas, A. P.; McCreery, R. L., 'Soft' Au, Pt and Cu contacts for molecular junctions through surface-diffusion-mediated deposition. *Nat. Nanotech.* **2010,** 5, (8), 612-617.

3. Bergren, A. J.; Harris, K. D.; Deng, F. J.; McCreery, R. L., Molecular electronics using diazonium-derived adlayers on carbon with Cu top contacts: critical analysis of metal oxides and filaments. *J. Phys. Condens. Matter* **2008,** 20, (37), 11.

4. Ranganathan, S.; Steidel, I.; Anariba, F.; McCreery, R. L., Covalently bonded organic monolayers on a carbon substrate: A new paradigm for molecular electronics. *Nano Lett.* **2001,** 1, (9), 491-494.

5. Anariba, F.; DuVall, S. H.; McCreery, R. L., Mono- and multilayer formation by diazonium reduction on carbon surfaces monitored with atomic force microscopy "scratching". *Anal. Chem.* **2003,** 75, (15), 3837-3844.

6. Anariba, F.; McCreery, R. L., Electronic Conductance Behavior of Carbon-Based Molecular Junctions with Conjugated Structures. *J. Phys. Chem. B* **2002,** 106, 10355-10362.

7. Dunker, M. F. W.; Starkey, E. B.; Jenkins, G. L., The preparation of some organic mercurials from diazonium borofluorides. *J. Am. Chem. Soc.* **1936,** 58, 2308-2309.

8. Brooksby, P. A.; Downard, A. J., Electrochemical and atomic force microscopy study of carbon surface modification via diazonium reduction in aqueous and acetonitrile solutions. *Langmuir* **2004,** 20, 5038-5045.

9. Pinson, J.; Podvorica, F., Attachment of organic layers to conductive or semiconductive surfaces by reduction of diazonium salts. *Chem. Soc. Reviews* **2005,** 34, 429-439.

10. Kariuki, J. K.; McDermott, M. T., Formation of multilayers on glassy carbon electrodes via the reduction of diazonium salts. *Langmuir* **2001,** 17, 5947-5951.

11. Racz, Z.; Seabaugh, A., Characterization and control of unconfined lateral diffusion under stencil masks. *J. Vac. Sci. Technol. B* **2007,** 25, (3), 857-861.

12. Ohring, M., *Materials Science of Thin Films Deposition and Structure*. 2nd ed.; Academic Press: 2002.

13. Jaeger, R. C., *Introduction to Microelectronic Fabrication*. 2nd Edition ed.; Prentice-Hall: Upper Saddle River, NJ, 2002.

14. Kaiser, N., Review of the fundamentals of thin-film growth. *Appl. Optics* **2002,** 41, (16), 3053-3060.

15. Markov, I.; Kaischew, R., Influence of supersaturation on mode of crystallization on cyrstalline substrates. *Thin Solid Films* **1976,** 32, (1), 163-167.

16. Wynblatt, P., The effects of interfacial segregation on wetting in solid metal-on-metal and metal-on-ceramic systems. *Acta Mater.* **2000,** 48, (18-19), 4439-4447.

17. Doron-Mor, I.; Barkay, Z.; Filip-Granit, N.; Vaskevich, A.; Rubinstein, I., Ultrathin gold island films on silanized glass. morphology and optical properties. *Chem. Mater.* **2004,** 16, (18), 3476-3483.

18. Du, R. B.; Ssenyange, S.; Aktary, M.; McDermott, M. T., Fabrication and characterization of graphitic carbon nanostructures with controllable size, shape, and position. *Small* **2009,** 5, (10), 1162-1168.

19. Abelmann, L.; Lodder, C., Oblique evaporation and surface diffusion. *Thin Solid Films* **1997,** 305, (1-2), 1-21.

20. Liu, C. L.; Cohen, J. M.; Adams, J. B.; Voter, A. F., EAM Study of Surface Self-Diffusion of Single Adatoms of FCC Metals Ni, Cu, Al, Ag, Au, Pd, and Pt. *Surf. Sci.* **1991,** 253, (1-3), 334-344.

21. Speller, S.; Molitor, S.; Rothig, C.; Bomermann, J.; Heiland, W., Surface Mobility on the Au(110) Surface Observed with Scanning Tunneling Microscopy. *Surf. Sci.* **1994,** 312, (1-2), L748-L752.

22. Bhattacharyya, S.; Henley, S. J.; Mendoza, E.; Gomez-Rojas, L.; Allam, J.; Silva, S. R. P., Resonant tunnelling and fast switching in amorphous-carbon quantum-well structures. *Nat. Mater.* **2006,** 5, (1), 19-22.

23. Ittah, N.; Yutsis, I.; Selzer, Y., Fabrication of highly stable configurable metal quantum point contacts. *Nano Lett.* **2008,** 8, (11), 3922-3927.

24. Li, J. Z.; Kanzaki, T.; Murakoshi, K.; Nakato, Y., Metal-dependent conductance quantization of nanocontacts in solution. *Appl. Phys. Lett.* **2002,** 81, (1), 123-125.

25. Agrait, N.; Yeyati, A. L.; van Ruitenbeek, J. M., Quantum properties of atomic-sized conductors. *Phys. Rep.* **2003,** 377, (2-3), 81-279.

26. Zhuang J; L, L., Exchange mechanism for adatom diffusion on metal fcc(100) surfaces. *Phys. Rev. B* **1998,** 58, (3), 1173-1176.

27. Ranganathan, S.; McCreery, R. L., Electroanalytical performance of carbon films with near-atomic flatness. *Anal. Chem.* **2001,** 73, (5), 893-900.

28. Deinhammer, R. S.; Ho, M.; Anderegg, J. W.; Porter, M. D., Electrochemical oxidation of amine-containing coumpounds - a route to the surface modification of glassy-carbon electrodes. *Langmuir* **1994,** 10, (4), 1306-1313.

29. Xu, B. Q.; Tao, N. J. J., Measurement of single-molecule resistance by repeated formation of molecular junctions. *Science* **2003,** 301, (5637), 1221-1223.

30. Muller, K. H., Effect of the atomic configuration of gold electrodes on the electrical conduction of alkanedithiol molecules. *Phys. Rev. B* **2006,** 73, (4), 6.

31. Venkataraman, L.; Klare, J. E.; Tam, I. W.; Nuckolls, C.; Hybertsen, M. S.; Steigerwald, M. L., Single-molecule circuits with well-defined molecular conductance. *Nano Lett.* **2006,** 6, (3), 458-462.

32. He, J.; Sankey, O.; Lee, M.; Tao, N. J.; Li, X. L.; Lindsay, S., Measuring single molecule conductance with break junctions. *Faraday Discuss.* **2006,** 131, 145-154.

33. Mujica, V.; Ratner, M. A., Current-voltage characteristics of tunneling molecular junctions for off-resonance injection. *Chem. Phys.* **2001,** 264, (3), 365-370.

34. Engelkes, V. B.; Beebe, J. M.; Frisbie, C. D., Length-dependent transport in molecular junctions based on SAMs of alkanethiols and alkanedithiols: Effect of metal work function and applied bias on tunneling efficiency and contact resistance. *J. Am. Chem. Soc.* **2004,** 126, (43), 14287-14296.

35. Liu, B.; Bard, A. J.; Mirkin, M. V.; Creager, S. E., Electron transfer at self-assembled monolayers measured by scanning electrochemical microscopy. *J. Am. Chem. Soc.* **2004,** 126, (5), 1485-1492.

36. Akkerman, H. B.; Blom, P. W. M.; de Leeuw, D. M.; de Boer, B., Towards molecular electronics with large-area molecular junctions. *Nature* **2006,** 441, (7089), 69-72.

37. Li, C.; Pobelov, I.; Wandlowski, T.; Bagrets, A.; Arnold, A.; Evers, F., Charge transport in single Au vertical bar alkanedithiol vertical bar Au junctions: Coordination geometries and conformational degrees of freedom. *J. Am. Chem. Soc.* **2008,** 130, (1), 318-326.

38. Vilan, A.; Shanzer, A.; Cahen, D., Molecular control over Au/GaAs diodes. *Nature* **2000,** 404, (6774), 166-168.

39. Holmlin, R. E.; Haag, R.; Chabinyc, M. L.; Ismagilov, R. F.; Cohen, A. E.; Terfort, A.; Rampi, M. A.; Whitesides, G. M., Electron transport through thin organic films in metal-insulator-metal junctions based on self-assembled monolayers. *J. Am. Chem. Soc.* **2001,** 123, (21), 5075-5085.

40. Haick, H.; Ambrico, M.; Ghabboun, J.; Ligonzo, T.; Cahen, D., Contacting organic molecules by metal evaporation. *Phys. Chem. Chem. Phys.* **2004,** 6, (19), 4538-4541.

41. Bergren, A. J.; McCreery, R. L.; Stoyanov, S. R.; Gusarov, S.; Kovalenko, A., Electronic characteristics and charge transport mechanisms for large area aromatic molecular junctions. In *J. Phys. Chem. C*, 2009; Vol. 114, pp 15806-15815.

42. Downard, A. J., Electrochemically assisted covalent modification of carbon electrodes. *Electroanal.* **2000,** 12, (14), 1085-1096.

CHAPTER 5

1. Chen, J.; Reed, M. A.; Rawlett, A. M.; Tour, J. M., Large on-off ratios and negative differential resistance in a molecular electronic device. *Science* **1999,** 286, (5444), 1550-1552.

2. Chen, F.; He, J.; Nuckolls, C.; Roberts, T.; Klare, J. E.; Lindsay, S., A molecular switch based on potential-induced changes of oxidation state. *Nano Lett.* **2005,** 5, (3), 503-506.

3. Kiehl, R. A.; Le, J. D.; Candra, P.; Hoye, R. C.; Hoye, T. R., Charge storage model for hysteretic negative-differential resistance in metal-molecule-metal junctions. *Appl. Phys. Lett.* **2006,** 88, (17).

4. Chen, J.; Wang, W.; Klemic, J.; Reed, M. A.; Axelrod, B. W.; Kaschak, D. M.; Rawlett, A. M.; Price, D. W.; Dirk, S. M.; Tour, J. M.; Grubisha, D. S.; Bennett, D. W., Molecular wires, switches, and memories. In *Molecular Electronics Ii*, New York Acad Sciences: New York, 2002; Vol. 960, pp 69-99.

5. Blum, A. S.; Kushmerick, J. G.; Long, D. P.; Patterson, C. H.; Yang, J. C.; Henderson, J. C.; Yao, Y. X.; Tour, J. M.; Shashidhar, R.; Ratna, B. R., Molecularly inherent voltage-controlled conductance switching. *Nat. Mater.* **2005,** 4, (2), 167-172.

6. Martin, A. S.; Sambles, J. R.; Ashwell, G. J., Molecular Rectifier. *Phys. Rev. Lett.* **1993,** 70, (2), 218-221.

7. Chabinyc, M. L.; Chen, X. X.; Holmlin, R. E.; Jacobs, H.; Skulason, H.; Frisbie, C. D.; Mujica, V.; Ratner, M. A.; Rampi, M. A.; Whitesides, G. M., Molecular rectification in a metal-insulator-metal junction based on self-assembled monolayers. *J. Am. Chem. Soc.* **2002,** 124, (39), 11730-11736.

8. Kalakodimi, R. P.; Nowak, A. M.; McCreery, R. L., Carbon/molecule/metal and carbon/molecule/metal oxide molecular electronic junctions. *Chem. Mat.* **2005,** 17, (20), 4939-4948.

9. Jang, S. S.; Jang, Y. H.; Kim, Y. H.; Goddard, W. A.; Flood, A. H.; Laursen, B. W.; Tseng, H. R.; Stoddart, J. F.; Jeppesen, J. O.; Choi, J. W.; Steuerman, D. W.; DeIonno, E.; Heath, J. R., Structures and properties of self-assembled monolayers of bistable [2]rotaxanes on Au(111) surfaces from molecular dynamics simulations validated with experiment. *J. Am. Chem. Soc.* **2005,** 127, (5), 1563-1575.

10. Lortscher, E.; Ciszek, J. W.; Tour, J.; Riel, H., Reversible and controllable switching of a single-molecule junction. *Small* **2006,** 2, (8-9), 973-977.

11. Gale, R. J., *Spectroelectrochemistry, Theory and Practice* Plenum Press: New York, 1988.

12. Ruiz, V.; Colina, A.; Heras, M. A.; Lopez-Palacios, J., Potential regulation of the spectroelectrochemical response of monolayer-protected gold cluster films by electrolyte composition. *J. Phys. Chem. C* **2007,** 111, (11), 4277-4284.

13. Itoh, T.; McCreery, R. L., In situ Raman spectroelectrochemistry of electron transfer between glassy carbon and a chemisorbed nitroazobenzene monolayer. *J. Am. Chem. Soc.* **2002,** 124, (36), 10894-10902.

14. Nowak, A. M.; McCreery, R. L., In situ Raman spectroscopy of bias-induced structural changes in nitroazobenzene molecular electronic junctions. *J. Am. Chem. Soc.* **2004,** 126, (50), 16621-16631.

15. de Boer, B.; Meng, H.; Perepichka, D. F.; Zheng, J.; Frank, M. M.; Chabal, Y. J.; Bao, Z. N., Synthesis and characterization of conjugated mono- and dithiol oligomers and characterization of their self-assembled monolayers. *Langmuir* **2003,** 19, (10), 4272-4284.

16. Richter, C. A.; Hacker, C. A.; Richter, L. J., Electrical and spectroscopic characterization of metal/monolayer/Si devices. *J. Phys. Chem. B* **2005,** 109, (46), 21836-21841.

17. Richter, C. A.; Hacker, C. A.; Richter, L. J.; Kirillov, O. A.; Suehle, J. S.; Vogel, E. M., Interface characterization of molecular-monolayer/SiO2 based molecular junctions. *Solid-State Electron.* **2006,** 50, (6), 1088-1096.

18. Brown, T. M.; Kim, J. S.; Friend, R. H.; Cacialli, F.; Daik, R.; Feast, W. J., Built-in field electroabsorption spectroscopy of polymer light-emitting diodes incorporating a doped poly(3,4-ethylene dioxythiophene) hole injection layer. *Appl. Phys. Lett.* **1999,** 75, (12), 1679-1681.

19. Ziemelis, K. E.; Hussain, A. T.; Bradley, D. D. C.; Friend, R. H.; Ruhe, J.; Wegner, G., Optical Spectroscopy of Field-Induced Charge in Poly(3-Hexyl Thienylene) Metal-Insulator-Semiconductor Structures - Evidence for Polarons. *Phys. Rev. Lett.* **1991,** 66, (17), 2231-2234.

20. Stipe, B. C.; Rezaei, M. A.; Ho, W., Single-molecule vibrational spectroscopy and microscopy. *Science* **1998,** 280, (5370), 1732-1735.

21. Palmer, R. E.; Rous, P. J., Resances in electron-scattering by molecules on surfaces. *Rev. Mod. Phys.* **1992,** 64, (2), 383-440.

22. Gimzewski, J. K.; Joachim, C., Nanoscale science of single molecules using local probes. *Science* **1999,** 283, (5408), 1683-1688.

23. Lindsay, S. M.; Ratner, M. A., Molecular transport junctions: Clearing mists. *Adv. Mater.* **2007,** 19, (1), 23-31.

24. Solak, A. O.; Ranganathan, S.; Itoh, T.; McCreery, R. L., A mechanism for conductance switching in carbon-based molecular electronic junctions. *Electrochem. Solid State Lett.* **2002,** 5, (8), E43-E46.

25. McCreery, R. L.; Wu, J.; Kalakodimi, R. P., Electron transport and redox reactions in carbon-based molecular electronic junctions. *Phys. Chem. Chem. Phys.* **2006,** 8, (22), 2572-2590.

26. Facchetti, A.; Mushrush, M.; Yoon, M. H.; Hutchison, G. R.; Ratner, M. A.; Marks, T. J., Building blocks for n-type molecular and polymeric electronics. Perfluoroalkyl-versus alkyl-functionalized oligothiophenes (nT; n=2-6). Systematics of thin film microstructure, semiconductor performance, and modeling of majority charge injection in field-effect transistors. *J. Am. Chem. Soc.* **2004,** 126, (42), 13859-13874.

27. Asadi, K.; Gholamrezaie, F.; Smits, E. C. P.; Blom, P. W. M.; de Boer, B., Manipulation of charge carrier injection into organic field-effect transistors by self-assembled monolayers of alkanethiols. *J. Mater. Chem.* **2007,** 17, (19), 1947-1953.

28. Blackstock, J. J.; Rostami, A. A.; Nowak, A. M.; McCreery, R. L.; Freeman, M. R.; McDermott, M. T., Ultraflat carbon film electrodes prepared by electron beam evaporation. *Anal. Chem.* **2004,** 76, (9), 2544-2552.

29. Allongue, P.; Delamar, M.; Desbat, B.; Fagebaume, O.; Hitmi, R.; Pinson, J.; Saveant, J. M., Covalent modification of carbon surfaces by aryl radicals generated from the electrochemical reduction of diazonium salts. *J. Am. Chem. Soc.* **1997,** 119, (1), 201-207.

30. Brooksby, P. A.; Downard, A. J., Multilayer nitroazobenzene films covalently attached to carbon. An AFM and electrochemical study. *J. Phys. Chem. B* **2005,** 109, (18), 8791-8798.

31. Hoekstra, K. J.; Bein, T., Adsorption of zirconium-phosphonate multilayers onto phosphate-derivatized glassy carbon substrates. *Chem. Mat.* **1996,** 8, (8), 1865-1870.

32. Downard, A. J., Electrochemically assisted covalent modification of carbon electrodes. *Electroanal.* **2000,** 12, (14), 1085-1096.

33. Anariba, F.; DuVall, S. H.; McCreery, R. L., Mono- and multilayer formation by diazonium reduction on carbon surfaces monitored with atomic force microscopy "scratching". *Anal. Chem.* **2003,** 75, (15), 3837-3844.

34. Ingle JR., J. D.; Crouch, S. R., *Spectrochemical Analysis*. Prentice Hall: Englewood Cliffs, 1988.

35. Frisch, M. J. T., G. W.; Schlegel, H. B.; Scuseria, G. E.; Robb, M. A.; Cheeseman, J. R.; Montgomery, Jr., J. A.; Vreven, T.; Kudin, K. N.; Burant, J. C.; Millam, J. M.; Iyengar, S. S.; Tomasi, J.; Barone, V.; Mennucci, B.; Cossi, M.; Scalmani,

G.; Rega, N.; Petersson, G. A.; Nakatsuji, H.; Hada, M.; Ehara, M.; Toyota, K.; Fukuda, R.; Hasegawa, J.; Ishida, M.; Nakajima, T.; Honda, Y.; Kitao, O.; Nakai, H.; Klene, M.; Li, X.; Knox, J. E.; Hratchian, H. P.; Cross, J. B.; Bakken, V.; Adamo, C.; Jaramillo, J.; Gomperts, R.; Stratmann, R. E.; Yazyev, O.; Austin, A. J.; Cammi, R.; Pomelli, C.; Ochterski, J. W.; Ayala, P. Y.; Morokuma, K.; Voth, G. A.; Salvador, P.; Dannenberg, J. J.; Zakrzewski, V. G.; Dapprich, S.; Daniels, A. D.; Strain, M. C.; Farkas, O.; Malick, D. K.; Rabuck, A. D.; Raghavachari, K.; Foresman, J. B.; Ortiz, J. V.; Cui, Q.; Baboul, A. G.; Clifford, S.; Cioslowski, J.; Stefanov, B. B.; Liu, G.; Liashenko, A.; Piskorz, P.; Komaromi, I.; Martin, R. L.; Fox, D. J.; Keith, T.; Al-Laham, M. A.; Peng, C. Y.; Nanayakkara, A.; Challacombe, M.; Gill, P. M. W.; Johnson, B.; Chen, W.; Wong, M. W.; Gonzalez, C.; and Pople, J. A. *Gaussian 03, Revision C.02*, Gaussian, Inc.: Wallingford CT, 2004.

36. Kwasniewski, S. P.; Deleuze, M. S.; Francois, J. P., Optical properties of trans-stilbene using semiempirical and time-dependent density functional theory: A comparative study. *Int. J. Quantum Chem.* **2000,** 80, (4-5), 672-680.

37. FTG Software Associates: Princeton, NJ, www.ftgsoftware.com.

38. DiLabio, G. A.; Litwinienko, G.; Lin, S. Q.; Pratt, D. A.; Ingold, K. U., Revised structure for the diphenylaminyl radical: The importance of theory in the assignment of electronic transitions in Ph2X center dot (X = CH, N) and PhY center dot (Y = CH2, NH, O). *J. Phys. Chem. A* **2002,** 106, (48), 11719-11725.

39. Pedersen, S. U.; Christensen, T. B.; Thomasen, T.; Daasbjerg, K., New methods for the accurate determination of extinction and diffusion coefficients of aromatic and

heteroaromatic radical anions in N,N-dimethylformamide. *J. Electroanal. Chem.* **1998,** 454, (1-2), 123-143.

40. Shamsipur, M.; Hemmateenejad, B.; Babaei, A.; Faraj-Sharabiani, L., Use of multivariate curve resolution analysis in the spectroelectrochemistry of 9,10-anthraquinone reduction in dimethylformamide solution. *J. Electroanal. Chem.* **2004,** 570, (2), 227-234.

41. Tian, H.; Bergren, A. J.; McCreery, R. L., UV-vis Spectroelectrochemistry of Chemisorbed Molecular Layers on Optically Transparent Carbon Electrodes. *Appl. Spectrosc.* **2007,** in press.

42. Bard, A. J.; Faulkner, L. R., *Electrochemical Methods Fundamentals and Applications*. 2nd ed.; John Wiley: New York, 2001.

43. Matsuda, H.; Aoki, K.; Tokuda, K., Theory of Electrode-Reactions of Redox Couples Confined to Electrode Surfaces at Monolayer Levels .1. Expression of the Current Potential Relationship for Simple Redox Reactions. *J. Electroanal. Chem.* **1987,** 217, (1), 1-13.

44. Matsuda, H.; Aoki, K.; Tokuda, K., Theory of Electrode-Reactions of Redox Couples Confined to Electrode Surfaces at Monolayer Levels .2. Cyclic Voltammetry and Ac Impedance Measurements. *J. Electroanal. Chem.* **1987,** 217, (1), 15-32.

45. Khodier, S. A.; Sidki, H. M., The effect of the deposition method on the optical properties of SiO2 thin films. *J. Mater. Sci.-Mater. Electron.* **2001,** 12, (2), 107-109.

46. Rao, K. N.; Shivlingappa, L.; Mohan, S., Studies on single layer CeO2 and SiO2 films deposited by rotating crucible electron beam evaporation. *Mater. Sci. Eng. B-Solid State Mater. Adv. Technol.* **2003,** 98, (1), 38-44.

47. Nowak, A. M.; McCreery, R. L., Characterization of carbon/nitroazobenzene/titanium molecular electronic junctions with photoelectron and Raman spectroscopy. *Anal. Chem.* **2004,** 76, (4), 1089-1097.

CHAPTER 6

1. Pickup, P. G.; Kutner, W.; Leidner, C. R.; Murray, R. W., Redox conduction in single and bilayer films of redox polymers. *J. Am. Chem. Soc.* **1984,** 106, (7), 1991-1998.

2. Karl, N., Charge carrier transport in organic semiconductors. *Synth. Met.* **2003,** 133, 649-657.

3. Bredas, J. L.; Street, G. B., Polarons, bipolarons, and solitons in conducting polymers. *Acc. Chem. Res.* **1985,** 18, (10), 309-315.

4. Zuppiroli, L.; Bussac, M. N.; Paschen, S.; Chauvet, O.; Forro, L., Hopping in disordered conducting polymers. *Phys. Rev. B* **1994,** 50, (8), 5196-5203.

5. Salomon, A.; Cahen, D.; Lindsay, S.; Tomfohr, J.; Engelkes, V. B.; Frisbie, C. D., Comparison of electronic transport measurements on organic molecules. *Adv. Mater.* **2004,** 16, (6), 477-477.

6. Adams, D. M.; Brus, L.; Chidsey, C. E. D.; Creager, S.; Creutz, C.; Kagan, C. R.; Kamat, P. V.; Lieberman, M.; Lindsay, S.; Marcus, R. A.; Metzger, R. M.; Michel-Beyerle, M. E.; Miller, J. R.; Newton, M. D.; Rolison, D. R.; Sankey, O.; Schanze, K. S.;

Yardley, J.; Zhu, X. Y., Charge transfer on the nanoscale: current status. *J. Phys. Chem. B* **2003,** 107, (28), 6668-6697.

7. Lindsay, S. M.; Ratner, M. A., Molecular Transport Junctions: Clearing Mists. *Adv. Mat.* **2007,** 19, (1), 23-31.

8. Lee, K.; Cho, S.; Park, S. H.; Heeger, A. J.; Lee, C. W.; Lee, S. H., Metallic transport in polyaniline. *Nature* **2006,** 441, (7089), 65-68.

9. Sugiyasu, K.; Swager, T. M., Conducting-polymer-based chemical sensors: transduction mechanisms. *Bull. Chem. Soc. Jpn.* **2007,** 80, (11), 2074-2083.

10. Barman, S.; Deng, F. J.; McCreery, R. L., Conducting polymer memory devices based on dynamic doping. *J. Am. Chem. Soc.* **2008,** 130, (33), 11073-11081.

11. Lee, D.; Swager, T. M., Toward isolated molecular wires: a ph-responsive canopied polypyrrole. *Chem. Mater.* **2005,** 17, (18), 4622-4629.

12. Janata, J.; Josowicz, M., Conducting polymers in electronic chemical sensors. *Nat. Mater.* **2003,** 2, (1), 19-24.

13. Ramanavicius, A.; Ramanaviciene, A.; Malinauskas, A., Electrochemical sensors based on conducting polymer- polypyrrole. *Electrochim. Acta* **2006,** 51, (27), 6025-6037.

14. Zhao, J. H.; Thomson, D. J.; Pilapil, M.; Pillai, R. G.; Rahman, G. M. A.; Freund, M. S., Field enhanced charge carrier reconfiguration in electronic and ionic coupled dynamic polymer resistive memory. *Nanotechnology* **2010,** 21, (13), 134003.

15. Lu, W.; Fadeev, A. G.; Qi, B. H.; Smela, E.; Mattes, B. R.; Ding, J.; Spinks, G. M.; Mazurkiewicz, J.; Zhou, D. Z.; Wallace, G. G.; MacFarlane, D. R.; Forsyth, S. A.;

Forsyth, M., Use of ionic liquids for pi-conjugated polymer electrochemical devices. *Science* **2002,** 297, (5583), 983-987.

16. Berdichevsky, Y.; Lo, Y. H., Polypyrrole nanowire actuators. *Adv. Mater.* **2006,** 18, (1), 122-125.

17. Xu, L.; Wang, J. X.; Song, Y. L.; Jiang, L., Electrically tunable polypyrrole inverse opals with switchable stopband, conductivity, and wettability. *Chem. Mater.* **2008,** 20, (11), 3554-3556.

18. Saunders, B. R.; Fleming, R. J.; Murray, K. S., Recent advances in the physical and spectroscopic properties of polypyrrole films, particularly those containing transition-metal complexes as counterions. *Chem. Mater.* **1995,** 7, (6), 1082-1094.

19. Neoh, K. G.; Lau, K. K. S.; Wong, V. V. T.; Kang, E. T.; Tan, K. L., Structure and degradation behavior of polypyrrole doped with sulfonate anions of different sizes subjected to undoping redoping cycles. *Chem. Mater.* **1996,** 8, (1), 167-172.

20. Waser, R.; Dittmann, R.; Staikov, G.; Szot, K., Redox-based resistive switching memories - nanoionic mechanisms, prospects, and challenges. *Adv. Mater.* **2009,** 21, (25-26), 2632-2663.

21. Scott, J. C.; Bozano, L. D., Nonvolatile memory elements based on organic materials. *Adv. Mater.* **2007,** 19, (11), 1452-1463.

22. Heremans, P.; Gelinck, G. H.; MuÌˆller, R.; Baeg, K.-J.; Kim, D.-Y.; Noh, Y.-Y., Polymer and Organic Nonvolatile Memory Devices *Chem. Mater.* **2010,** 23, (3), 341-358.

23. Chih-Yuan, L.; Kuan, H., Nonvolatile semiconductor memory revolutionizing information storage. *Nanotechnol. Mag. IEEE* **2009,** 3, (4), 4-9.

24. Nowak, A. M.; McCreery, R. L., Characterization of carbon/nitroazobenzene /titanium molecular electronic junctions with photoelectron and raman spectroscopy. *Anal. Chem.* **2004,** 76, 1089.

25. Wu, J.; Mobley, K.; McCreery, R., Electronic characteristics of fluorene/tiO2 molecular heterojunctions. *J. Chem. Phys.* **2007,** 126, 24704.

26. Wu, J.; McCreery, R. L., Solid-state electrochemistry in molecule/tio2 molecular heterojunctions as the basis of the tio2 ``memristor''. *J. Electrochem. Soc.* **2009,** 156, (1), P29-P37.

27. Panzer, M. J.; Frisbie, C. D., Polymer electrolyte gate dielectric reveals finite windows of high conductivity in organic thin film transistors at high charge carrier densities. *J. Am. Chem. Soc.* **2005,** 127, (19), 6960 - 6961.

28. Panzer, M. J.; Frisbie, C. D., High carrier density and metallic conductivity in poly(3-hexylthiophene) achieved by electrostatic charge injection. *Adv. Funct. Mater.* **2006,** 16, (8), 1051-1056.

29. Panzer, M. J.; Frisbie, C. D., Polymer electrolyte-gated organic field-effect transistors: low-voltage, high-current switches for organic electronics and testbeds for probing electrical transport at high charge carrier density. *J. Am. Chem. Soc.* **2007,** 129, (20), 6599-6607.

30. Kaake, L. G.; Zou, Y.; Panzer, M. J.; Frisbie, C. D.; Zhu, X. Y., Vibrational spectroscopy reveals electrostatic and electrochemical doping in organic thin film transistors gated with a polymer electrolyte dielectric. *J. Am. Chem. Soc.* **2007,** 129, (25), 7824-7830.

31. Skaarup, S.; West, K.; Zachauchristiansen, B.; Jacobsen, T., Insitu spectroscopy of electrochemical doping of polypyrrole. *Synth. Met.* **1992,** 51, (1-3), 267-275.

32. Christensen, P. A.; Hamnett, A., Insitu spectroscopic investigations of the growth, electrocehmical cycling and overoxidation of polyrrole in aqueous-solution. *Electrochim. Acta* **1991,** 36, (8), 1263-1286.

33. Okur, S.; Salzner, U., Theoretical modeling of the doping process in polypyrrole by calculating uv/vis absorption spectra of neutral and charged oligomers. *J. Phys. Chem. A* **2008,** 112, (46), 11842-11853.

34. Turcu, R.; Brie, M.; Leising, G.; Niko, A., Reflection and absorption studies on polypyrrole films electrochemically prepared with different electrolyte types. *Synth. Met.* **1999,** 100, (2), 217-221.

35. Bredas, J. L.; Scott, J. C.; Yakushi, K.; Street, G. B., Polarons and bipolarons in polypyrrole - evolution of the band-structure and optical-spectrum upon doping. *Phys. Rev. B* **1984,** 30, (2), 1023-1025.

36. Genies, E. M.; Pernaut, J. M., Characterization of the radical cation and the dication species of polypyrrole by spectroelectrochemistry - kinetics, redox properties, and strucutral-changes upon electrochemical cycling. *J. Electroanal. Chem.* **1985,** 191, (1), 111-126.

37. Kim, Y. T.; Collins, R. W.; Vedam, K.; Allara, D. L., Real-time spectroscopic ellipsometry - insitu characterization of pyrrole electropolymerization. *J. Electrochem. Soc.* **1991,** 138, (11), 3266-3275.

38. Anariba, F.; DuVall, S. H.; McCreery, R. L., Mono- and multilayer formation by diazonium reduction on carbon surfaces monitored with atomic force microscopy "scratching". *Anal. Chem.* **2003,** 75, (15), 3837-3844.

39. Deinhammer, R. S.; Ho, M.; Anderegg, J. W.; Porter, M. D., Electrochemical oxidation of amine-containing compounds - a route to the surface modification of glassy-carbon electrodes. *Langmuir* **1994,** 10, (4), 1306-1313.

40. Bonifas, A. P.; McCreery, R. L., 'Soft' Au, Pt and Cu contacts for molecular junctions through surface-diffusion-mediated deposition. *Nat. Nanotechnol.* **2010,** 5, (8), 612-617.

41. Anariba, F.; Steach, J.; McCreery, R., Strong effects of molecular structure on electron transport in carbon/molecule/copper electronic junctions. *J. Phys. Chem. B* **2005,** 109, 11163-11172.

42. Jaramillo, A.; Spurlock, L. D.; Young, V.; Brajter-Toth, A., XPS characterization of nanosized overoxidized polypyrrole films on graphite electrodes. *Analyst* **1999,** 124, (8), 1215-1221.

43. Kim, D. Y.; Lee, J. Y.; Kim, C. Y.; Kang, E. T.; Tan, K. L., Difference in doping behavior between polypyrrole films and powders. *Synth. Met.* **1995,** 72, (3), 243-248.

44. Kwasniewski, S. P.; Deleuze, M. S.; Francois, J. P., Optical properties of trans-stilbene using semiempirical and time-dependent density functional theory: a comparative study. *Int. J. Quantum Chem.* **2000,** 80, (4-5), 672-680.

45. DiLabio, G. A.; Litwinienko, G.; Lin, S. Q.; Pratt, D. A.; Ingold, K. U., Revised structure for the diphenylaminyl radical: the importance of theory in the assignment of

electronic transitions in Ph2X center dot (X = CH, N) and PhY center dot (Y = CH2, NH, O). *J. Phys. Chem. A* **2002,** 106, (48), 11719-11725.

46. Nekrasov, A. A.; Ivanov, V. F.; Vannikov, A. V., Analysis of the structure of polyaniline absorption spectra based on spectroelectrochemical data. *J. Electroanal. Chem.* **2000,** 482, (1), 11-17.

47. Malinauskas, A.; Holze, R., Cyclic uv-vis spectrovoltammetry of polyaniline. *Synth. Met.* **1998,** 97, (1), 31-36.

48. Cabala, R.; Skarda, J.; Potje-Kamloth, K., Spectroscopic investigation of thermal treatment of doped polypyrrole. *Phys. Chem. Chem. Phys.* **2000,** 2, (14), 3283-3291.

49. Chakrabarti, S.; Das, B.; Banerji, P.; Banerjee, D.; Bhattacharya, R., Bipolaron saturation in polypyrrole. *Phys. Rev. B* **1999,** 60, (11), 7691-7694.

50. Kaufman, J. H.; Colaneri, N.; Scott, J. C.; Street, G. B., Evolution of Polaron States into Bipolarons in Polypyrrole. *Phys. Rev Lett.* **1984,** 53, 1005-1008.

51. Lee, D.; Swager, T. M., Defining space around conducting polymers: reversible protonic doping of a canopied polypyrrole. *J. Am. Chem. Soc.* **2003,** 125, (23), 6870-6871.

52. Li, Y. F.; Qian, R. Y., Studies on the chemical compensation of conducting polypyrrole by naoh solution. *Synth. Met.* **1988,** 26, (2), 139-151.

53. Jernigan, J. C.; Chidsey, C. E. D.; Murray, R. W., Electrochemistry of polymer-films not immersed in solution - electron-transfer on an ion budget. *J. Am. Chem. Soc.* **1985,** 107, (9), 2824-2826.

54. Saraji, M.; Bakhshi, M., Determination of phenols in water samples by single-drop microextraction followed by in-syringe derivatization and gas chromatography-mass spectrometric detection. *J. Chromatogr. A* **2005,** 1098, (1-2), 30-36.

55. Swager, T. M., The molecular wire approach to sensory signal amplification. *Acc. Chem. Res.* **1998,** 31, (5), 201-207.

56. Lee, D. W.; Swager, T. M., Defining space around conjugated polymers: new vistas in self-amplifying sensory materials. *Synlett* **2004**, (1), 149-154.

57. Hass, K. C.; Schneider, W. F.; Curioni, A.; Andreoni, W., The chemistry of water on alumina surfaces: reaction dynamics from first principles. *Science* **1998,** 282, (5387), 265-268.

58. McHale, J. M.; Auroux, A.; Perrotta, A. J.; Navrotsky, A., Surface energies and thermodynamic phase stability in nanocrystalline aluminas. *Science* **1997,** 277, (5327), 788-791.

59. Kwon, D. H.; Kim, K. M.; Jang, J. H.; Jeon, J. M.; Lee, M. H.; Kim, G. H.; Li, X. S.; Park, G. S.; Lee, B.; Han, S.; Kim, M.; Hwang, C. S., Atomic structure of conducting nanofilaments in TiO2 resistive switching memory. *Nat. Nanotechnol.* **2010,** 5, (2), 148-153.

60. Kim, S.; Choi, Y. K., A comprehensive study of the resistive switching mechanism in Al/TiOx/TiO2/Al-structured RRAM. *IEEE Trans. Electr. Dev.* **2009,** 56, (12), 3049-3054.

CHAPTER 7

1. Li, T.; Hu, W. P.; Zhu, D. B., Nanogap electrodes. *Adv. Mater.* **2010,** 22, (2), 286-300.

2. Reed, M. A.; Zhou, C.; Muller, C. J.; Burgin, T. P.; Tour, J. M., Conductance of a molecular junction. *Science* **1997,** 278, (5336), 252-254.

3. Xiao, X. Y.; Xu, B. Q.; Tao, N. J., Measurement of single molecule conductance: benzenedithiol and benzenedimethanethiol. *Nano Lett.* **2004,** 4, (2), 267-271.

4. Guo, X. F.; Myers, M.; Xiao, S. X.; Lefenfeld, M.; Steiner, R.; Tulevski, G. S.; Tang, J. Y.; Baumert, J.; Leibfarth, F.; Yardley, J. T.; Steigerwald, M. L.; Kim, P.; Nuckolls, C., Chemoresponsive monolayer transistors. *Proc. Natl. Acad. Sci. U. S. A.* **2006,** 103, (31), 11452-11456.

5. Strachan, D. R.; Smith, D. E.; Johnston, D. E.; Park, T. H.; Therien, M. J.; Bonnell, D. A.; Johnson, A. T., Controlled fabrication of nanogaps in ambient environment for molecular electronics. *Appl. Phys. Lett.* **2005,** 86, (4), 3.

6. Guo, L. J., Nanoimprint lithography: Methods and material requirements. *Adv. Mater.* **2007,** 19, (4), 495-513.

7. Austin, M. D.; Ge, H. X.; Wu, W.; Li, M. T.; Yu, Z. N.; Wasserman, D.; Lyon, S. A.; Chou, S. Y., Fabrication of 5 nm linewidth and 14 nm pitch features by nanoimprint lithography. *Appl. Phys. Lett.* **2004,** 84, (26), 5299-5301.

8. Austin, M. D.; Zhang, W.; Ge, H. X.; Wasserman, D.; Lyon, S. A.; Chou, S. Y., 6 nm half-pitch lines and 0.04 mu m(2) static random access memory patterns by nanoimprint lithography. *Nanotechnology* **2005,** 16, (8), 1058-1061.

9. Chou, S. Y.; Krauss, P. R., Imprint lithography with sub-10 nm feature size and high throughput. *Microelectron. Eng.* **1997,** 35, (1-4), 237-240.

10. Jung, G. Y.; Johnston-Halperin, E.; Wu, W.; Yu, Z. N.; Wang, S. Y.; Tong, W. M.; Li, Z. Y.; Green, J. E.; Sheriff, B. A.; Boukai, A.; Bunimovich, Y.; Heath, J. R.; Williams, R. S., Circuit fabrication at 17 nm half-pitch by nanoimprint lithography. *Nano Lett.* **2006,** 6, (3), 351-354.

11. *International Technology Roadmap for Semiconductors, 2010 Edition*. Semiconductor Industry Association: San Jose, CA, 2010.

12. Aryal, M.; Buyukserin, F.; Mielczarek, K.; Zhao, X. M.; Gao, J. M.; Zakhidov, A.; Hu, W. C., Imprinted large-scale high density polymer nanopillars for organic solar cells. *J. Vac. Sci. & Technol. B* **2008,** 26, (6), 2562-2566.

13. Aryal, M.; Trivedi, K.; Hu, W. C., Nano-confinement induced chain alignment in ordered P3HT nanostructures defined by nanoimprint lithography. *ACS Nano* **2009,** 3, (10), 3085-3090.

14. Cheyns, D.; Vasseur, K.; Rolin, C.; Genoe, J.; Poortmans, J.; Heremans, P., Nanoimprinted semiconducting polymer films with 50 nm features and their application to organic heterojunction solar cells. *Nanotechnology* **2008,** 19, (42), -.

15. Kim, M. S.; Kim, J. S.; Cho, J. C.; Shtein, M.; Guo, L. J.; Kim, J., Flexible conjugated polymer photovoltaic cells with controlled heterojunctions fabricated using nanoimprint lithography. *Appl. Phys. Lett.* **2007,** 90, (12), -.

16. Ishihara, K.; Fujita, M.; Matsubara, I.; Asano, T.; Noda, S.; Ohata, H.; Hirasawa, A.; Nakada, H.; Shimoji, N., Organic light-emitting diodes with photonic crystals on glass substrate fabricated by nanoimprint lithography. *Appl. Phys. Lett.* **2007,** 90, (11), -.

17. Jeon, S.; Kang, J. W.; Park, H. D.; Kim, J. J.; Youn, J. R.; Shim, J.; Jeong, J. H.; Choi, D. G.; Kim, K. D.; Altun, A. O.; Kim, S. H.; Lee, Y. H., Ultraviolet nanoimprinted polymer nanostructure for organic light emitting diode application. *Appl. Phys. Lett.* **2008,** 92, (22), -.

18. Kim, J. G.; Sim, Y.; Cho, Y.; Seo, J. W.; Kwon, S.; Park, J. W.; Choi, H. G.; Kim, H.; Lee, S., Large area pattern replication by nanoimprint lithography for LCD-TFT application. *Microelectron. Eng.* **2009,** 86, (12), 2427-2431.

19. Broers, A. N.; Hoole, A. C. F.; Ryan, J. M., Electron beam lithography - resolution limits. *Microelectron. Eng.* **1996,** 32, (1-4), 131-142.

20. Cord, B.; Yang, J.; Duan, H. G.; Joy, D. C.; Klingfus, J.; Berggren, K. K., Limiting factors in sub-10 nm scanning-electron-beam lithography. *J. Vac. Sci. & Technol. B* **2009,** 27, (6), 2616-2621.

21. Vieu, C.; Carcenac, F.; Pepin, A.; Chen, Y.; Mejias, M.; Lebib, A.; Manin-Ferlazzo, L.; Couraud, L.; Launois, H., Electron beam lithography: resolution limits and applications. *Appl. Surf. Sci.* **2000,** 164, 111-117.

22. Gottscho, R. A.; Jurgensen, C. W.; Vitkavage, D. J., Microscopic uniformity in plasma-etching. *J. Vac. Sci. & Technol. B* **1992,** 10, (5), 2133-2147.

23. Nakamura, T.; Ogawa, T.; Hosoya, N.; Adachi, S., Effects of thermal oxidation on the photoluminescence properties of porous silicon. *J. Lumin.* **2010,** 130, (4), 682-687.

24. Summers, M. A.; Brett, M. J., Thermal oxidation of periodically aligned silicon square-spirals. *Microelectron. Eng.* **2008,** 85, (5-6), 1222-1224.

25. Sofield, C. J.; Stoneham, A. M., Oxidation of silicon - the Vlsi gate dielectric. *Semiconduct. Sci. Tech.* **1995,** 10, (3), 215-244.

26. Zhang, D.; Kolbas, R. M.; Milewski, P. D.; Lichtenwalner, D. J.; Kingon, A. I.; Zavada, J. M., Light-Emission from Thermally Oxidized Silicon Nanoparticles. *Appl. Phys. Lett.* **1994,** 65, (21), 2684-2686.

27. Sasaki, M.; Kimura, T., The impact of oxidation of channel polysilicon on the trap-density of submicron bottom-gate tfts. *Ieee Electron Dev. Lett.* **1994,** 15, (1), 1-3.

28. Yaung, D. N.; Fang, Y. K.; Chen, C. H.; Hung, C. C.; Tsao, F. C.; Wuu, S. G.; Liang, M. S., To suppress photoexcited current of hydrogenated polysilicon TFTs with low temperature oxidation of polychannel. *Ieee Electron Dev. Lett.* **2001,** 22, (1), 23-25.

29. Hug, T. S.; de Rooij, N. F.; Staufer, U., Fabrication and electroosmotic flow measurements in micro- and nanofluidic channels. *Microfluid. Nanofluid.* **2006,** 2, (2), 117-124.

30. Lai, L.; Irene, E. A., Limiting Si/SiO2 interface roughness resulting from thermal oxidation. *J. Appl. Phys.* **1999,** 86, (3), 1729-1735.

31. Juan, W. H.; Pang, S. W., Control of etch profile for fabrication of Si microsensors. *J. Vac. Sci. & Technol. A* **1996,** 14, (3), 1189-1193.

32. Lee, K. K.; Lim, D. R.; Kimerling, L. C.; Shin, J.; Cerrina, F., Fabrication of ultralow-loss Si/SiO2 waveguides by roughness reduction. *Op. Lett.* **2001,** 26, (23), 1888-1890.

33. Jung, G. Y.; Li, Z. Y.; Wu, W.; Chen, Y.; Olynick, D. L.; Wang, S. Y.; Tong, W. M.; Williams, R. S., Vapor-phase self-assembled monolayer for improved mold release in nanoimprint lithography. *Langmuir* **2005,** 21, (4), 1158-1161.

34. Deal, B. E.; Grove, A. S., General relationship for thermal oxidation of silicon. *J. Appl. Phys.* **1965,** 36, (12), 3770-&.

35. Massoud, H. Z.; Plummer, J. D.; Irene, E. A., Thermal-oxidation of silicon in dry oxygen growth-rate enhancement in the thin regime .1. experimental results. *J. Electrochem. Soc.* **1985,** 132, (11), 2685-2693.

36. Massoud, H. Z.; Plummer, J. D.; Irene, E. A., Thermal-oxidation of silicon in dry oxygen - accurate determination of the kinetic rate constants. *J. Electrochem. Soc.* **1985,** 132, (7), 1745-1753.

37. Jaeger, R. C., *Introduction to Microelectronic Fabrication*. 2nd Edition ed.; Prentice-Hall: Upper Saddle River, NJ, 2002.

38. Massoud, H. Z.; Plummer, J. D.; Irene, E. A., Thermal-oxidation of silicon in dry oxygen - growth-rate enhancement in the thin regime .2. physical-mechanisms. *J. Electrochem. Soc.* **1985,** 132, (11), 2693-2700.

APPENDIX A

ADDITIONAL RESULTS AND STATISITICS FOR

SINGLE MOLECULE CONDUCTANCE MEASUREMENTS

This appendix contains additional experimental results and statistics for single molecule conductance measurements through the in-situ SDMD technique discussed in Chapter 4. The conductance data and associated statistics are presented first for azobenzene, in order to illustrate the technique with multiple samples and current-time traces, then for a series of aminoalkane molecules, and finally for NAB and DAB, to correspond to the order presented in the Chapter 4. In this appendix, all measured conductance data points were average over one power line cycle (1/60 Hz = 16.7 msec).

Single Molecule Conductance: Azobenzene

Current-time traces for four separate AB/Au junctions are shown in Figure A1 and their corresponding histograms in Figure A2. The histograms were constructed with a bin size of 7.5×10^{-6} G_o. The averages and standard deviations of the four AB junctions are listed in Table S2.

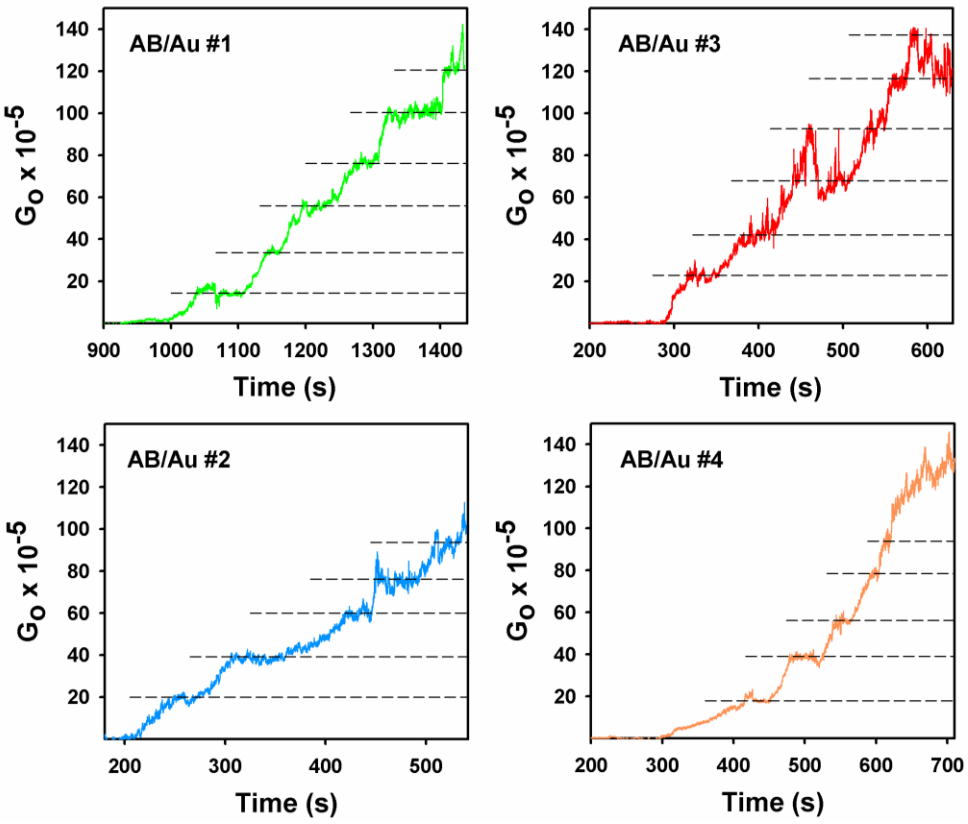

Figure A1: Current-time traces for four separate AB/Au junctions. Each trace represents an individual experiment where the conductance was monitored during the formation of an AB/Au junction. The projected dashed lines are the center of the fitted Lorentzian distributions to their respective histogram. Plateaus in the conductance vs. time traces occur until an additional molecule is incorporated into the growing Au contact. Since the Au-Au spacing (2.885 Å) is less than the molecular spacing in the monolayer, several Au atoms are needed to be added at the molecule/Au interface to incorporate an additional molecule.

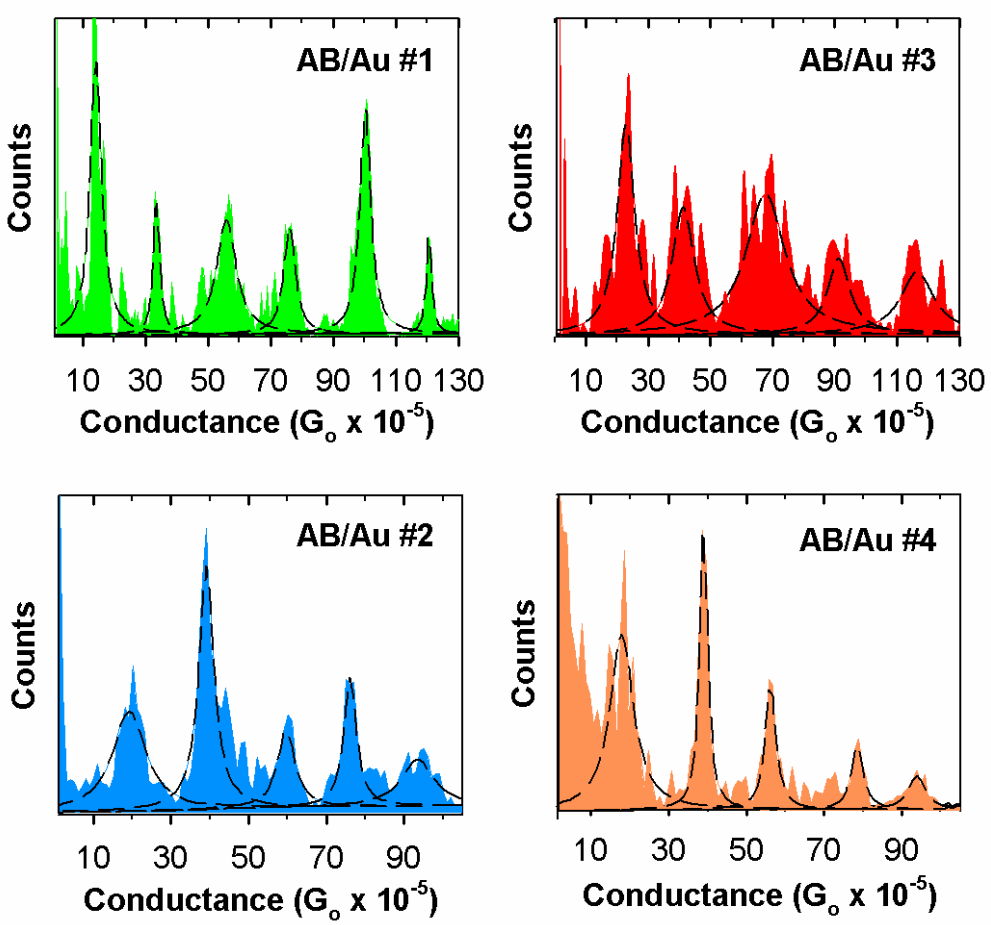

Figure A2: Histograms of the four separate AB/Au junctions shown in Figure A1. Each histogram represents an individual junction where the conductance was monitored during the formation of an AB/Au junction. The histogram peaks were fitted to Lorentzian distributions shown as black dashed lines. The center of the conductance peaks have been projected as dashed lines in Figure A1. All statistics reported in Chapter 4 and this appendix are determined from the conductance peak spacing of the center of the fitted Lorentzian distributions. Substructure within the individual conductance peaks is most likely caused by the various bonding geometries between the molecules and the Au contact.

Single Molecule Conductance: Series of Aminoalkane Molecules

Statistics of eleven separate aminoalkane/Au junctions fabricated through in-situ SDMD is shown in Table A1. For each reported aminoalkane/Au junction, the junction was formed on different regions along the PPF/molecule sidewall. Figure A3 shows a

scatter plot of the measured conductance peak spacing for all the aminoalkane/Au junctions. Figure A4 shows the histograms of the C_4, C_6, and C_{10} where the histograms were constructed from adding the histograms from all junctions for each type of aminoalkane molecule.

Experiment #	Molecule	# of Hisogram Peaks	Average ± Standard Deviation Peak Spacing (G_o x 10^{-5})
1	C_4-NH	8	69.1 ± 6.0
2	C_4-NH	9	73.2 ± 10.1
3	C_4-NH	4	89.2 ± 27.4
4	C_6-NH	7	9.8 ± 1.8
5	C_6-NH	5	9.1 ± 1.2
6	C_6-NH	5	11.7 ± 1.7
7	C_8-NH	7	1.44 ± 0.29
8	C_8-NH	3	1.33 ± 0.08
9	C_8-NH	3	1.34 ± 0.23
10[a]	C_{10}-NH	5	0.33 ± 0.06
11[a]	C_{10}-NH	5	0.32 ± 0.09
Total	C_4-NH	21	75.5 ± 15.4
Total	C_6-NH	17	10.2 ± 1.9
Total	C_8-NH	13	1.39 ± 0.23
Total	C_{10}-NH	10	0.32 ± 0.07

[a] *Data averaged with a simple 7 point moving average*

Table A1: Fitted peak spacing derived from the conductance histograms for three separate C_4 junctions, three separate C_6 junctions, three separate C_8 junctions, and two C_{10} junctions. For each junction, the number of fitted conductance peaks, average conductance peak spacing, and standard deviation of the peak spacing is identified. For C_{10}, the measured conductance data points were signal averaged with a simple seven point moving average. The last four lines in the table are the total number of fitted peaks, average conductance peak spacing, and standard deviation of the peak spacing for all junctions fabricated for an individual type of aminoalkane molecule.

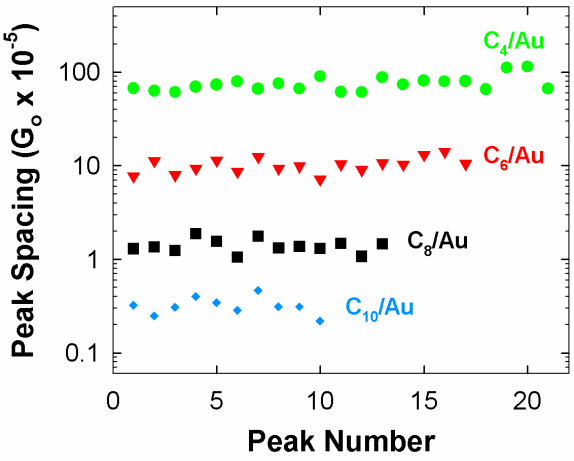

Figure A3: Scatter plot of the measured conductance peak spacing for each aminoalkane junction type. The peak spacing is plotted on a logarithmic scale. The averages and standard deviations of the plotted peak spacings are shown in Table A1.

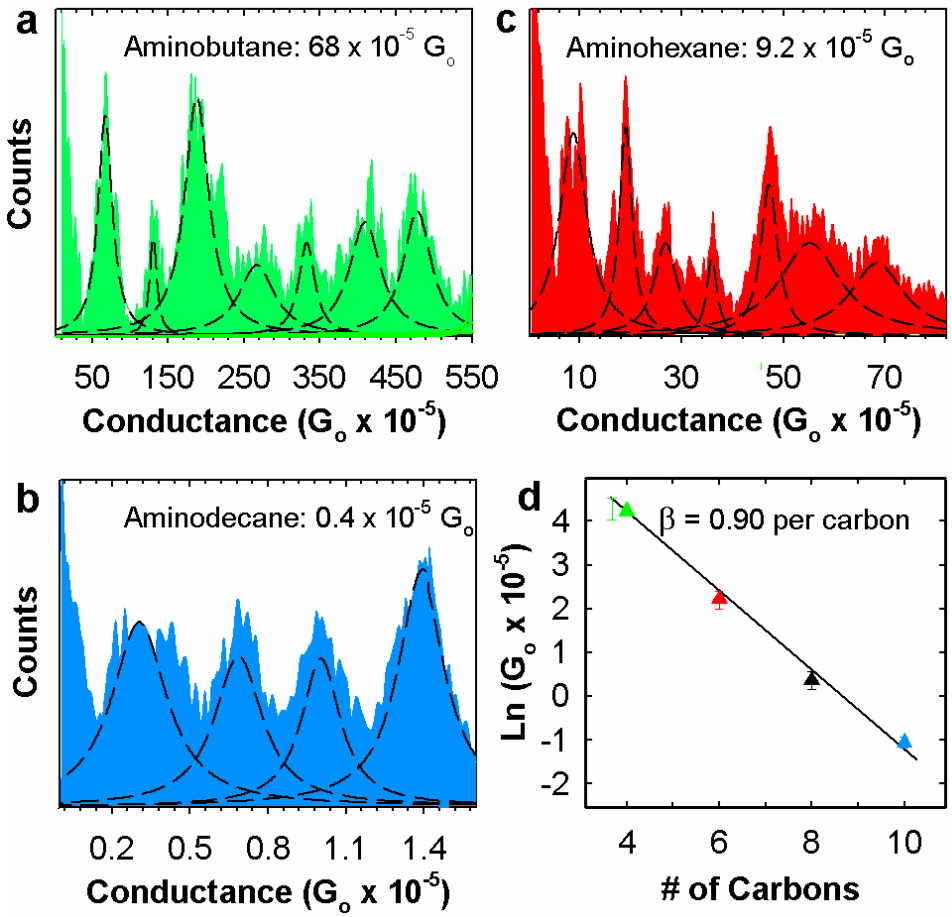

Figure A4: Histograms of C_4, C_6, and C_{10} Au junctions constructed by adding the histograms of separate junctions for each type of aminoalkane molecule. **a,** Constructed from three separate junctions of C_4/Au. **b,** Constructed from three separate junctions of C_6/Au. **c,** Constructed from two separate junctions of C_{10}/Au. **d,** Plot of the logarithm of the measured single molecule conductance vs. the molecular length shows that the conductance exponentially decreases with molecular length which is consistent with off-resonant tunneling.

Single Molecule Conductance: Series of Azobenzene molecules

Statistics of fourteen separate NAB, AB, and DAB Au junctions fabricated through in-situ SDMD are shown in Table A2. For each reported junction, the junction was formed on different regions along the PPF/molecule sidewall. Figure A5 shows a scatter plot of the measured conductance peak spacing for all junctions. Figure A6 shows

histograms of NAB, AB, and DAB Au junctions where the histograms were constructed from adding the histograms from several junctions. Figure A7 shows that the measured single molecule conductance of NAB, AB, and DAB does not correlate with LUMO tunneling through the molecular layers. This result confirms the conclusions in Chapter 4 where the operative charge transport mechanism was shown to be consistent with HOMO tunneling.

Experiment #	Molecule	# of Hisogram Peaks	Average ± Standard Deviation Peak Spacing (G_0 x 10^{-5})
1	NAB	6	2.05 ± 0.21
2	NAB	5	2.00 ± 0.34
3	NAB	7	2.92 ± 0.58
4	NAB	4	1.83 ± 0.10
5	NAB	5	1.47 ± 0.14
6	AB	6	20.1 ± 3.1
7	AB	6	22.9 ± 2.3
8	AB	5	20.1 ± 3.1
9	AB	5	18.7 ± 1.9
10	DAB	8	68.5 +/-9.2
11	DAB	6	69.0 ± 14.9
12	DAB	5	74.2 ± 12.0
13	DAB	3	69.9 ± 10.9
14	DAB	5	65.1 ± 7.5
Total	NAB	27	1.96 ± 0.43
Total	AB	22	20.2 ± 3.1
Total	DAB	27	69.2 ± 10.7

Table A2: Fitted peak spacing derived from the conductance histograms for five separate NAB junctions, four separate AB junctions, and five separate DAB junctions. For each junction, the number of fitted conductance peaks, average conductance peak spacing, and standard deviation of the peak spacing is identified. The last three lines in the table are the total number of fitted peaks, average conductance peak spacing, and standard deviation of the peak spacing for all junctions fabricated for each molecule type.

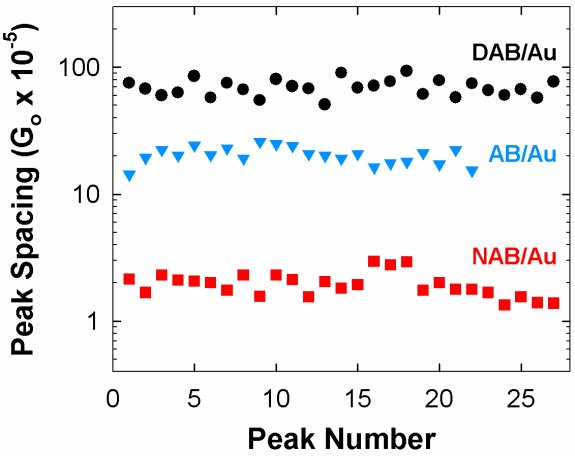

Figure A5: Scatter plot of the measured conductance peak spacing for NAB, AB, and DAB. The peak spacing is plotted on a logarithmic scale. The averages and standard deviations of the plotted peak spacings are shown in Table A2.

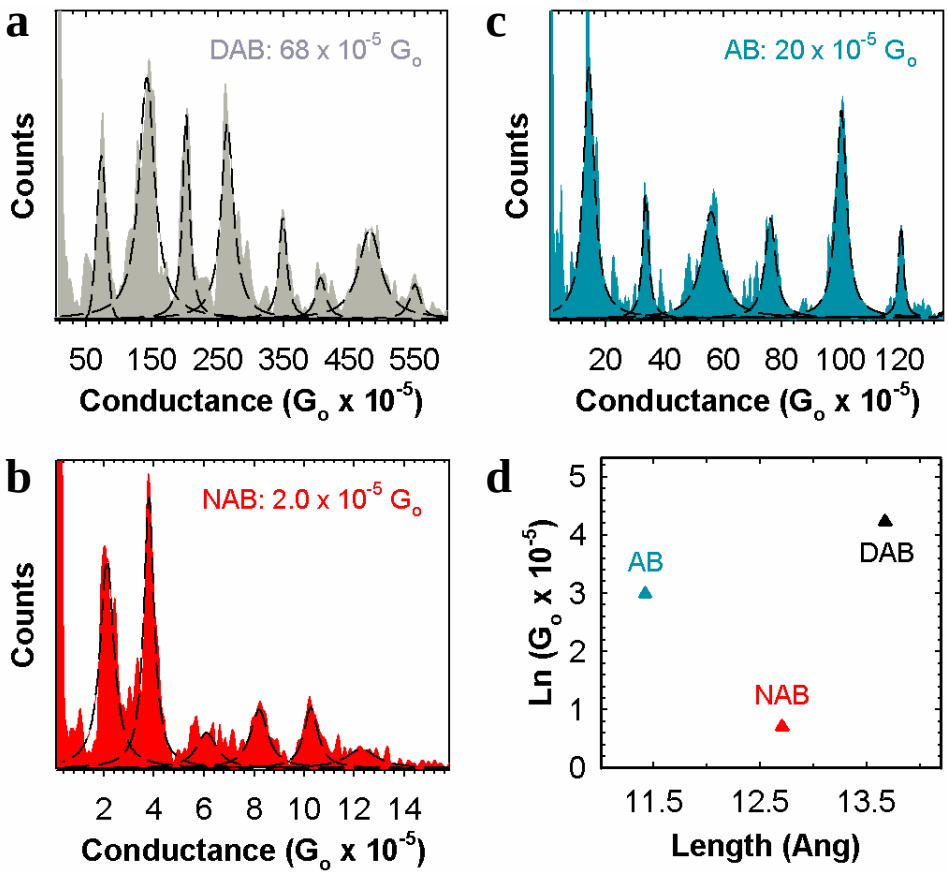

Figure A6: Histograms of the NAB, AB, and DAB Au junctions constructed by adding the histograms of separate junctions for each molecule. **a,** Constructed from five separate junctions of DAB/Au. **b,** Constructed from five separate junctions of NAB/Au. **c,** Constructed from four separate junctions of AB/Au. **d,** Plot of the logarithm of the measured single molecule conductance vs. the molecular length shows that the conductance does not solely depend on the molecular length but also depends on the difference in the tunnel barrier for each molecule.

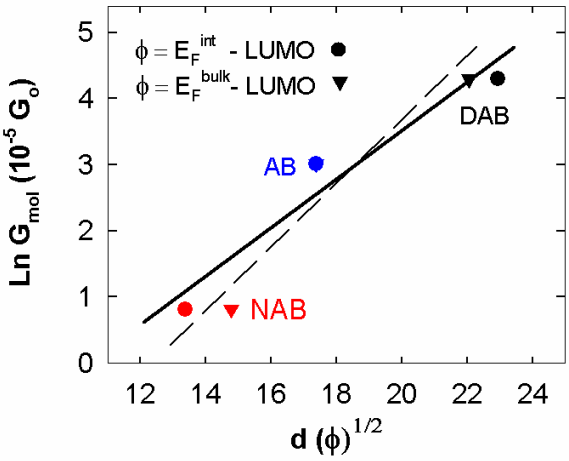

Figure A5: Plot of the natural logarithm of the measured single molecule conductance for NAB, AB, and DAB molecules vs. d $(\varphi)^{1/2}$. The tunneling barrier (φ) was calculated as the energy offset between the molecular LUMO of the free molecules and the bulk Fermi energy (E_F^{bulk}) or the interfacial Fermi energy (E_F^{int}) of the PPF. This plot shows that the molecular conductance is anti-correlated with off-resonant tunneling models, as an increase in d $(\varphi)^{1/2}$ caused an increase in molecular conductance. This result provides strong evidence that HOMO tunneling is the operative charge transport mechanism in the reported azobenzene/Au junctions.